UNIVERSIDADE D
COIMBRA

Daniel Alexandre Cruz Gatões

SMART CONTROL OF DEFECTS IN ADDITIVE MANUFACTURING 3D OBJECTS FUNCTION OF APPLICATION

Doctoral Thesis in Mechanical Engineering, branch of Advanced Production Systems, supervised by Professor Maria Teresa Freire Vieira, submitted to the Department of Mechanical Engineering, Faculty of Sciences and Technology of the University of Coimbra

December 2022

UNIVERSIDADE DE COIMBRA

Smart Control of Defects in Additive Manufacturing 3D Objects Function of Application

Daniel Alexandre Cruz Gatões

Doctoral Thesis in Mechanical Engineering, branch of Advanced Production Systems, supervised by Professor Maria Teresa Freire Vieira, submitted to the Department of Mechanical Engineering, Faculty of Sciences and Technology of the University of Coimbra

December 22, 2022

Abstract

Additive Manufacturing (AM) is a key driver of Industry 4.0, with metallic AM, in particular, driving innovation in the production of materials with tailored geometrical, functional, and aesthetic characteristics. This has led to a new era of material science, providing an understanding of the physical and chemical phenomena related to AM production. However, until recently, the study of defects in additive manufacturing has been considered only as a characteristic of AM processing.

To achieve a repeatable, reliable, and sustainable process, defects in AM must be categorised by their origin, and their consequences on the final 3Dobject properties must be understood. Metal AM defects differ greatly between solid-state-based AM (SSAM) and liquid-state-based AM (LSAM) processes. In SSAM, densification occurs without melting or partial melting, while LSAM achieves full melting, resulting in different mechanisms of defect emergence.

Detecting defects in AM is crucial for qualifying AM parts for critical uses. Non-destructive testing (NDT) is essential, and micro-computed tomography (μCT) is a unique tool for defect observation in small metal parts. μCT is capable of assessing defects with a resolution in the micron order and can be used to construct a digital twin that models 3Dobject mechanical properties and consolidation behaviour, which is essential for critical/structural AM applications.

This work selected two representative processes of SSAM and LSAM for defect observation through μCT: Material Extrusion (MEX) and Selective Laser Melting (SLM). Stainless Steel 316L (AISI) was used due to its high densification, good mechanical properties, and ease of handling and processing.

The work revealed feedstock, shaping, and consolidation defects in SSAM. The influence of shaping parameters was highlighted through a test group encompassing shaping optimisation using μCT. This tool was shown to be useful not only for defect observation but also for defect reduction and optimisation when coupled with a deep understanding of material science.

LSAM research focused on establishing the capacity for defect observation in small parts and assessing its capability when used on highly dense objects with different microstructures. Copper was used as a defect inducer due to its known processing difficulty with conventional SLM. Defect emergence was then compared to a tailored copper:steel alloy

that altered the melting dynamics and material response. μμCT was proven capable of assessing density improvement and adequate alloy mixing.

Finally, LSAM was studied using four stainless steels with increasing carbon content, highlighting the role of microstructure in the mechanical properties of materials processed through SLM. μCT was capable of providing more information than commonly used density methods, assuring high density while being impervious to phasic or microstructural defects.

This work can serve as a guide for adequate material characterisation with the fewest possible steps, streamlining the 3Dobject qualification procedure through the development of standards for NDT qualification of AM-produced 3Dobjects.

Keywords: Additive Manufacturing, Defects, Material Extrusion, Selective Laser Melting, Micro-computed tomography.

Resumo

A fabricação aditiva (FA) é a tecnologia de fabricação principal no contexto da Indústria 4.0. O FA de metais, em particular, tem liderado a inovação científica na produção de materiais com características sob medida, sejam elas geométricas, funcionais ou estéticas. Uma nova era de ciência dos materiais desenvolve-se ao providenciar um conhecimento profundo dos novos fenómenos físico-químicos relacionados com a FA. Não obstante, o estudo de defeitos em FA está apenas atualmente a ser considerado mais que uma característica do FA.

Os defeitos em FA devem ser categorizados pela sua origem. Para além disso, as suas consequências nas propriedades do objecto3D devem ser compreendidas a fim de conseguir um processo reproduzível, fiável e sustentável. Em FA metálico, dois grupos de processos podem ser distinguidos no que concerne os defeitos: FA em estado sólido (FAES) e FA em estado líquido (FAEL). O primeiro grupo, FAES, abrange os processos onde a densificação ocorre sem fusão ou com fusão parcial. Devido a esse facto, os mecanismos de origem de defeitos são largamente diferentes do que a sua contraparte, FAEL, onde há fusão do material.

A importância da deteção de defeitos em FA está ligada à capacidade de observar o tamanho, localização e geometria dos defeitos sem comprometer a aplicabilidade dos objectos3D. Os testes não-destrutivos (TND) são essenciais na qualificação de objetos fabricados por via aditiva com aplicações críticas/estruturais. A microtomografia computadorizada (μCT) é, neste contexto, uma ferramenta única na observação de defeitos em objetos metálicos de pequena dimensão. Capaz de detetar defeitos com uma resolução na ordem do mícron, é, para além disso, capaz de construir um gémeo digital que poderá ser usado na modelação das propriedades mecânicas e comportamento à consolidação, essencial em FA para aplicações críticas/estruturais.

Neste trabalho, duas tecnologias representativas dos processos de FAES e FAEL, para peças de pequena dimensão, foram selecionados para a observação de defeitos através de μCT - Extrusão de Material (MEX do inglês *material extrusion*) e Fusão Seletiva por Laser (SLM do inglês *selective laser melting*). O aço inoxidável 316L (AISI) foi processado através de MEX e SLM. Este material é considerado como uma referência no FA metálico. A ausência de transformações de fase na gama de temperaturas de processamento do MEX e SLM, aliado ao baixo conteúdo de carbono, conduz a uma elevada densificação e boas propriedades mecânicas, mantendo a facilidade de processamento e manuseamento.

Os defeitos em FAES forem estudados, recorrendo aos defeitos originados em MEX. O presente trabalho revelou defeitos originários na matéria-prima, no fabrico e na consolidação. A influência dos parâmetros de fabrico é destacada através da produção de um grupo de testes que engloba a otimização de parâmetros recorrendo ao μCT. Consequentemente, foi mostrado que esta ferramenta poderá não só ser usada para observação de defeitos, mas para a sua redução e otimização, quando aliada a um conhecimento profundo da ciência de materiais.

A investigação em FAEL, neste trabalho, teve dois focos principais. Estabelecer a capacidade de observação de defeitos em peças de pequena dimensão e estabelecer essa capacidade quando usado em objetos de elevada densidade, qualquer que seja a microestrutura obtida. O cobre foi selecionado como um material que induz defeitos devido à sua conhecida problemática em ser processado através de SLM convencional. O aparecimento de defeitos em cobre foi comparado com uma liga de cobre:aço (316L) que alterou fortemente a dinâmica de fusão, e obviamente, a resposta do material. A utilização do μCT foi comprovada como capaz de confirmar o aumento de densidade e a mistura de liga adequada.

Finalmente, o FAEL foi estudado aquando das condições de fabricação são favoráveis a uma elevada densificação, recorrendo a quatro aços inoxidáveis com um crescente quantidade de carbono. Este trabalho sublinhou o papel da microestrutura nas propriedades mecânicas de materiais fabricados por SLM. O μCT foi capaz de acrescentar mais informação que os métodos convencionais de medição de densidade, assegurando a elevada densidade dos objectos3D enquanto imune aos defeitos fásicos/microestruturais.

No geral, este trabalho pode ser considerado como um guia para a caracterização de objetos3D recorrendo ao menor número de passos. Isto pode assim agilizar o procedimento de qualificação de materiais produzidos por FA através do desenvolvimento de normas para a qualificação não-destrutiva destes.

Palavras-chave: Fabrico Aditivo, Defeitos, Extrusão de Material, Fusão Seletiva por Laser, Micro-tomografia.

Acknowledgements

This journey had six wonderful and unforgettable years. From the moment I entered the materials group of CEMMPRE, a life-changing voyage began. It is only fair that I acknowledge all the people that made this work possible.

Undoubtedly and firstly, I must thank Prof. Teresa Vieira. More than an adviser, Prof. Teresa was a scientific mother in the whole sense of the expression. The sincere thirst for knowledge, the renewed energy to be the best, and to be ahead when the resources are not always corresponding, have been an inspiration. For the guidance without a leash, which in conjunction with the responsibilities given, demonstrated trust and exigence again and again. For the ever-present resources and funding, most times at a high cost, whatever the necessities demanded, were essential to making this thesis possible. Additive Manufacturing, my passion, has been a door that was opened to me by Prof. Teresa, and I will always be thankful for that.

To CEMMPRE and to the Department of Mechanical Engineering, my scientific houses, which hosted me and provided the resources that I needed to prosecute this thesis.

To PAMI for providing the funding for the acquisition of the characterisation equipment that is the bulk of this thesis, the micro-computed tomography.

To CDRsp, in the person of Professor Artur Mateus, for the long collaboration and for providing free access to their selective laser melting equipment used for copper production.

To the many colleagues that contributed to this work, Xavi, Renata, Cristiano, Francisco, António, Bernardo and Tomás. Your help was essential for the quality of this work. You allowed me to rest well, knowing that someone always had my back when needed.

To my friends from CEMMPRE. You have been the best daily companions and were always willing to give a hand whenever necessary, and that was not overseen. Your continuous support would encourage anyone to achieve this Herculean task. That I may reciprocate all that you gave me.

Last, I'd like to take my parents and brother for all the support in me to be able to achieve this academic degree; you have been the foundation for all that I am in all that I do. Your work and dedication are never forgotten, and your love made the best times better and the worst times shorter.

For these reasons and more, thank you!

Daniel Gatões

"Weakness of character is the only defect which cannot be amended."

Francois De La Rochefoucauld

"By nature we have no defect that could not become a strength
no strength that could not become a defect"

Johann Wolfgang Von Goethe

"In a true zero-defects approach, there are no unimportant items."

Phil Crosby

Contents

List of Figures

List of Tables

Abbreviations

μCT	Micro-Computed Tomography
3Dobject	Three dimensional object
AM	Additive Manufacturing
BJT	Binder Jetting
CAD	Computer-Aided Design
CHMA	Cyclohexyl Methacrylate
CPVC	Critical Powder Volume Concentration
DED	Direct Energy Deposition
DSC	Differential scanning calorimetry
EDM	Electric Discharge Machining
EBSD	Electron Backscattering Diffraction
FDM	Fused Deposition Modelling
HDPP	High-density Polypropylene
LDPP	Low-density Polypropylene
LOF	Lack of Fusion
LSAM	Liquid-State Additive Manufacturing
MAM	Metal Additive Manufacturing
MEX	Material Extrusion
MIM	Metal Injection Moulding
NDT	Non-Destructive Testing
PA	Polyamide
PBF	Powder Bed Fusion
PE	Polyethylene
PIM	Powder Injection Moulding
PLA	Poly(Lactic Acid)
PO	Polyolefin
POM	Polyacetyl
PP	Polypropylene
PW	Paraffin Wax
SA	Stearic Acid
SDS	Shaping, Debinding and Sintering
SLM	Selective Laser Melting
SLS	Selective Laser Sintering
SSAM	Solid-State Additive Manufacturing
STL	Stereolitography

TPE	Thermoplastic Elastomer
UC	University of Coimbra
ULDPP	Ultra-low-density Polypropylene
VED	Volumetric Energy Density
VF	Virtual Foundry

Introduction

Additive manufacturing (AM) is an inescapable reality. Customers demand celerity, customisation and constant innovation, in pair with local and European goals for sustainability and efficiency. In response to this new worldview, the industry is adapting itself to new pillars of development, achieving what has now been established as a new industrial revolution. This is an inevitable consequence of market demands and the growing cost-efficiency needed in a globalised world, in tandem with the technological advances made in the last decennia. The interconnectivity between all cyber-physical technologies has been designated by industry 4.0 [1, 2]. The new possibilities brought by these technologies have a significant impact on industry standards and methodologies, disrupting conventional fabrication procedures. More efficient materials and manufacturing sustainability, by reducing waste and bringing fast adaptation to ever-changing industries, are developed. AM was the only manufacturing process resulting from this new 4.0 revolution.

Metal additive manufacturing (MAM) had enormous growth in the last few years due to the huge and valuable market for engineered metallic 3Dobjects [3]. The possibilities in MAM are endless: new designs with "impossible" geometries, complex internal systems (e.g. constructal cooling systems); new structural and functional designs of parts/systems/devices; sensorisation for new characteristics and applications; and elimination/reduction of secondary processes, like welding. These are associated with the weight reduction of materials, and decreasing waste, which can effectively improve sustainability [4]. In MAM, there is a possibility of separating the processes into two distinct groups: solid and liquid-state-based additive manufacturing. Solid-state-based AM (SSAM) processes do not reach the material melting temperature or only achieve it partially during sintering. SSAM commonly has the thermal energy applied in a series of fabrication steps to achieve the final part in an SDS approach (Shaping, Debinding and Sintering) [5].

In what concerns liquid-state AM (LSAM), the energy is directly applied to the feedstock, and a metallic 3Dobject with different topographies is achieved. The melting point

is reached (liquid state) in LSAM, which origins a complex history on the final 3Dobject, without post-heat treatment, due to successive heating and cooling cycles of the subsequent layers. 3Dobjects with non-standard properties often result from the processes (e.g. high hardness and tensile strength associated with a low fatigue resistance). Due to the difference in the main thermal energy application in SSAM (e.g. SLS, MEX, BJT...), it is possible during sintering to promote new metallic materials (i.e. intermetallic, high entropy alloys, metamaterials...), as demonstrated by the extensive knowledge from metal injection moulding, for the same conditions.

Whatever the additive processing selected, defects are a characteristic/consequence of the relationship between materials/technology. A non-atomic defect is "an imperfection or abnormality that impairs quality, function or utility" [6]. They can contribute to an enormous influence on the behaviour of the additive manufactured 3Dobject. MAM presents a unique set of recurring defects that are mainly connected to thermal energy material response. Consequently, this means that an effective optimisation of particle powder characteristics and processing parameters can largely mitigate defect formation. However, a completely defect-free 3Dobject is yet impossible to achieve, even with conventional powder manufacturing methodologies. Nevertheless, this may not disqualify the 3Dobjects for use in critical applications. A sustainable knowledge of defect formation causes and consequences must be the focus for the qualification of AM 3Dobjects. Moreover, the properties of 3Dobjects can be predicted if sufficient information is retrieved from the 3Dobject characterisation and accounted for in specific applications. Thus, defects must be observed through a holistic approach, from feedstock to final 3Dobject, and accounting for the consequences of each step in the intended end user application of those objects [7–9].

This major obstacle supports a new age of material science engineering, with a new perspective regarding physical and chemical transformations of the materials throughout these complex manufacturing techniques [10, 11]. Many variables can influence the building of AM parts, and new tools and methods are emerging to respond to these new challenges. Destructive characterisation techniques are, in general, utilised to analyse deterministic defects. However, they can impair the part for further analysis and cannot provide information regarding stochastic defects. X-ray micro-computerised tomography (μCT) is one of the most promising characterisation techniques proving to have an essential role in AM. Denominated a non-destructive testing (NDT) technique, this allows the defect inspection without damaging the analysed object.

CT scan shows the defect by multiple slices. Defect morphology and dimension could

be easily acquired. The defect can also be reconstructed into a 3D model for the best visualisation. Based on the results, μCT can be considered an appropriate way of detecting defects in additive manufactured parts. μCT is suitable to detect stochastic defects, whatever the parameters selected, depending essentially on the analysed material. μCT uses an x-ray beam to radiate a rotating 3Dobject. The attenuation of the beam is detected on a flat panel, and a projection is obtained. A 3D high-resolution representation of the selected volume is achieved by rotating the object as low as hundreds of nanometers [12].

Since reproducibility and properties dispersion are the major drawbacks for qualification MAM parts, μCT must be used as an essential tool for predicting their behaviour when used in conjunction with other characterisation techniques, e.g. SEM (EBSD), from feedstock to 3Dobject. This procedure allows an accurate knowledge of defect location, size and shape. Moreover, it also contributes to the detection of chemical heterogeneities that may occur.

The main thesis work focuses on defect detection for two representative MAM technologies applied to 3Dobject manufacturing: Material Extrusion (MEX) and Selective Laser Melting (SLM). MEX is an emergent technology normally used to build a 3Dobject with low thickness. Its methodology was supported by the extensive knowledge acquired in the homothetic formative process denominated PIM. Through filaments made by feedstocks with a similar high metal/ceramic volume ratio [13]. For this solid technology, state of the art is almost non-existent. The research work performed concerns stochastic defects and is focused on 3Dobjects resulting from liquid processing. SLM is one of the leading established liquid technologies for structural metal AM parts and is already being used in industries like aerospace, medical, and automotive regularly. However, the influence of microstructure from process characteristics is not highlighted.

Whatever the type of additive manufacturing selected, the presence of defects can contribute to an enormous detrimental influence on the mechanical behaviour of the additive manufactured 3Dobject.

The main objective of the present study is to reinforce the quadrinomial: material-processing-properties-structure (micro-) on two of the most promising technologies of additive manufacturing: SLM and MEX. This can support the welcome of the modelling approach, which could contribute definitively to a sustainable methodology.

Motivation and Goals

In the frame of the present thesis, three main goals are achieved, as follows:

- Establishment of μCT as an essential tool for MAM, evaluation of significant defects in SSAM and LSAM;
- Defects analyse on SSAM and LSAM processes: non-ferrous and ferrous metallic materials;
- Highlight the role of the new microstructures resulting from LSAM of the same types of steel (stainless steel).

This research work intends to be a guide to establish an effective qualification methodology for modelling AM 3Dobjects for sustainable applications using advanced characterisation methodologies.

Scientific Outputs

Various scientific works were published as a result of the research presented in this thesis.

Published papers (Appendixes)

- **D. Gatões**, R. Alves, B. Alves, and M. T. Vieira, 'Selective Laser Melting and Mechanical Properties of Stainless Steels', Materials, vol. 15, no. 21, Art. no. 21, Jan. 2022, doi: 10.3390/ma15217575. (Appendix A)
- F. Cerejo, **D. Gatões**, and M. T. Vieira, 'Optimisation of metallic powder filaments for additive manufacturing extrusion (MEX)', Int J Adv Manuf Technol, vol. 115, no. 7–8, pp. 2449–2464, Aug. 2021, doi: 10.1007/s00170-021-07043-0. (Appendix B)
- C. Santos, **D. Gatões**, F. Cerejo, and M. T. Vieira, 'Influence of Metallic Powder Characteristics on Extruded Feedstock Performance for SSAM Additive Manufacturing', Materials, vol. 14, no. 23, p. 7136, Nov. 2021, doi: 10.3390/ma14237136. (Appendix C)
- P. Carreira, **D. Gatões**, N. Alves, A. S. Ramos, and M. T. Vieira, 'Searching New Solutions for NiTi Sensors through Indirect Additive Manufacturing', Materials, vol. 15, no. 14, p. 5007, Jul. 2022, doi: 10.3390/ma15145007. (Appendix D)

Conference papers:

- **D. Gatões**, A. Mateus, C. Azevedo, R. Santos, and M. T. Vieira, 'Adjustment of Selective Laser Melting parameters as function of different geometries of metallic components to improve dimensional and surface quality', in Dimensional Accuracy and Surface Finish in Additive Manufacturing, KU Leuven, BE, October 2017, KU Leuven, BE, Oct. 2017.

Posters:

- **D. Gatões**, R. J. Santos, P. Carreira, A. Mateus, and M. T. Vieira, 'Selective Laser Melting (SLM) Fabrication of Shape Memory NiTi functional parts', presented at the PMTI 2017, Xi'an, China, Sep. 2017. (BEST POSTER AWARD)

- **D. Gatões**, A. Mateus, and M. T. Vieira, 'Surface characteristics of austenitic stainless and tool steel parts manufactured by Selective Laser Melting', presented at the Materials 2017, Aveiro, Portugal, April 2017.

- **D. Gatões**, R. Alves, H. Reis Marques, A. Mateus, and M. T. Vieira, 'Influence of protective atmosphere on the mechanical properties of 420 Stainless Steel (AISI) processed by Selective Laser Melting (SLM)', presented at the Jornada de Materiais Estruturais, Lisbon, Portugal, June 2019.

Thesis Structure

This document is divided into six chapters. The driving force of the document is to demonstrate a practical methodology for the detection and characterisation of defects. The influencing factors that contribute to defect emergence in each selected technology must be laid out. A detailed state of the art of the known physical and chemical phenomena that occur within the process is necessary to understand the defect origin and how to mitigate its occurrence, in the most detailed manner, with a deep connection between additive manufacturing & material and mechanical properties.

After the introduction, Chapters 1 and 2 concern the state of art of additive manufacturing processes and the detection/characterisation of defects focused on additive manufacturing processes.

Chapter 3 concerns the particle powder materials and techniques and methodologies used for the prosecution of the work. Moreover, detailed information regarding 3Dobject production is achieved.

Chapters 4 – Study of the defects in SSAM (MEX) resulting from homemade feedstock filaments and compares it to commercial alternatives. Then, a large test group with different layer heights and strand widths is analysed regarding defect origin. Finally, consolidation analysis is linked to feedstock and green defects, and NDT possibilities are discussed regarding defect prediction and observation. The powder material selected for 3Dobject was stainless steel 316L.

Chapter 5 - Study of the defects in LSAM (SLM) resulting from pure copper with and without addition of stainless steel alloy.

Chapter 6, a case study of SS 3Dobject manufactured by SLM using similar powder and SLM parameters, with maximum densification of 99%, to highlight the effect of different carbon contents in the microstructure and mechanical properties (strain, tensile stress and hardness) induced by the processing.

Finally, the conclusions and detailed future research work that can be achieved from this work are proposed.

Thesis Outline

Figure 1 summarises the thesis outline in a graphical way.

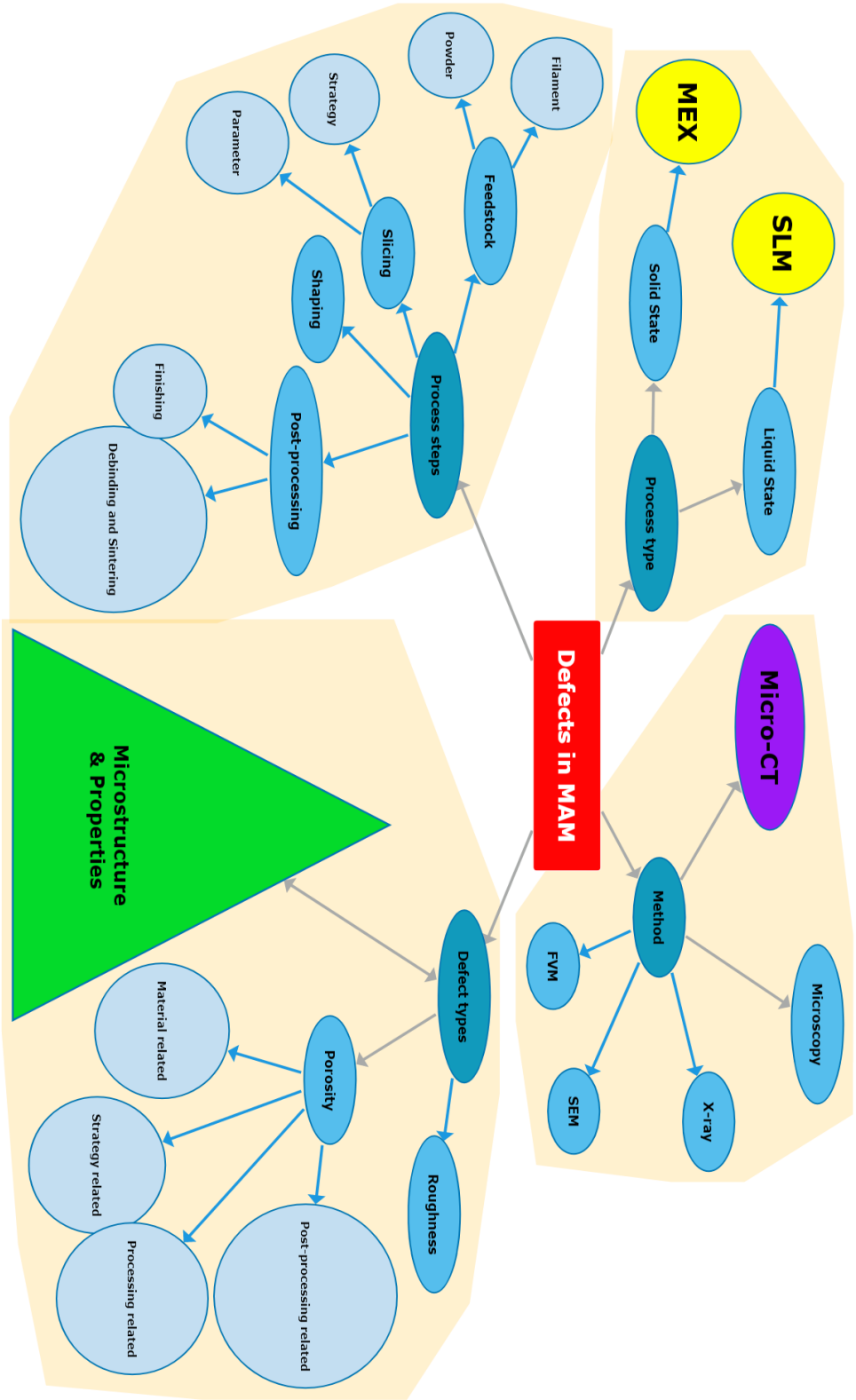

Figure 1: Thesis Outline.

Chapter 1

State of The Art

1.1 Metal Additive Manufacturing

Industry 4.0 has developed from utopia to reality in the last few years. The conjunction of the different disruptive pillars (Additive Manufacturing, Augmented Reality, Autonomous Robots, Big Data and Analytics, Cloud, Cybersecurity, Horizontal and Vertical System Integration, Internet of Things, Simulation) (figure 1.1) are bringing forward the full potential of the industry to adapt itself to a constantly changing world. The global market now depends on an ever-growing exigent customer base who want celerity, customisation, and sustainability without cost increases. The industry has to adapt by being closer, faster, and more innovative. This demands more industry investment in research and development and exclusive know-how that differentiates the product, being at the forefront of innovation [1].

In this new industrial revolution, Additive Manufacturing (also designated over time as additive fabrication, processes, techniques, additive layer manufacturing, layer manufacturing, solid freeform fabrication, and freeform fabrication [15]) is the only disruptive technology present [16]. Its capacity for fast adaptation, customisation, freedom of design, weight and waste reduction is highly appealing for the new industrial perspective [10]. The industry of the future must have agility and flexibility in its production while product complexity is rapidly increasing. AM processes fit these demands by being cost-effective for low production volumes and high-complexity applications. Due to their associated digital process, a rapid adjustment of the design and product iterations can be made with great agility, answering the 4.0 market paradigm since the consumer will have an almost unlimited range of products chosen to customise [17].

Figure 1.1: Pillars of Industry 4.0 [14].

ASTM designated AM as a "process of joining materials to make parts from 3D model data, usually layer upon layer, as opposed to subtractive manufacturing and formative manufacturing methodologies" [15]. The AM process starts with a 3D model in a computer-aided design (CAD) file, later translated into a stereolithography file (STL), rendering the solid surface into a series of triangles, known as tessellation [18]. Although many alternatives to STL have appeared, like AMF, it still is the most relevant file type. This file is usually input into another software, such as *Magics*, *Cura* or *PrusaSlicer*, which defines, through a series of user preferences, the path of the AM tool, deposition parameters, and, if necessary, supports to overhanging features. Then, the 3D model is divided layer by layer with a user-defined height in a step called slicing [19]. When the feedstock is loaded and the resulting file is fed into the machine, the shaping can be started [20]. Low-level user input should be required during processing, which is primarily automatic. However, feedstock and process preparation requires technical prowess, a trained user, and continuous inspection to guarantee that no unexpected error may have occurred during fabrication [21]. Finally, despite some AM techniques being able to attain a near-net-shape 3Dobject after shaping, post-processing is almost always required to achieve a serviceable part (figure 1.2) [22].

AM was initially developed for, and only limited to, polymeric materials. Still, the requirement and possibility of producing metal parts were observed early on, mainly driven by the powder metallurgy knowledge, which is tightly connected to MAM and is the basis for the bulk of these technologies [24]. On a historical note, MAM starts with Selective Laser Sintering (SLS), recognised as the first metal AM technology. It allows the layer-per-layer sintering of metal powder particles. It was first developed 30 years ago

Figure 1.2: General process flow in AM [23].

in Austin, Texas, and the first 3Dobject, "Betsy", made of a mix of copper, tin, and Pb-Sn solder, was achieved by Frayre and Bourell [25]. Due to the low laser power, only partial sintering was attained, resulting in the very high porosity of the 3Dobject. The main technological disadvantage was the low laser material absorption due to the high laser wavelength. The development of more powerful and efficient lasers, with lower wavelengths, like the Ytterbium fibre laser, allowed for the complete melting of powders, achieving higher densities, in a process referred to as Selective Laser Melting (SLM) [26]. In alternative to powder bed fusion processes, Direct Energy Deposition (DED) was then developed as a process not dependent on the powder bed, feeding the feedstock to the energy source directly, like wire and powder [27]. After SLS, Binder Jetting, which uses inkjet printing to deposit metal powder mixed with a binder, was then introduced at MIT.

Metal and its alloys are the main focus of the scientific community, as it carries the most industrial interest, complexity and the most promising added value applications [28]. Moreover, the complexity of the metal additive processes must be recognised when evaluating the scientific importance of these processes [10]. Figure 1.3 shows the number of scientific publications on the themes regarding MAM, mainly SLM, MEX and BJT, as well as the prevalence of steel on these technologies.

MAM can produce virtually unlimited geometric complexity, allowing customisation, improving performance, reducing development times, and eliminating process steps, like tooling, while being low cost and effective [1]. These advantages lead to MAM being applied in several fields, such as aerospace, automotive, and medical devices, where flexibility and functionality are particularly significant [29, 30].

ISO/ASTM classified MAM processes into seven categories: material extrusion, material jetting, binder jetting, sheet lamination, vat polymerisation, powder bed fusion, and

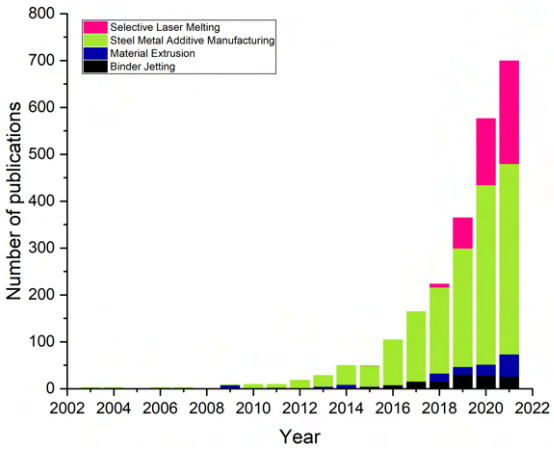

Figure 1.3: Number of AM related articles throughout the last two decades [28].

direct energy deposition [15] (figure 1.4). Two main process groups can be distinguished, solid or liquid-state-based technologies. The main difference between them is that no melting or only partial melting is achieved in the solid state, and complete melting is required in liquid-based additive manufacturing [31].

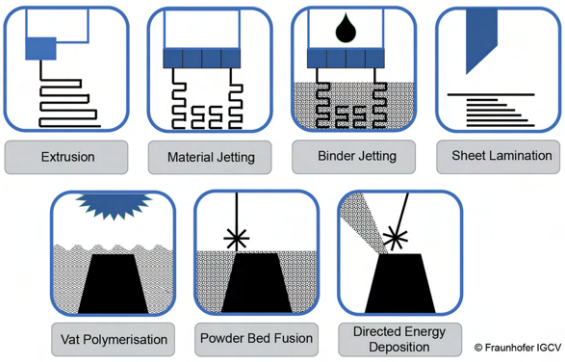

Figure 1.4: Types of AM processes [32].

The most relevant MAM processes are, for liquid-state processes, powder bed fusion (PBF, e.g. SLM) and DED, and for SSAM, MEX and BJT. In PBF, a powder bed is selectively scanned by thermal energy. DED requires that focused thermal energy melts the material as its being deposited. Regarding solid-state processes, the MEX process involves selectively extruding material through an orifice or nozzle, and in BJT, a liquid bonding agent is deposited to join powder.

The growth of MAM has shown great potential, but two of the main hurdles to fully implementing these technologies are the capacity to be repeatable. This is mainly due to

the intrinsic defects related to the complex set of physical and chemical changes brought by a new processing paradigm, which will be explored in this work [33].

Furthermore, the material range for each technology is still minimal, where liquid-state additive processes are more affected in what concerns highly-conductive materials. The challenge in material development when melting (PBF/DED) is related to the complex interactions that occur when there are consecutive material fusion (e.g. the loss of carbon in high-carbon steels due to laser interaction leading to vaporisation) [34]. These paradigm changes from conventional materials result in the choice of metastable materials within processing temperatures that have more reliability and similar characteristics to their subtractive manufactured counterparts [3].

Due to the announced difficulties in controlling material properties, SSAM has been assumed as an alternative. Through polymeric vehicles, indirect processes can emulate debinding the polymeric counterparts, with the difference that they are mainly constituted from metal powders. These metal powders in a polymer matrix must be higher than 50 vol.% [35]. The use of MEX and Binder Jetting is a viable alternative to LSAM since they use a similar manufacturing process to PIM.

1.2 Solid-State Additive Manufacturing

Material extrusion is a process in which material is selectively dispensed through a nozzle or orifice [15]. MEX was initially developed for polymer extrusion under the name of Fused Deposition Modelling (FDM™), marketed by Stratasys, and patented by its co-founder Scott Crump in 1991. However, the term was broad, and the denomination Fused Filament Fabrication (FFF) became more common to refer to MEX using filament as feedstock. However, in the last few years, the process name MEX has become blended with the technology of extruding polymers with metallic or ceramic powder particles in general, in volume concentrations higher than 50% [36, 37].

Metal MEX promotes, by combining a polymeric binder (and additives) with metallic powder particles promotes new capabilities to process metals as polymeric materials. This methodology name evolved with the same pattern as its polymeric counterpart and was first introduced as Fused Deposition of Metals (FDMet) and then associated with FFF, metal FFF (or MF^3) [38].

Moreover, MEX technology is cheap, easy to use, simple and very low-risk while having a wide selection of materials [39]. MEX methodology is inspired by the combination of FFF with PIM, acting as a shaping substitute to injection moulding, in an SDS (shaping, debinding, sintering) approach [40]. In both technologies, a feedstock must be produced. In general, using a polymeric binder with metallic powder particles in a high concentration and, in MEX, some addition of polymeric additives is necessary to promote flexibility and toughness of the filament [41].

MEX involves two steps: first, the materials must be selected considering the rheological properties, which are related to the optimal powder concentration; after, an effective mixing must be achieved using the selected materials. For the next step, shaping, PIM technology differs by injecting the feedstock into a mould, producing a green 3Dobject (object prior to consolidation). Alternatively, MEX uses an FFF 3D printer for the same effect. Subsequently, in a similar method, to produce a fully ceramic/metallic object, the green 3Dobject must undergo a debinding process, creating the denominated brown. The brown must contain no polymeric components, which should have been totally ustulated, and the previously selected shape. Finally, a sintering process consolidates the powders into a fully dense 3Dobject (figure 1.5) [42].

The similarity between the two processes - MEX and PIM - makes them share almost the same advantages and disadvantages. PIM technology requires a mould, making the process extremely expensive for small series and complex 3Dobjects, that require complex

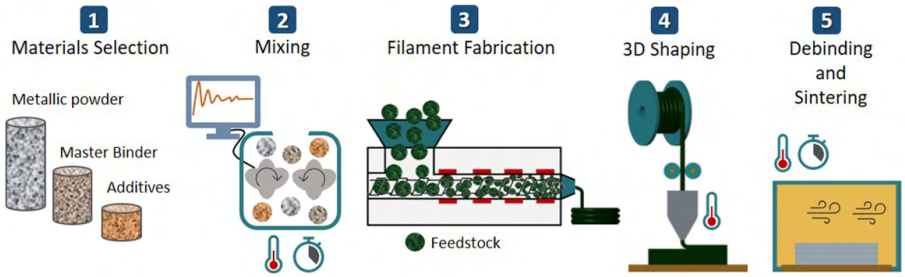

Figure 1.5: Steps in MEX production [42].

moulds, which are very difficult to achieve and make the process more costly. Moreover, AM brought forward the feasibility of 3Dobjects that cannot be produced by any conventional process, which in PIM are governed by mould injection rules. However, the lack of high extruding pressure in MEX leads to higher inter-particulate space, worsening green density [43].

On a historical note, the MEX process seems to have appeared around 1996, with an extensive review of different materials, where are already included several binder system compositions with good performance (silicon nitride, fused silica, piezoelectric ceramics, stainless steel, WC-Co, and alumina) [44]. Nevertheless, a major patent, US Patent 5738817, from 1998, based on the MEX technology for producing metallic and ceramic 3Dobjects from a particulate-binder system [45] and other alternative AM technologies hindered the market growth of MEX. The patent existence and the development of LSAM processes contributed to a decrease in interest in SSAM.

In the last few years, a new interest has been in MEX revealed due to the difficulties and costs of LSAM processes. LSAM difficulties regarding the production of highly thermally conductive and reflective materials; maintaining the original material characteristics and properties; low reproducibility and lack of definitive standards; high equipment costs; hinder the evolution of these methodologies and open the door to SSAM processes (MEX or BJT). Since the patent expiration [46], multiple studies on the feasibility of MEX for different materials have been growing exponentially (c.f. figure 1.3).

Although MEX is commonly associated with FFF, different extrusion types for MEX exist. They are divided into three categories: screw, plunger, or filament-based (Figure 1.6). Each type of feeding system requires different feedstock compositions and constituents in order to guarantee the optimal extrusion conditions [47].

Screw-type extruders use granulates (or pellets) as feedstock. These granulates are achieved after binder and powder mixing through the use of a granulator to achieve

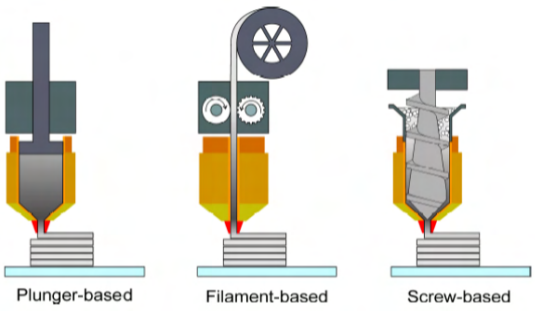

Figure 1.6: Types of extruders used in MEX.

smaller particles. The granulates are fed continuously using the screw rotation, continuously heated above the glass transition temperature (T_g) of the polymer(s) and forced through the nozzle. This extruder aims to guarantee a similar result to PIM when doing MEX through the presence of higher extrusion pressures. Thus, it allows for the use of PIM feedstocks, which guarantees material versatility since the PIM know-how is directly applied without requiring new binder formulas, additives or debinding and sintering test groups. Therefore, the powder content is usually the highest in this type of system [48–50]. Furthermore, it does not need an extra extruding filament or bar feedstock production step. This guarantees no thermal degradation after mixing occurs and facilitates feedstock handling since other feedstocks are usually brittle. Moreover, the granulate size must be carefully controlled (less than 5 mm). Screws for MEX are usually smaller in diameter than in PIM, which affects the feeding system since they are connected to extruding efficiency. Large granulates can hamper the rotation movement due to insufficient heat to soften the material. Small granulates can clog the hopper and, therefore, lead to gaps in extruding, which are detrimental to 3D printing. Air entrapment is the main consequence of irregular feeding of the screw [51–53]. AIM 3D has solved some of these issues by including a pneumatic component to the extrusion, guaranteeing that there is a material buffer to be extruded, but, due to this movement, the feeding is not continuous, unlike the alternative systems. Direct3D also has a pellet extruder in their catalogue [54, 55].

Plunger-based extrusion can use rods or granulates as feedstock, which is loaded into a chamber and then subjected to compression pressure, forcing the material to go through the nozzle. When the plunger is at its end, the printing stops temporarily, the plunger is brought back to its initial position, the new feedstock is loaded into the compression chamber, and the process is repeated. This system has the disadvantage of needing to refill the chamber repeatedly. Feedstocks similar to PIM are usually employed in this technique since higher extrusion pressure allows for the extrusion of higher loads on the

rod feedstock. However, like screw-type extruders, special 3D printers must be bought to allow for the usage of such feedstocks. Commercial systems like Desktop Metal and Markforged assumed the plunger technique for their MEX systems [56, 57].

In traditional filament-type extrusion, a filament based on a feedstock (inorganic material and polymers) is extruded. The filament is fed to a couple of gears that ensure the path from the extruder motor to the nozzle. This is an attractive process since no complicated and expensive equipment development is needed to force the material into the nozzle (ramming), and no specialised printer is needed. This allows the usage of most low-cost 3D printers available in the market. However, it is important to consider that the drive pulley force on the filament may cause plastic deformation and buckle, clogging the extruder and stopping the process, losing overall process reliability. The filament production process must consider this behaviour and guarantee sufficient friction with the pulleys and shear resistance during spooling. This gives rise to many constraints for the binder system composition [51, 58, 59]. The last type of extrusion will be the main focus of this thesis due to its prevalence, low cost, and no commercial attachment being needed while maintaining the possibility of feedstock modification.

Metal MEX with filament is defined by three steps (figure 1.5):

1. Feedstock production (1.2.1), which encompasses: materials selection (powder, binder, and additives); torque value in mixing; and filament fabrication;

2. Shaping using a conventional 3D printer equipment (1.2.2), optimising the inputted process parameters;

3. Debinding and sintering (1.2.3) or consolidation, where the organic component is eliminated and a final metallic 3Dobject is achieved [60–62].

An insight into each of these steps will be highlighted hereafter.

1.2.1 Feedstock

Materials Selection

Feedstocks are the starting point of the MEX process. While the main concern is the desired metallic material of the final 3Dobject, all the feedstock constituents should have a specific purpose to be present. Three different components can be distinguished for the filament: metallic powder, binder, and additives [63].

The metallic powder should take into account the particles complete sintering, meaning that it should be controlled in terms of size, size distribution, shape factor, surface area, structural composition, and surface topography [42].

Spherical powders are usually recommended for sintering since they have a high specific surface and allow for a high packing density. Powder size is usually recommended in the order of 5-20 µm to avoid gas entrapment during debinding while maintaining low interparticle distance. The powder structure should provide a guarantee that the powder has the intended characteristics and does not suffer any structural transformation during atomisation and/or milling [64].

Binder formulation must contain components with physical properties that allow extrusion at low temperatures (180-250°C), essential to material extrusion with a low-cost machine. Also, gradual degradation of the organic constituents is necessary to guarantee the 3Dobject design and to avoid organic residues, like carbon. In fact, the organic residues must be zero, since they affect the final 3Dobject chemical composition and properties. Any binder system must be analysed using thermogravimetry sustained by differential scanning calorimetry (DSC) in order to ensure that within debinding temperatures, all the binder is eliminated, and the degradation is gradual [65, 66].

Additives are different chemical compounds that confer some characteristics to the feedstock, not particularly related to debinding or sintering. A too-significant increase in the number of additives can result in incorrect properties for the complete debinding of the green. In PIM, additives are usually employed to facilitate the mixing (i.e. stearic acid) and reduce the torque, allowing the mixture to be injected. In MEX, the filament must behave in a way that allows continuous feeding to the printer. This means that it has to have the ability to go through the path to the gears and then endure the gear shear forces, be rammed into the nozzle, and then withstand the change in pressure resultant from the change from 1.75 mm (standard filament diameter) to 0.4 mm of the standard nozzle diameter. Flexibility and stiffness are then the essential characteristics of filaments for metal AM. Some essential additives to achieve these characteristics are denominated backbone and plasticisers [67, 68].

Mixing

In the MEX context, mixing is obliged to use equipment with a heated chamber and torque application to the mixed material to induce feedstock homogeneity. Thus, the mixing temperature should be greater than the softening temperature of each component

in the binder, but to avoid the decomposition of components, this temperature should be kept as low as possible while allowing the mixing of the components. The mixing is usually done using a mixer that is capable of controlled temperature and rotation, ensuring measuring the mixing torque, that a homogeneous mix is achieved through the analysis of torque evolution and stability [69–71].

After the material selection, the first step toward filament production is "coating" the metallic powders with several polymers and waxes (binder and additives) made in a high-shear mixer until a homogeneous mixture is achieved. The optimal concentration of each component is usually achieved by the capillary rheometry method, density method or torque rheometry and must be the support for new material selection [72, 73].

The evaluation of mixture torque has been shown to optimise the rheological behaviour of feedstock for injection or extrusion. These techniques lie on the concept that there is a point where a maximum feasible concentration is achieved [74]. Particularly, an in-house developed methodology by Barreiros et al. [75] defines it as the true critical powder volume concentration (CPCV). CPVC is the maximum inorganic solids fraction which provides mixing stability. Since the maximum powder concentration is essential to achieve a high sintered density, a methodology to achieve high powder concentration while guaranteeing the extrudability of the feedstock is essential. CPVC defines a critical powder concentration when the binder & additives occupy the space between the particles, but no excessive interparticle distance exists (Figure 1.7)

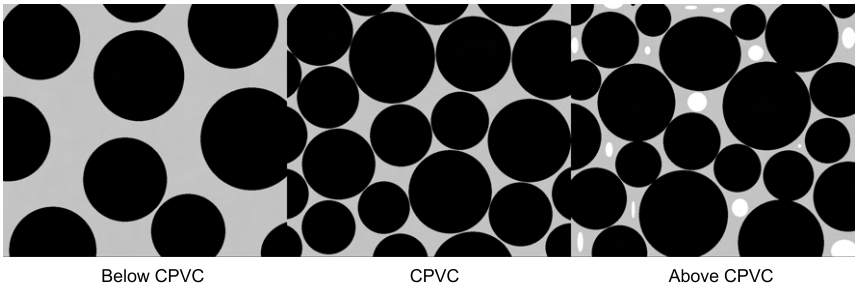

Figure 1.7: Wettability in different powder content conditions.

Filament Fabrication

In order to attain the filament for the shaping step, the mixed material must undergo a granulator, attaining small pellets that can be fed through an extruder. Screw extruders are generally used for filament production (figure 1.8). The filament is extruded through a nozzle with a diameter suitable for MEX (usually 1.75 mm) [76].

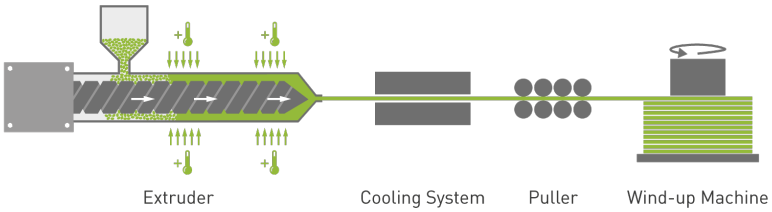

Figure 1.8: Filament extrusion process flow [77].

Filament diameter is usually controlled through screw speed. Controlling the screw speed, or extruding speed can guarantee different diameters. A high-speed increase can lead to gas entrapment which decreases the filament density. Alternatively, a decrease in speed can lead to higher torques that may hinder extrusion. The manual setting of this parameter can lead to a highly inconsistent filament. This is usually connected to measuring equipment that detects the filament diameter change and sets the extruding speed accordingly. Gravity can also be used to guarantee that the filament diameter is as desired. The drop between the extruder nozzle and the surface can be used as a way to oblige the filament to achieve the correct diameter. The filament diameter variation should be no greater than ±0.05 mm in order to achieve a continuous extrusion when shaping [78, 79].

Various organic material combinations have been developed to guarantee filament characteristics while shaping, stiffness and flexibility.

As established (1.2.1), several binder systems and powder loading can be used for filament production. Table 1.1 summarizes the common binder systems for PIM and filaments feedstocks which are commercial or were developed in research works.

Table 1.1: Powder content and Binder System for PIM feedstock and filaments (ND - non-disclosed).

Material	Powder content	Powder size (d_{50})	Binder System	Reference
SS 17-4PH (ASTM)	93 wt.% (PIM)	10.3 µm (water atomized); 12 µm (gas atomised)	Paraffin wax (PW), Stearic acid (SA), Polyethylene (PE)	[80] (2015)
	60 vol.% (PIM)	9.77 µm	Polyacetal (POM)-based (Mould Research, Co., Ltd.)	[81] (2017)
	60 vol.%	43 µm	30% wax, 35% polymer, 20% elastomer and 15% tackifier (RU1 binder)	[82] (1996)
	58 vol.%	22 µm (spherical powder); 10 µm (irregular powder)	ECG2 binder and SA	[83] (2002)
	55 vol.%	12.3 µm	ND (Multicomponent binder)	[84] (2017)
	55 vol.%	12.3 µm	ND (Two-component binder)	[47] (2018)
	55 vol.%	12.3 µm	Thermoplastic Elastomer (TPE) and grafted Polyolefin (PO)	[56] (2019)
	60 vol.%	10 µm	POM, Polypropylene (PP) and PW	[85] (2021)
	63 vol.%	3.97 µm	ND (Polymeric blended binder)	[86, 87] (2022)
SS 316L (AISI)	60 vol.% (PIM)	d_{80} = 22 µm	Acrylic resin and cyclohexyl methacrylate (CHMA)	[88] (2003)

Table 1.1 Continued: Powder content and Binder System for PIM feedstock and filaments (ND - non disclosed).

65 vol.% (PIM)	16-22 µm	PW, PP and LDPP (Low-density polypropylene)	[89] (2004)
62 vol.% (PIM)	10.21 µm	LDPE (low-density polyethylene), HDPE (high-density polyethylene), PW, SA	[90] (2009)
60 vol.% (PIM)	ND	PW, HDPE, acetic acid-vinyl acetate copolymer and SA	[91] (2010)
83 wt.%	ND	Two types of binder (Virtual foundry)	[92] (2019)
88 wt.%	30-50 µm	POM, PP, DOP, DBP and ZnO - Ultrafuse 316LX (ξ)	[30, 93] (2019)
80 wt.%	30-50 µm	ξ(3 mm)	[94] (2020)
88 wt.%	30-50 µm	ξ(1.75 mm)	[95] (2020)
80 wt.%	3-15 µm	PE and SA	[96] (2021)
80 wt.%	30-50 µm	ND	[97] (2021)
83.5 wt.%	0.87-76 µm	Polylactic acid (PLA)	[36] (2021)
88 wt.%	30-50 µm	ξ	[67, 98, 99] (2021)
88 wt.%	30-50 µm	ξ	[100] (2022)
50 vol.%; 55 vol.%	6.9 µm	Polyamide (PA)	[101] (2016)
55 vol.%	ND	ND (Thermoplastic)	[102] (2016)

Table 1.1 Continued: Powder content and Binder System for PIM feedstock and filaments (ND - non disclosed).

	55 vol.%	ND	TPE, three types of PO and two types of compatibiliser	[103] (2016)
	40-70 vol.%	(0.1-30 µm)	POM, PO, dispersant, and confidential polymer (BASF patented binder system)	[104] (2016)
	55 vol.%	6.05 µm	TPE, PO and compatibilizer	[105] (2017)
	55 vol.%	(d_{90}<45 µm)	Confidential polymer, TPE, PO and dispersant	[106] (2017)
	55 vol.%	15.1 µm	ND (Multicomponent binder)	[84] (2017)
	55 vol.%	8.6 µm	ND (Two-component binder)	[47] (2018)
	55 vol.%	17.7 µm	TPE and PO	[107] (2019)
	60 vol.%	ND	POM and PW	[46] (2020)
	50 vol.%	2.8 µm	LDPE, TPE and SA	[108] (2021)
	50 vol.%	10 µm; 30.8 µm	PP, TPE, PW and SA	[70] (2021)
	60 vol.%	9.4 µm	POM, TPE, ULDPE (ultra-low-density polyethylene)	[42] (2021)
	65 vol.%	20-53 µm	LDPE	[109] (2021)

1.2.2 3Dobject Shaping

3Dobject fabrication begins in 3Dobject preparation. A slicer translates the geometry into individual strands distributed per user input. Interaction between strands of extruded material must result in bonding between adjacent material lines. This is affected by the temperature of the nozzle, but other parameters, such as the amount of extruded filament

per transversal movement (feed rate), speed of the extruding head, nozzle diameter, etc., can largely affect the quality of the deposited strand (figure 1.9) [59, 110]. Regardless, the binder system is the driving force for parameter selection and should be carefully considered since no universal parameters are possible due to different compositions behaving in different ways [51, 76].

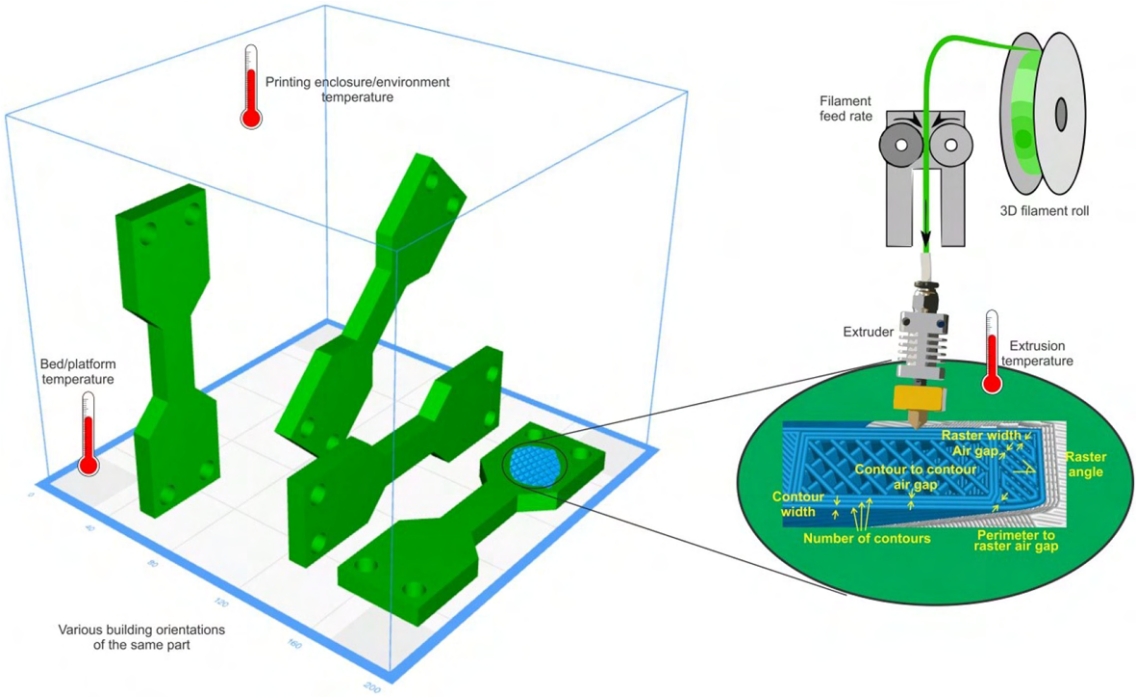

Figure 1.9: Shaping parameters in MEX [111].

Numerous parameters influence the quality of MEX 3Dobjects. Selecting the optimal parameters is crucial for attaining 3Dobjects with high densities. Some of the most relevant parameters are summarised in table 1.2.

Table 1.2: Shaping parameters in MEX.

Shaping Parameter	**Explanation**	**Consequence**
Layer thickness	Height of each layer of deposited material	Has an influence on the strand geometry, features/geometric quality, and process time [112].
Extrusion temperature	Heating block temperature for nozzle heating	Affects the rheological properties of the extrusion; too low, ⇒ clogging may occur due to insufficient gear force to push the filament through the nozzle; too high ⇒ causes drooping, and to polymer degradation [55].
Bed temperature	Temperature of the printing surface	Reduces the warping; increases the adhesion between the deposited material and the printing surface [113].
Environment temperature	Temperature of the enclosure	Usually carefully controlled when an enclosure is available, can highly reduce warping caused by rapid cooling of the strand [114].
Feed rate (extrusion multiplier)	The amount of extruded material per XY movement (mm/mm)	A compensation mechanism for extrusion for eliminating the disparity between the feeding gear movement and XY motor movement. Necessary when the filament has some diameter/rheological anomaly [49].
Strategy	The path of the extruder when depositing	Number of contours, infill angle, seam creation and type of infill must be carefully controlled to achieve the desired 3Dobject functionality [115].
Infill %	3Dobject inside density	Affects 3Dobject mechanical properties and process time [116].
Cooling	Cooling fan speed	Essential for the rapid cooling of polymers that have enough thermal energy for movement [117].

Table 1.2 Continued: Shaping parameters in MEX

Extrusion width	Strand width prediction	Affects the calculated distance between the strands for optimal densification; a lower than suitable distance may mean higher densification but can lead to clogging and geometrical distortion; higher values can lead to a low-density 3Dobject with fragile features [118].

A uniform deposition with superior extrusion characteristics is developed by numerical modelling of the extruded strand that allows the optimal selection of printing parameters. Moreover, this could be used for optimising MEX parameters [119].

Davis et al. [120] designed a method for measuring the bonding strength between two strands of extruded material. This methodology shows the influence of strand thickness on the final 3Dobject quality. Other printing parameters, such as temperature and printing speed, also have a significant influence on the quality of the final 3Dobject.

The other two aspects to be considered regarding the quality of the green 3Dobject are dimensional/geometrical accuracy and surface roughness. It was shown that even the first steps of tessellation and slicing could promote geometric errors and aggravate the surface roughness of a printed 3Dobject. Pérez et al. [121] studied the most important parameters that influence surface quality for a specific material, concluding that layer height and wall thickness are critical factors that have a negative influence on the quality of the printed 3Dobject. It was also shown that path, speed, and temperature might have a low influence when compared to other announced parameters. Powder size and composition can wear the nozzle, so a suitable material should be chosen for this component function of wear aggressivity [58, 59].

Dimensional and geometrical accuracy must be carefully attested since subsequent steps exacerbate errors. Literature reports anisotropy in this step since material deposition, combined with equipment imprecisions and wrong support structure, may increase this characteristic [110, 122].

Parenti et al. [61] have been trying to show that a hybrid additive/subtractive technology (green machining) may solve the geometrical error in MEX 3Dobjects, improving surface finish. This can decrease the need for smaller nozzle sizes, boost production, correct interior features, and allow shrinking compensation techniques. In parallel with this work,

Kuriakose et al. [123] take this concept further to micro-milling MEX 3Dobjects with exciting results.

1.2.3 Debinding and Sintering

Debinding and sintering are the most essential steps in MEX since these two stages can determine whether the final 3Dobject is achieved or not, independently of the quality of the green 3Dobject. Thermal processes should be optimised by carefully studying the 3Dobject behaviour at various thermal cycles (holding time and temperature).

Debinding is the elimination of the polymer by thermal processes. It is the most time-consuming step and one of the most important in the MEX process. Defects in debinding result from gas trapped inside the 3Dobject, from the organic material degradation. The debinding process results in separation between powder particles, essential to maintain the 3Dobject integrity.

Debinding, as a thermal process, can have two consequences: binder flowability improvement, and hence it flows out of the desired 3Dobject or binder degradation and gas removal by diffusion, preferably quickly and efficiently. Due to their composition, binder and additives degrade at different temperatures in a vacuum or gas atmosphere. Usually, an inert atmosphere is used to reduce chemical reactions within the organic binder constituents. Thus, a suitable heat treatment for binder removal is essential for optimal processing. This process should depend on the knowledge of 3Dobject weight loss and shrinkage characteristics during the thermal process since stresses may occur inside the 3Dobject, leading to failure if enough diffusion is not achieved for the expulsion of created gases. Finishing the procedure is essential to guarantee that the internal gaps will not cause the collapse/failure of the 3Dobject [56, 74].

Some techniques are used to guarantee this diffusion. Wu et al. [83] covered the 3Dobject with high surface carbon powder to aid the removal of the binder through capillary suction at low temperatures.

The sintering process (figure 1.10) uses 2/3 to 4/5 of the brown 3Dobject material melting point to create a liquid phase that bonds the particles together due to free surface energy and material-related wettability. The selection of powder concerning size and shape and the sintering procedure is essential to achieve a fully dense 3Dobject since it undergoes a series of complex physical and chemical changes [124].

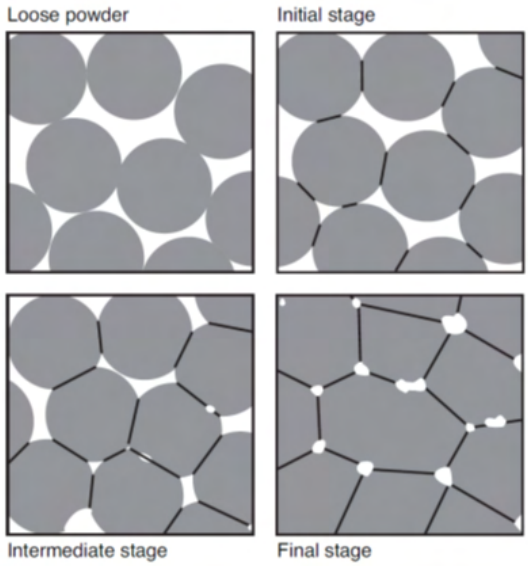

Figure 1.10: Illustration of the sintering process [125].

Similarly to the PIM process, 3Dobject resulting from MEX after sintering can increase the anisotropy. This is related to 3D printing layer-per-layer wich may affect how the 3Dobject will behave in this process [30, 56, 102, 126].

Zhigang Zak Fang (as editor) contributed to one of the most complete compilations of the sintering process in "Sintering of Advanced Materials" [127], from thermodynamics, kinetics, and mechanisms of densification to computer modelling and sintering behaviours of different materials, providing an excellent insight into this technology. Table 1.3 summarises a literature review of sintering temperatures and atmospheres, final density and powder content.

Table 1.3: Powder Content, Sintering temperatures, environmental atmospheres and final relative density of sintered steel 3Dobjects.

Material	Powder content	Sintering temperature	Sintering atmosphere	Relative density	Reference
SS 17-4PH (ASTM)	ND (PIM)	Sintering at 1325°C for 2h	Ar	98.8-99.2%	[128] (2007)
	93 wt.% (PIM)	Pre-sintering for 15 min at 1000°C; Sintering for 2h at 1350°C	Vacuum with Ar partial pressure	98.8%	[80] (2015)

Table 1.3 Continued: Powder Content, Sintering temperatures, environmental atmospheres and final relative density of sintered steel 3Dobjects

	60 vol.% (PIM)	Sintering at 1350°C for 2h	Ar	97.5%	[81] (2017)
	60 vol.%	Sintering for 1h at 1350°C	H_2 + N_2	92-95%	[44, 82] (1996)
	58 vol.%	Sintering for 3h at 1260°C	H_2	ND	[83] (2002)
	55 vol.%	Sintering for 3h at 1050°C	ND	ND	[47, 84] (2018)
	55 vol.%	Pre-sintering for 1.5h at 900°C; Sintering for 5h at 1380°C	ND	95.7%	[56] (2019)
	60 vol.%	Sintering for 2h at 1280°C	Ar	97.3-98.2%	[85] (2021)
	63 vol.%	Sintering for 3h at 1200°C	96% Ar + 4% H_2	96.5-98.6%	[86, 87] (2022)
SS 316L (AISI)	60 vol.% (PIM)	Sintering for 1h at 1350°C	Ar	95%	[88] (2003)
	65 vol.% (PIM)	Pre-sintering for at 1000°C; Sintering for 1h at 1360°C	H_2	95.45-98.35%	[89] (2004)
	62 vol.% (PIM)	Pre-sintering for at 1050°C; Sintering for 3h at 1380°C	Vacuum	95.4-97.2%	[90] (2009)
	60 vol.% (PIM)	Sintering for 1h at 1380°C	H_2	70.3-78.1%	[91] (2010)
	83 wt.%	Sintering at 1100°C	Ar	ND	[92] (2019)

Table 1.3 Continued: Powder Content, Sintering temperatures, environmental atmospheres and final relative density of sintered steel 3Dobjects

	88 wt.%	ND	H_2/Vacuum	98.5%	[30] (2019)
	88 wt.%	Sintering for 3h at 1380°C	H_2	98.3-99.5%	[93] (2019)
	80 wt.%	Sintering for 3h at 1380°C	H_2	82.2%	[94] (2020)
	88 wt.%	Sintering for 2h at 1380°C	Ar	92.2%	[95] (2020)
	80 wt.%	Sintering for 2h at 1320°C	Vacuum	92-99.7% (HIP)	[96] (2021)
	80 wt.%	Sintering for 3h at 1380°C	Ar	97.9-98.1%	[97] (2021)
	83.5 wt.%	Sintering for 1h; 6h; and 12h at 1310-1400°C	Ar	72-92%	[36] (2021)
	88 wt.%	Sintering for 3h at 1380°C	H_2	95.6%	[129] (2021)
	90 wt.%	ND	ND	95%	[98] (2021)
	90 wt.%	Sintering for 3h at 1380°C	H_2	84%	[99] (2021)
	88 wt.%	Sintering for 3h at 1380°C	H_2	ND	[100] (2022)
	50 vol.%; 55 vol.%	Sintering at 1250°C	H_2	89%	[101] (2016)
	55 vol.%	ND	ND	97.1%	[102] (2016)
	55 vol.%	Sintering at 1100°C	H_2/Ar	88.6-90.6%	[106] (2017)
	55 vol.%	Sintering for 1.5h at 1250°C	Vacuum	ND	[84] (2017)

Table 1.3 Continued: Powder Content, Sintering temperatures, environmental atmospheres and final relative density of sintered steel 3Dobjects

	55 vol.%	Sintering for 2h at 1360°C	Vacuum	95%	[107] (2019)
	60 vol.%	Sintering for 2h at 1280°C	Ar	91-93%	[46] (2020)
	50 vol.%	Sintering for 4h at 1350°C	97.5% Ar + 2.5% H_2	75-96%	[70] (2021)
	60 vol.%	Sintering at 1250°C	H_2	ND	[42] (2021)
	65 vol.%	Sintering for 3h at 1380°C	H_2	93%	[109] (2021)

1.2.4 Post-processing

Low post-processing is needed, in MEX, to attain the maximum quality of the final metallic 3Dobject. Moreover, the final microstructure resulting from sintering is close to its conventional counterparts. However, many processes can be used to increase final accuracy and density. The use of green machining (as previously stated) has been taken selected for MEX 3Dobjects treatment since the low tool wear means that the cost of machining prior to sintering is very low. Moreover, it increases the design possibilities since outward connecting tubes should not be horizontal in relation to the layer growth direction. Machining allows for this possibility [130]. Final density can be improved using isostatic pressing, approaching bulk density [131]. Sufficient pressure and temperature avoids defects that can be filled by the surrounding material, largely reducing or completely eliminating interior porosity. However, material migration can also mean 3Dobject deformation. Consequently, the volume of voids inside the 3Dobject must be low. Moreover, inside features can be eliminated if pressure is not carefully controlled, as well as polymer degradation may occur if the temperature is not suitable [96, 131].

1.3 Liquid State Additive Manufacturing

Selective Laser Melting (SLM) is the most prevalent technology of the PBF process for metals [3]. F&S Stereolithographietechnik GmbH developed SLM to produce dense metallic components from metallic powders, using a high-energy-density laser to melt the powders layer-per-layer, according to CAD data [132].

SLM has been growing in the industry and is yet the AM technology for able to build complex small/medium metal parts [133]. This technology starts by depositing a thin layer of powder inside a closed chamber. After the powder bed is laid on the substrate, a high-power laser is used to scan the layer selectively. The slicing information file is used as a guide for the laser beam, melting the powder particles in successive interconnected melt pools. When the laser scanning path is finished, the platform is lowered, and a new powder layer is applied, looping the procedure until the component is fully built (figure 1.11).

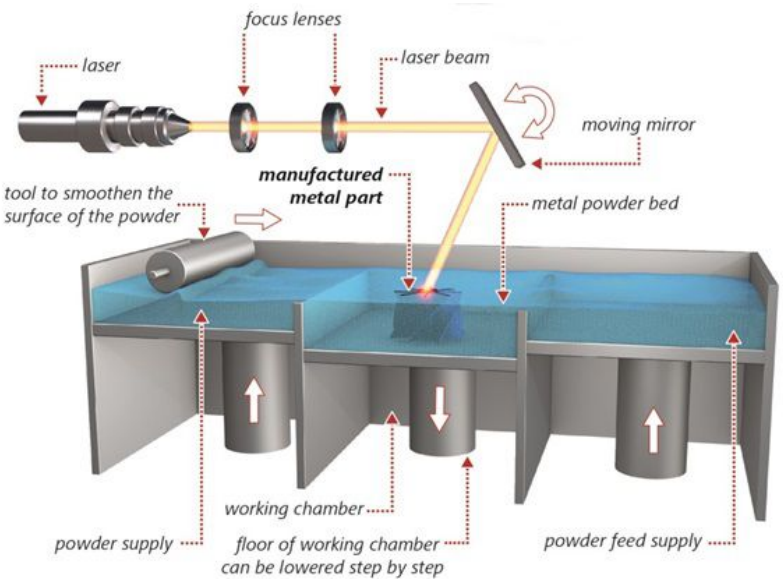

Figure 1.11: Schematic of the SLM technology (adapted from [134]).

The build chamber is under inert gas, which avoids forming unwanted compounds, mainly oxides [135]. Once the part is made, it is completely submersed in powder. The powder is collected, sifted, and reused until possible (typically 5-6 cycles). The attained part can be separated from the substrate (base) by electric discharge machining (EDM) or directly separated from the substrate when using supports [136]. The area of the building chamber and platform, the number of lasers and the sieving mechanism can be varied, as well as the laser type and output [137].

Although the concept of SLM technology is relatively simple, many variables affect the quality of 3Dobjects during the process (figure 1.12). The main bulk of these variables cannot be considered parameters since they cannot be fully controlled by the operator and will be discarded in future discussions regarding the influence of SLM parameters on the 3Dobjects, but they are important to have in mind and correlate them to the intrinsic properties and failure/results of producing SLM parts [138–140].

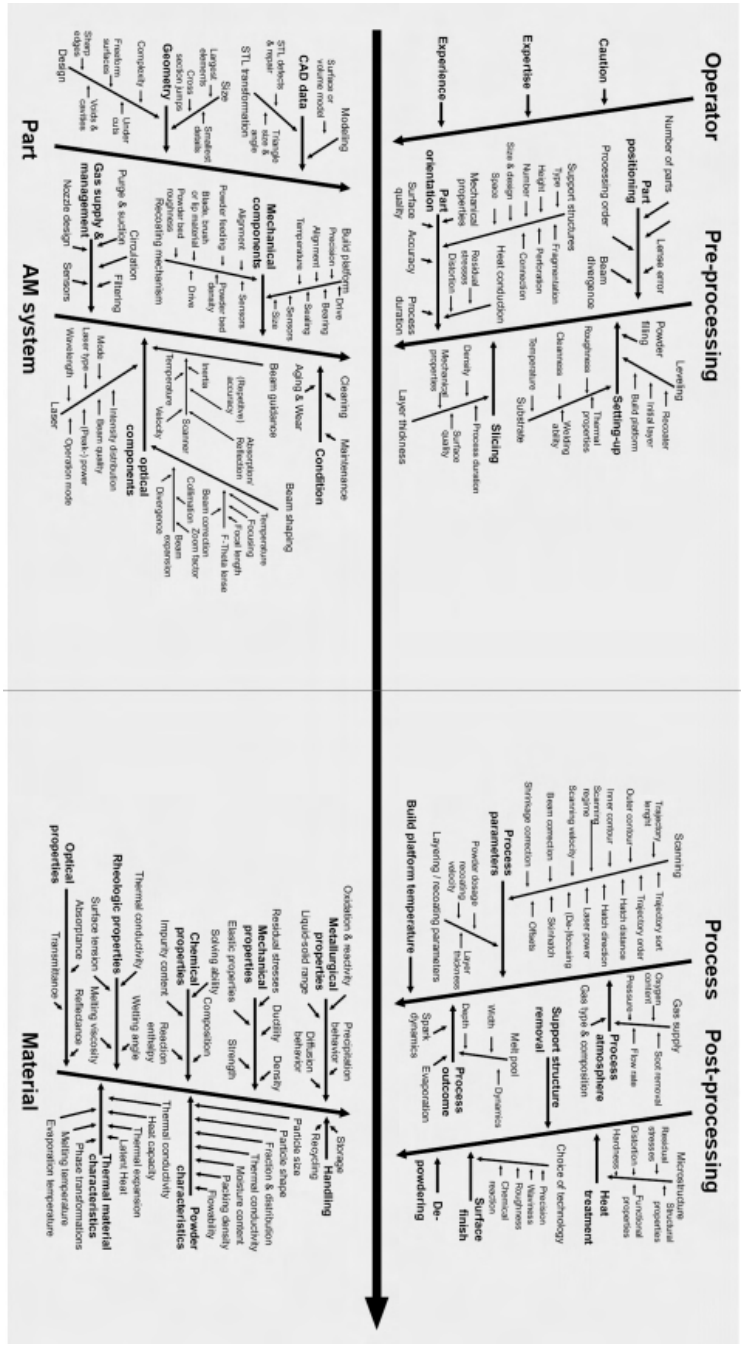

Figure 1.12: Technology variables involved in SLM (adapted from [141]).

1.3.1 Physical Phenomena in SLM

Understanding the physical phenomena in SLM is essential to know the mechanism of defect formation. The radiation absorbed by the powder bed promotes the melting of the powder. This leads to a melting pool, growing in the scanning direction and continuously cooling as it reaches the solidification temperature. Nevertheless, laser-matter interaction is very complex and dependent on a myriad of variables, as previously shown in figure 1.12. Whatever the application, mechanisms like heat transfer, molten metal flow, Marangoni effect and phase transformation are present and influence the quality of the 3Dobject [142].

Melting pool physics are the basis of SLM. Each melting pool can be envisaged as a construction block. Thus, each layer can be analysed as a collection of overlapped melting pools. This means that the understanding of the behaviour of the melting pool and its correlation to the input parameters is essential [143, 144].

Two main factors are essential in the analysis of melting pool quality: depth and width. An ideal melting pool should have sufficient depth to promote good adhesion to the previous layer without originating a keyhole effect resulting in porosity. Also, it must have a constant width to allow for the correct calculation of hatching space, layer thickness, and overlaps. These factors are connected to the shaping parameters input by the operator [145, 146].

The melting pool behaviour on a workable set of parameters, is usually translated by the volumetric energy density (VED) equation 1.1, which encompasses the most influencing parameters: laser power (P); scanning speed (v) (the speed at which the laser advances); layer thickness or layer height (e); and space between laser passes (hatching space - h) [147].

$$VED = \frac{P(W)}{e(mm)h(mm)v\left(\frac{mm}{s}\right)}, \frac{J}{mm^3} \tag{1.1}$$

A graphical description of these parameters can be seen in figure 1.13.

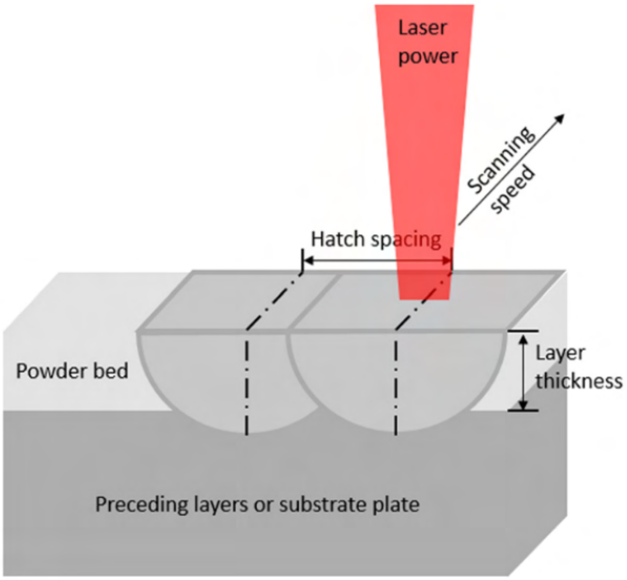

Figure 1.13: Parameters in SLM [148].

All VED parameters can affect the melting pool, but the main driving force is the laser power [149]. Power output is usually the main parameter for the production of specific materials in SLM. However, laser wavelength has an influence on the material absorptivity of the laser power [150].

Ytterbium fibre lasers are currently mainstream and typically have a maximum output of 200 to 400 W and a wavelength of ≈1.070 µm. Considered ideal for low laser power scanning of most metallic materials (figure 1.14), it is deemed insufficient for most conductive materials. New laser technology development is still ongoing in response to these issues, such as the development of green and blue wavelength lasers ($\lambda \approx 0.515$ µm and ≈0.420 µm, respectively) [151, 152]. Spot size is another major factor in SLM, concentrated energy results in more controlled melting pools with a smaller width, which is essential for excellent resolution. Usually, the spot size for ytterbium fibre lasers is around 70 µm, but this value can be offset for different scanning strategies. Spot size is essential for controlling the VED, to effectively melt the powder and reach sufficient dimensional precision and surface roughness [153].

A detailed analysis of parameters is done bellow.

P. Power output, whatever the wavelength and spot size, has a deep effect on melting pool dynamics. It affects melting, solidification rate, spatter creation, vapour recoil, and microstructure of the final 3Dobject [155]. Consequently, changing the power

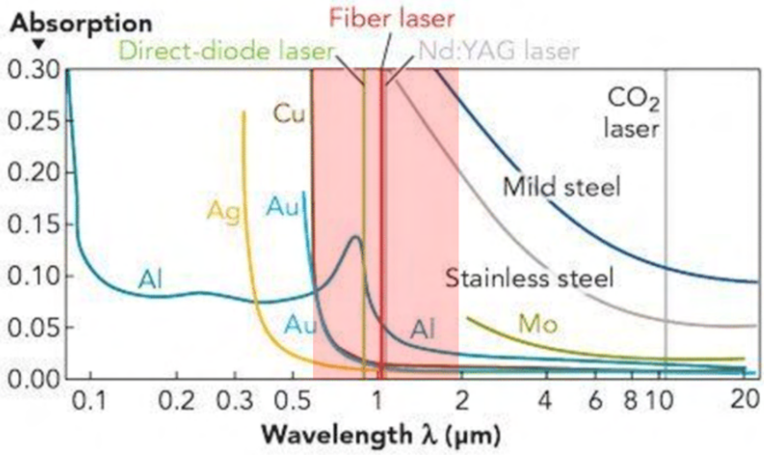

Figure 1.14: Wavelength-absorption for several metallic materials [154]

output variable can have severe repercussions on the material behaviour during processing [156–158].

e- Layer thickness is the distance between two consecutive layers (usually set at 20 or 30 μm), it depends on the desired layer quality or intended features, affecting the building time by increasing the number of layers necessary to achieve the desired building height. However, the layer thickness must be adjusted according to the melting pool depth, it should be sufficient for partial remelting the previous layer. This guarantees that low (or no) interlayer gaps occur. If the layer thickness is set too low, the depth may affect the quality of overhanging features by melting undesired powder and blocking interior channels or degrading 3Dobject features [159–161].

h- Hatching distance is intended as the distance between the centre of two consecutive melting pools. Essential in the intralayer connection between melting pools is usually set regarding the selected overlap: the amount of the previous melting pool that is remelted when a new melting pool is scanned. This results in a strong connection on consecutive melting pools. Hatching space must be set up while considering the variables that affect melt pool widths, such as the material response to the thermal energy, the spot size and the scanning speed. Although usually a fixed parameter per material, hatching distance can greatly affect the final density [162, 163].

v- Scanning speed is the last variable on the equation. It is defined as the speed the deflection mirror moves to scan the powder bed, normally dependent on the laser power output. Since hatching space and layer thickness are typically set per material, laser power and scanning speed are the only parameters that can be changed.

As previously enounced, laser power is the driving force of melting pool physics. Thus, scanning speed is usually input as a means of attaining an ideal VED. Nevertheless, that must be sufficient for the material to be affected by the material energy, essential for the material width and depth [129, 157].

A closer analysis of the melting pool, complex fluid dynamics guide the molten flow. Vapour pressure, Marangoni currents, capillary effect and surface tension are all affected by the process parameters. The laser creates a vapour pressure in the centre of the melting pool during the processing. This leads to the recoil of the material, while the Marangoni currents - where the fluid flows from low to high surface tension - drive the dynamics of the molten material [160, 164]. Sufficient knowledge of the melting pool physics and their relation to the VED allows for the grouping of different consequences regarding the variation of laser output and scanning speed, as follows:

– high laser power at low scanning speed leads to a keyhole regime that occurs when the depth-to-width ratio is less than 0.5, resulting in a very deep and thin melting pool occurs and leads to deep pores due to molten flow mobility, which solidifies while in movement [165, 166];

– high laser power at medium scanning speeds results in elements vaporization due to the high temperatures related to SLM processing; contact with the laser can lead to overcoming the boiling temperature of the processed material or its constituents, resulting in the modification of the chemical composition of the powder, and unexpected 3Dobject properties [167–169];

– high laser power at high scanning speeds affects the continuity of the melting pool, thus leading to random pores throughout the part; as previously stated, a consistent melting pool is essential for building a dense 3Dobject, this regime can be avoided by reducing the laser power and scanning speed simultaneously [157, 170];

– low laser power at medium to high scanning speeds result in a shallow melting pool or balling effect, the lack of fusion that results from this set of parameters is the most present defect in powder bed fusion; interlayer connection is deeply affected in this mode and can lead to process failure due to delamination between the layers [139, 171].

1.3.2 Feedstock Preparation

While the melting pool dynamics are usually the main phenomena when producing 3Dobjects using PBF, the complexity starts with the feedstock. The metallic powder can have different origins: gas and water atomisation, milling, oxide reduction, precipitation, plasma. Gas and water atomisation are yet the main processes for steel powder production. Gas atomisation gives a more uniform shape distribution at a higher cost than its water counterpart, which is normally when the powder particle material is not reactive.

Usually, the factors that determine the quality of powder for SLM are particle size and particle size distribution, shape, structure (including topography)/flowability. The methodology of powder production highly affects these powder characteristics and, consequently, their behaviour in the powder bed construction [76]. Optimal powder particle characteristics for SLM is summarised bellow:

- particle size must be between 20 and 50 µm, which are in line with the usual layer sizes (around 20-30 µm) for an insignificant surface roughness they contribute to the best packing behaviour (also named powder bed density); a normal, narrow, symmetric distribution is recommended, but some prevalence of smaller powders can be beneficial for the packing behaviour [172, 173];
- spherical powder (shape factor of 1) is usually advised since it contributes to the compaction behaviour, meaning that the layer deposition results in a higher packing density since high interparticle space tends to result in voids from a lack of material [174];
- powder structure is highly affected by the powder production technique; stresses can be due to the high cooling rates inherent and/or environment atmosphere [175];
- powder flowability depends on the surface quality and surface tension, which contributes to powder agglomeration; the decrease of these characteristics improves powder bed density [176].

The powder is usually provided in controlled environment containers, with moisture control and vacuum sealed, which means that opening the container in a harsh environment can immediately affect the powder. For this reason, the powder must be handled under controlled conditions that start now to exist in real-life industrial facilities [177, 178].

Moisture control in powder is usually done by silica packets and heating the powders, in a furnace, to around 90°C [178]. For reactive powders, this can be impossible, and the powder must be subjected to a close loop of an inert gas-protected atmosphere for

any handling. Some SLM machines integrate sieving systems. At the end of the process, the powder spatter is vacuum cleaned, and the one that does pass through the sieve is discarded. Therefore, there is a risk for the operator and environment regarding powder handling since there is direct contact with the small metallic particles that may cause undesired health complications due to airborne particles [177].

Handling problems lead to low reusability and recyclability in SLM powder, lowering the overall quality of the produced parts per powder use, and this has been a major topic of investigation in the last few years. Consequently, powder costs increase, and environmental issues appear due to the quantity of discarded powder that may originate from this issue [179, 180].

1.3.3 3Dobject Shaping

Shaping, in the SLM context, usually involves powerful software, such as Materialise Magics, to process the STL and input the parameters [181].

The position of the 3Dobjects is usually centred in the printing bed. Laser is deflected from source to powder bed, which means that angle deviation from the centre has small but noticeable changes in laser beam focus due to increased path. SLM manufacturers have been developing systems with multiple lasers to overcome this disadvantage on large systems, as well as to increase production speed. Furthermore, object angle in relation to the bed is extremely important and must consider the application. It is recommended that the larger surface area is fixed on the powder bed to provide more anchoring points. However, 3Dobject features, such as holes and overhangs, require different positions if the feature quality is the target. Moreover, mechanical properties are affected by the 3Dobject position since there structural/properties anisotropy can be present. For this reason, design for AM has been growing in the last few years, and objects must be designed having taken into account the process limitations [182, 183].

SLM technology requires direct contact with the substrate (platform), which means that a metallic bond between part and substrate exists and is not usually possible to easy removal. Supports are necessary if EDM is not a possibility. Moreover, supports provide a fine connection, with micrometric walls that are easy to remove by the use of simple tools. There is still no automatic software easily available for automatic support generation, and it is necessary expertise to ensure that support density, height from the bed and strategy are suitable to guarantee sufficient adhesion and thermal conductivity. Supports are necessary for some features, such as overhanging areas. However, a bottom anchor is not always

possible to guarantee for the supports, which in some cases can be the object itself, which will increase the post-processing time to eliminate the supports. Moreover, some features may usually not supported due to inaccessibility for their removal [182, 184, 185].

Moreover, it must be highlighted that 3Dobject texture and residual stresses are connected to the scanning strategy. An angle increase per layer is input to avoid thermal stress concentrations on one specific object zone, which can result in part warping and processing failure. Some of the most common strategies are [186]:

- orthogonal strategy scans the layer in a linear pattern, with 0° in relation to the substrate, and adds 90° per layer;
- angled scanning is similar to orthogonal but scans the surface at a selected angle;
- islands or chessboard scan with an orthogonal or angled strategy, dividing the layer into several small areas and applying to each a 90° angle in relation to the neighbouring areas; avoids stress concentration, but mechanical properties are affected.

1.3.4 SLM of common materials

Different materials are being processed by SLM with and without success. In this item, it was selected as powder, copper and copper alloys (hard to be processed by SLM) and stainless steels (considered easy to manufacture by SLM technology).

1.3.4.1 Copper and copper alloys

Copper has consecutively researched materials in SLM due to its challenging characteristics. The search for a material that would harvest the unique possibilities of MAM, such as the new thermal diffusion geometries, cooling channels and embedded sensors, puts copper on the forefront of the most desirable materials to be efficiently used, due to its optimum thermal and electrical conductivity. Copper is a metallic element with a wide range of applications due to its thermal and electrical properties while maintaining good mechanical strength. Consequently, it has been the subject of multiple studies in MAM, but with limited results. The thermal properties of copper make it a difficult material to be processed under a direct energy source since its absorptivity is low and heat dissipation is high. Moreover, the reflectivity of metal copper to the beam also contributes to thermal loss, resulting in incomplete melting and, consequently, low density.

A summary of studies regarding copper and copper alloys produced by SLM is summarised in table, where new approaches are being used to achieve high densities, while 1.4.

Table 1.4: State of the art summary of copper and copper alloys produced by SLM.

Material	VED $\left(\frac{J}{mm^3}\right)$ (P)	Relative density (%) (Method)	Reference
Pure copper	533 (800 W)	96.60 % (Archimedes)	[187] (2018)
	310 (200 W)	99.10 % (Archimedes)	[188] (2020)
	210 (300 W)	98.80 % (Archimedes)	[189] (2020)
	95 (500 W)	69.40 % (Archimedes)	[190] (2020)
	350 (400 W)	95.00 % (Archimedes)	[191] (2020)
	533 (800 W)	96.60 % (Archimedes)	[192] (2020)
	350 (140 W)	96.00 % (Optical)	[193] (2021)
	350 (140 W)	96.00 % (Optical)	[193] (2021)
	740-1120 (800 W)	98.00 % (Archimedes)	[152] (2021)
Cu-Cr-Zr	158 (370 W)	99.43 % (Archimedes)	[194] (2020)
	242 (425 W)	99.43 % (Archimedes)	[195] (2021)
Cu-Ni-Sn	142 (340 W)	99.40 % (Archimedes)	[196] (2018)
Cu-Cr-Zr-Ti	570 (800 W)	99.20 % (Archimedes)	[197] (2018)

1.3.4.2 Stainless Steel

316L as been one the most researched material since the development of SLM due to the lack of phase changes. SS 316L is considered a standard material for MAM due

to its characteristics since any material-related issues are reduced, and the parameters influence is elevate has been the most researched material due to its properties. Such as the combination of corrosion behaviour, mechanical properties, carbon content and lack of phase changes within the process temperature [30].

As an alternative, precipitation-hardening stainless steels have been widely researched due to their increased mechanical properties while maintaining a low carbon content through the application of heat treatments. The interest, however, in producing high-hardness stainless steels, such as 420, was not hindered, although issues like cracking, carbon depletion and fragility are usually present [198].

Table 1.5 summarises research works that produce stainless steels with the same equipment as the one used in this work, an EOS system.

Table 1.5: VED as function of density regarding stainless steels produced with EOS®systems.

Material	**VED** $\left(\frac{J}{mm^3}\right)$	**Tensile Strength (MPa)**	**Hardness (HV)**	**Relative density (%)**	**Reference**
SS 316L (AISI)	39-75	NA	NA	99.97 (Optical)	[199] (2017)
	127	NA	NA	99.37 (Archimedes)	[200] (2018)
	43	660	219 ($HV_{0.5}$)	99.75 (Optical)	[201] (2018)
	50;200	630	NA	98.00 (XCT)	[202] (2018)
	325	620	NA	99.95 (Optical)	[203] (2020)
	28-74	NA	NA	99.60 (Optical)	[204] (2020)
	96	690	270 ($HV_{0.3}$)	99.50 (Archimedes)	[205] (2020)
	100	NA	NA	99.30 (Archimedes)	[206] (2021)
	92.5	NA	230 ($HV_{0.2}$)	99.80 (Optical)	[162] (2022)
	100	NA	NA	99.80 (XCT)	[207] (2022)

Table 1.5 Continued: State of the art summary regarding stainless steels produced with EOS®systems.

SS 630 (AISI)	41	NA	NA	98.70 (Archimedes) 99.40 % (Optical)	[208] (2013)
	60	1550	NA	NA	[209] (2014)
	40	NA	373 ($HV_{0.1}$)	99.90 (Archimedes) 99.40 (Optical)	[210] (2019)
	62	NA	368 (HV_1)	99.50 (Archimedes) 99.40 (Optical)	[210] (2019)

1.3.5 Post-processing

Post-processing in SLM usually obliges to powder cleaning on 3Dobjects and removal of supports or the separation from the platform (substrate). Moreover, heat treatments are usually performed to attain mechanical properties closer to the bulk metals and alloys. Regarding surface treatments, polishing, sandblasting, shot-peening or laser shock-peening are performed to improve surface finishing quality [211]. Although costly, due to improved hardness common in SLM 3Dobjects, machining (milling) must be employed for specific features, and overall object accuracy [212]. Hot isostatic pressing has been proven to be successful in removal interior voids and has been growing as an essential tool for parts produced by MAM [213–215].

Chapter 2

Defects in Additive Manufacturing

Defect is understood as "an imperfection or abnormality that impairs quality, function or utility". Consequently, it is of extreme importance to report known types of defects and their origin if a complete understanding of MAM is to be ensured. Defects in MAM, as detailed in chapter 1, are mainly associated with the processing step that occurs in each technology. However, MAM defects must be studied not only focusing on the processing step but a holistic approach to know how the feedstock material affects the final properties and defect emergence must be performed. Depending on the melting or sintering thermal cycles of the feedstock, the metal powder will affect the final properties differently. A detailed glossary of observed defects is laid down per process type.

2.1 Defects in SSAM

Defects in MEX can be divided into three categories, feedstock, shaping, and consolidation. They are dependent on each of these steps in what concerns their origin, but they are correlated. Feedstock defects can lead to shaping and consolidation defects due to lack of material or conditions to achieve high densification or the intended material properties. For example, shaping defects can lead to delamination in sintering; consolidation defects can undermine the previous steps.

2.1.1 Feedstock defects

Defects occur when feedstock preparation is done inadequately. A correct combination of material selection, homogenous mixing and filament extrusion must be ensured in order

to minimise defect occurrence. Moreover, CPVC will affect the behaviour of the filament, as well as the 3Dobject.

The main defects that occur in the feedstock are due to:

- uneven distribution of powder, binder or additives in the feedstock, resulting from uneven mixing or lack of wettability of the binder & additives and metallic powder [37, 216];
- filament diameter variations leads to variable extrusion quantity and strands with inconsistent width, which results in underextrusion or overextrusion if the filament diameter is smaller or bigger than expected [76, 93];
- filament slipping and deformation due to inconsistent stiffness can lead to clogging, which is a major issue in MEX feedstocks [217].

2.1.2 Shaping defects

Shaping step is the main source of the defects in MEX. A fully-dense 3Dobject is very difficult to translate in a series of ≈0.40 mm strand lines, which will cause resolution defects. A nozzle size of 0.45 mm is usually considered since smaller nozzles can increase clogging due to pressure build-up. Furthermore, joining adjacent strands requires careful control of the thermal conditions, which is very difficult to achieve and demands optimal parameters. Some of the more relevant shaping defects are:

- **movement voids**, resultant from rapid nozzle movement change, leads to a gap or inconsistent extrusion; a moving head carrying the extruder is deeply connected to the extruding behaviour since transversal movement is a function of extrusion rate; any rapid movement change or jump can result in defects [218];
- **under or overextrusion** occurs when the strand has a smaller or bigger size than expected; if smaller, it results in constant voids parallel to the strand; if bigger, an expansion in that layer results in geometrical deviations; can be controlled by changing the extrusion multiplier parameter [219–221];
- **base bulging** is visible in the first layer due to the increased pressure between the nozzle and the substrate, leading to an exaggerated flattening of the strand and an X-Y growth on the first layer when compared to the CAD; solved by increasing the distance between the base and the nozzle or by compensating the value on the digital model in order to improve adhesion [218];

- **drooping**, resulting from enough thermal energy for polymer flowability, causing its exit from the nozzle; results in a lack of material in the object and can be solved by tuning the nozzle temperature when not extruding or overall decreasing the printing temperature [100];

- **strand bonding weakness** occurs when the thermal energy is not enough to join the strands and layers together; two adjacent strands must be joined together in order to avoid voids or polymer excess in the interface between them; which implies using a higher process temperature [222];

- **delamination** occurs when the layers of the print separate from each other, resulting in a poor-quality object can occur due to incorrect bed levelling, incorrect nozzle height, or poor adhesion between the material; nozzle height is an important aspect of shaping in MEX, if the nozzle is too close to the bed, the strand will not have enough time to cool and connect with the previous layer causing delamination [223, 224];

- **geometrical deviations** include warping, curling, sagging, and stringing; warping is caused by unequal cooling rates in the material, which can be caused by the 3Dobject geometry being too large or too thin; curling is caused by unequal contraction of the material, which can be attributed to the 3Dobject being too small or thick; sagging is caused by the weight of the 3Dobject, which can be caused due to being too tall or narrow; stringing is caused by the material sticking to the build platform or the extruder nozzle, which can be associated to the feedstock being too viscous or the temperature of the build platform; geometrical deviations can be minimised by using a suitable feedstock, optimised shaping conditions, and post-processing treatment; [100, 225, 226].

Understanding the causes of these deviations, it is possible to produce parts with very tight tolerances.

2.1.3 Consolidation Defects

Debinding and sintering are affected by feedstock and shaping defects. It was demonstrated that sintering could solve small porosities, but if not optimised, it can generate different defects, as follows:

- **incomplete debinding**, which can result from faulty debinding or uneven debonding, occurs when some of the unwanted polymers are still present in the green;

caused by insufficient temperature or time for complete debinding [227, 227];

– **internal voids** resulting from high thermal rates, leading to fast polymer degradation, but they may also result from a heterogeneous feedstock [228, 229];

– **blistering** are bumps that result from local delamination due to polymer degradation and bonding issues, characterised by the formation of small, raised areas on the surface of the metal during sintering or post-sintering; these raised areas, or blisters, can be of a few millimetres or more; the cause of blistering in sintering is thought to be related to the presence of impurities in the metal; when the metal is heated, these impurities can react with the metal to form gas that becomes trapped in the metal, and as they expand, cause the formation of blisters; in some cases, blistering can be prevented by careful control of the sintering process and the addition of certain additives to the metal [68, 126, 230];

– **cracking** due to thermal stresses that, when cooling, lead to fissures; an unsuitable heating rate also induces cracks in the 3Dobject [79, 230];

– **microstructural defects** due to chemical alterations when producing the feedstock or polymer incomplete ustulation, leading to impurities or carbon contamination of the metallic powder [231, 232];

– **warpage** due to uneven shrinking when sintering [100].

2.2 Defects in LSAM

2.2.1 Defects in Powder

Powder characterisation is essential in SLM. Packing density is one of the primary drivers of 3Dobject density. If too low, interparticle space results in a lack of fusion due to low material presence [233–235]. Although the presence of voids within the powder bed is usually connected to the powder size and size distribution, powder defects can negatively affect the resulting powder bed density, such as:

– **agglomeration** is typically characterised by joint powder, can be caused by high impacts between the particles or hollow particle filling (figure 2.1) [11, 236, 237];

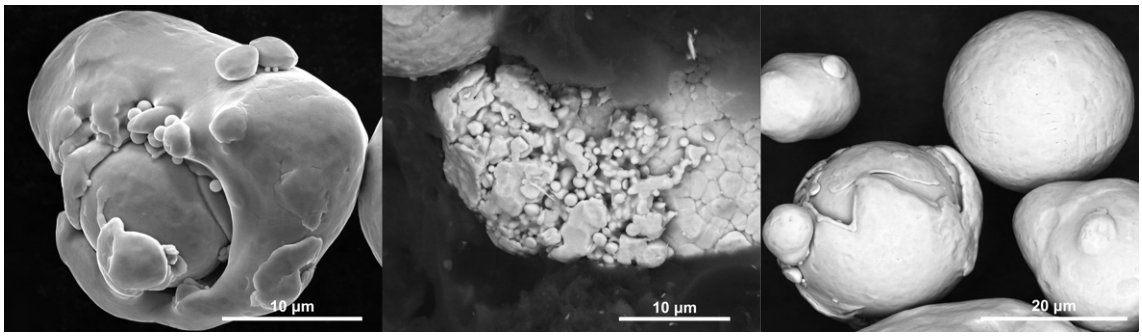

Figure 2.1: Different shapes of powder agglomeration.

– **dendrites** occurs when the surface has a phase change due to rapid cooling; it usually emerges in powder subjected to phase transformation within atomising temperatures;

– **microstructural defects**, oxides presence and inclusions due to atomisation procedure and powder handling; the atomisation process is usually undertaken on the same atomising system, paraphernalia of environmental conditions may occur; thus cross-contamination may occur, and different elements may appear in the powder (in almost insignificant quantity, but its consequences may not be insignificant) and affect porosity; oxidation may occur during powder cooling or be the result of bad handling (figure 2.2) [238–241]; phase modifications can affect the powder spreadability [236], caused by magnetic behaviour of some undesirable phases; the sieving system, which usually uses screens bigger than 100 µm, is meant to separate the sintered powders and spatter;

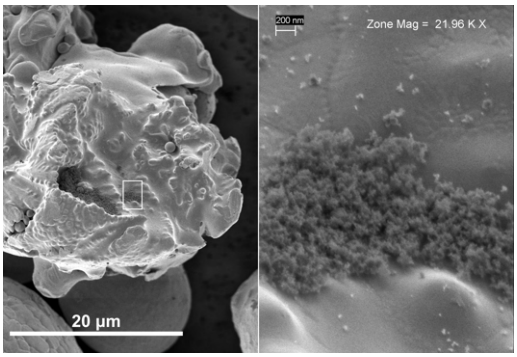

Figure 2.2: Inclusions in powder.

– **powder deformation** is usually the resultant of powder handling that has been subjected to impacts and friction (figure 2.3) [238];

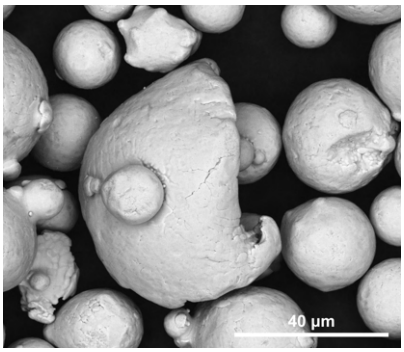

Figure 2.3: Deformed powders.

– **powder porosity** is usually the result of gas entrapment inside the particle during atomisation, caused by high-pressure jets and high cooling rates (figure 2.4) [242, 243];

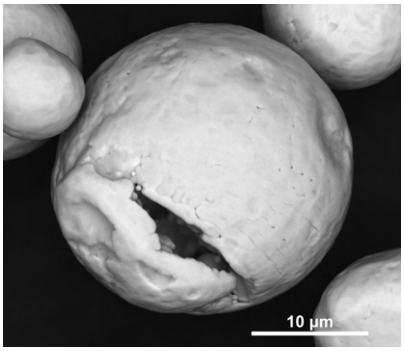

Figure 2.4: Powder porosity.

– **satellites** are smaller powders that surround and agglomerate in bigger powder, effectively affecting its morphology, and consequently, the flowability (figure 2.5) [237, 244, 245];

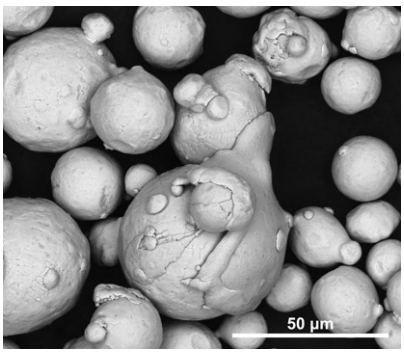

Figure 2.5: Satellites in a large powder.

2.2.2 Defects in 3Dobjects

Although powder quality can be correctly characterised and handled, SLM processing also induces a series of different defects, as follows:

– **lack of fusion (LOF)** occurs when the volumetric energy density (VED) is insufficient to create a melt pool deep enough to penetrate the substrate or wide enough to overlap sufficiently to the next parallel scanning line; this defect can be reduced by increasing the VED or decreasing the hatching space; appears at the surface and inside defects in the order of hundreds of micrometers (figure 2.6) [246–252];

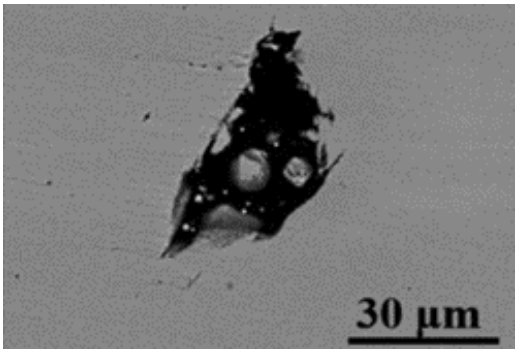

Figure 2.6: Lack of fusion defect [244].

– **balling** occurs when localised energy is insufficient to guarantee the melt pool continuity, thus resulting in an uncontrolled scan track melting, resulting in small spherical melted zones; increasing the laser power, or decreasing scan speed contributes to avoid it (figure 2.7) [219, 247, 253–255];

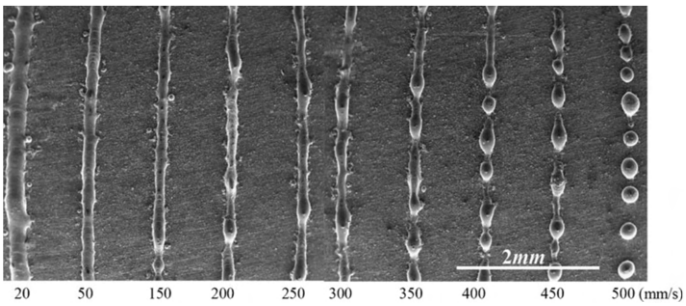

Figure 2.7: Balling defect evolution with scanning speed [256].

– **keyhole porosity** occur when the melt pool penetration is excessively high (figure 2.8) [248, 257–260];

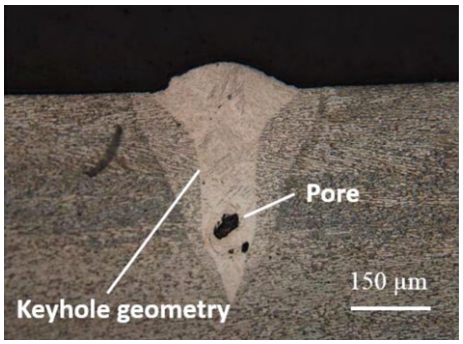

Figure 2.8: Keyhole pore [261].

– **roughness** is a consequence of inadequate melt pool geometry; protrusions and depressions are the results of the melt pool centre and sides, respectively; although impossible to be completely mitigated in the SLM process, a wavy surface may be resultant of low hatching space or high energy input, due to melting pool z-growth; can be mitigated by tuning parameters; Different authors argue that a direct correlation can be established between porosity and surface quality (figure 2.9); an excessive roughness on the lateral walls of the SLMed 3Dobject can be caused by particle aggregation due to sufficient heat to form a neck between part and wall [9, 247, 262]; roughness can also be highly detrimental to the performance of 3Dobject features, like internal channels or lattice structures and the consequential changes to diameter and overall design can negatively affect object qualification;

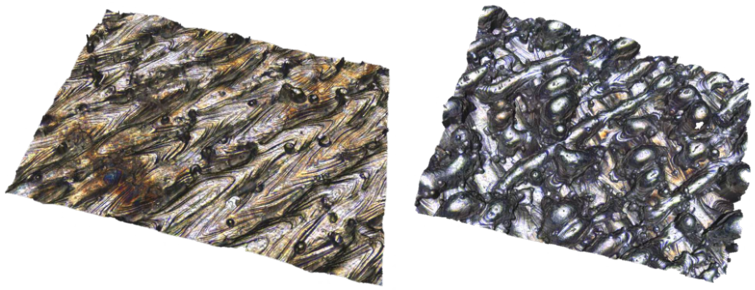

Figure 2.9: Surface roughness in SLM.

– **gas entrapment** results from the presence of protective or degradation-resultant gas, which is trapped by the melting pool within the 3Dobject; the porosity can be identified through small (tens of micrometre), perfectly spherical pores distributed throughout the 3Dobject (figure 2.10) [243];

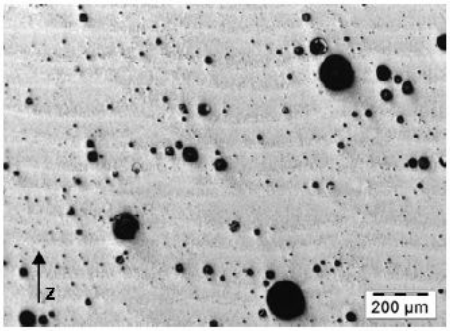

Figure 2.10: Porosity caused by gas entrapment [263].

– **cracks** result from thermal stresses during production, they can occur still during processing (hot-cracking) or during final cooling of the part (figure 2.11) [264–266];

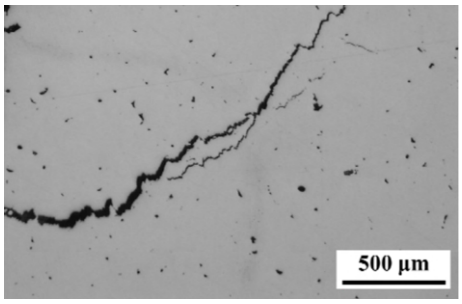

Figure 2.11: Cracking.

– **inclusions** not soluble in the base material can originate voids and chemical heterogeneities (figure 2.12); may result from inclusions already present in the powder or from deficient powder handling [267–269];

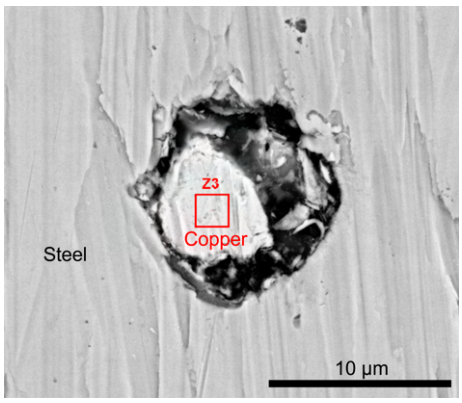

Figure 2.12: Copper inclusion in steel causing a defect.

– **geometrical defects** like distortion or warping are resultant of the complex thermal history that the 3Dobject is subjected to during SLM processing; other geometrical errors, like deviations, usually result from a bad translation of the scanning parameters to the true physical phenomena that are occurring since the melting pool width may not be well calculated; the stair-case effect is relative to the Z-resolution that is being input to the SLM process [270, 271];

– **spatter-related defects** are due to the spattered particles that are thrown back into the powder bed. Due to laser contact, abnormal particle shape and surface metallurgy can affect the melting pool [159, 272];

– **microstructural defects** are related to grain size, phase changes and anisotropy throughout the height of the 3Dobject. They are mainly caused by the complex thermal treatment that the 3Dobject is submitted to during processing and may impose different-than-expected properties; heat treatments are usually employed to solve some of the problems, but they are expensive, and some properties unique to SLM, like higher than normal tensile strength and hardness, may be lost after heat treatment [183, 272, 273].

A summary of porosity defects in 316L is shown in figure 2.13.

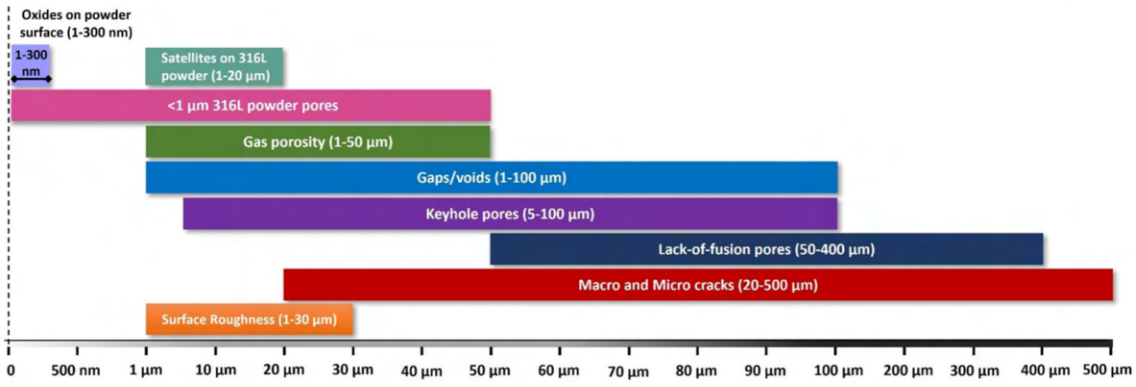

Figure 2.13: SLM defects and size [238].

2.3 Non-destructive Testing for Defect Detection

NDT techniques refer to a wide group of analysis techniques used to evaluate the properties of materials, parts/systems or devices without destroying their applicability. NDT is essential in a wide range of industries, including aerospace, automotive, power generation, oil and gas.

There are many different NDT techniques, each one with its own advantages and disadvantages. The most common NDT methods are radiographic testing, ultrasonic testing, magnetic particle testing, and eddy current testing. Radiographic testing uses X-rays or gamma rays to create an image of the object being tested. This method is often used to detect internal defects that are not surface-connected. Ultrasonic testing uses high-frequency sound waves. This method is often applied to inspect metal components for cracks or other defects. Magnetic particle testing uses a magnetic field to detect surface defects, often used in welding inspection. Eddy current testing uses an electric current; this method is often used to inspect non-metallic materials.

The low reliability of 3Dobjects in AM demands that a high number of objects is to be observed when critical applications are concerned. However, this can be a wasteful and meaningless process if repeatability is low, as is common in AM processes. NDT has been growing in AM as an essential tool to guarantee that the minimum standard is attained and the part is still usable, lowering waste and having higher reliability than random inspections.

Defect detection is dependent on the characterisation technique resolution and limitations. From visual/optical inspection to x-ray computed tomography, there is an established history of defect detection technologies that must be understood in order to assess the quality of the results of each selected technology. Moreover, certain NDT can be used for inline and real-time defect inspection, which might guarantee further knowledge of defect formation.

Since the dawn of AM, NDT has been developed for defect inspection, whatever the step of the manufacturing technology. Various reviews on this subject have been published since 2013, demonstrating the importance of these techniques for MAM [274]. Most of these techniques have already been subject to standards for metal applications, and specific MAM methodologies are in advanced phases of development [275].

2.3.1 Visual/Optical Method

Visual or optical method is the main form of defect observation. Generally, performed by the operator, using their knowledge and experience, is essential for cheap and rapid qualification of parts outside of the scientific quantification method. Naked eye inspection, optical microscopy, and scanning electron microscopy (cameras, mirrors, etc...) have, historically, been the main methods for 3Dobject observation and analysis. The use of

cameras for inline process inspection has been the main standard for MAM machines and is essential for cost and waste savings.

This type of technique is limited to surface observation and does not have access to any interior flaws without the total or partial destruction of the object (such as grinding and polishing). However, they can be used as an early qualification method to save time in the further costlier analysis of an already visible low-quality object. Nevertheless, an inline inspection can, through the use of video or layer photographs, be used as an input for optical tomography, resulting in a digital twin for further analysis, and correct information about interior features. Arguably more important, video can be an effective tool for observation of in-layer defect formation and as a way for parameter optimisation. Techniques such as optical emission spectroscopy can be associated with conventional recording to assess process-dependent emitted light to perform a temperature profile.

The main advantages of the described techniques are: they are well-established, mainly low-cost and quick. When used in tandem with other methods for measuring interior porosity, it can give a general idea of the overall quality of the object but not qualify the part for critical uses [276–278].

2.3.2 Liquid Penetrant Method

One of the most used NDT, due to its low-cost, and minimal expertise requirement, works on the basis that a liquid penetrant flows into part surface flaws, and excess liquid is removed. Defects are then revealed using a developer. Like optical testing, this method can only detect surface-connected defects. In additive manufacturing, some changes to the dye or liquid penetrant may be necessary due to the surface roughness, which can be signalised as a defect, affecting the technique capability to spot "hidden" defects. Typical resolution is limited to defects bigger than 750 µm [279, 280].

2.3.3 Magnetic Particle Method

Limited only to ferromagnetic materials, these techniques induce a magnetic field and analyse the behaviour of magnetic ferrous particles scattered around the surface. A discontinuity in the material will affect the magnetic field, and the particle behaviour will be changed, hence concluding that a surface defect is present. Defects smaller than 1000 µm are not suitable for this method [281].

2.3.4 Electromagnetic (Eddy Current) Method

These techniques measure changes in the electrical properties of the conductive materials. Porosity causes changes in capacitance, which is measured and analysed. In conventional Eddy current testing, a coil with alternating current induces two opposing magnetic fields. Defects affect the Eddy currents in the secondary magnetic field, which is measured by the impedance. The resolution for this testing method is reportedly bigger than 350 µm [282–284].

2.3.5 Ultrasonic Method

Ultrasonic methods involves the measurement of the reflection, transmission, mode conversion and diffraction of the ultrasonic wavelength when transmitted through a 3Dobject. Acoustic impedance affects the reflection and transmission of ultrasounds. Defects must be large enough to affect the ultrasonic beams, and resolution is considered to be one-half of the used wavelength (at least 500 µm). But this technique can be adapted for inline inspection by means of laser ultrasonic spectroscopy or phase array variation, and the use of laser ultrasonic testing can reportedly improve resolution to 100 µm. However, it is mainly material dependent, as well as other limiting factors, such as complex geometries, multimaterial or wide array of features, can make the use of this methodology impossible [285–287].

2.3.6 Acoustic Method

Acoustic emission uses a piezoelectric or electromagnetic transducer placed near the surface of the object to detect defects during manufacturing processing. Alternatively, it uses an optical microphone in the vicinity of the object. Used for inline inspection, the object must be subjected to forces for this technique to be effective. No resolution is reported for this technique; it depends mainly on the present material stresses.

For conventional acoustic emission, the main disadvantages are the contact with the surface, which might be impossible for some MAM processes [288, 289].

2.3.7 Infrared/Thermal Method

Thermography is an established technology that can detect geometrical defects, lack of material, inclusions and interior porosity. It uses infrared (IR) cameras to detect the temperature difference caused by objects to the energy input. Thermal energy can be essentially given by electrical current, laser and vibrations. The presence of a flaw in the

object will cause a disruption in an otherwise homogeneous heat distribution within the material.

One of the most exciting uses of this technology is the easiness to adapt for inline defect inspection, mainly on high heat-dependent processes, such as DED and PBF. Reading online melt pool status can be a powerful tool for parameter optimisation due to the fact that in-layer defect formation mechanisms can become clear under thermography. This technology has been adapted to be used paired with powerful software to warn or point out discontinuities in object scanning. Resolution is considered to be bigger than 400 µm; it is mainly connected to IR camera resolution and frequency. Moreover, the heat generation mechanism is extremely important since the fast material response to the given heat is necessary for disruption detection [290–292].

2.3.8 Other Methods/Techniques

Technologies such as Laser Induced Breakdown Spectroscopy (LIBS) can be a great addition to the inline object information. Capable of real-time chemical analysis, this technology can provide qualitative and quantitative results. This technology uses the wavelength and intensity of a laser-induced plasma. MAM laser-based processes are ideal for this technology since laser-caused vaporization is already present [293].

Conventional profilometry is an established testing method that has been substituted, in AM, for technologies that can give integral information about the surface defects (roughness). Since roughness in MAM is dependent on the scanning method, a pattern and a preferential direction are usually present, making 2D profilometry obsolete for qualifying the part. Laser and optical-based methods, such as focus variation microscopy, have been growing as effective testing methods for roughness evaluation of AM parts [294–296].

2.3.9 Radiology Method

Radiographic testing is a nondestructive testing that uses chi (χ) rays, gamma (γ) rays or neutrons (n) to inspect materials and objects for hidden flaws. X-ray is undoubtedly the most used radiation for NDT. X-ray radiography or radiographic testing uses an x-ray beam to measure the attenuation caused by an object in its path. X-ray computed tomography (XCT) takes this concept and uses a full 360° scan to slice the object into a volume rendering. These techniques are limited by the radiation absorption of the 3Dobject, thicker materials or higher atomic weight materials being more difficult to transmit through. In order to overcome this issue, higher energy and intensity are required, which

is longer and more costly. Image quality is dependent on the resolution, contrast and artefacts (such as noise) [297, 298].

Growing research regarding μCT use in MAM inspection is now a reality. The possibility of detecting microdefects, their geometry and their accurate location contribute to the analysis of the so-called "effect of defect". Studies on the influence of porosity size, location and shape have been used as an input to a new age of material research, using modelling for predicting final material properties and fatigue behaviour [9, 299].

The most common methodology for micro-computed tomography is the use of a 3D cone x-ray source and a flat panel detector. The source or the object rotates continuously for 180° (symmetrical objects) or 360° until a half or full scan is achieved. A brief history of the relation of μCT and AM is established by Thompson et al. in 2016 [300]. As an NDT methodology, μCT has been used as a transversal technique, from powder to final part porosity.

μCT has been relatively scarce in MEX research. Damon et al. and Santamaria et al. [93, 301] used the technique to measure the process-induced porosity in sintered parts. Singh et al. [302] used μCT to validate the optimised extrusion parameters for copper production. As far as the authors are aware, no other metallic material extrusion research has been focused on using μCT for the study of MEX defects. Moreover, no transversal study of the MEX process from feedstock to final 3Dobject, using μCT, has been published.

μCT in SLM, on the opposiotion, has been developing in the last few years, and a few reviews have already been published [300, 303–305]. μCT has mainly been used for defect reconstruction, and visualisation [306–308]. However, research studies on the use of μCT as an input for modelling are still growing and are limited to lattice structure behaviour [309–313]. A deep study of dense specimens has often been hindered by process resolution or source power. Nevertheless, the contribution of μCT to the qualification of small SLM 3Dobjects must be explored and put into evidence.

Chapter 3

Materials and Methods

In this study, copper and stainless steels were selected for the production of 3Dobjects. MEX, and its parent technology, PIM, used SS 316L homemade filaments. Homemade filaments were compared to commercial filament alternatives - BASF (BASF SE, Ludwigshafen, Germany) and Virtual Foundry (The Virtual Foundry, Wisconsin, USA).

In SLM, to study the influence of additive manufacturing limitations on the production of highly conductive materials, copper was chosen as the master material. This material was selected due to its high demand, related to its unique thermal and electrical properties, which are highly desirable to associate with novel complex geometries and applications, and to its particular challenge for MAM production. Furthermore, a tailored copper alloy, copper + 316L steel (80:20 weight), was mixed through manual tumbling of the two different powders. This copper-based iron alloy is known as a high-strength, electrical and thermal conductivity material with magnetoresistance. However, this material is an extremely difficult copper:iron alloy to produce due to the positive enthalpy between liquid Cu and Fe. Moreover, four different stainless steels powder were selected to evaluate the material reaction to a constant VED value: 316L, 630, 420 and 440C (AISI).

Different powder characteristics are needed for SSAM and LSAM for the production of 3Dobjects.

For MEX, powder particles were furnished from Sandvik Osprey Ltd. Powders for SLM, SS 316L and 630 (17-4PH) were provided from SLM Solutions (SLM Solutions Group AG, Lübeck, Germany), and 420, 440C and copper powder were furnished from Sandvik Osprey Ltd (Sandvik AB, Sandviken, Sweden).

The chemical compositions of the copper and steel powder provided by the supplier are summarized in table 3.1.

Table 3.1: Chemical composition of the studied powder (wt.%).

Element	Fe	C	Cr	Ni	Cu	Mo	Nb+Ta	Si	Mn	N	P	S	O
316L (SLM)	Balance	0.030	16-18	10-14	-	2-3	-	1	2	0.100	0.045	0.030	0.100
316L (MEX)	Balance	0.030	16-18	10-14	-	2-3	-	1	2	-	0.040	0.030	-
630 (SLM)	Balance	0.070	15-17	3-5	3-5	-	0.150-0.450	1	1	0.100	-	0.030	0.100
420 (SLM)	Balance	min 0.150	12-14	-	-	-	-	1	1	-	0.040	0.030	-
440C (SLM)	Balance	0.950-1.200	16-18	-	-	0.750	-	1	1	-	0.040	0.030	0.100
Copper	<0.05	-	-	-	Balance	-	-	-	-	-	-	-	<0.100

3.1 Powder characterisation

Particle size and particle size distribution (PSD), as well as specific surface area were evaluated by laser diffraction spectrometry LDS, Malvern Mastersizer 3000 (Malvern Panalytical, Egham, UK). SEM Quanta 400 FEG STEM (FEI Company, Oregon, USA) was applied for powder shape factor evaluation. Powder density was measured (5 samples per powder material) by helium pycnometry with Accupyc 1330 (Micrometrics, Georgia, USA).

The phasic composition was evaluated by X-ray diffraction. A Philips X'Pert diffractometer (Philips, Egham, UK) at 40 kV, with Bragg–Brentano geometry (θ–2θ), cobalt anticathode ($\lambda(k\alpha 1) = 0.178897$ nm and $\lambda(k\alpha 2) = 0.179285$ nm), and a current intensity of 35 mA. The x-ray diffraction scans were carried out in steps of 0.025°, with an acquisition time of 1s per step. The copper was indexed with ICDD 004-0836, austenite phase was indexed with ICDD 33-0397 and ferrite/martensite with ICDD 87-0722.

3.1.1 Stainless Steel powder for MEX production

Concerning the powder particles used in MEX, shape factor for the stainless steel (316L) was close to 1 (figure 3.1).

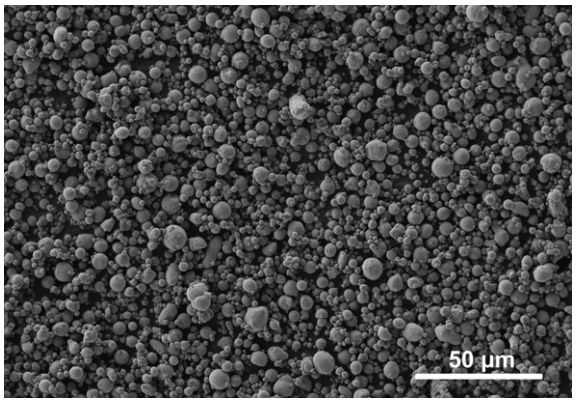

Figure 3.1: Particle shapes of the MEX 316L powder.

Powder size was suitable to be processed, for filament fabrication followed by sintering, with a D_{50} of 6.8 µm with the distribution observed in figure 3.2.

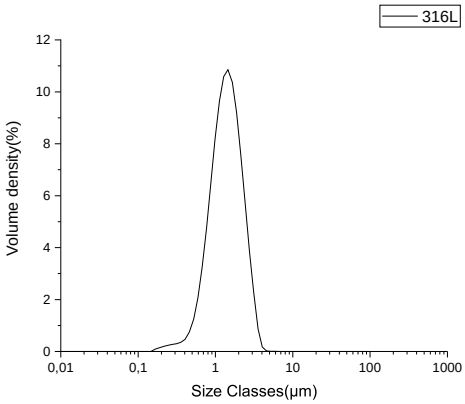

Figure 3.2: Particle size of the MEX 316L powder.

The powder phasic structure was constituted of austenite with a relevant residual martensite phase (figure 3.3).

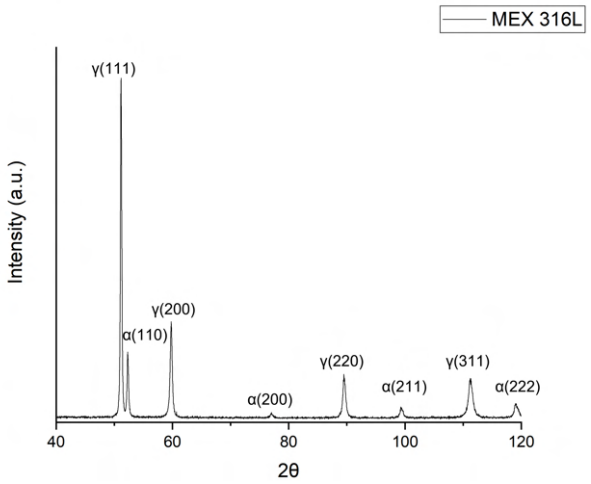

Figure 3.3: X-ray diffractogram of the MEX 316L powder.

3.1.2 Copper powder

Copper powder had a mostly spherical shape with a low dispersion of sizes (figure 3.4). The D_{50} of the copper powder was slightly bigger than optimal for SLM processing (figure 3.5).

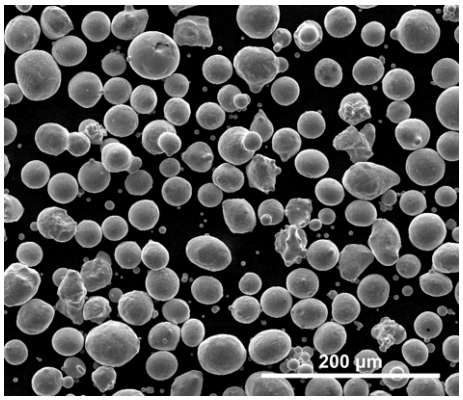

Figure 3.4: Particle shapes of the copper powder (SEM).

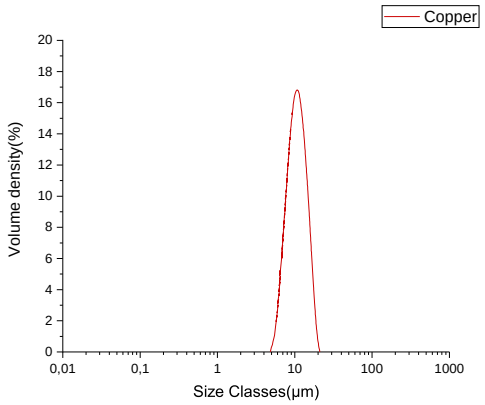

Figure 3.5: Particle size distribution of the copper powder.

X-ray diffraction shows only copper (figure 3.6).

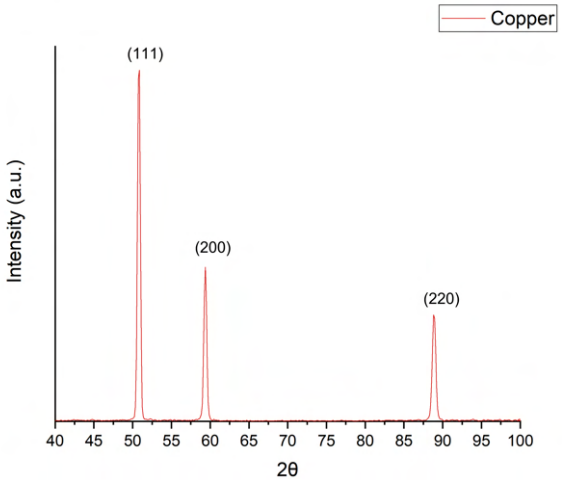

Figure 3.6: X-ray diffractograms of the SLM copper powder.

3.1.3 Stainless Steel powder

The stainless steels selected in the present study are related to their characteristics and applications. Stainless steel 316L has been the most studied material in SLM [314] and is used as a standard in this thesis. SS 630 was selected due to its low carbon content, and excellent mechanical properties [315]. 420 martensitic stainless steel is also of significant interest due to its high strength and corrosion resistance [316]. Consequently, many studies have been published concerning the microstructure, mechanical properties, and roughness of these stainless steels produced by SLM ([252, 317, 318] – 316L, [319–321] – 630, [153, 198, 322] – 420). SS 440C, which is also a martensitic stainless steel, with

the highest carbon content of all stainless steels studied. This steel is used in applications where high hardness and corrosion resistance are required (e.g. bearings and other automotive parts, and knives) [323].

All stainless steel powder had an adequate shape factor (1) for SLM, but with some satellites only on 440C that could modify the bed density and powder flowability (figure 3.7).

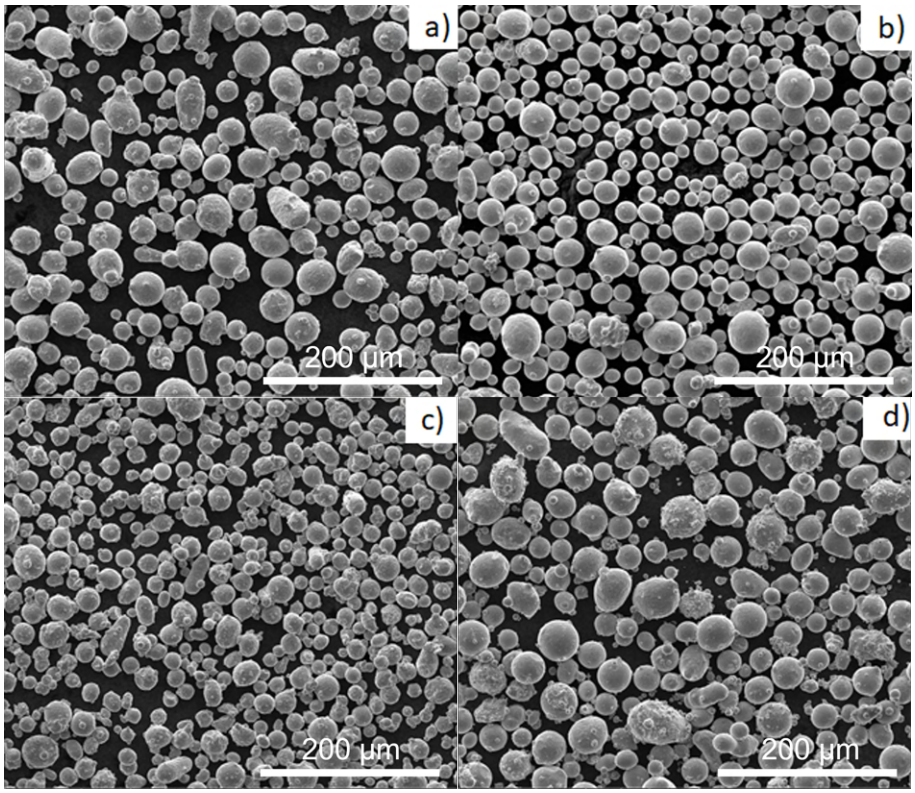

Figure 3.7: Particle shapes of the 316L (a), 630 (b), 420 (c) and 440C (d) powder (SEM).

The powder particle size and particle size distribution were similar for all selected steels, which guarantees that the packing density is similar (figure 3.8).

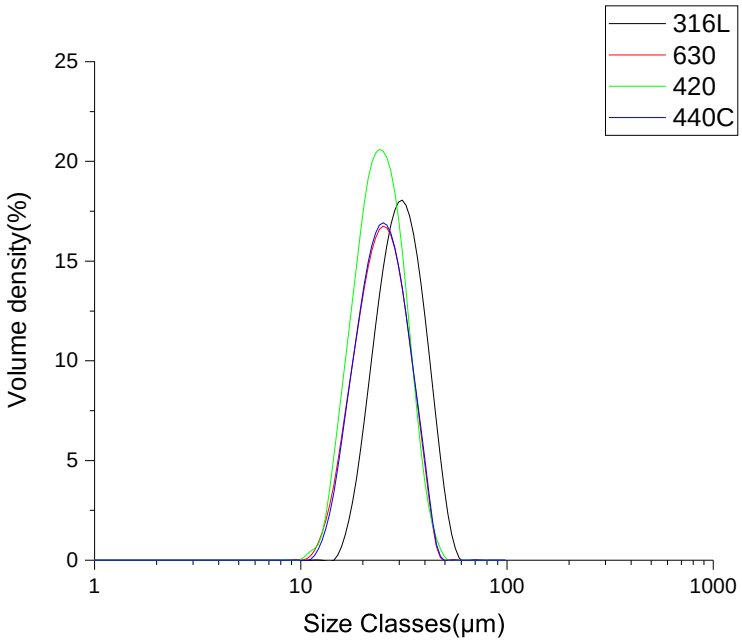

Figure 3.8: Particle size distribution of the 316L (black), 630 (red), 420 (green) and 440C (blue) powder particles.

Two phases, austenite and ferrite/martensite, can be distinguished in 316L, 630, 420 powder particles. In 440C steel, usually martensitic, the austenite presence can be due to the high carbon content or high cooling rate (figure 3.9).

Table 3.2 summarizes the main powder characteristics for all studied particle powder, including density.

Table 3.2: Powder characteristics.

Powder	Particle Size D_{10} (µm)	Particle Size D_{50} (µm)	Particle Size D_{90} (µm)	Shape factor	Phase Composition	Density $\rho\left(\frac{Kg}{m^3}\right)$
316L (MEX)	3.6	6.8	12.0	$\simeq$1	Austenite and residual martensite	7342
316L (SLM)	22.7	32.4	45.2	$\simeq$1	Austenite and residual martensite	7880
630 (SLM)	17.8	26.2	37.6	$\simeq$1	Austenite and martensite	7880
420 (SLM)	17.0	24.3	34.3	$\simeq$1	Austenite and martensite	7820
440C (SLM)	18.1	26.4	37.9	$\simeq$1	Austenite	7940
Copper (SLM)	30.7	46.7	69.0	$\simeq$1	Pure Copper	8940

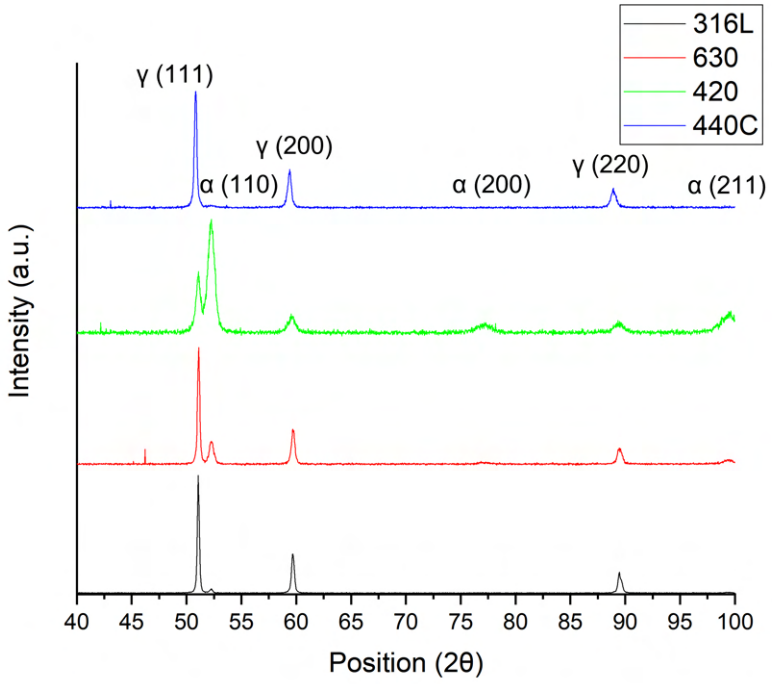

Figure 3.9: X-ray diffractograms of the 316L, 630, 420 and 440C powder particles (from bottom to top).

3.2 Feedstock production

In MEX, an effective mixture between the powder, binder and additives is essential for the success of the debinding and sintering steps. In this study, an optimised mixture of 316L powder [42, 324], master binder and additives (backbone and plasticizer) were mixed on a Plastograph® Brabender W50 torque rheometer (Brabender GmbH & Co. KG, Duisburg, Germany) at 180°C, 30 rpm, with a 38.5 cm^3 mixture chamber. Previous studies on the CPVC of 316L stated that 60 vol.% for this particular metallic powder [42].

The resulting mixture was granulated and extruded into filament, on a Brabender single-screw extruder, with five different heating zones. The nozzle diameter was the same as the intended final filament diameter, 1.75 mm. The heating steps were set, from feeder to nozzle, to 160, 165, 170, 175 and 180°C.

3.3 3Dobject Production

3.3.1 Solid State AM (MEX)

The filaments were processed through a Prusa i3 MK3S (Prusa Research, Prague, Czech Republic) with a 0.4 mm nozzle diameter. For the production of SS 316L, the nozzle temperature was set at 195°C for the first layer and 190°C for the other layers. Bed temperature was set at 60°C. Print speed was 20 mm/s, and the extrusion multiplier was 1.1, with the objective of offsetting the overlap and creating a more homogenous layers. A large test group for the analysis of shaping parameters is summarised in table 3.3.

Table 3.3: MEX production conditions for 316L 3Dobjects.

3Dobject	Layer Height (mm)	Strand Width (mm)
H0.15W0.45	0.15	0.45
H0.15W0.35	0.15	0.35
H0.10W0.45	0.10	0.45
H0.10W0.35	0.10	0.35
H0.05W0.45	0.05	0.45
H0.05W0.35	0.05	0.35

The selected 3Dobjects were cylindrical (10 mm diameter and 5 mm height) in order to assess the geometrical accuracy of the MEX process (figure 3.10).

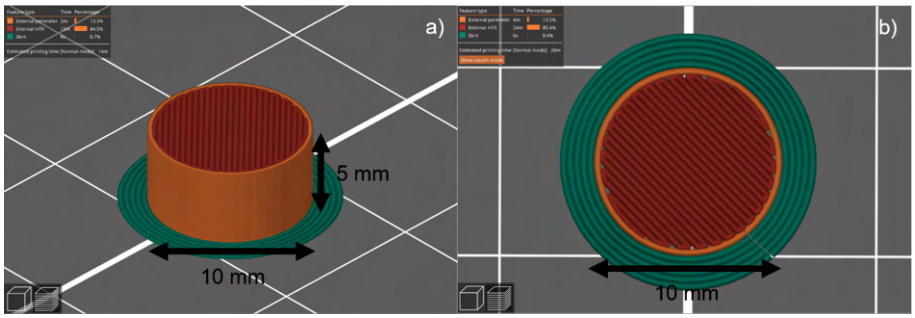

Figure 3.10: Cylinders dimensions for MEX production: a) isometric and b) top views.

All 3Dobjects were debinded and sintered in an Ar + H_2 atmosphere (5 vol.% H_2). The thermal cycles selected for debinding (1°C/min) and sintering (10°C/min) 316L green are shown in figure 3.11, respectively.

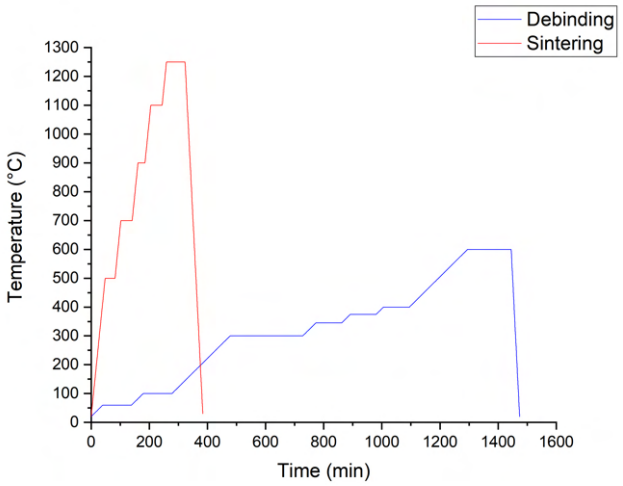

Figure 3.11: Debinding and Sintering Thermal Cycles for SS 316L.

3.3.2 Liquid State Based AM (SLM)

For all copper productions, an SLM 125HL from SLM Solutions was utilised, equipped with a Yb-fiber laser (λ=1064 nm) with a maximum power of 400 W and a spot size of 100 µm, under an argon atmosphere. Pure copper was processed using a fixed power of 400 W due to the aforementioned absorption issues. The design test group for the optimisation of pure copper production is summarised in table 3.4.

Table 3.4: Test group for pure copper production.

Position	Parameter	A	B	C
1	Scanning Speed (v)	-	240	270
	VED $\left(\frac{J}{mm^3}\right)$	-	220	200
2	Scanning Speed (v)	300	330	360
	VED $\left(\frac{J}{mm^3}\right)$	180	160	150
3	Scanning Speed (v)	390	420	-
	VED $\left(\frac{J}{mm^3}\right)$	140	130	-

Copper Steel production, due to the uncertainty of the response of the mixture to the laser energy, was more broad. Test group parameters are summarised in table 3.5

Table 3.5: Test group for copper-steel production.

Position	Parameter	A	B	C	D	E
1	Power (W)	200	200	200	200	200
	VED $\left(\frac{J}{mm^3}\right)$	140	160	180	200	220
2	Power (W)	250	250	250	250	250
	VED $\left(\frac{J}{mm^3}\right)$	140	160	180	200	220
3	Power (W)	300	300	300	300	300
	VED $\left(\frac{J}{mm^3}\right)$	140	160	180	200	220
4	Power (W)	350	350	350	350	350
	VED $\left(\frac{J}{mm^3}\right)$	140	160	180	200	220
5	Power (W)	400	400	400	400	400
	VED $\left(\frac{J}{mm^3}\right)$	140	160	180	200	220

Following the position of the 3Dobjects, the proposed nomenclature is: VXXXWYYY, where V identifies the VED, W identifies the power and XXX and YYY are the set values for each of these parameters, respectively.

The SLM equipment used for stainless steel production was an EOS M290 system (EOS GmbH, Krailling, Germany) equipped with a Yb-fiber laser (λ=1064 nm) with a maximum power of 400 W and a spot size of 100 µm.

SLM processing of stainless steels was undertaken with an oxygen content below 0.1 vol.% in the working chamber using a continuous flow of nitrogen. Laser power was set at 260 W, scanning speed at 1060 mm/s, hatch space at 100 µm, and a layer thickness of 30 µm (VED 82 J/mm^3). The scanning strategy was a zigzag pattern with a rotation angle of 67° between adjacent layers. Each batch included density cubes ($10 \times 10 \times 10$ mm^3) and tensile test specimens. Additionally, a 10° rotation relative to the substrate position was added to avoid contamination by spattering. All 3Dobjects were studied as-SLMed, without post-processing treatment.

3.4 3Dobject characterisation

The final density for all 3Dobjects was evaluated through the Archimedes method. Materialography was supported by optical microscopy using a Leica DM 4000 M LED (Leica Microsystems AG, Wetzlar, Germany) with a Leica camera, model MC 120 HD.

Copper surface etching was performed with $FeCl_3$, HCl , H_2O and $C_3H_8O_3$ (1:1:3:5). For 316L, 630 and 420 steels, etching treatment was Vilella solution. For 440C, Kalling solution etching was selected.

Surface roughness was evaluated using focus variation microscopy Alicona Infinite Focus - IFM (Bruker, Kontich, Belgium) following ISO 4287 and 4288.

Copper and copper alloy thermal conductibility was measured with a TPS2500 from Hot Disk (Hot disk AB, Göteborg, Sweden) based on the Transient Source Plane (TPS) method and suitable for measuring a wide range from 0.005 – 1800 W/m.K.

Microhardness measurements were performed on a Fisherscope H100 (Fischer Instrumentation LTD, Pershore, UK), equipped with a Vickers indentor (10 measurements per sample, maximum load of 1000 mN, holding time of 30 s). Tensile tests were performed on a SHIMADZU Autograph (Shimadzu, Kyoto, Japan), with a 100 kN load cell, according to ISO 6892, at room temperature with a rate of 10 MPa per second. Tensile specimens dimensions are in accordance to figure 3.12. All bulk values were taken from CES Edupack material selection software [325].

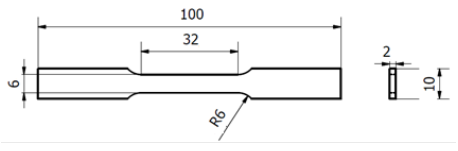

Figure 3.12: Tensile test specimen measurements, in mm.

3.4.1 μCT

μCT is the main defect characterisation technique used in the present study, Surface and inside defects tensile specimens were evaluated by X-ray micro-computed tomography using a Bruker SkyScan 1275 (Bruker, Kontich, Belgium). Tensile specimens of SLMed were polished on both the top and bottom surfaces until a thickness of 2 mm was achieved. For all 3Dobjects, an acceleration voltage of 100 kV and a beam current of 100 µA were set using a 1 mm copper filter with step-and-shoot mode. The images were acquired at 0.4° angular step with 10 frames average per step using an exposure time of 245 ms. The µCT images were reconstructed with the dedicated manufacturer software. The pixel size was set to the minimum value possible, and the random mode was used. For tensile specimens, 10 µm was used; for MEX 316L and copper, pixel size was set at 8 µm.

Chapter 4

MEX as a Paradigm of Defects in Solid State Additive Manufacturing

This chapter highlights the groundwork necessary to attain the main objective of the thesis, smart control of defects – in additive manufacturing – and their origin, in order to achieve the necessary quality for structural/functional applications. Powder technologies for manufacturing objects are supported in phenomena that generally occur in solid state (e.g. pressing and sintering, powder injection moulding, ...). In additive manufacturing, the challenge is not only in solid state, but also when using technologies where cooling at high rates of a liquid phase is essential to attain the final object (liquid state additive manufacturing). Thus, this chapter analyses defects in solid-state processes (MEX) and is followed by two chapters where the liquid phase is essential to attain consolidation (SLM).

The preselection of solid state additive processes as the demonstration, with universal character, is due to the complexity of stages necessary to attain a 3Dobject. This enlarges the spectra associated with the common type of defects in additive manufacturing. The target is to highlight, but not establish, the report between defect and application, whatever the additive manufacturing technology. The MEX is the most suitable indirect additive manufacturing technology to achieve the disclosed goals. This technology, based on PIM, accentuates the gaps between layers, which is uncharacteristic in PIM, so new challenges for effective densification emerge. Moreover, the addition of additives to the binder (PIM) may bring unforeseen consequences to the debinding step. Consequently, it is essential to provide a critical overview of the defects and defect-inducing mechanisms existent in MEX.

As stated in chapter 2, defects in MEX can be separated into three specific steps: feedstock, shaping and consolidation (which includes debinding and sintering). As such, each of these phases must be analysed separately to assess the processes of defect emergence.

4.1 Feedstock Preparation

Three types of filaments with different particle sizes and particle size distribution were effectively analysed using µCT. One was developed at UC, and the other are commercially available. UC filament presented some random defects throughout its volume, which might be mainly related to trapped gas when mixing/extruding the filament. Furthermore, elongated defects can be present close to the surface. This type of porosity is mainly due to material recuperation after passing through the nozzle (figure 4.1).

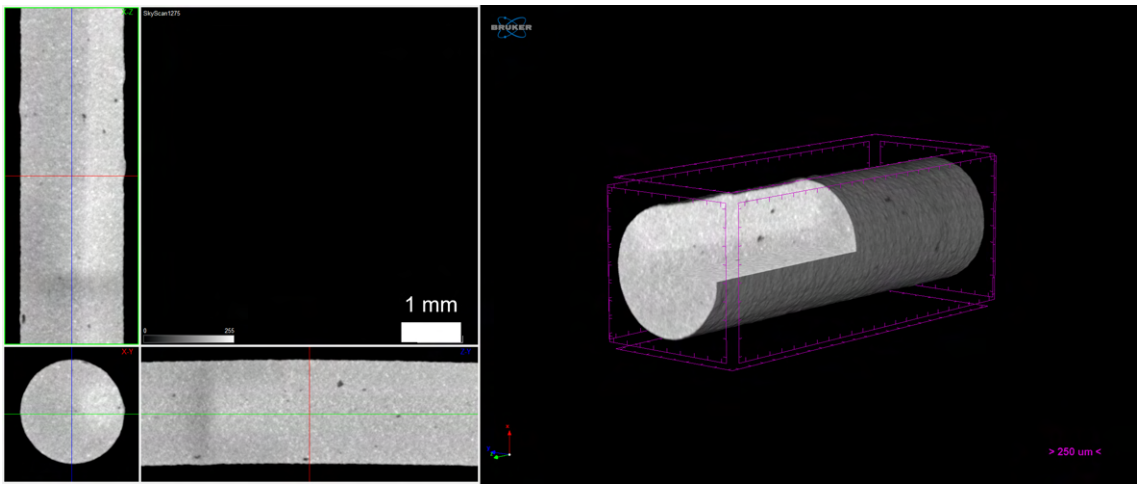

Figure 4.1: 2D and 3D visualisation of defects location in UC filament cross-section (left and right).

In what concerns BASF filaments, they show a large number of minor defects in the filament volume (figure 4.2). These defects may be related to a lack of effective binder wettability between 316L powder and binder+additives (figure 4.3, right). Moreover, BASF opted for using a solution of "encapsulating" their filaments with a polymeric coating, providing strength and flexibility to the filament, making it effectively easier for handling, which is visible by SEM (figure 4.3, left). It must be highlighted that this solution may contribute to problems during 3Dshaping (nozzle clogging and excess of polymer in the interface layers that constitute the green of the 3Dobject).

Virtual Foundry (VF) uses a different approach from UC and BASF filaments (figure 4.4). With a single binder polymer (PLA), bigger 316L powder particles, visible by μCT, reveals stochastic defects and enormous interparticular spaces.

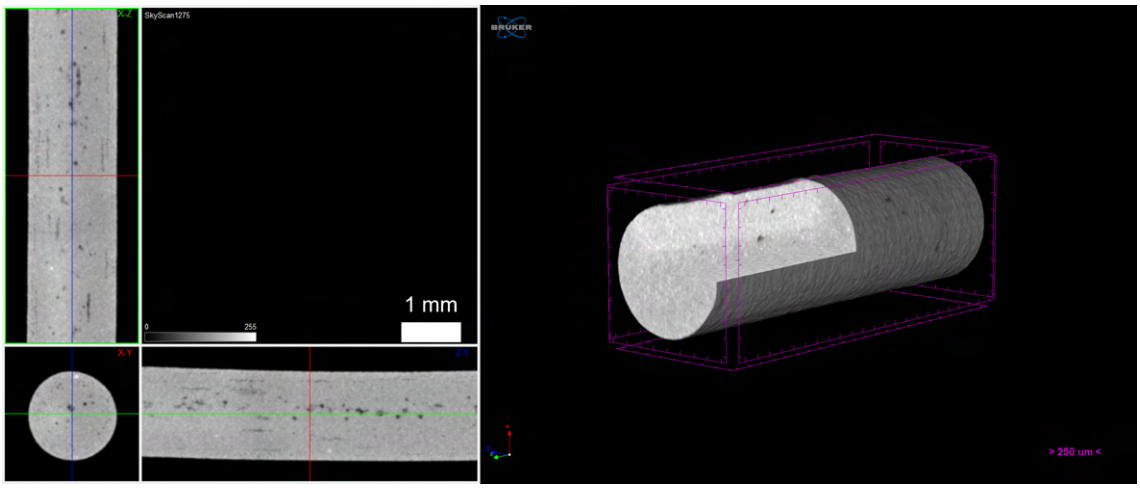

Figure 4.2: 2D and 3D visualisation of defects location in BASF filament cross-section (left and right).

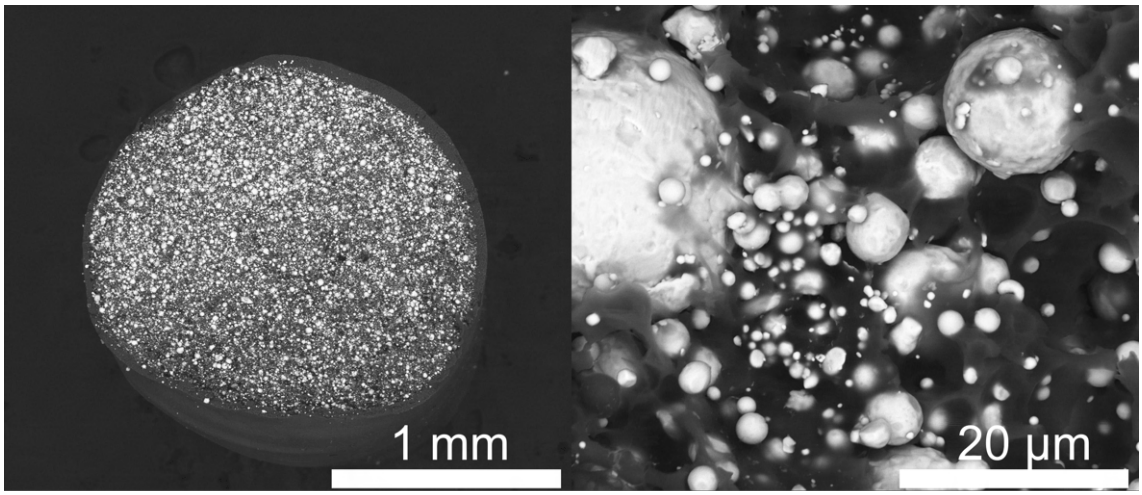

Figure 4.3: SEM of BASF filament cross-section.

Analysis of geometrical defects (e.g. eccentricity) through μCT demonstrates that higher than optimal diameter filament is achieved through extruding with a 1.75 mm nozzle due to the filament elastic recuperation. BASF and VF filaments have lower-than-optimal filament diameters. All filaments studied have a small and similar eccentricity.

All filaments were submitted to the printer nozzle to assess the particle reorganisation within the strand (feedstock after exiting the 0.4 mm nozzle) and mainly the polymer response to the heat temperature. The UC strand shows the nonexistence of defects larger than 10 µm (µCT resolution). On the other, it is clear that the strand maintains the cylindrical aspect of filament (figure 4.6). Regarding BASF strands, they show small defects throughout the length of the filament (figure 4.7). VF strands are deformed and full of defects. This is to be expected from the larger metallic powder particle size when com-

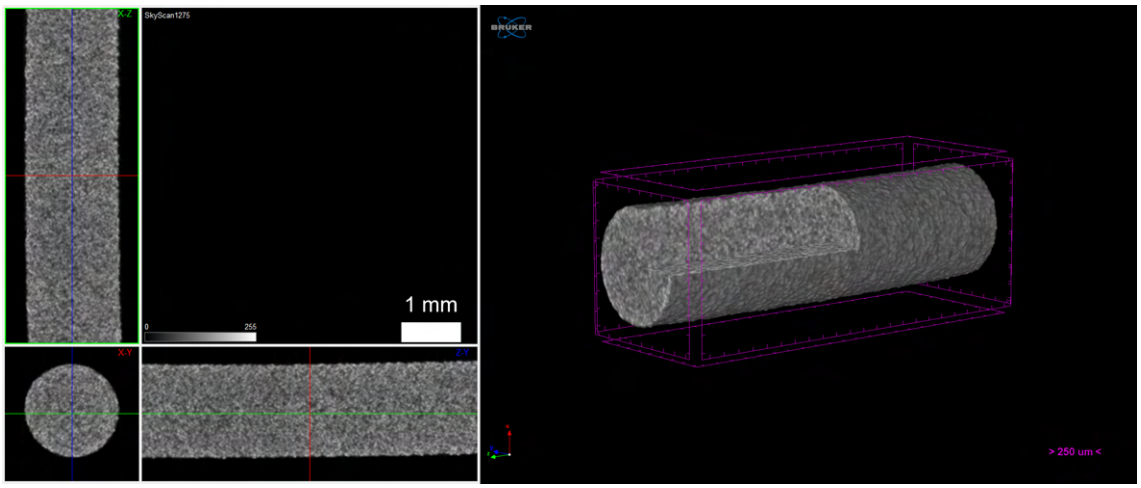

Figure 4.4: 2D and 3D visualisation of defects location in VF filament cross-section (left and right).

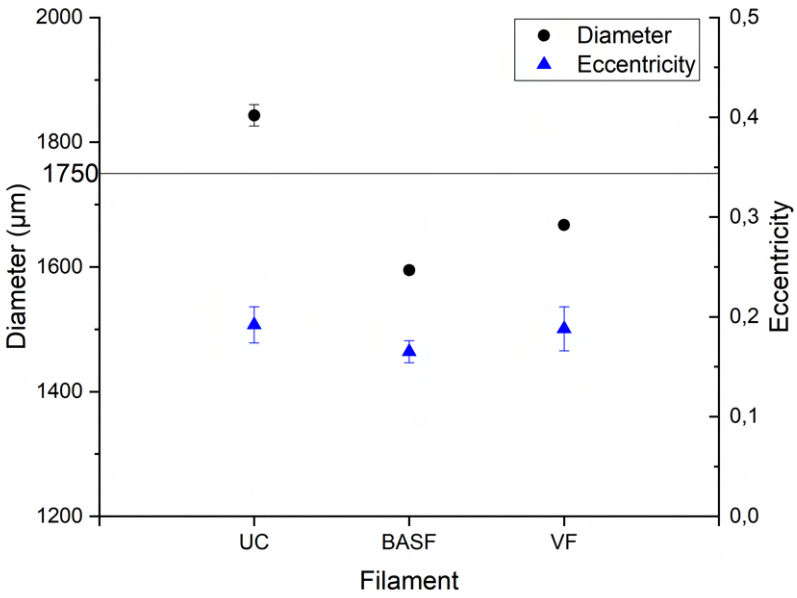

Figure 4.5: Measured diameter and eccentricity of the different analysed filaments.

pared with UC and BASF filament since the diameter change from 1.75 mm (filament) to 0.4 mm (strand) leads to massive particle stress and to an almost hollow cylinder with irregular size (figure 4.8).

Eccentricity analysis (figure 4.9) seems to demonstrate that only the UC strand remains a quasi-perfectly cylindrical shape, with a diameter closer to 0.4 mm. The wide eccentricity range of values for the VF strand is a clear indicator of extreme shaping difficulties that

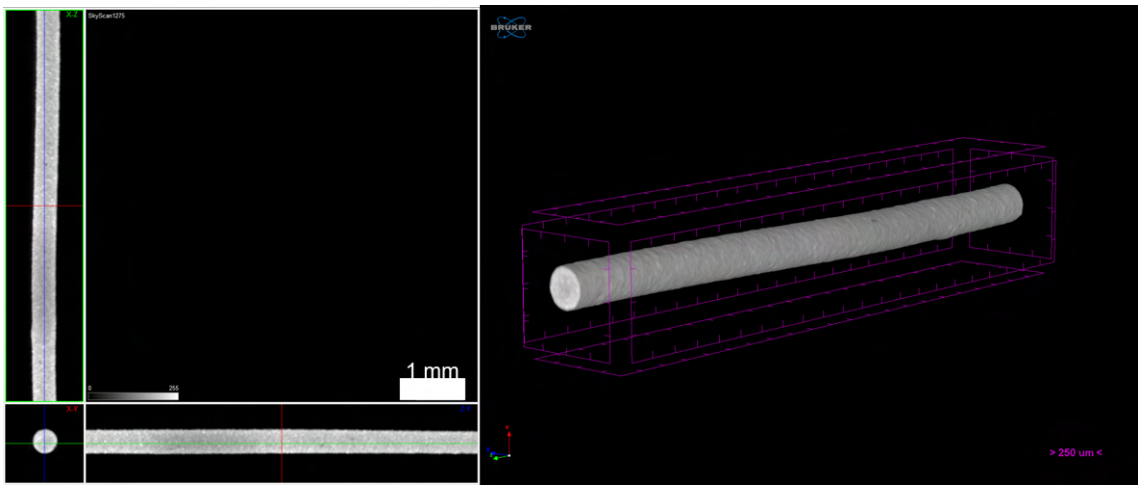

Figure 4.6: 2D and 3D visualisation of defects location in UC strand cross-section (left and right).

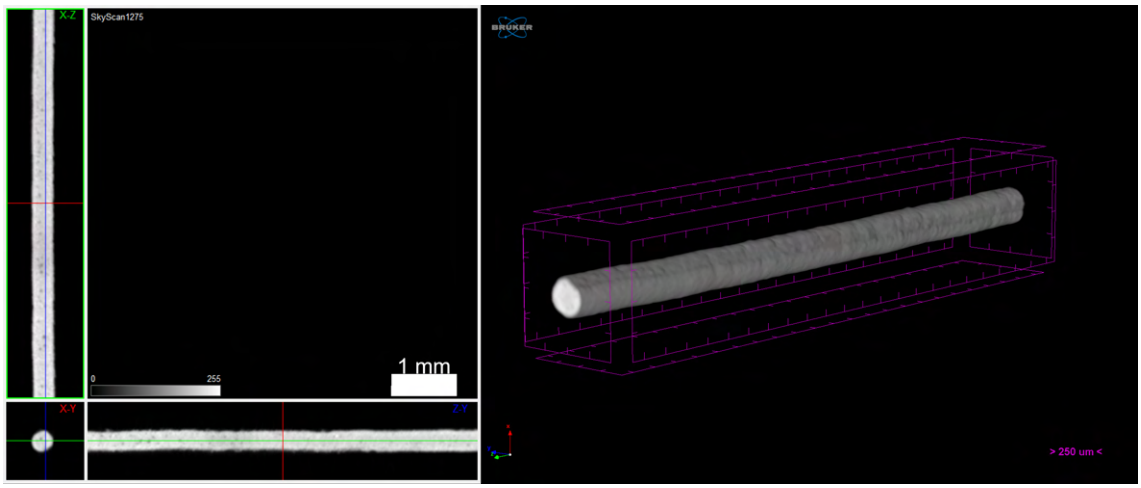

Figure 4.7: 2D and 3D visualisation of defects location in BASF strand cross-section (left and right).

may arise from irregular strands within the 3Dobject.

As can be observed, μCT evaluation of the feedstock can be an effective tool for assessing some of the expected defects that will occur during shaping and sintering. Some feedstock characteristics can be previewed, such as powder size inadequacy and irregular filament and strand sizes, as well as uneven powder/polymer distribution.

4.2 Green 3Dobject from UC filament

As stated in methodology (chapter 3), a test group of cylinders with different shaping parameters was manufactured. Layers of 0.15 mm from 0.45 mm strand size were selected

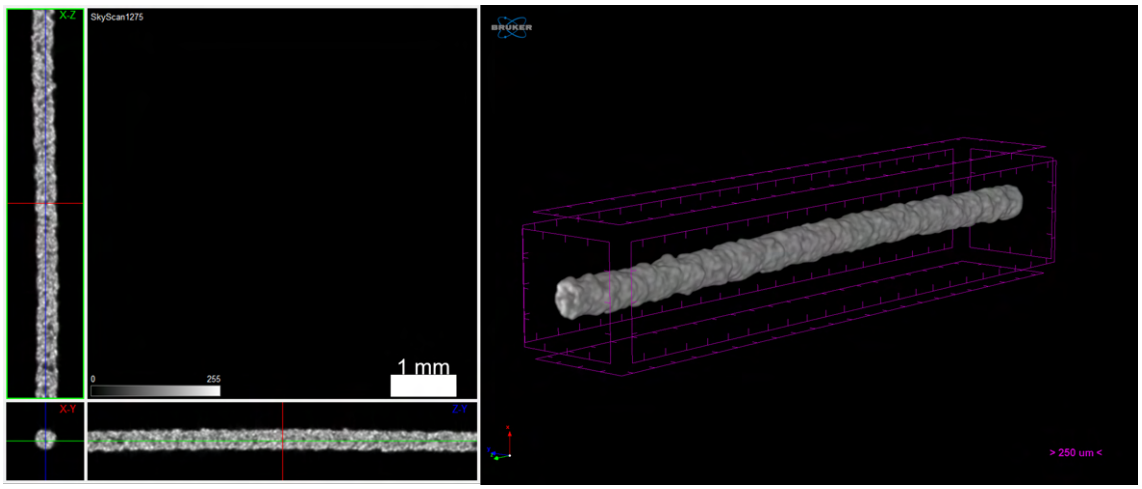

Figure 4.8: 2D and 3D visualisation of defects location in VF strand cross-section (left and right).

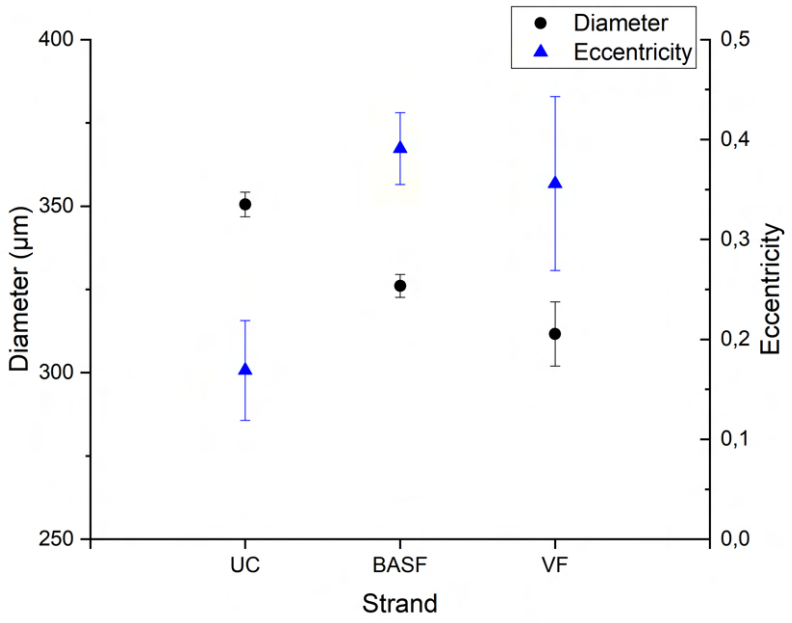

Figure 4.9: Diameter and eccentricity of the strands (UC, BASF, VF).

to be the standard for this study. It assesses the filament capability to be processed through a 0.4 mm nozzle, whatever the layer height. A 0.05 mm final layer height was selected, which is the equipment minimum capability. Strand size considerations are complex due to the extruding physics involved in the process. When a strand is deposited, multiple factors must be considered due to nozzle movement, flow and interaction with the substrate. Consequently, strand width is usually regarded as 0.45 mm for a 0.4 mm nozzle. Nevertheless, when layer height was set to 0.15 mm, single, separated strands were evident

(figure 4.10). This means that there is a general inadequacy of standard parameters for this strand size and flow. Moreover, defects relating to path generation are clearly visible. The comparison with the shaping input (figure 4.11), top 2D layer image to object clarifies the observed intralayer defects. Moreover, a seam (the point where a single strand starts and finishes) is visible, which causes a defect, impossible to avoid in MEX.

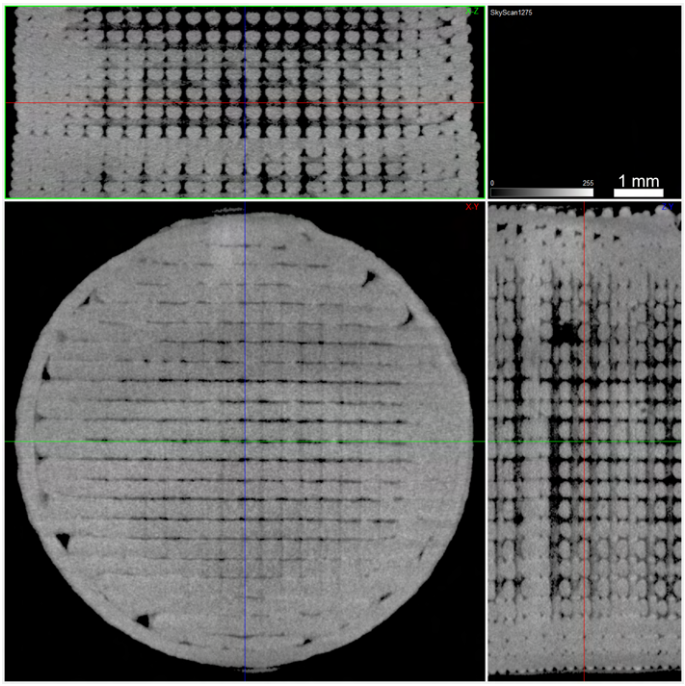

Figure 4.10: 2D cross-section of the H0.15W0.45 cylinder.

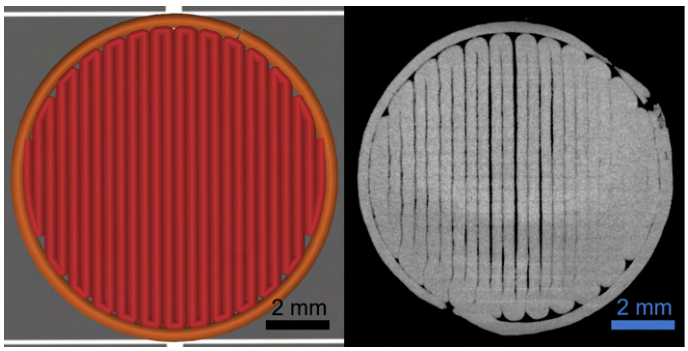

Figure 4.11: Top layer comparison between slicing input and final object (left and right).

Through defect and volume separation, using μCT, it is possible to observe them inside the 3Dobject (figure 4.12). Volume rendering allows for the clear visualisation of stacked porosity, with strand direction, layer per layer. This corresponds to the general inadequacy of the strand width parameter to the selected height. Furthermore, a kind of corner defect is visible and related to the stated inevitable strategy defects.

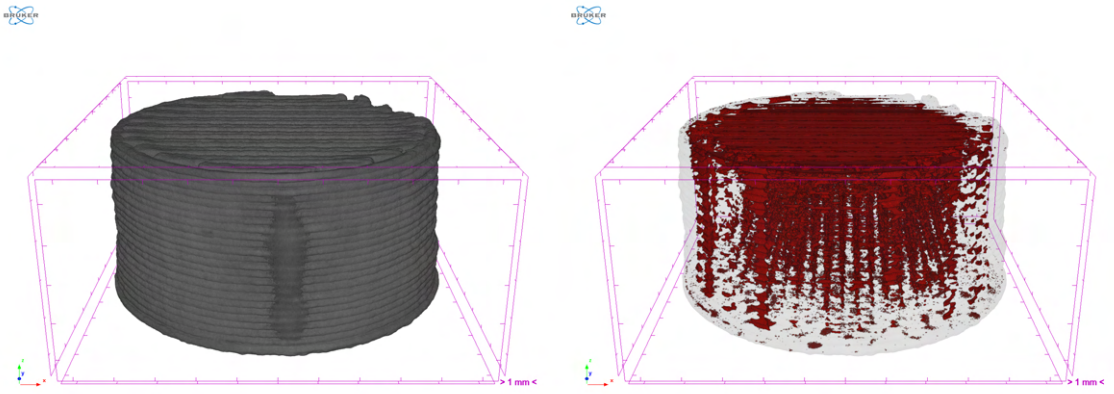

Figure 4.12: 3D rendering of the H0.15W0.45 cylinder volume and defects (left and right).

Further decreasing the layer size did not have a significant influence on the overall lack of density of the 3Dobject (figures 4.13 and 4.14). Poorly stacked strands are visible throughout the object, which seems to affect its geometric accuracy. Besides infill strand width inadequacy, lack of contour-infill overlap is also evident and prejudicial to the quality of structural/functional application.

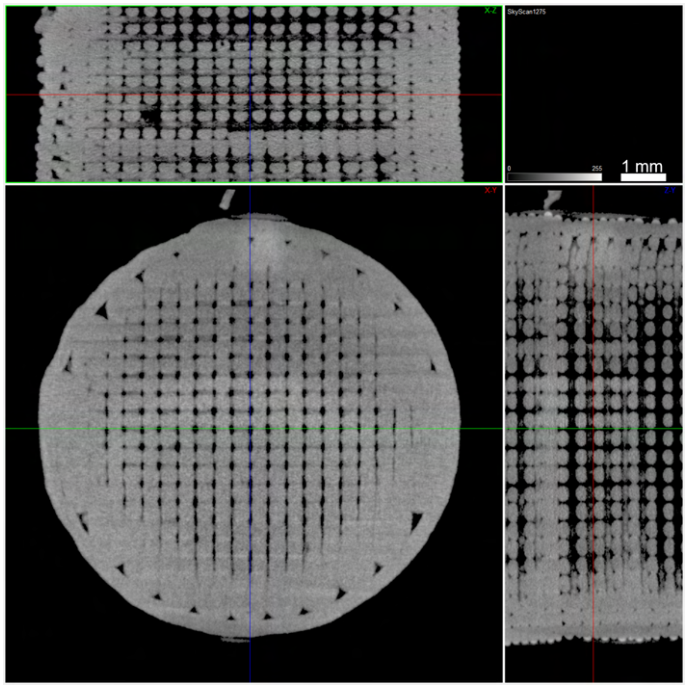

Figure 4.13: 2D cross-section of the H0.10W0.45 cylinder.

Layer height reduction to 0.05 mm resulted in major alterations regarding the 3Dobject density (figure 4.15 and 4.16). Stochastic porosity is the dominant defect. However, a single layer of width inadequacy, related to flow changes due to filament geometrical

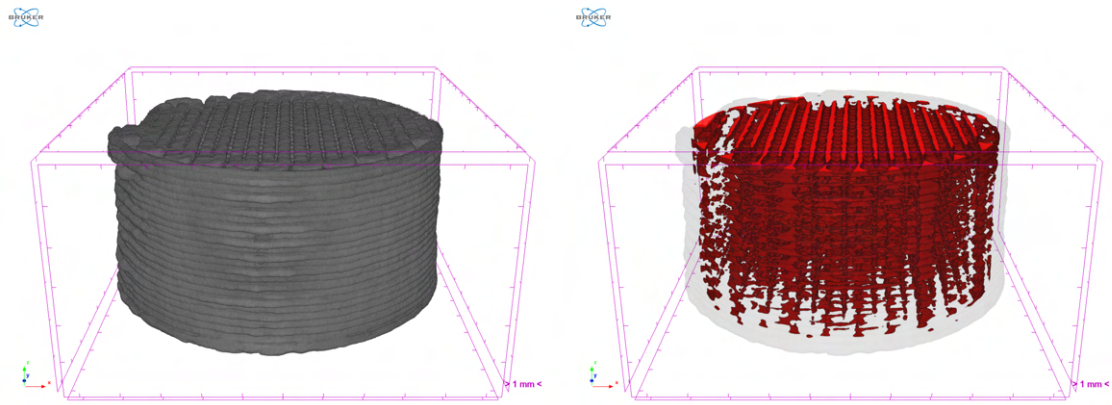

Figure 4.14: 3D rendering of the H0.10W0.45 cylinder volume and defects (left and right).

variation or partial clogging, is the origin of the detected defects. This effect is more connected with layer height reduction due to pressure increases in the nozzle. Nevertheless, density is much higher in these 3Dobjects; geometrical dimensions were affected due to over-extrusion, as is visible on the cross-section (X-Z) (Figure 4.15).

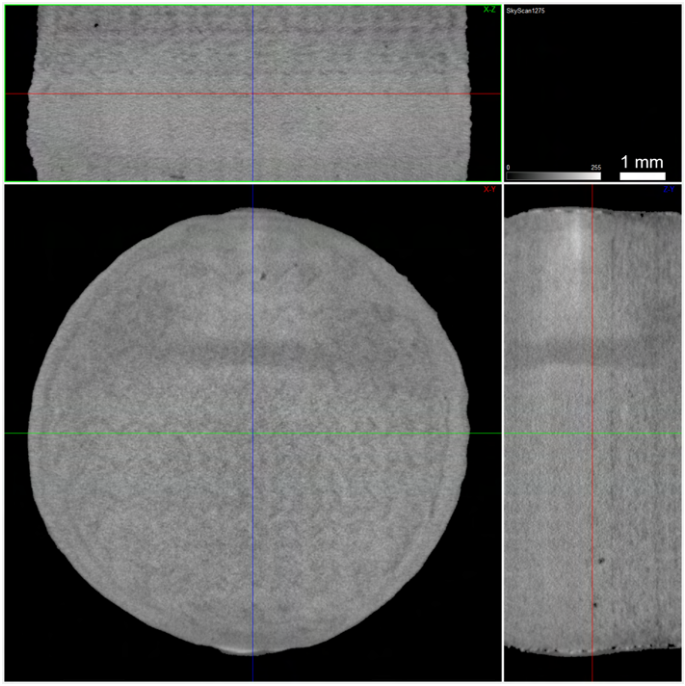

Figure 4.15: 2D cross-section of the H0.05W0.45 cylinder.

μCT measurements were applied to determine the actual width regarding 0.15 mm layer height (figure 4.17). Measurements of 320-370 µm were attained, and a width size of 350 µm was set as the standard for the following productions.

Width adjustment was effective in reducing the gaps between strands (figure 4.18 and

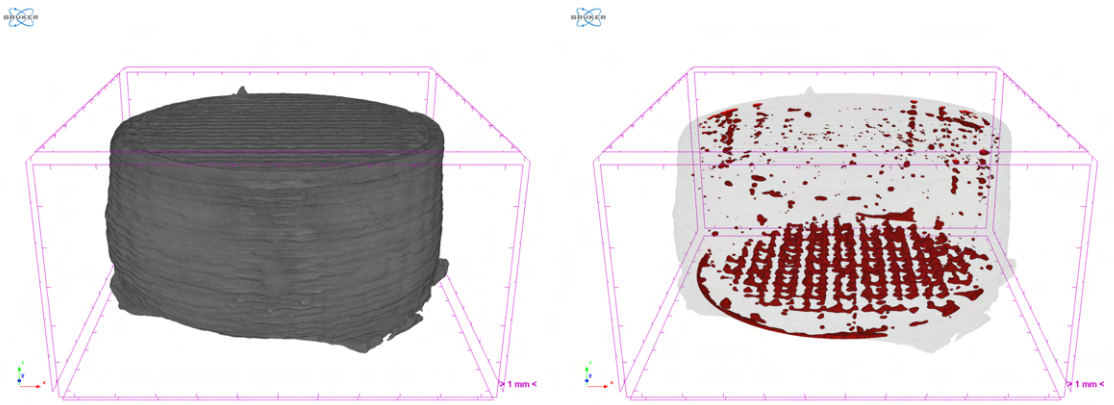

Figure 4.16: 3D rendering of the H0.05W0.45 cylinder volume and defects (left and right).

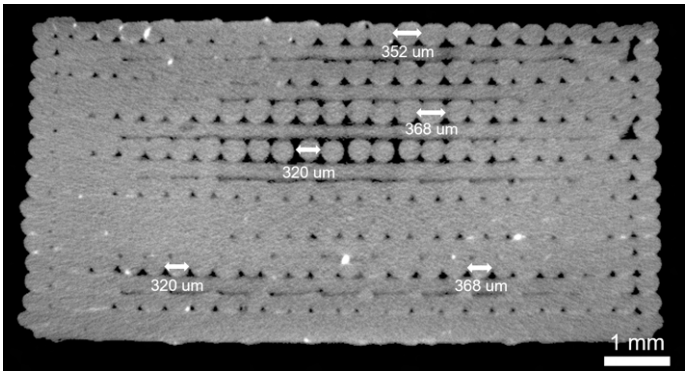

Figure 4.17: X-Z cross-section measurements of the H0.15W0.45 strand width.

4.19). However, it increases the chances of clogging. This led to a reduced volume of defects but higher random defects and defect distribution. Moreover, it is visible that the pressure between the nozzle and the printing bed had a densification effect by strand deformation.

Cylinder H0.10W0.35 further demonstrates the difficulties and consequences of inconsistent extrusion (figure 4.20 and 4.21). Otherwise a defect-free infill cylinder, underextrusion caused a significant number of defects concentrated on the central part of 6-8 layers. Overpressure caused by part growth in Z-direction due to overextrusion may result in the opposite defect by clogging.

Similar to cylinder H0.10W0.35, cylinder H0.05W0.35 presents the same defect type (figure 4.22 and 4.23). However, the larger diameter before the defect, reversed immediately when the underextrusion mechanism is present, seems to support the advanced hypothesis. Thus, effective control of nozzle pressure is essential for process reliability in MEX of dense parts.

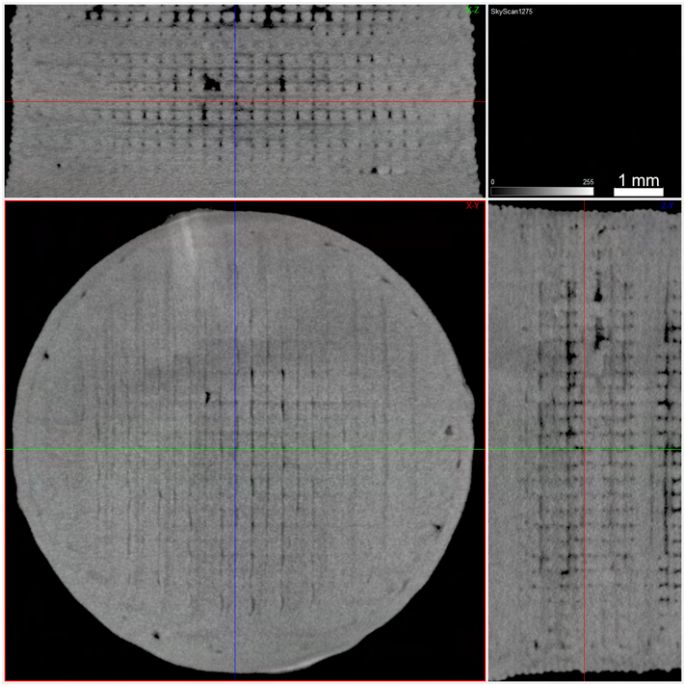

Figure 4.18: 2D cross-section of the H0.15W0.35 cylinder.

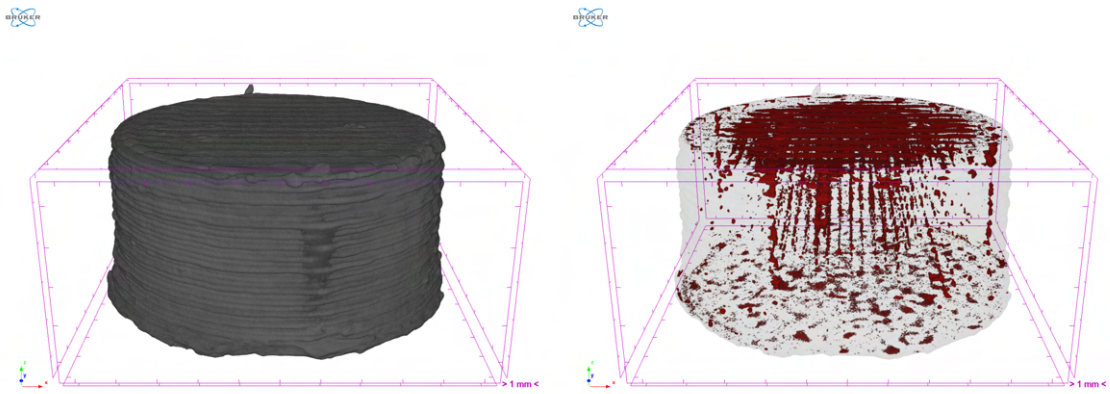

Figure 4.19: 3D rendering of the H0.15W0.35 cylinder volume and defects (left and right).

All the cylinders produced in different conditions are collected in figure 4.24. The main conclusion is that defect type is largely dependent on the selected shaping parameters. Moreover, other assumptions can be highlighted:

– strand geometry is controlled by the pressure between the nozzle and the substrate; thus, a complete prediction is only possible if real-time analysis is performed;

– overextrusion leads to clogging or geometrical deviations, which can be prejudicial for part interior features, which cannot be accessed by machining the green;

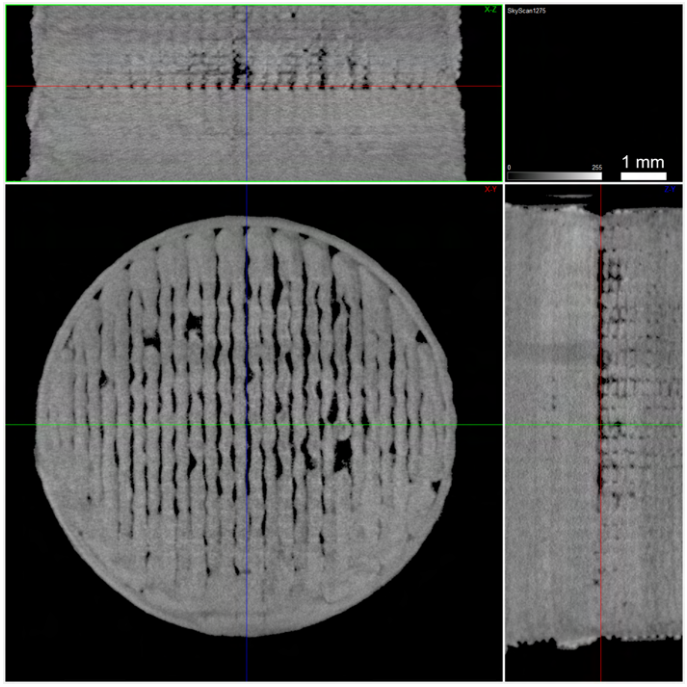

Figure 4.20: 2D cross-section of the H0.10W0.35 cylinder.

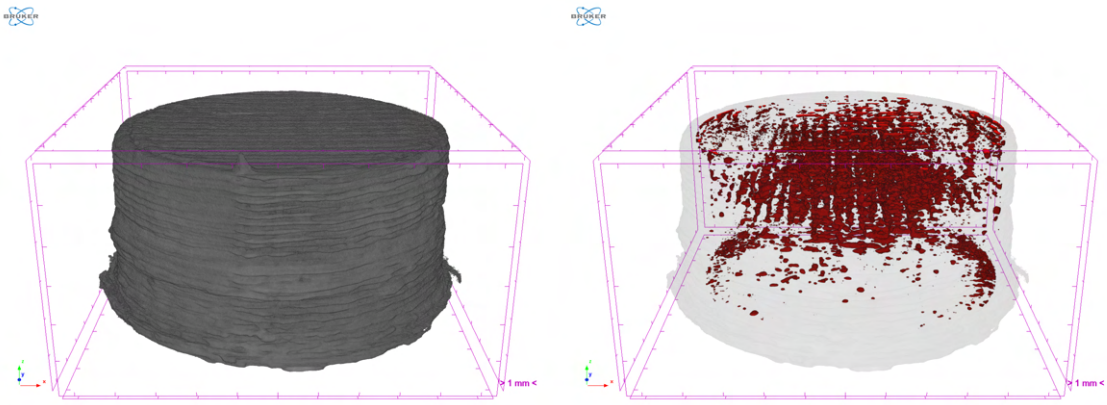

Figure 4.21: 3D rendering of the H0.10W0.35 cylinder volume and defects (left and right).

– random defects are mostly unavoidable in the production of the green due to the intrinsic nature of the extrusion process.

To highlight the importance of filament-to-strand quality, several objects were produced with VF filament. As expected, the quality of the part was primarily affected by the inconsistent individual strands (figure 4.25).

Thus, μCT is an essential tool for observing the shaping quality in MEX products. Moreover, it is relevant as an optimisation tool. Feedstock quality defects consequences were visible in the final 3Dobject. The shaping strategy is revealed as the main inducer of

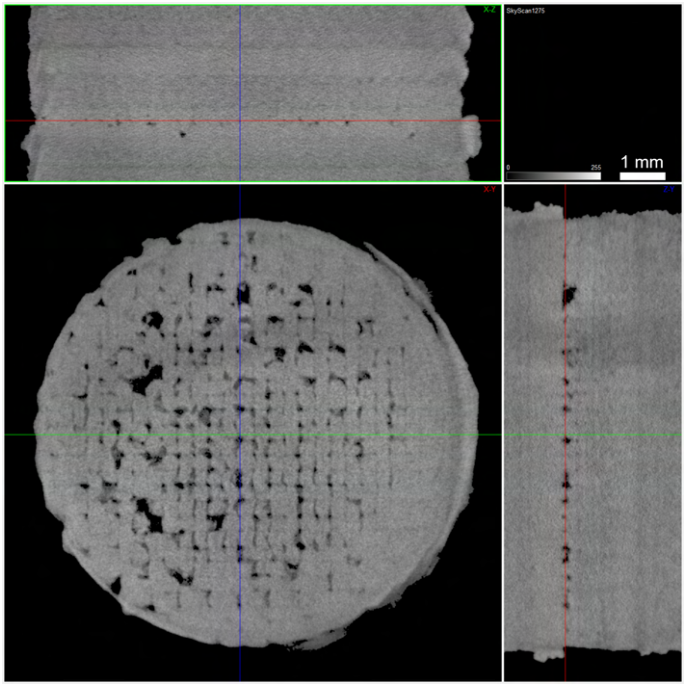

Figure 4.22: 2D cross-section of the H0.05W0.35 cylinder.

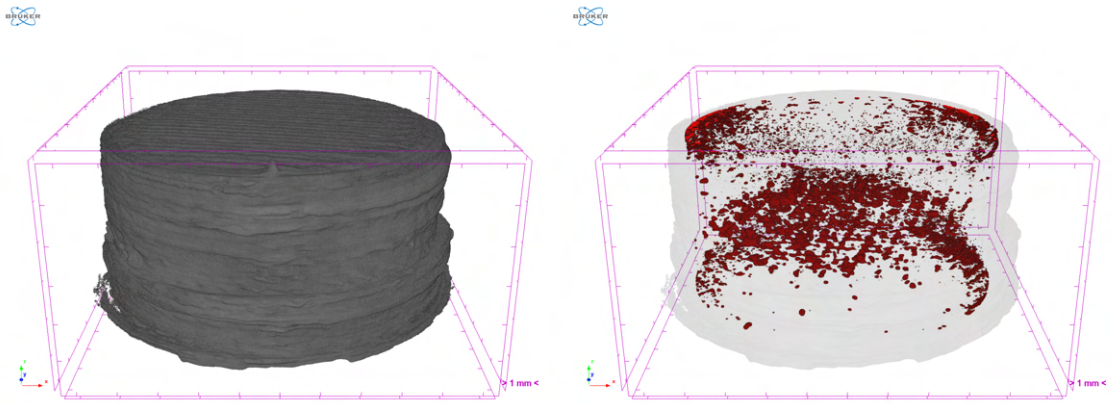

Figure 4.23: 3D rendering of the H0.05W0.35 cylinder volume and defects (left and right).

defects, which are repeated in all the layers. The next relevant defect type is irregular extrusion and underextrusion, which affects densification negatively. This is affected by feedstock characteristics, such as powder size and filament diameter.

4.3 Consolidation (Debinding and Sintering)

The evaluation of the capability of the feedstock to be consolidated, independent of the shaping parameters or reheating influence, was performed. Sections of all studied filaments were sintered. UC sintered filament had no detectable porosity, maintaining

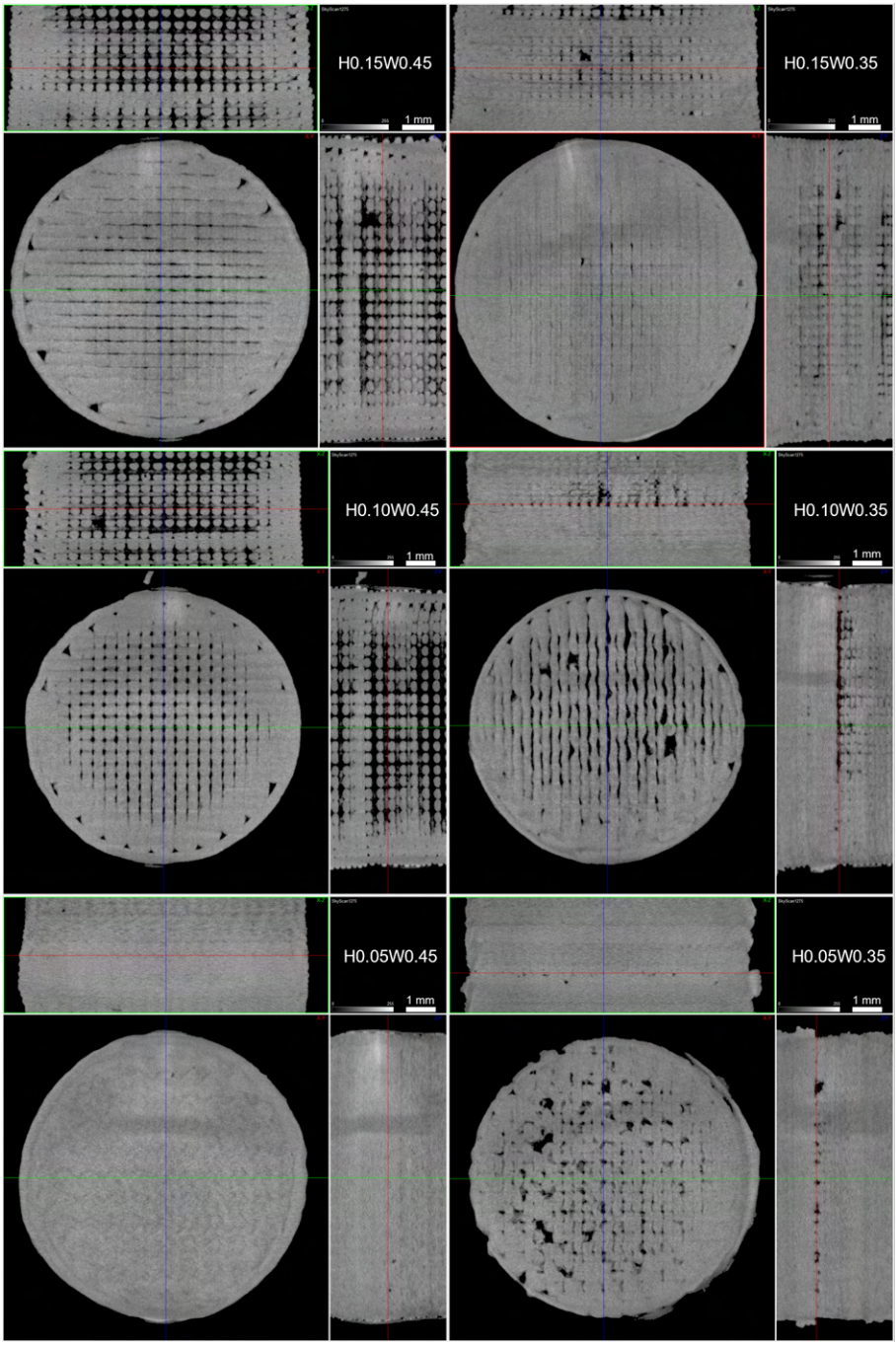

Figure 4.24: 2D green cylinders cross-section comparison.

its integrity, despite being cylindrical. It must be highlighted that no support was used during sintering (figure 4.26). Also, BASF filament maintained structural integrity, but defects already present in the green filament were not resolved by sintering (figure 4.27). Moreover, the sintering of BASF filament presents cracking of the filament, despite the reduced width of the green. Consequently, further studies on the thermal sintering of BASF filaments were not developed.

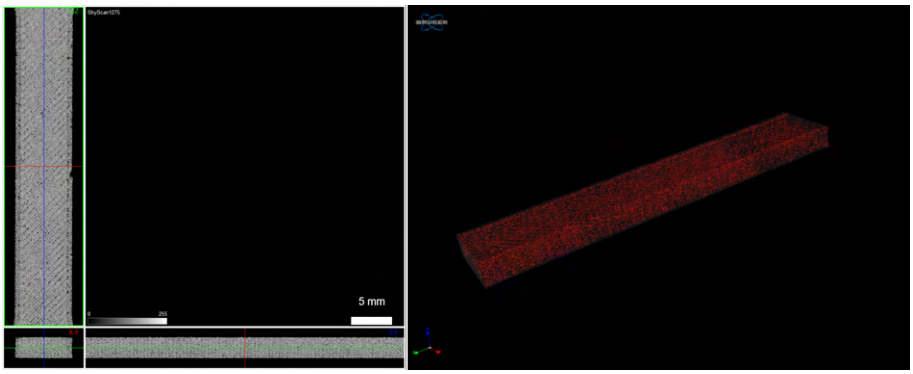

Figure 4.25: 2D and 3D visualisation of defects location in VF green object cross-section (left and right).

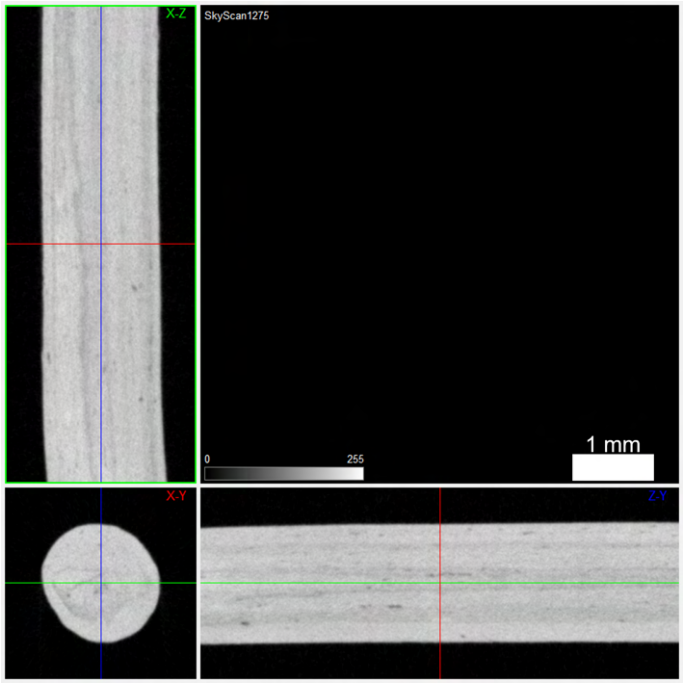

Figure 4.26: 2D cross-section of the sintered UC filament.

A comparison between green and sintered UV cylinders was performed. In the case of cylinder H0.15W0.45, virtual interior channels caused by the non-optimal shaping parameters led to partial sintering of the part. The content defects after sintering are similar to the green (figure 4.28). Moreover, intense warping is observed. This behaviour may be due to the debinding-related stresses resulting in geometrical distortion. The base of the cylinder contraction led to warping. Exhausted gas (from polymer ustulation) from the cylinder interior helped to increase the distance between the strands since the inter-strand connection was almost non-existent. Furthermore, during the shaping step, there is a possibility of inducing thermal stresses that, when starting the debinding process, can result in object warping. 3D digital image comparison of the defects in the green and

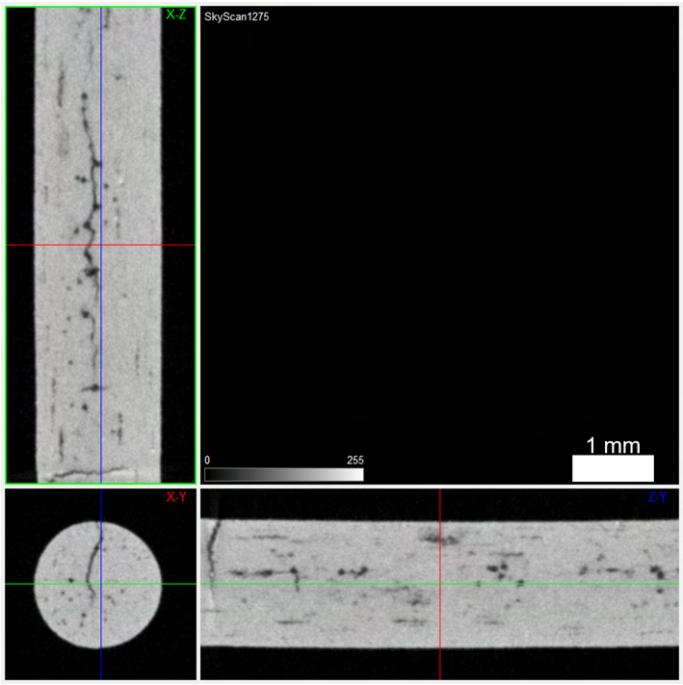

Figure 4.27: 2D cross-section of the sintered BASF filament.

sintered part shows that no major defects have disappeared, and the geometrical aspect has degraded, like in PIM manufacturing process (figure 4.29).

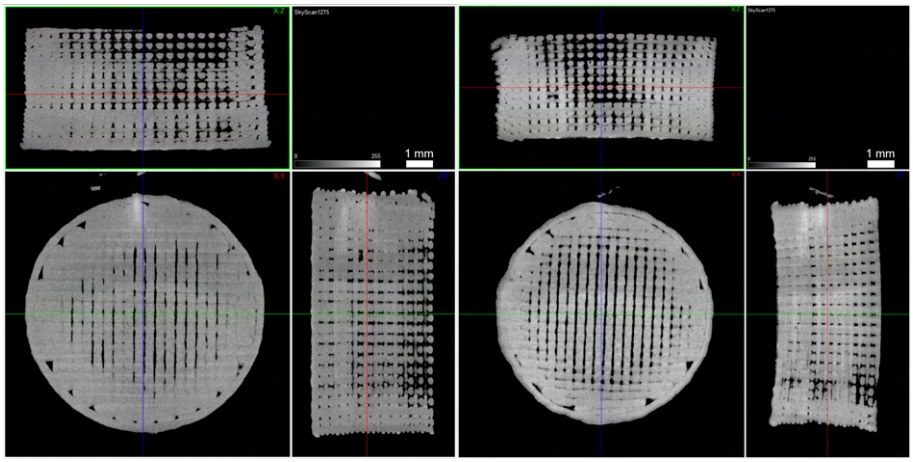

Figure 4.28: 2D cross-section comparison of H0.15W0.45 cylinder, green and sintered (left and right).

Since the consolidation had similar behaviour regarding the same shaping heights and was less affected by strand width, in this section, cylinders were grouped per height and not per width. Thus, cylinders shaped with 0.35 mm strand width (H0.15W0.35) showed similar behaviour to H0.15W0.45 (figure 4.30). The interspace between strands was increased, and some warping is yet clearly visible. The magnitude of the warping seems

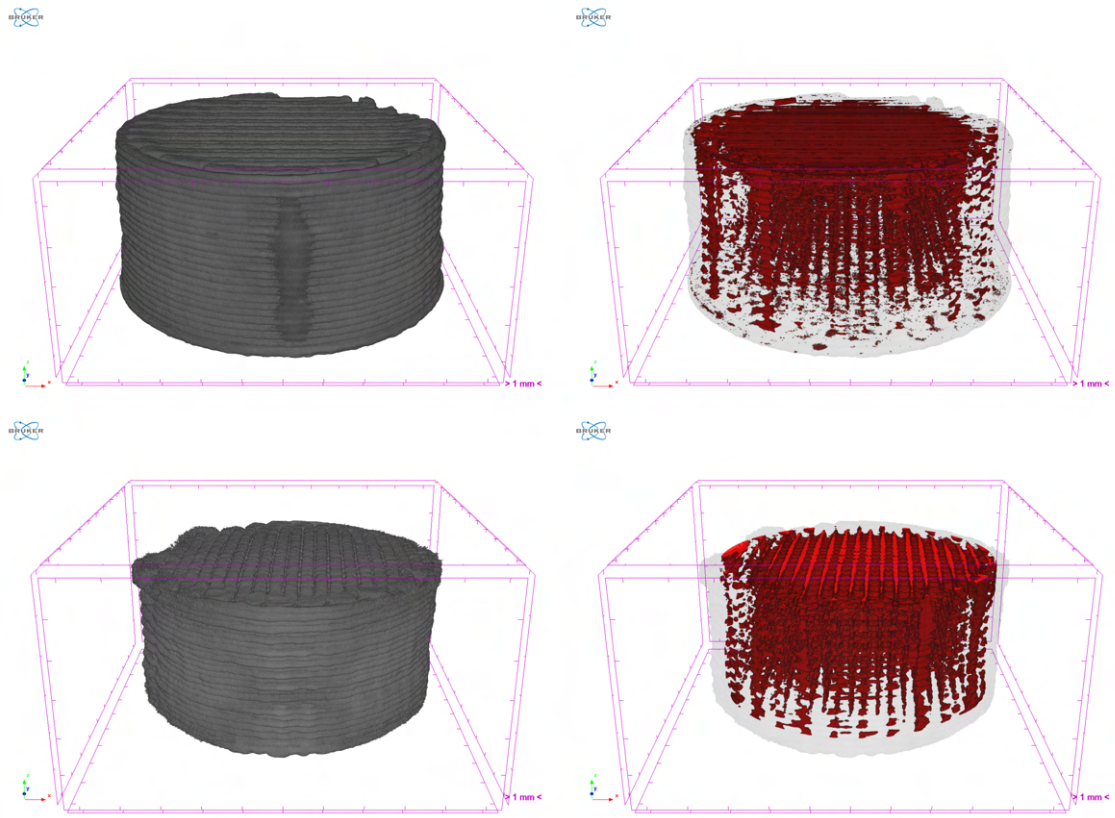

Figure 4.29: 3D rendering comparison between green and sintered (top and bottom) H0.15W0.45 cylinder volume and defects (left and right).

to be reduced by the improvement of green density, as expected. Furthermore, some small defects were reduced on the lower half of the cylinder, mainly due to the warping movement leading to void closure (figure 4.31).

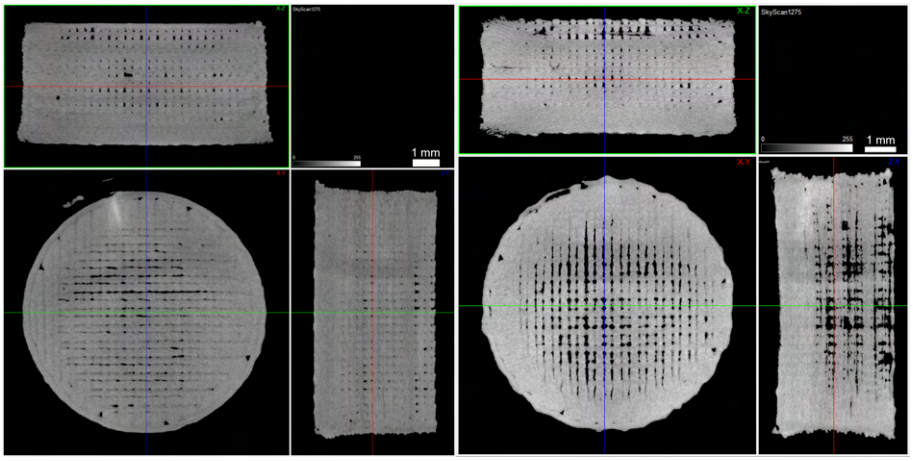

Figure 4.30: 2D cross-section comparison of H0.15W0.35 cylinder, green and sintered (left and right).

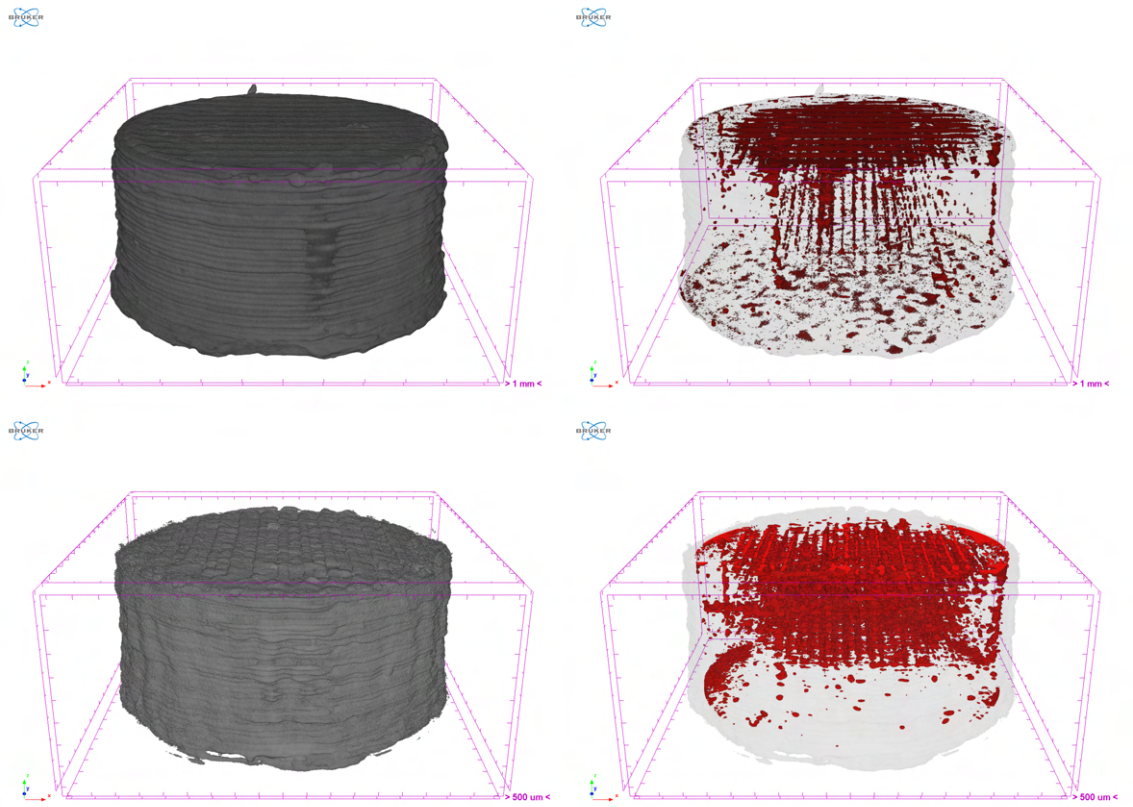

Figure 4.31: 3D rendering comparison between green and sintered (top and bottom) H0.15W0.35 cylinder volume and defects (left and right).

The cylinders H0.10W0.45 had a different sintering behaviour from the H0.15W0.45 (figure 4.32). The compaction from the green to sintered object is clear. The reduction of the cylinder in the Z direction (height) must be due to an effective increase of weight resulting from the relation H:W and the variation of linear defects in XY directions. This occurs typically during debinding. After sintering, this led to a smaller 3Dobject with a higher density than H0.15W0.45. However, the increased density in the central zone induced a crack in the 3Dobject (figure 4.33). This was not to be expected when the defects/voids are connected to the surface, which significantly reduces the stresses caused by the possible concentration of gas from debinding ustulation. Consequently, the structural collapse of the reticulated infill can be observed in figure 4.32 (bottom right).

Cracking issues increased when the strand width was reduced (figure 4.34). Moreover, cracking occurred in two distinct zones. The first one, from the top, was initiated on the underextruded layer, which is mainly a delamination phenomenon. The second crack occurred on the lower half of the object, where the density was higher. Since warping is observed, some internal stresses during sintering could have led to the delamination due to cracking (figure 4.35).

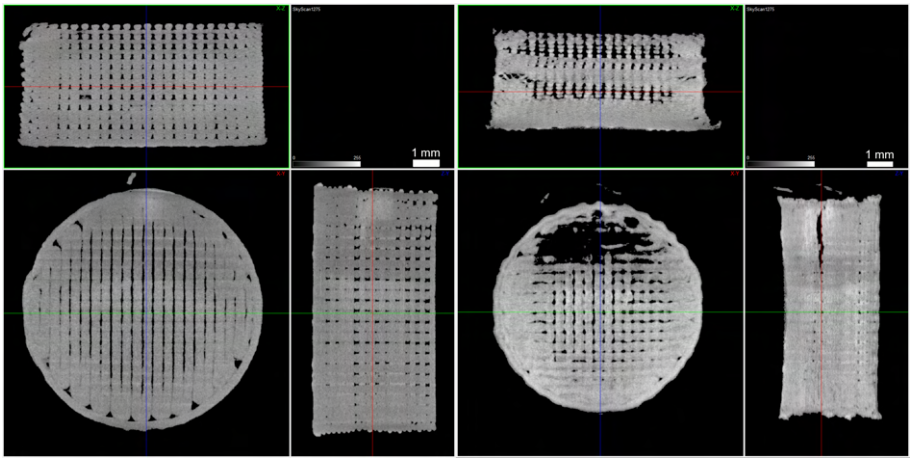

Figure 4.32: 2D cross-section comparison of H0.10W0.45 cylinder, green and sintered (left and right).

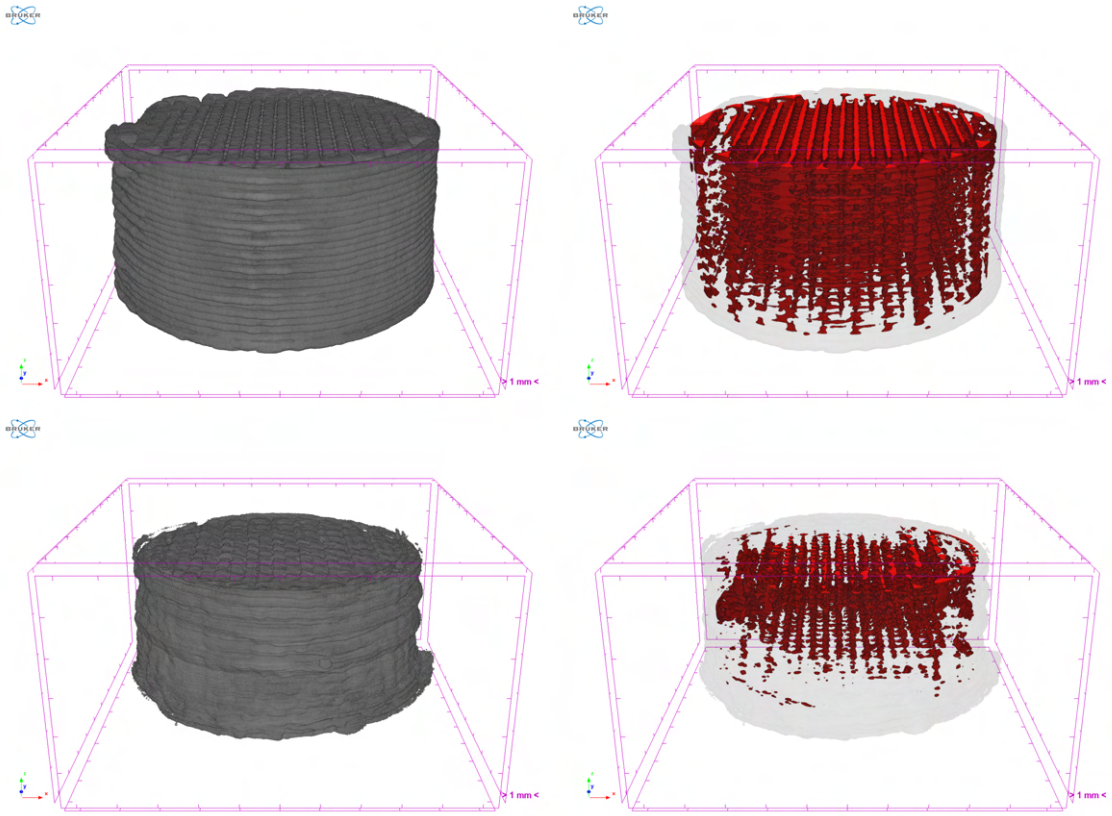

Figure 4.33: 3D rendering comparison between green and sintered (top and bottom) H0.10W0.45 cylinder volume and defects (left and right).

Observations from cylinder H0.05W0.45 confirm that the debinding cycle seems not to be optimised to the binder & additives debinding behaviour (figure 4.32). The pressure from gas entrapment led to delamination in the 3Dobject. Even in dense parts, this is the demonstration that in MEX, intralayer strength is stronger than interlayers. This resulted

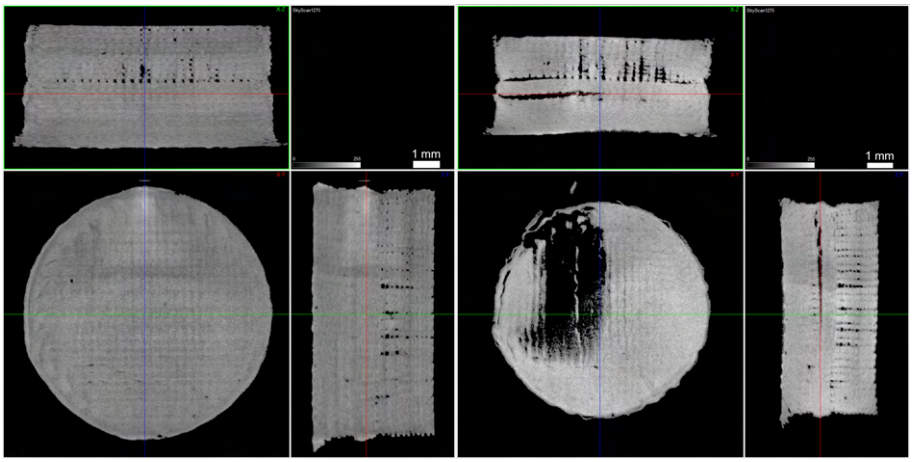

Figure 4.34: 2D cross-section comparison of H0.10W0.35 cylinder, green and sintered (left and right).

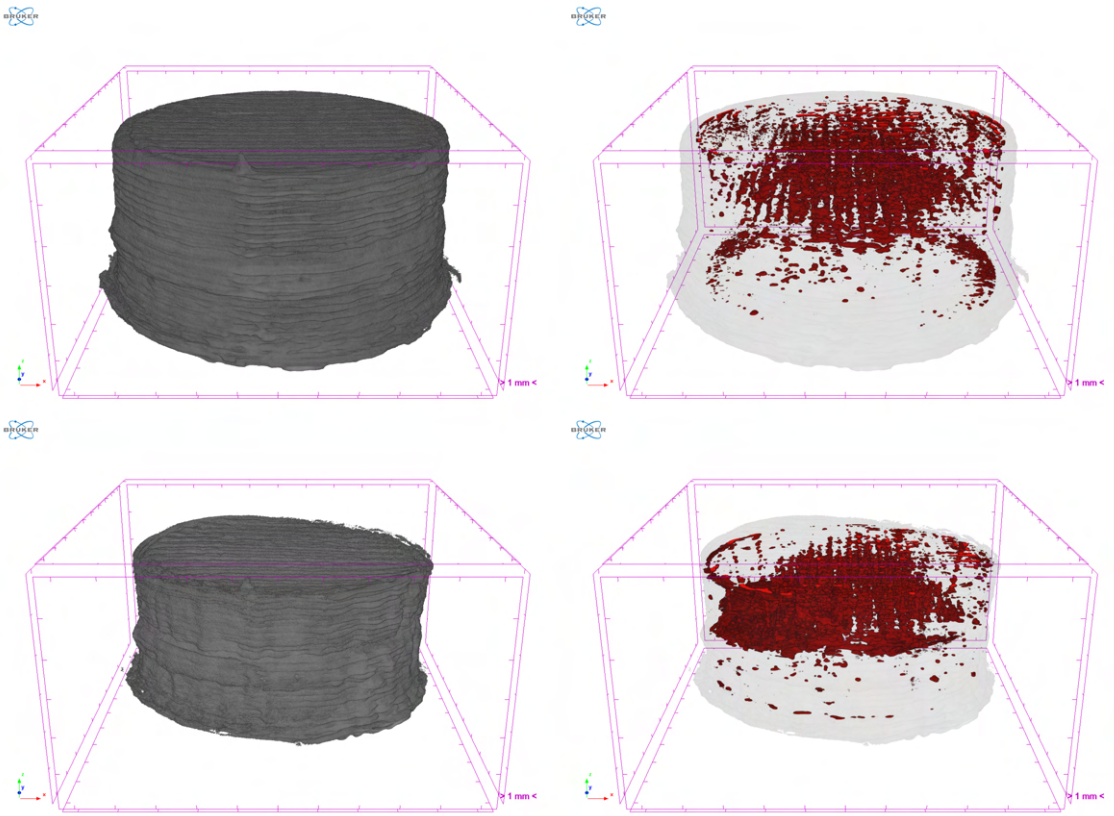

Figure 4.35: 3D rendering comparison between green and sintered (top and bottom) H0.10W0.35 cylinder volume and defects (left and right).

in some highly deformed layers with wide gaps. Otherwise a relatively dense cylinder, some of the green voids were reduced, delamination during consolidation caused wide interior defects that compromised the geometrical integrity of the 3Dobject (figure 4.37).

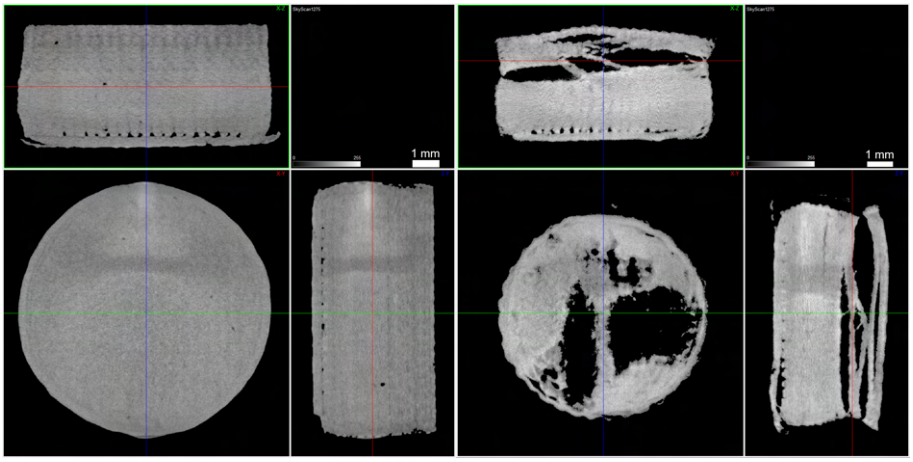

Figure 4.36: 2D cross-section comparison of H0.05W0.45 cylinder, green and sintered (left and right).

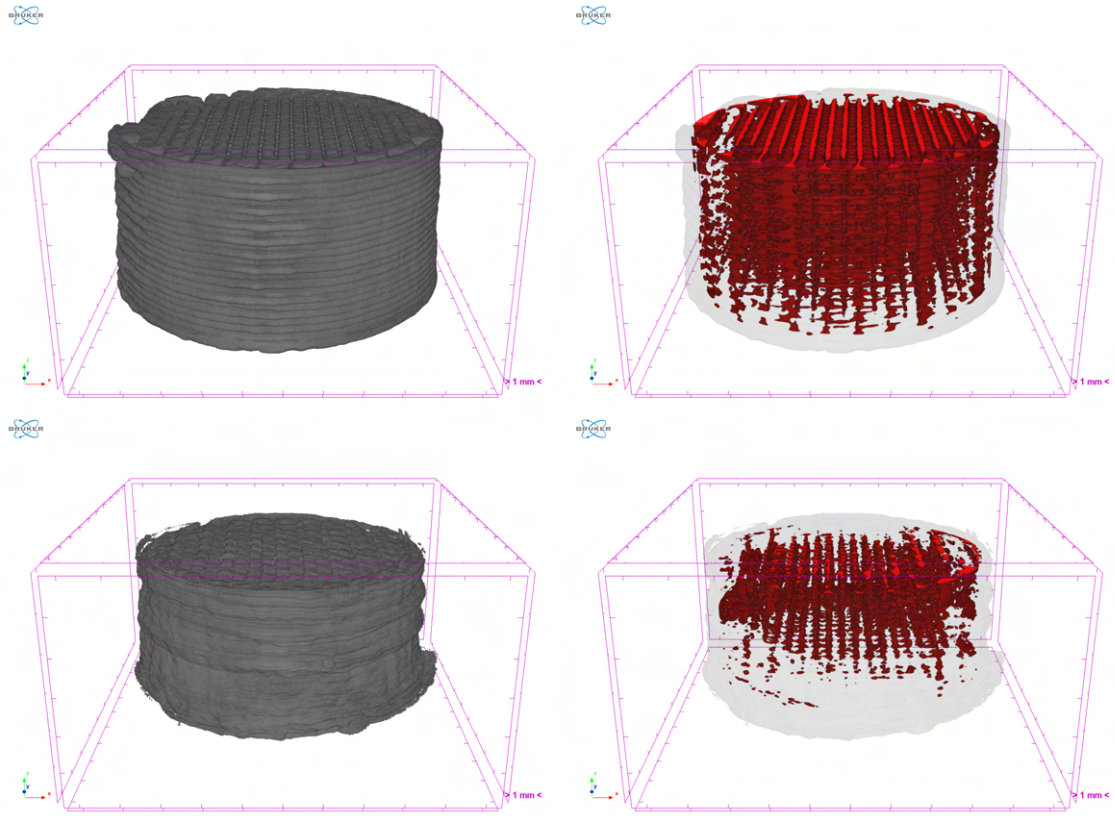

Figure 4.37: 3D rendering comparison between green and sintered (top and bottom) H0.05W0.45 cylinder volume and defects (left and right).

The presence of an underextruded layer on the bottom half of the cylinder leads to low consolidation changes relative to the green object. However, the dense top half showed severe cracking. The presence of "chimneys" for gas flow during sintering is deemed essential for thicker objects, as in PIM. However, the binder and additives can widely affect

the object thickness range for sintering. Consequently, deep insight into the influence of these defects caused by gas flow must be the object of future studies.

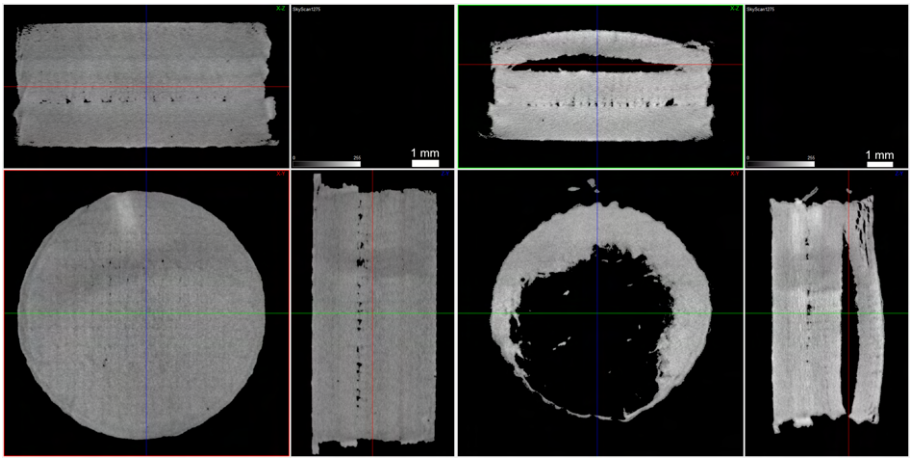

Figure 4.38: 2D cross-section comparison of H0.05W0.35 cylinder, green and sintered (left and right).

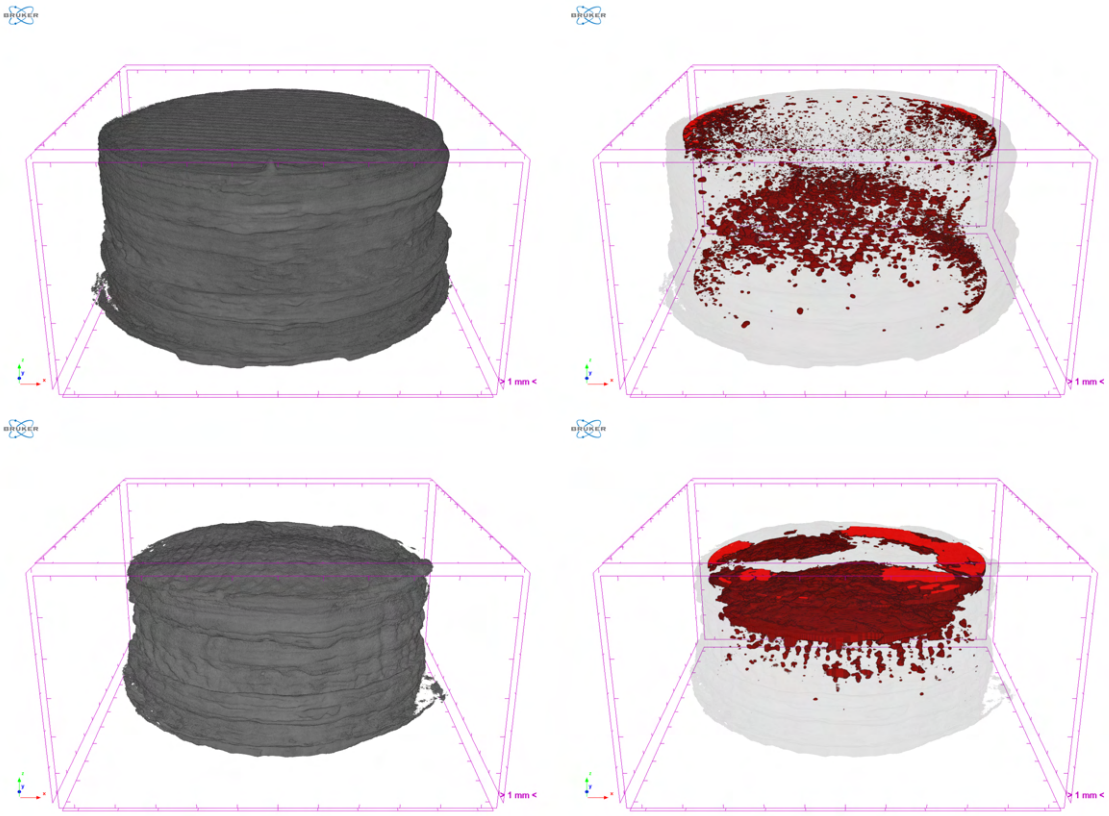

Figure 4.39: 3D rendering comparison between green and sintered (top and bottom) H0.05W0.35 cylinder volume and defects (left and right).

All the sintered cylinders produced are collected in figure 4.40. Debinding and sintering issues are evident for all the manufactured 3Dobjects. Total debinding and sintering

time, including dwell times, must be optimised according to the physical and chemical behaviour of the feedstock components.

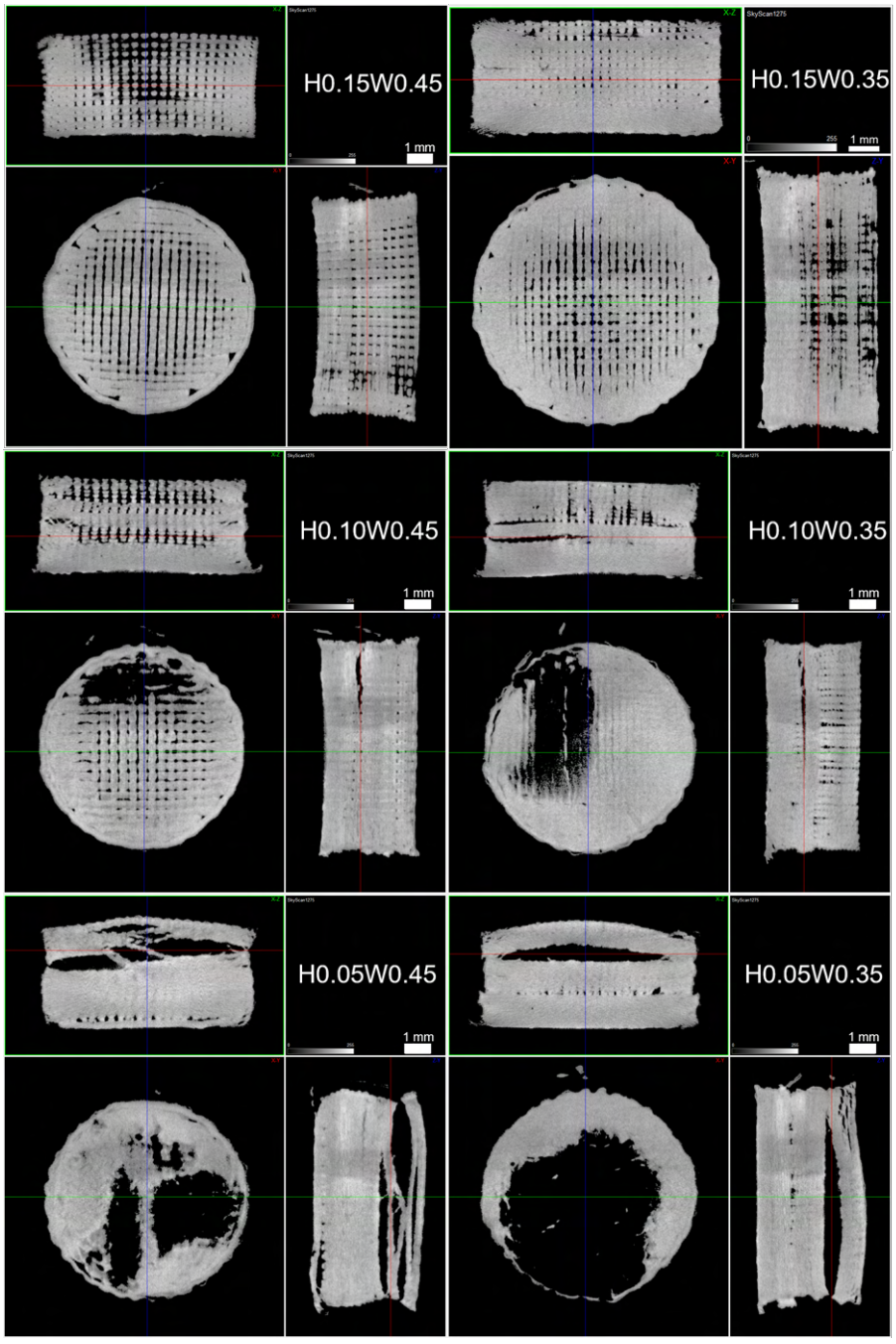

Figure 4.40: 2D cross-section comparison of the sintered cylinders.

Whatever the sintering atmosphere, consolidation did not produce good results (figures 4.41 and 4.43). Besides the large gaps due to sintering, cracking, and delamination, intrastrand porosity is widespread due to precarious consolidation (figures 4.42).

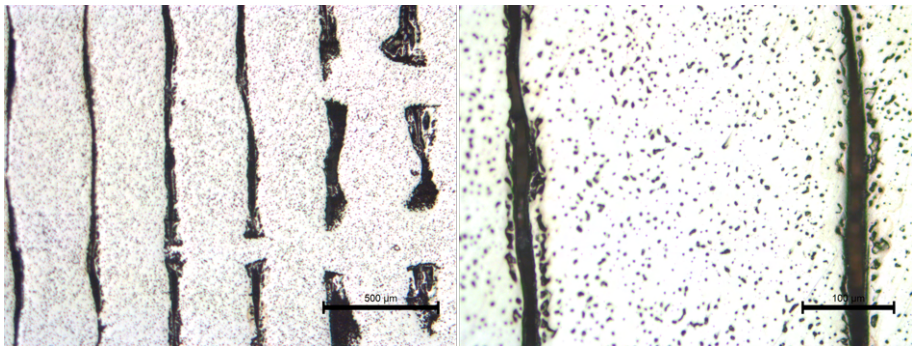

Figure 4.41: Micrographies of the polished surface of a 316L cylinder sintered under hydrogen atmosphere.

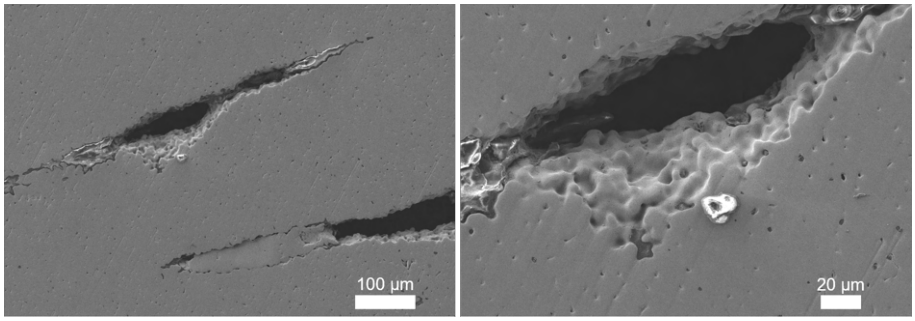

Figure 4.42: SEM detail of the polished surface of a 316L cylinder sintered under hydrogen atmosphere.

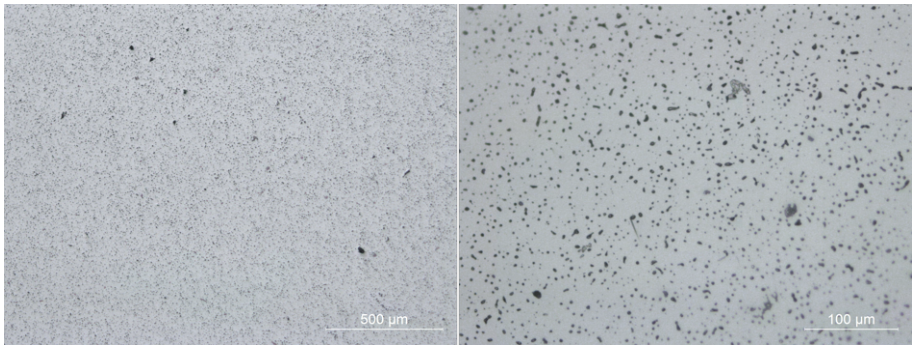

Figure 4.43: Micrographies of the polished surface of a 316L cylinder sintered under argon atmosphere.

A part produced by MIM undertook the same consolidation parameters as its MEX counterparts, resulted also in disastrous effects (figure 4.44). The prevalence of widespread porosity in the thin part corroborates the anticipated theory of general inadequacy of the feedstock to thermal treatment.

An overlook of defects in MEX revealed that μCT is an essential tool for AM quality evaluation. Moreover, green defects consequences on the consolidation behaviour could be effectively predicted. The use of modelling, combined with μCT is, therefore, a smart

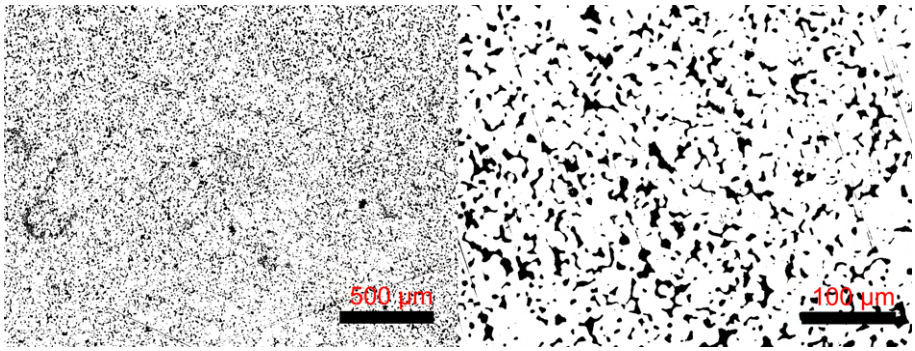

Figure 4.44: Micrographies of the polished surface of MIM 316L, sintered under argon atmosphere.

development that can be achieved to predict the consolidation behaviour, thus saving high sintering costs, contributing for MEX to become a sustainable technology. This can be achieved through a series of rules regarding the consequences of each green defect type on the consolidation, feeding a digital model attained on the μCT to the modelling software.

Chapter 5

Conventional SLM of Copper and Copper Alloys Powder

Up to now, one of the metals that gives rise to enormous problems during its processing by SLM is copper. In the last decennia, SLM equipments were constituted by a fibre laser of ytterbium, with a wavelength of 1070 nm. This radiation was not suitable for copper powder and, therefore, it was not possible to attain the desired quality for copper 3Dobjects. A significant quantity of defects could be present in the 3Dobject. Thus, the selection of this metal had the goal of enhancing the role of μCT in the detection of defects.

SLM defects resulting from AM of copper powder were also complemented with the defects present after the addition of other significant elements.

5.1 SLM of Pure Copper

Up to now, it has been a challenge to process copper by SLM due to its reflectivity and high thermal conductivity. In order to mitigate this problem, high laser power (P) should be used, contributing to the increase of the VED. However, uncontrolled melting pool and laser backfire (reflection shattering the laser deflection mirror), may occur [326]. Nevertheless, research works do not point to a specific set of VED to attain high densification in reproducible conditions, so a test group was designed, as previously indicated in table 3.5. A combination of high laser power and different scan speeds (different high VEDs) of a set of seven objects are shown in figure 5.1.

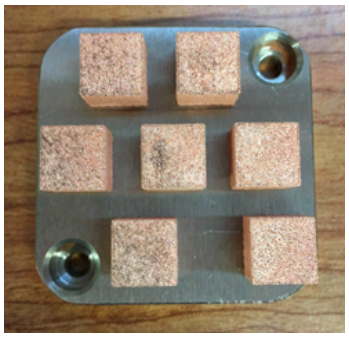

Figure 5.1: Pure copper 3Dobject by SLM.

All set parameters achieved a final 3Dobject. In spite of recent literature results [327], all 3Dobjects had less than 95% of the powder density. The low density of 3D cubes is highly detrimental to their thermal and electrical conductivity and is in line with state-of-the-art. Surface micrography (figure 5.2), as well as µCT of the 3Dobjects (figures 5.3 and 5.4) were analysed. Whatever the VED (130-220 J/mm3) or scanning speed selected, the low density seems to result from an irregular melting pool, as expected from the low absorption of copper, which should lead to partial melting. The balling effect is seen throughout the surface and is especially higher close to it, where thermal accumulation due to repeated laser scanning is low. A general remelting, whenever a new layer is scanned, does not seem to be sufficient to increase the overall density of the copper 3Dobjects, but only contribute to aggregate the particles.

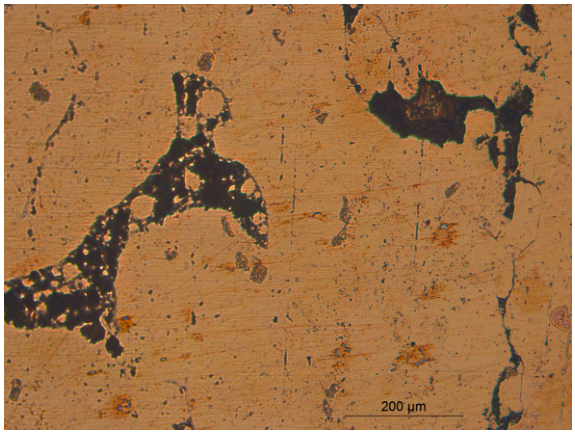

Figure 5.2: Optical micrography of pure copper SLMed 3Dobject.

For further investigation about thermal conductivity regarding pure copper produced by SLM, with the best parameters, a small disk with suitable diameter and thickness, according to equipment (hot disk thermal constants analyser) was produced. The overall thermal conductivity was below 60 W/m.K, which is far from the 398 W/m.K attributed to copper [325]. This significant decrease in thermal conductivity can be concluded that

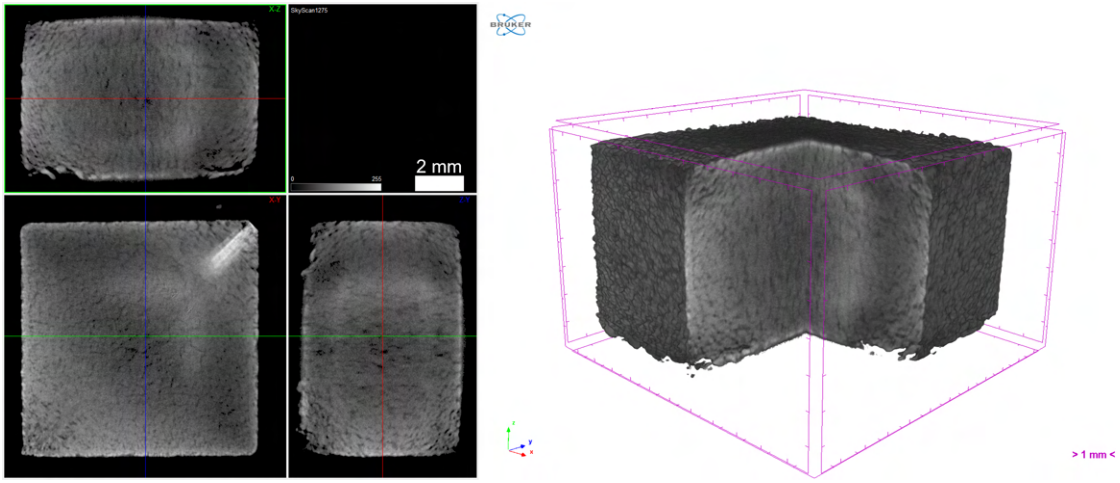

Figure 5.3: 2D cross-section of the SLMed B1 pure copper 3Dobject.

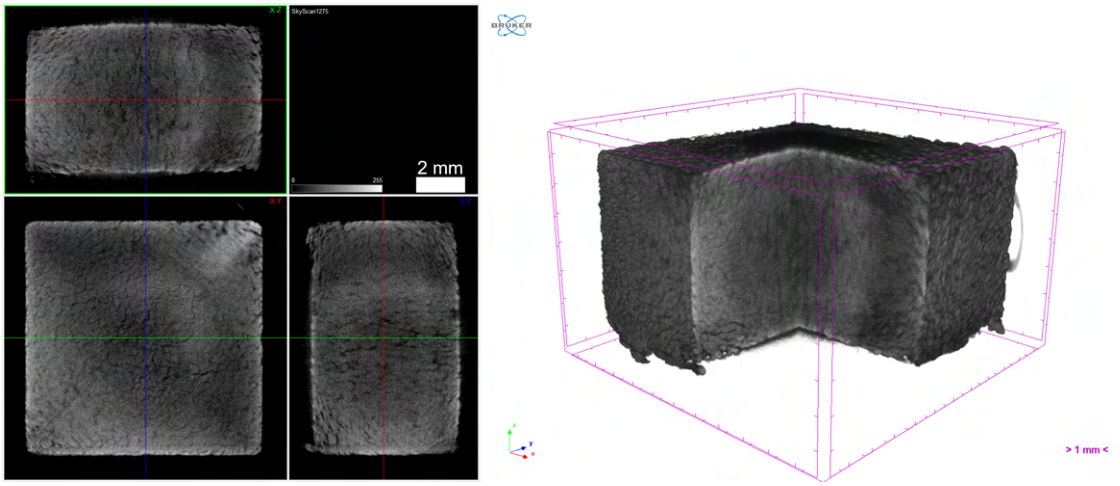

Figure 5.4: 2D cross-section of the SLMed C1 pure copper 3Dobject.

copper SLM objects produced with standard parameters are not suitable for copper applications. This occurrence was overcome by the addition/substitution of other materials when produced by SLM. This could aid in improving the thermal conductivity of SLM copper objects [328].

5.2 Tailored Copper Mixture for SLM

One of the more exciting opportunities brought forth by SLM is the possibility of developing new alloys for specific uses from powder particles. Furthermore, the opportunity of multimaterial processing through additive manufacturing, harvesting the described main advantages of copper alloys and the hardness (e.g. steels) is exciting. This has been a persuasive argument for the continued development of SLM-manufactured copper and

copper-based alloys, where the other metallic element may contribute to better bulk density and, and good thermal conductivity (> 60 W/mK). Conventional processes fail to produce a good Cu-Fe alloy due to the immiscibility of the Fe phase in the copper matrix. However, the different behaviour of iron versus copper when submitted to a laser source in SLM can induce a significant improvement of 3Dobject quality. Porosity decreases significantly because iron, which has no problems in SLM, avoids it.

In this work, the copper powder was mixed with austenitic stainless-steel powder - 316L (source of Fe), and not with pure iron due to eventual problems of oxidation and phase modification that could be present in iron. The weight ratio of copper:steel selected was 80:20 and was compared in what concerns the defects with pure copper. Due to the adjustments brought by steel addition, a large test group of powder was produced with medium to high laser power and volumetric energy density. This option has contributed to highlight the role of microtomography in establishing the limits of defect detection, whatever the metallic alloys processed by SLM.

Table 5.1 summarises the densities for all the 3Dobjects produced and compares them to a theoretical density of the copper element and stainless steel 316L studied mixture. As can be discerned, achieved densities are higher when power reaches 400 W. The steel presence seems to be an aggregating agent that serves as a stabilising presence to the pure copper.

Table 5.1: Cu-Fe test group objects density compared to a theoretical Cu-Fe mixture density.

3Dobject	**3Dobject Average Density** $\left(\frac{\mathbf{Kg}}{\mathbf{m^3}}\right)$	**Mixing Density Copper:Fe, Cr, Ni (Austenitic SS)** $\left(\frac{\mathbf{Kg}}{\mathbf{m^3}}\right)$
V140W200	8210	8678
V140W250	8420	
V140W300	8009	
V140W350	8350	
V140W400	8210	
V160W200	8310	
V160W250	8250	
V160W300	8290	
V160W350	8290	
V160W400	**8580**	
V180W200	8280	
V180W250	8300	
V180W300	8310	
V180W350	8370	
V180W400	**8490**	
V200W200	8280	
V200W250	8330	
V200W300	8270	
V200W350	8390	
V200W400	8460	
V220W200	8370	
V220W250	DNF	
V220W300	8360	
V220W350	8290	
V220W400	**8510**	

The highest density 3Dobjects (in bold on table 5.1) were selected for further analysis. Steel islands on the copper matrix are clearly visible throughout the 3Dobject. However, big steel islands can also be observed, which may arise from the remelting that occurs when a new layer is scanned, which increases element mobility within the matrix. EBSD images confirm the immiscibility of the steel in the copper matrix, as has been observed in

conventional fabrication processes (figure 5.8). Furthermore, EBSD quantification of the copper:steel relation is close to 80:20 with a weight percentage of iron $\approx 20.6 \pm 3.1\%$.

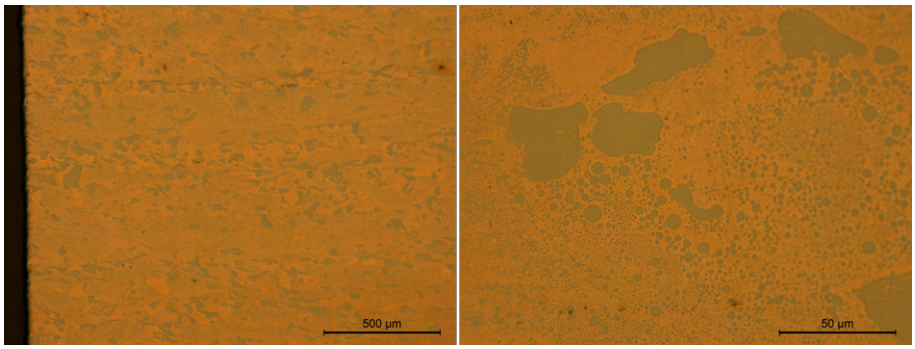

Figure 5.5: Optical micrographies of 3Dobject V160W400 surface.

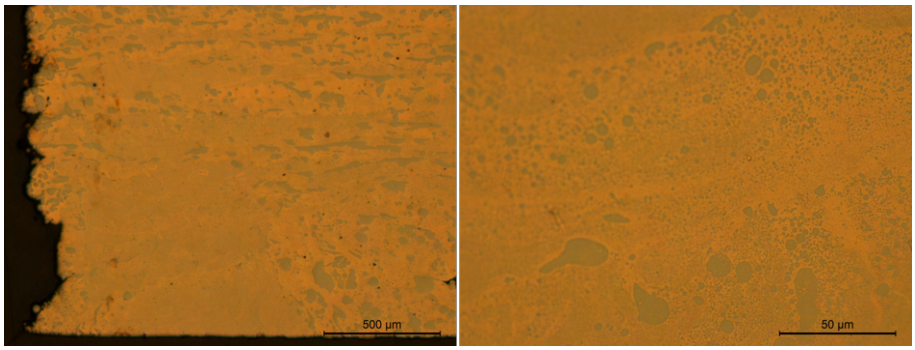

Figure 5.6: Optical micrographies of 3Dobject V180W400 surface.

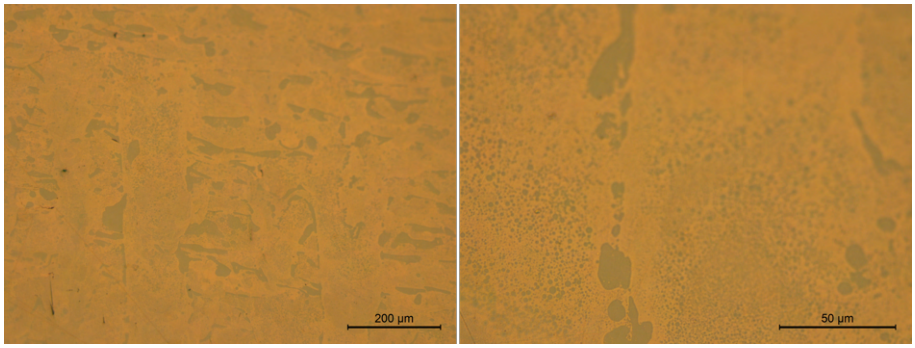

Figure 5.7: Optical micrographies of 3Dobject V220W400 surface.

The µCT of 3Dobjects V160W400, V180W400 and V220W400 (figures 5.9-5.11) corroborate the justification of the highest density measured by Archimedes method. Some random defects can be observed throughout the 3Dobject volume. These defects can be resultant of LOF defects due to the high thermal conductivity of copper.

For comparison, the worst finished 3Dobject was also µCT analysed (figure 5.12). The overall presence of defects is clear. These are mainly related to hatching space, being

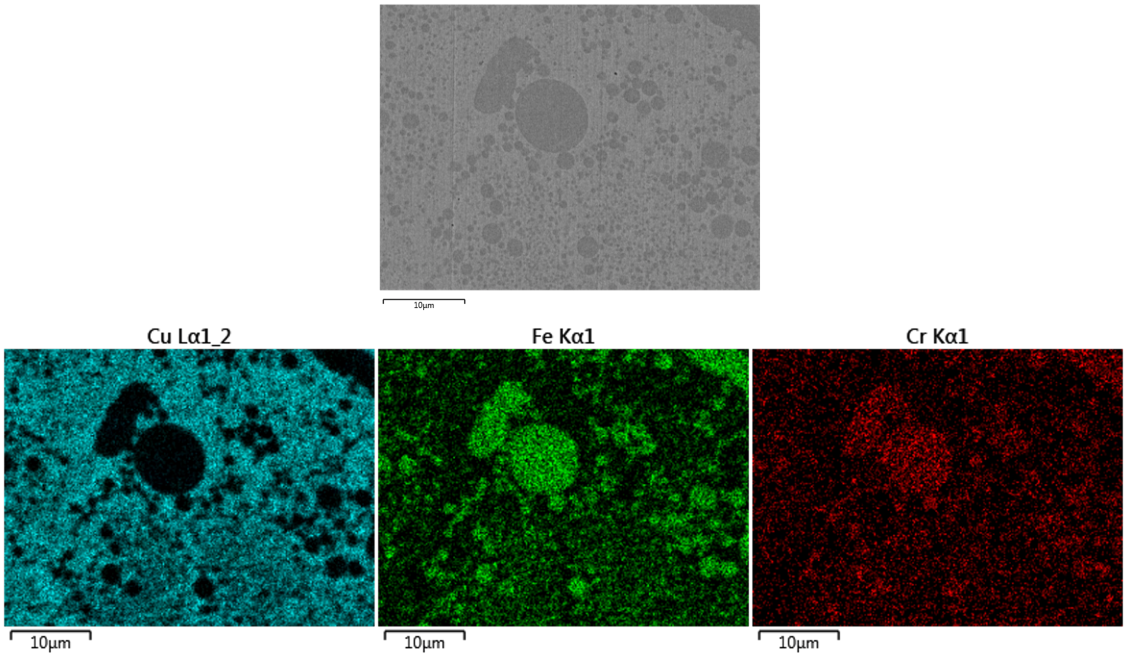

Figure 5.8: EBSD element distribution for 3Dobject V220W400.

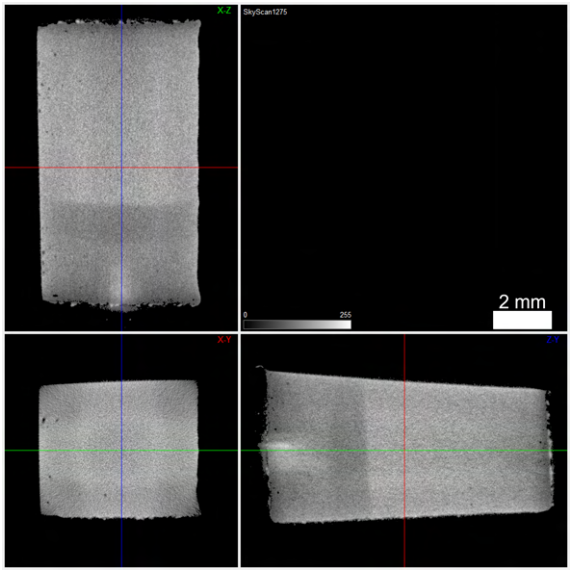

Figure 5.9: 2D visualisation of 3Dobject V160W400 cross-section.

visible as the separation between melting pools in the X-Z direction. Since all the observed defects can be related to this type of defect inducer, a corrected hatching space may provide better results, increasing the VED if maximum power is limited.

To understand the mechanism of copper:steel production in SLM, a test group of increasing 3Dobject building height was made, with heights of 0.5; 1.0; 2.0; 4.0 and 8.0 mm. Surprisingly, bigger steel islands seem to be less prevalent in the bigger objects.

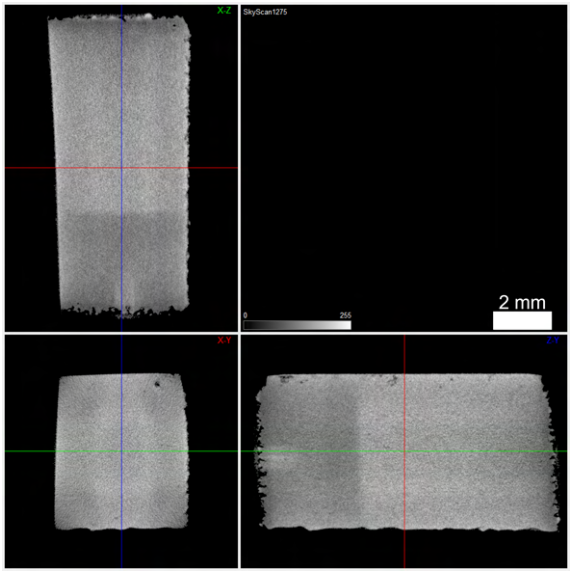

Figure 5.10: 2D visualisation of 3Dobject V180W400 cross-section.

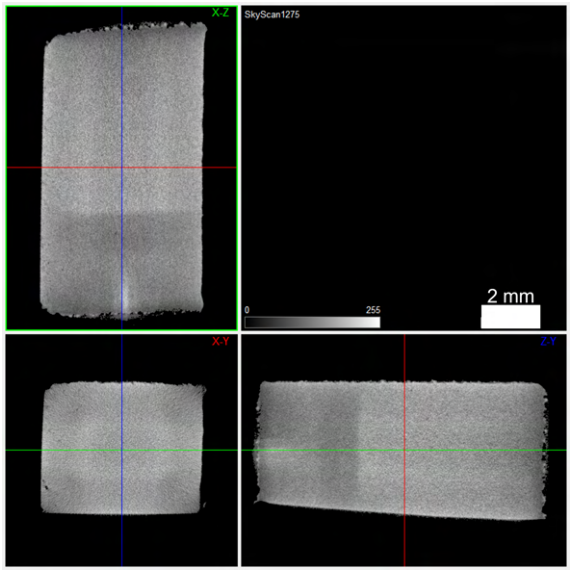

Figure 5.11: 2D visualisation of 3Dobject V220W400 cross-section.

An effective melting pool is shown, through Marangoni currents, to be an effective way of mixing elements in SLM processing. In accordance with that, a special prevalence of steel islands in the melting pool boundary is related to the density of this element within the alloy (figure 5.13).

Density was measured for all heights (table 5.2). An increase in density is apparent. A remelting effect may be acting as a porosity correction mechanism by filling the spaces that were not fully melted on the previous layer.

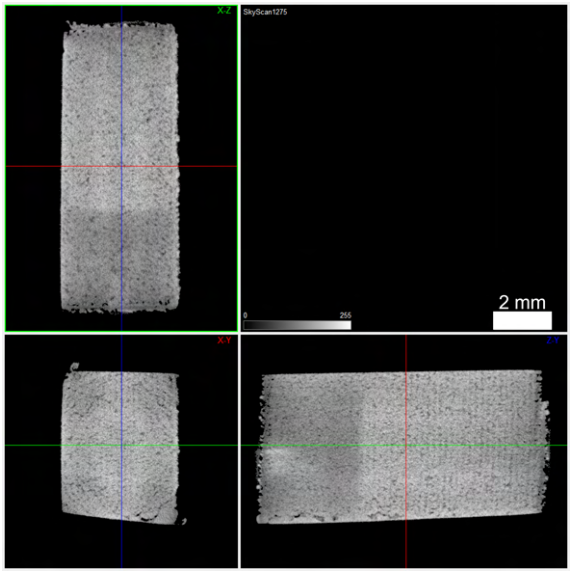

Figure 5.12: 2D visualisation of 3Dobject V140W300 cross-section.

Table 5.2: Density of copper-iron 3Dobjects with different heights.

3Dobject	3Dobject Density $\left(\frac{\mathbf{Kg}}{\mathbf{m}^3}\right)$
0.5 mm	7888
1.0 mm	8176
2.0 mm	8381
4.0 mm	8420
8.0 mm	8339

The μtomography upholds that the initial defects disappear with an increase in 3Dobject height (figures 5.14-5.18). LOF defects gradually disappear, and random porosity is more dominant. However, a further increase to 8.0 mm height seems to contribute to a slight increase in porosity, but can be mainly attributed to process reproducibility. Further characterisation fails to show any reason for this behaviour.

Diffractograms of the highest density copper:steel 3Dobject were compared to the smallest and highest height 3Dobjects (figure 5.19). When compared to the virgin powder, an austenitic phase corresponding to the steel addition is evident in the XRD. Furthermore, SLM production of copper-steel did not affect the powder material significantly, and the presence of copper oxide is not evident.

The addition of steel powder to copper decreases the defects, as detected by μCT, and emphasises density values. Inside SLM 3Dobject, it could attain 99% of densification against 95% of copper. This is associated with an improvement of alloy properties contributing to a significant increase of the 3Dobject hardness (table 5.3).

Table 5.3: Microhardness and density of copper-steel objects.

3Dobject	**Hardness (HV)**	**3Dobject Density** $\left(\frac{\mathbf{Kg}}{\mathbf{m}^3}\right)$
V160W400	164 ± 6	8580
0.5 mm	166 ± 3	7888
8.0 mm	173 ± 8	8339

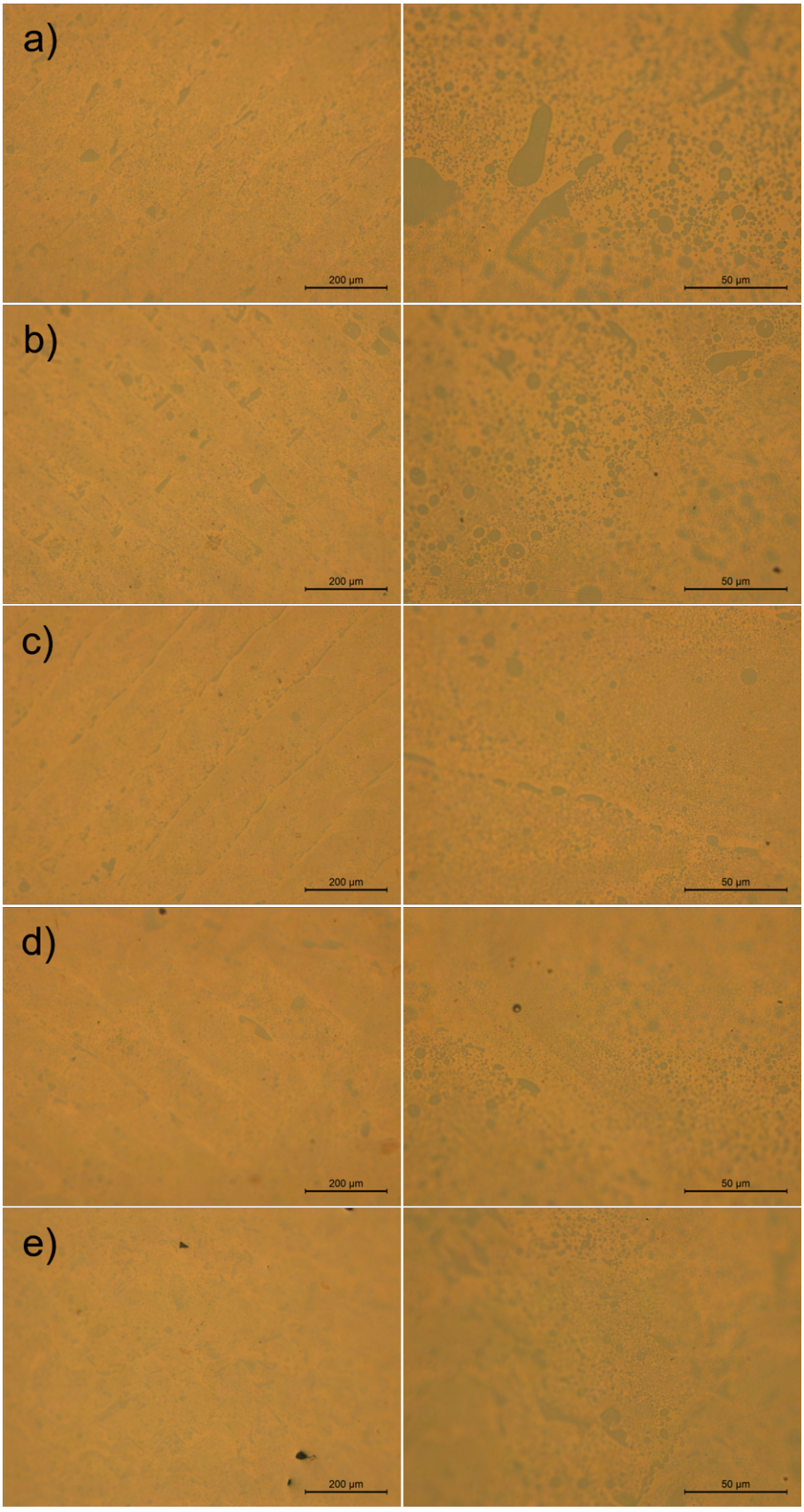

Figure 5.13: Optical micrographies of Cu-Fe 0.5 (a), 1.0 (b), 2.0 (c), 4.0 (d), 8.0 (e) mm height 3Dobjects.

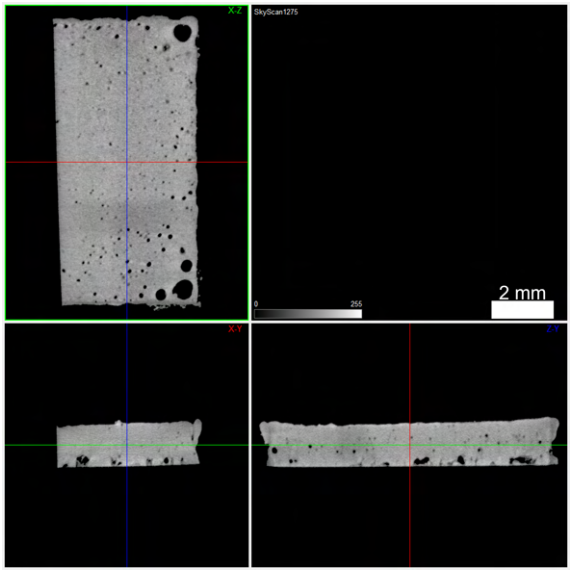

Figure 5.14: 2D visualisation of 3Dobject height 0.5 mm cross-section.

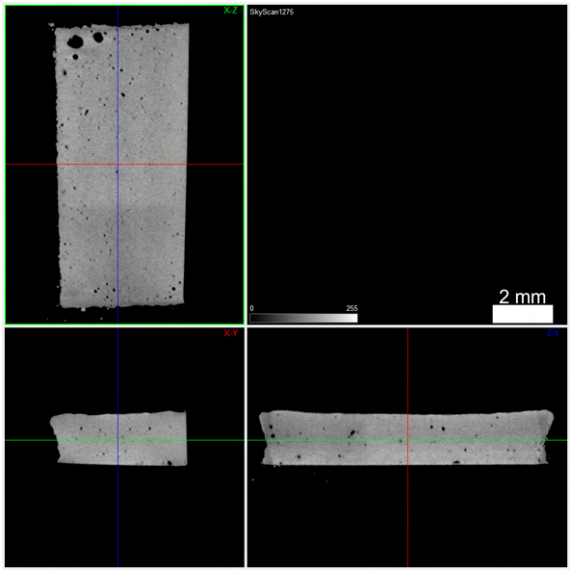

Figure 5.15: 2D visualisation of object height 1.0 mm cross-section.

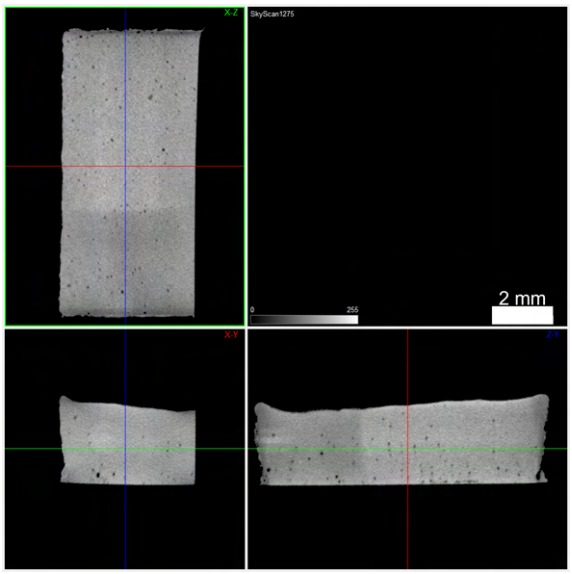

Figure 5.16: 2D visualisation of object height 2.0 mm cross-section.

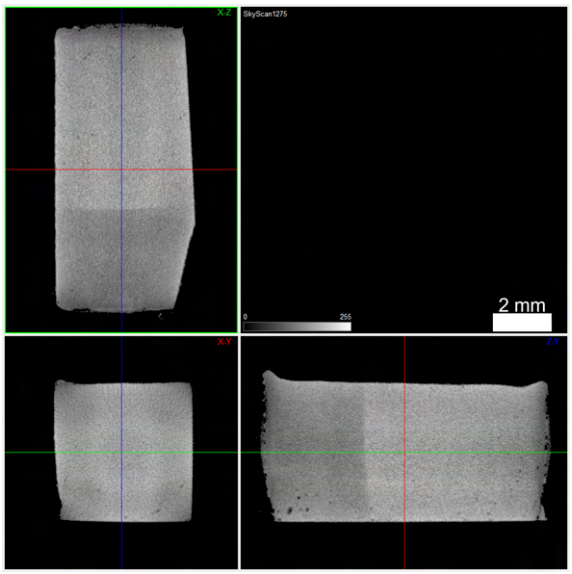

Figure 5.17: 2D visualisation of object height 4.0 mm cross-section.

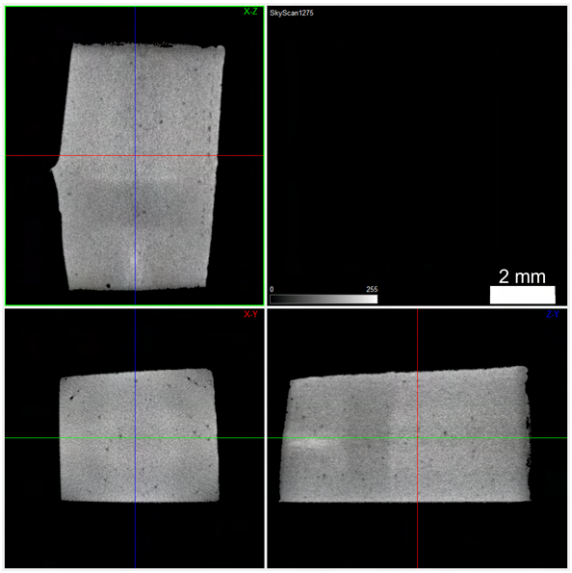

Figure 5.18: 2D visualisation of object height 8.0 mm cross-section.

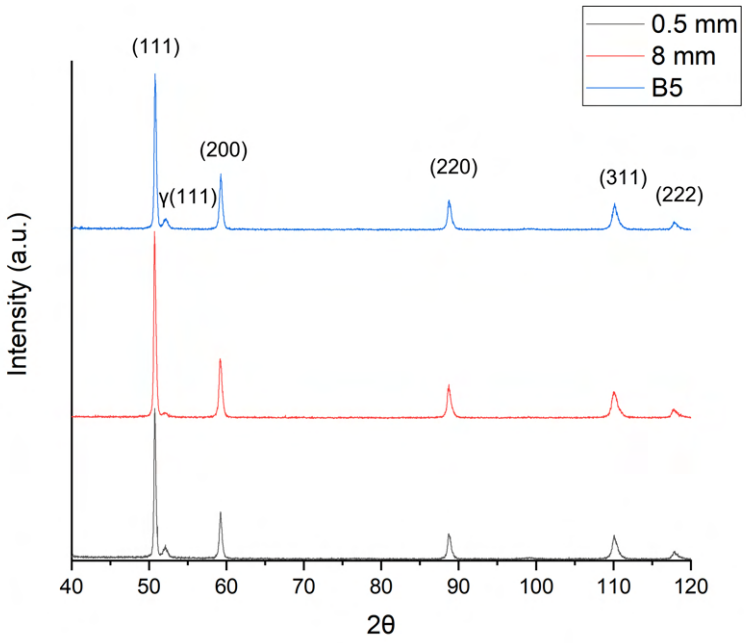

Figure 5.19: XRD diffractograms of the 0.5, 8.0 mm and V160W400 (B5 as a standard) copper-steel 3Dobjects.

Chapter 6

Case study: Role of additive manufacturing on SS 3Dobject properties with minor interference of process defects

The main objective of this chapter is to highlight the importance of defect minimisation due to the powder characteristics and SLM processing parameters. This contributes to demonstrate the role of structural modifications induced by additive manufacturing on the mechanical properties of the 3Dobjects. This case study also led to a better understanding of the carbon content role in SS processed by SLM.

6.1 SLM of Stainless Steels

First of all, the study was focused on one of the most studied powder materials processed by additive manufacturing – stainless steel 316L (AISI). Moreover, all the stainless steel powder studied was processed using the established parameters (EOS®). This allows to compare the results of the present research with the enounced in the state of the art.

6.1.1 Standard Stainless Steel Production

The EOS®parameters must be related to the lowest content defects, whatever their location inside the 3Dobject. However, μCT analyses reveal in the 3Dobject (tensile specimen), fabricated in the established conditions, that there is a small concentration of defects

close to the surface (>200 μm), but without contact with the exterior (closed defects). Figure 6.1 shows pores that have an irregular shape, which may correspond to lack-of-fusion defects due to deficient contour-infill hatching distance. This type of defect can be solved by decreasing this parameter or increasing the laser power in contour zones. Furthermore, the contour is usually at an angle in relation to infill scanning, which may result in LOF between the two scanning zones, even if the hatching space is correct. A 2D view of the object confirms the small prevalence of interior defects and the clear incidence of close-to-surface pores. Also, interior pores are low and mostly random since their size and location do not seem to be directly correlated to any μCT visible pattern. However, this can occur and, if spherical, can be attributed to high VED, resulting from the keyhole regimen.

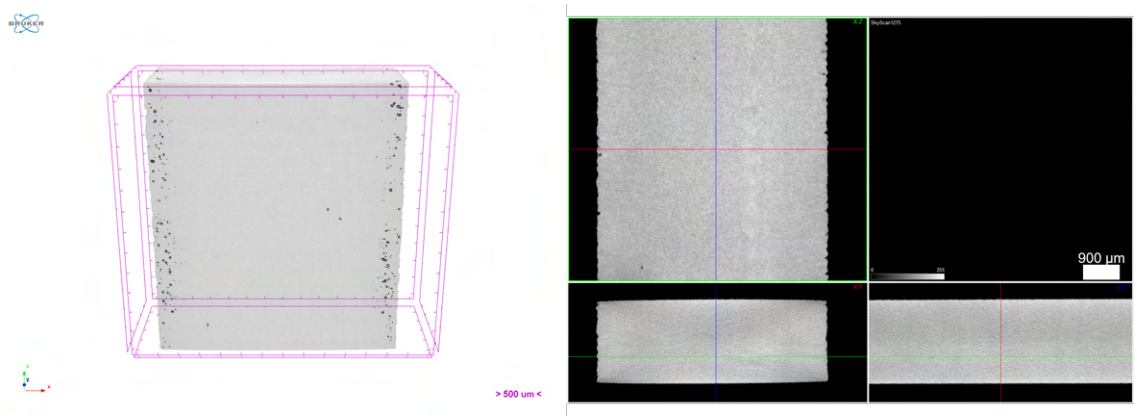

Figure 6.1: 3D rendering of defect location within the SS 316L 3Dobject volume.

In order to evaluate the degree of optimisation attained, the density of the 3Dobject was measured. Density values for 316L (table 6.1) correspond to $\approx$ 1% of defects in 3Dobjects, similar to other authors values and could also be attributed to phase modification during processing [224]. A direct comparison with the virgin powder is considered more important due to the intrinsic phase changes that the material is subjected to during atomisation, which is lacking when compared to standard bulk stainless steel.

Table 6.1: SS 316L powder and 3Dobject density.

Type	**Powder Density** $\left(\frac{\mathbf{Kg}}{\mathbf{m^3}}\right)$	**3Dobject Density** $\left(\frac{\mathbf{Kg}}{\mathbf{m^3}}\right)$	**Densification (%)**
316L	7880	7790	99

In fact, X-ray diffraction of the 316L virgin powder and 3Dobject (figure 6.2) show that the total austenitic phase results from the processing of the virgin powder, that is

constituted mainly by austenite but also by ferrite/martensite. This means that the residual ferrite/martensite phase disappears during processing. A strong orientation (220) can be observed in the 3Dobject. The preferential direction is according to <011>, resulting from thin and deep melting pools. Mechanical properties are often improved when this texture is attained, as reported by Sun et al. [329]. However, a recrystallisation procedure may be performed to achieve properties closer to bulk 316L.

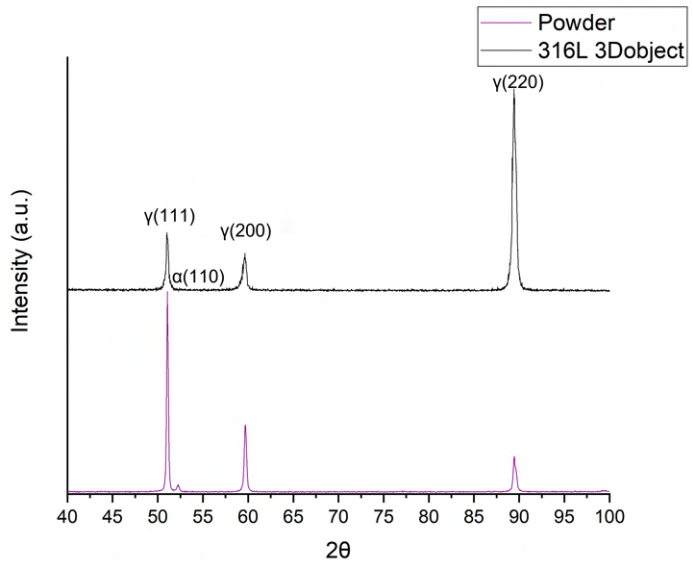

Figure 6.2: X-ray diffractograms of the 316L powder and 3Dobject (bottom and top).

After showing the reduced influence of defects on the 3Dobject densification, it was possible to analyse the effect of SLM on the microstructure, having as standard the 316L bulk. Micrographies of SLM-processed SS 316L powder (figure 6.3) show a homogenous equiaxial grain distribution. However, a typical microstructure resulting from SLM is anisotropic with preferential growth in the melting pool direction.

Roughness analysis of the 3Dobject surface (table6.2) reveals a prevalence of a waviness corresponding to the scanning direction (figure 6.4). Surface roughness (cf. chapter 2), can be an indicator of melting pool suitability. The extremely high roughness (≈16 µm) compared with the roughness of subtractive manufacturing (≈2-6 µm) of SS 316L. 3Dobject confirms the deep melting pools that result in high growth in ZZ' direction. Moreover, a thin melting pool corresponds to a texture that can also be observed through the valleys between solidified melting pools (figure 6.4). The optimal overlap in steels is considered to be around 30%. Thus, intermelting-pool distance can result in a lack of fusion pores on the lower layer space between the melting pools. Furthermore, an incidence of spattered

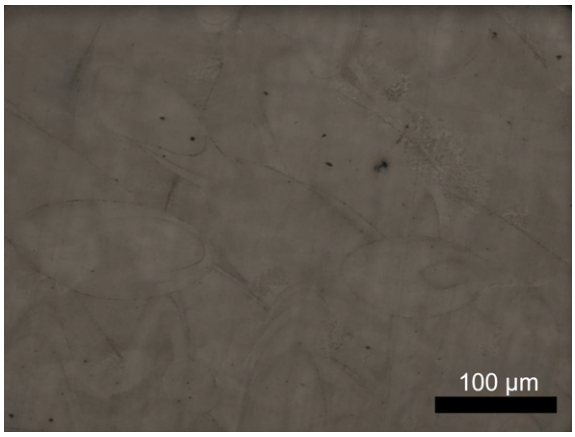

Figure 6.3: Optical micrography of etched surface of 316L stainless steel after SLM (200x).

powders can be seen scattered around the object surface, resulting from powder partial melting, which further decreases surface quality.

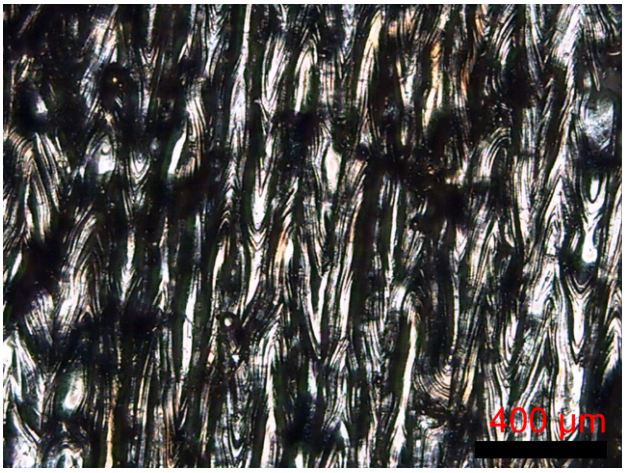

Figure 6.4: Optical micrography of the 316L stainless steel surface (50x).

Table 6.2: Average roughness values of 316L 3Dobjects.

Type	Ra (µm)	Rq (µm)	Rz (µm)
316L	16.204	19.864	94.401

Comparisons between CAD data and final measurements of the tensile specimens were made (table 6.3). A slight reduction in all directions is observed. This can be related to a bad translation of the actual measurements by the scanning. Generally, melting pool width is considered to be around 140 µm. Any modification in relation to this assumed value will result in a final 3Dobject variation. To mitigate this factor, an extra thickness is included in the design of the part and it can be machined after fabrication.

Table 6.3: Comparison between CAD and final SS 316L 3Dobject sizes of tensile test specimens.

Type	Width at Grip (%)	Width at Reduced Section (%)	Length (%)
316L	99.40 ± 0.24	98.50 ± 0.32	99.70 ± 0.03

Tensile tests validate the final quality of SLM products. All the specimens have similar tensile behaviour (figure 6.5). This reinforces the previous statement evaluated by μCT shown that the defect prevalence is indeed low. When compared to the bulk 316L, tensile properties have been improved, which can be connected to the resulting texture associated with the low defect prevalence. However, as is common in SLMed 3Dobjects, strain is slightly reduced. Table 6.4 summarises the tensile strain, and ultimate tensile strength and compares it to bulk 316L.

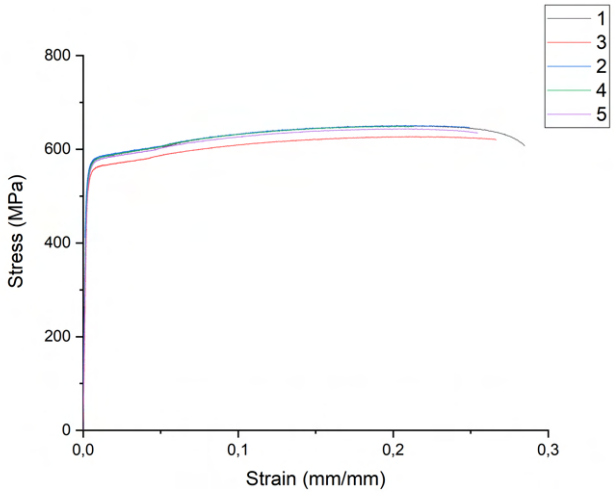

Figure 6.5: Stress–strain curves for the 316L tensile test specimens.

Table 6.4: Elongation and ultimate tensile strength for 316L 3Dobjects, compared to bulk.

Type	3Dobject ε (%)	Bulk ε (%)	3Dobject *UTS* (MPa)	Bulk *UTS* (MPa)
316L	25.4 ± 2.4	30–50	645 ± 10	550

Microhardness was also measured for the 316L 3Dobjects (table 6.5). Lower hardness than the bulk 316L was measured. This might be related to the nitrogen in the atmosphere, during atomisation and SLM processing, grain size, orientation, and surface porosity (figure 6.1).

Table 6.5: Microhardness of SS 316L objects.

Type	3Dobject $HV_{0.1}$	Bulk $HV_{0.1}$
316L	133 ± 17	170–220

6.1.2 Stainless Steels and Carbon Content

Material reaction to the given energy is dependent on its chemical composition. On this case study, stainless steels with three different carbon content but with similar alloying elements were processed. Comparison with the results attained by 316L standard, manufactured by SLM printing with similar processing parameters, was done. First of all, the defects analysed were highlighted using μCT. 3D rendering of 630 SS confirms the idea of inadequacy of contour to infill overlap as in 316L (figure 6.6). Large irregular pores can also be observed on the boundary between the two scanning patterns.

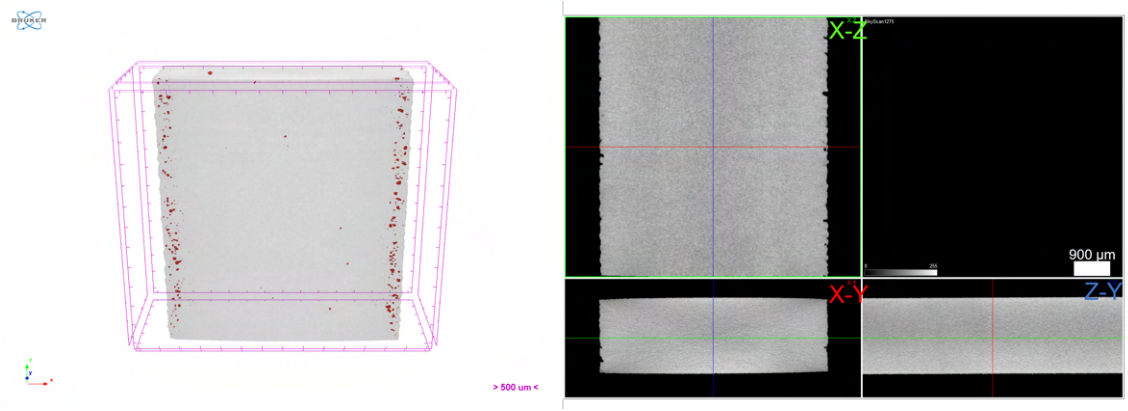

Figure 6.6: 3D rendering of defect location within the SS 630 3Dobject volume.

In what concerns SS 420, it displays the same inadequacy between contour and infill, visible for all studied steels (figure 6.7). Moreover, internal pores are also smaller and rarer.

Although 440C resulted in the lowest density, when measured by Archimedes method, it can be visible that it presents a high close-to-surface porosity (figure 6.8). However, 440C porosity is in accordance with the idea that the contour parameters become more inadequate as the melting pool is reduced in size. A bigger presence of pores can be detected closer to the surface. Overall lack of density is in line with LOF resulting from inadequate hatching space and is not mitigated by the deeper melting pools observed on the other stainless steels.

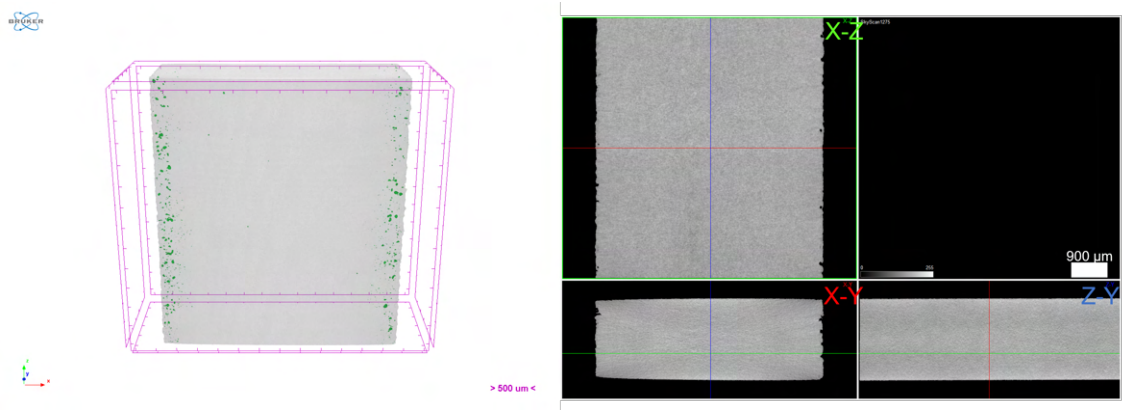

Figure 6.7: 3D rendering of defect location within the SS 420 3Dobject volume.

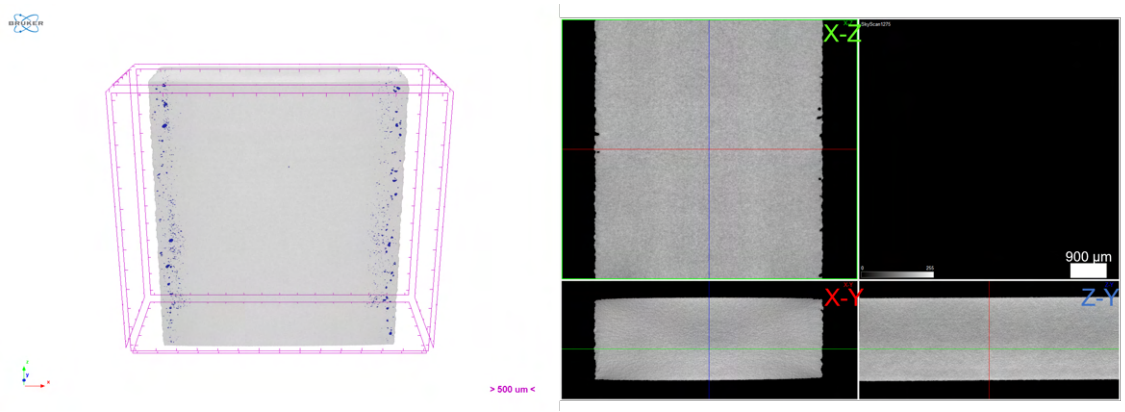

Figure 6.8: 3D rendering of defect location within the SS 440C 3Dobject volume.

As a remark, it must be highlighted that the contour/infill pores can be rectified, for example, by machining process if induced extra thickness, or offset, that must accounted for in the first stage of design, as previously stated.

Density was measured for the three stainless steels selected and compared to the virgin powder (table 6.6). An overall decrease in the density with carbon increase can be observed. One of the major challenges of producing high-carbon steels is the vaporisation of this element when directly affected by the laser beam.

Table 6.6: SS 630, 420 and 440C powder and 3Dobject density.

Type	**Powder Density** $\left(\frac{\mathbf{Kg}}{\mathbf{m^3}}\right)$	**3Dobject Density** $\left(\frac{\mathbf{Kg}}{\mathbf{m^3}}\right)$	**Densification (%)** (Disregarding phase modification)
630	7880	7660	97.2
420	7820	7590	97.0
440C	7940	7490	94.3

Having in mind that virgin powder phases and texture could be different after SLM, for a density understanding the diffractograms before and after SLM must be analysed.

XRD of the 630 stainless steel shows that an almost dual-phase steel was attained after SLM processing (figure 6.9). The phasic composition is similar to 316L, but a non-discernible preferential direction (220) is detected in 316L (figure 6.2).

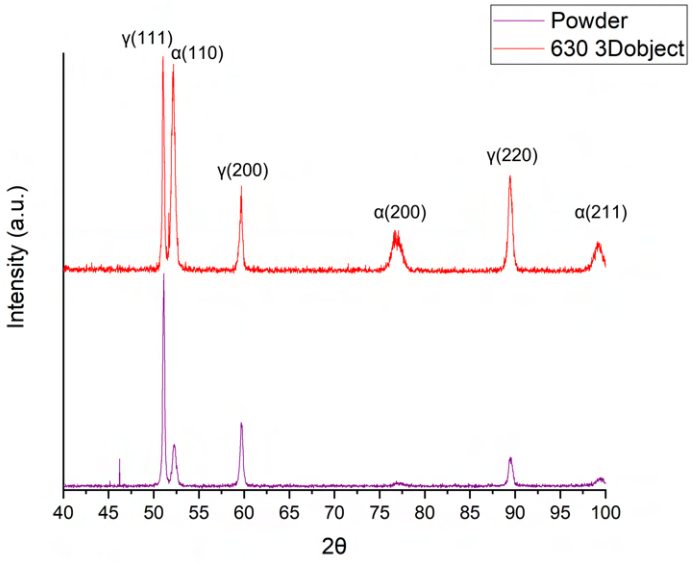

Figure 6.9: X-ray diffractograms of SS 630 powder and 3Dobject (bottom and top).

A change in texture in austenitic phase (220) in 420 stainless steels is also visible, just as observed in 316L (figure 6.10). A change in the austenite grain direction can be resulting from SLM processing regarding microstructure growth due to melting pool phenomena.

In what concerns phases and texture present in virgin powder and SLM 3Dobject, no change between virgin powder and SLM is visible in the 440C steel diffractograms (figure 6.11). Both have a unique phase - austenite, that shows a light tendency for a preferential direction (220). Parameters may not be as harsh when considering the ultra-high

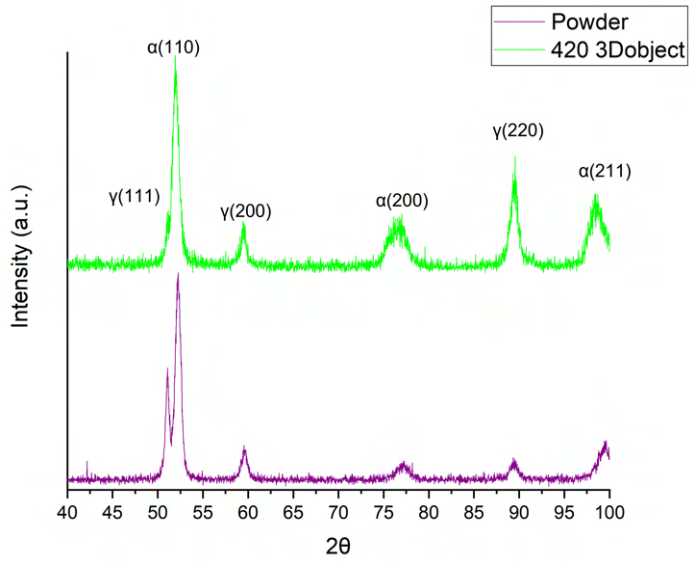

Figure 6.10: X-ray diffractograms of SS 420 powder and 3Dobject (bottom and top).

carbon content that is present in 440C steel, resulting in mitigated texture changes in the 3Dobject.

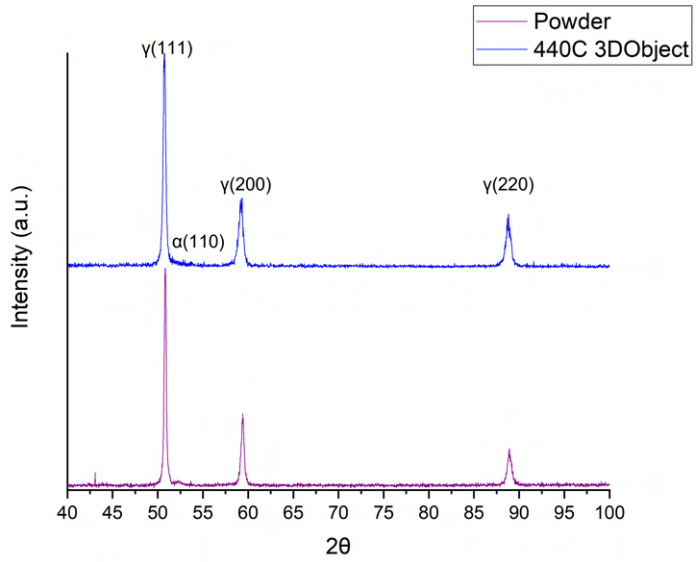

Figure 6.11: X-ray diffractograms of SS 440C powder and 3Dobject (bottom and top).

The micrographies can contribute to understanding the reason for the densification measured by Archimedes density method. A thorough observation of the microstructures of the selected stainless steels shows that the 630 and 420 SS have a more complex thermal history, with the two austenitic and ferritic/martensitic phases related to the melting pool

dynamics (figure 6.12). This contrasts with 440C SS, where the micrographies are similar to the 316L stainless steel, which is in pair with the austenitic phase dominance revealed by XRD. However, these results in 440C are in disagreement with the low-density values measured. These low values could be attributed to the highest porosity close to the surface in 440C detected by μCT, which could assume a density decrease in Archimedes density evaluation.

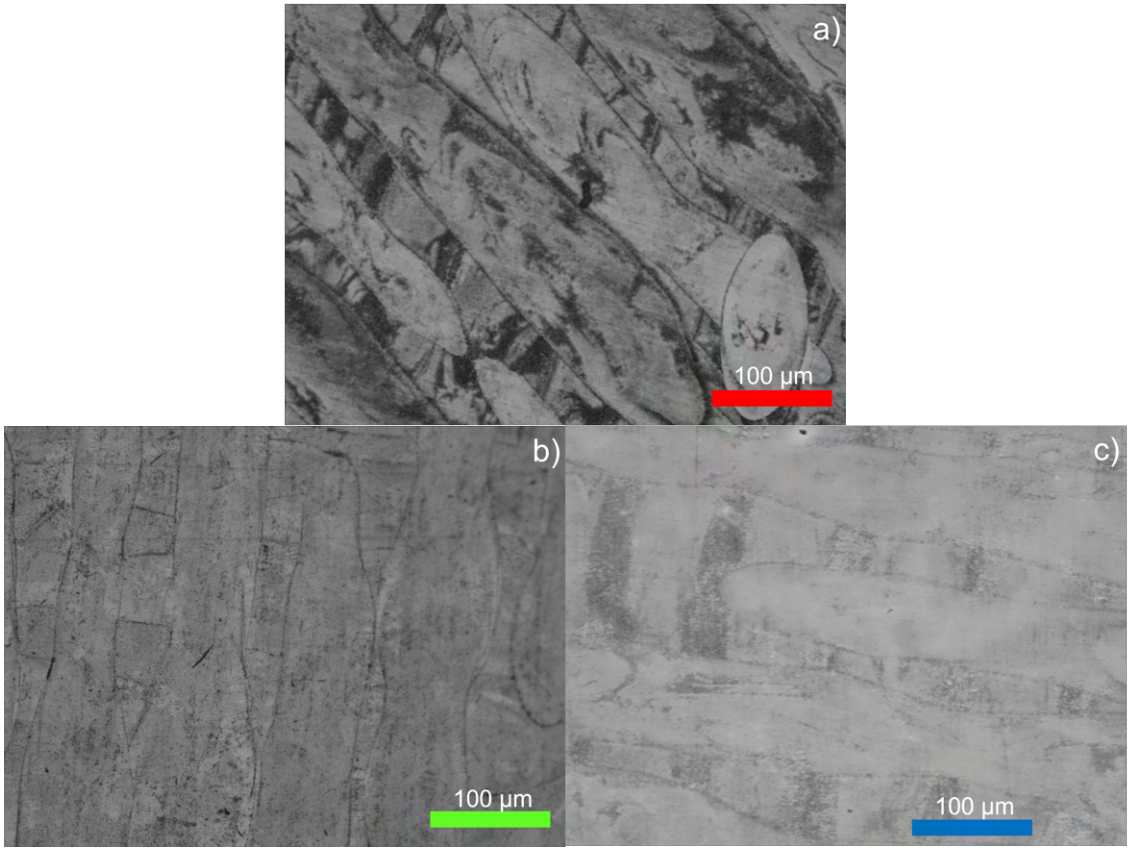

Figure 6.12: Optical micrographies of the etched surfaces of 630 (a), 420 (b) and 440C (c) stainless steels (200x).

The surface roughness (figure 6.13 and table 6.7) decreases as the carbon content increases. As stated before, roughness can be an assessment of parameter suitability. 440C melting pools are wider, and overlap is more acceptable. This corroborates the idea that texture changes may be resultant of deep and narrow melting pools since 440C texture changes are lighter.

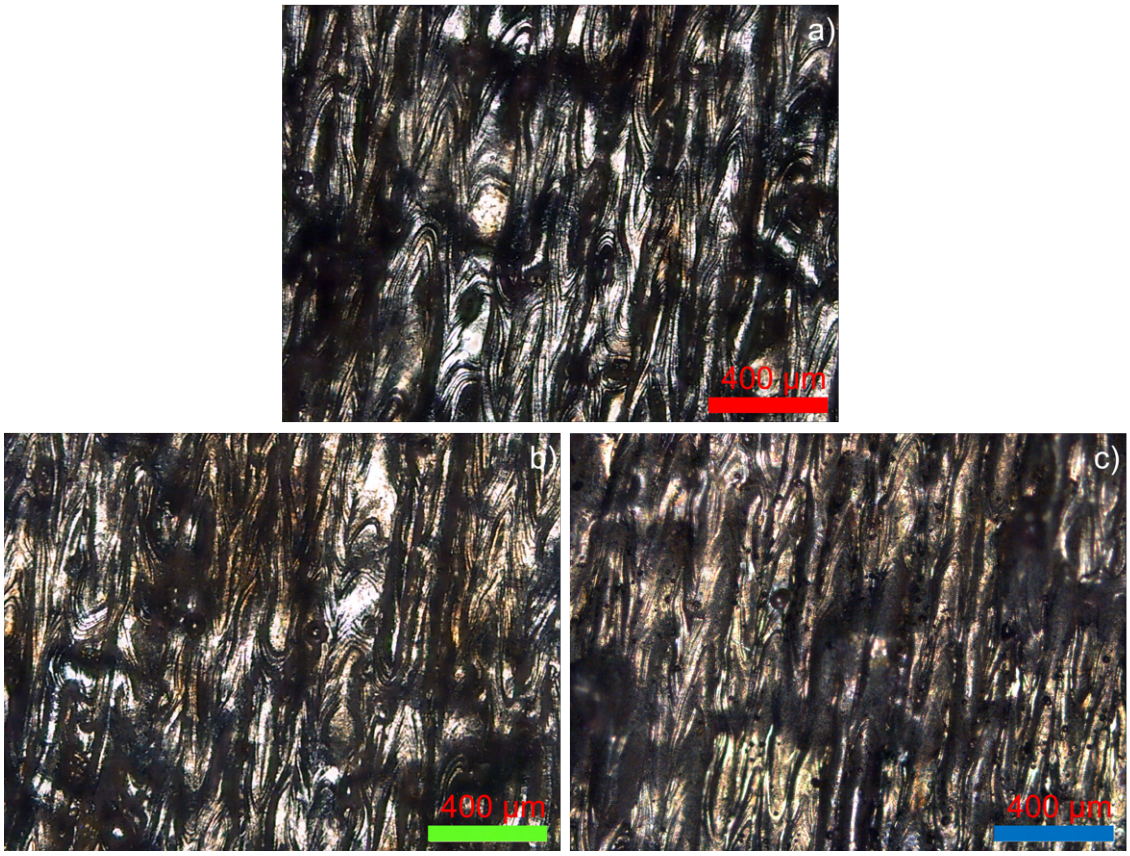

Figure 6.13: Optical micrographies of the 630 (a), 420 (b), 440C (c) surfaces (50x).

Table 6.7: Roughness values of SS 630, 420 and 440C 3Dobjects.

Type	Ra (µm)	Rq (µm)	Rz (µm)
630	12.988	16.030	79.347
420	7.669	9.440	53.783
440C	6.369	8.093	46.391

Reductions in specimen dimensions seem to be general for all steels and an answer to the selected inputs (table 6.8). 440C had a universal decrease in size, bigger than the other steels.

Table 6.8: CAD vs final 3Dobject percentage sizes of tensile test specimens (630, 420 and 440C).

Type	Width at Grip (%)	Width at Reduced Section (%)	Length (%)
630	99.60 ± 0.19	99.00 ± 0.27	99.81 ± 0.05
420	99.70 ± 0.25	98.67 ± 0.27	100.00 ± 0.06
440C	99.20 ± 0.03	98.83 ± 0.25	99.58 ± 0.05

Tensile tests (figure 6.14 and table 6.9) of the stainless steels studied show that 420 and 440C stainless steels have a completely fragile behaviour, without plastic strain when compared to bulk steels. Furthermore, they have an outstanding UTS when compared to the bulk, typicall in SLM 3Dobjects. SS 630 show a particular behaviour connected to the present dual phase (ferrite/martensite and austenite). TRIP (strain-induced martensite formation) effect is resultant of a high content of retained austenite [320, 321, 330]. This effect results in a higher strain than normally observed in heat-treated SS 630.

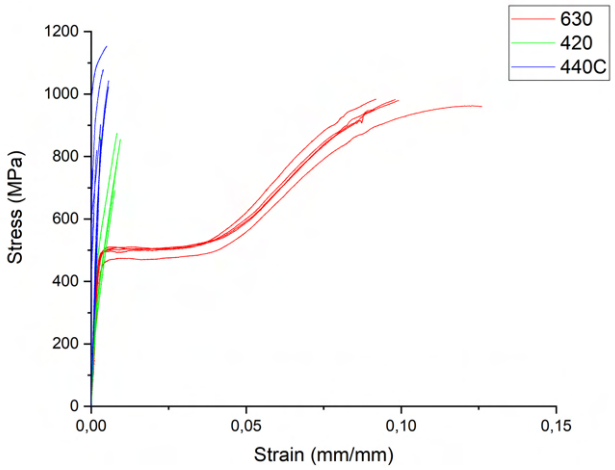

Figure 6.14: Strain–stress curves for SS 630 (red), 420 (green) and 440C (blue) steels.

Table 6.9: Elongation and ultimate tensile strength for 630, 420 and 440C 3Dobjects, compared to bulk (according to databases).

Type	**3Dobject** ε **(%)**	**Bulk** ε **(%)**	**3Dobject** ***UTS*** **(MPa)**	**Bulk** ***UTS*** **(MPa)**
630	10.0 ± 1.3	4–6	1020 ± 33	943
420	0.7 ± 0.2	5–11	814 ± 74	655
440C	0.4 ± 0.1	0.5–4	1164 ± 13	760

The microhardness values of the SLM 3Dobjects produced from the powders of SS 630, 420 and 440C were higher than the maximum hardness of the bulk steels processed by conventional approaches, including heat treatment (table 6.10).

Table 6.10: Microhardness of the SS 630, 420 and 440C objects, compared to bulk (according to databases).

Type	**3Dobject** $\mathbf{HV_{0.1}}$	**Bulk** $\mathbf{HV_{0.1}}$
630	306 ± 11	250–460
420	647 ± 27	260–641
440C	803 ± 26	510–760

Conclusions

The final quality of a 3D object produced using powder technology depends heavily on the size, distribution, and localization of defects, as well as the microstructure. This thesis aims to investigate the effect of metal 3D objects processed by additive manufacturing in solid (SSAM) and liquid states (LSAM) on their microstructure and extrinsic properties. The primary goal was to minimize the impact of stochastic defects that result from powder material and processing parameters, which are selected based on the metal additive technology used. This thesis highlights the microstructure induced in the final structural properties for the intended application.

A thorough analysis of stochastic defects was performed using the μCT technique, which provides an extraordinary and unique insight into internal defects. The studies on SSAM and LSAM 3D objects revealed that there is a significant difference in the type, localisation, and dimensions of defects between the two groups. LSAM processes, such as MEX, where 3D objects are built from a filament that is reduced from millimetric to micrometric thickness layers, lead to distinct defect types. The study also illustrates the tendency of SSAM products to present large pores that are generally harmful to the final quality. However, different powder materials can attain high densification values after suitable parameter selection, particularly if high pressure is applied in the green solid (such as cold isostatic pressing - CIP).

Regarding LSAM, Copper and standard material SS 316L were selected to establish the limits of the defects created during the processing. The μμCT technique led to a detailed analysis of the subsurface and internal characteristics of the 3D objects. The dimension of defects in LSAM tends to be smaller than in SSAM, with a preferential distribution closer to the surface. While these pores may be detrimental to the mechanical properties of the 3D objects, this is not always well understood or predictable. The effects of these defects on mechanical properties are not fully considered, which is due to the AM effect on final microstructures, which is usually not taken into account.

The study shows that SLM parameters used for SS 316L induce low porosity and high densification in other stainless steels with low nickel and higher carbon content. However, the study of attained LSAM microstructures, without post-processing treatments, is necessary to assess the mechanical behaviour of 3D objects. The hardness and UTS of SLM 3D objects are higher than those of bulk stainless steels with the same chemical compositions after heat treatments. This is due to a direct relationship between carbon and elements with high affinity to it (e.g., chromium, molybdenum) since the content of other elements of the selected stainless steels is insufficient for carbide formation. Moreover, the stabilisation of residual austenite present in the steels with higher carbon content can result from the processing atmosphere; nitrogen is more effective than other elements in the matrix.

The anisotropy observed in all stainless steels resulted from the selected scanning strategy and VED values. In the studied stainless steels, the microstructural difference, when compared to conventionally processed bulk materials, is mainly due to the processing atmosphere. Therefore, a constant VED can be used to process different stainless steels with varying carbon compositions. X-ray tomography, associated with new practical methodologies, emphasises, non-destructively, the true effect of defects and highlights the role of phase transformation and microstructures in the physical and mechanical behaviour of 3D objects.

By using advanced modelling techniques, it is possible to evaluate the impact of defects on the microstructure and macroscopic properties of the 3D object, and to optimise the production parameters to minimise the defects and enhance the performance of the final product. The integration of modelling with experimental methods can lead to a comprehensive understanding of the underlying physics and mechanics of the additive manufacturing process, and enable the development of reliable and efficient strategies for producing high-quality 3D objects.

Future Work

The fatigue properties of 3D objects are highly dependent on the extent of total porosity and the distance of defects from the surface. Pores located within 1 mm of the surface are known to act as typical crack initiators, which has previously been underestimated. However, the use of microcomputed tomography (μCT) can provide a better understanding of the impact of such defects on fatigue, as demonstrated by the Proof of Concept project

AM.PPT, CCDRC, PT2020. The effects of post-processing thermal and pressure treatments on the removal of pores and residual stresses must be thoroughly investigated to achieve a balance between their effectiveness and any potential negative impacts. Surface treatments, such as shot or laser peening, can also be considered, as they not only induce compressive stress in the material but also partially or totally close near-surface pores.

Furthermore, future studies should investigate the influence of carbon content on solid-state additive manufacturing of 3D objects.

References

[1] V. Alcácer and V. Cruz-Machado. Scanning the Industry 4.0: A Literature Review on Technologies for Manufacturing Systems. *Engineering Science and Technology, an International Journal*, 22(3):899, January 2019.

[2] Javaid Butt. A Strategic Roadmap for the Manufacturing Industry to Implement Industry 4.0. *Designs*, 4(2):11, May 2020.

[3] Ana Vafadar, Ferdinando Guzzomi, Alexander Rassau, and Kevin Hayward. Advances in Metal Additive Manufacturing: A Review of Common Processes, Industrial Applications, and Current Challenges. *Applied Sciences*, 11(3):1213, January 2021.

[4] Jon Iñaki Arrizubieta, Olatz Ukar, Marta Ostolaza, and Arantza Mugica. Study of the Environmental Implications of Using Metal Powder in Additive Manufacturing and Its Handling. *Metals*, 10(2):261, February 2020.

[5] Manuela Galati and Paolo Minetola. Analysis of Density, Roughness, and Accuracy of the Atomic Diffusion Additive Manufacturing (ADAM) Process for Metal Parts. *Materials*, 12(24):4122, December 2019.

[6] Mirriam-Webster. (n.d.). Defect. In Merriam-Webster.com dictionary. Retrieved October 15, 2022, from https://www.merriam-webster.com/dictionary/defect.

[7] Markus Baier, Mirko Sinico, Umberto Paggi, Ann Witvrouw, Lore Thijs, Wim Dewulf, and Simone Carmignato. Improving metal additive manufacturing part design and final part precision using feedback from X-ray computed tomography. In *Proceedings of the Joint Special Interest Group meeting between euspen and ASPE Advancing Precision in Additive Manufacturing 2019*, page 4, Nantes, France, September 2019. euspen.

[8] B A Bircher, S Wyss, D Gage, A Küng, C Körner, and F Meli. High-resolution X-ray computed tomography for additive manufacturing: Towards traceable porosity defect measurements using digital twins. In *Proceedings of Joint Special Interest Group meeting between euspen and ASPE Advancing Precision in Additive Manufacturing*, page 4, Inspire AG, St. Gallen, Switzerland 2021, September 2021. euspen.

[9] Anton du Plessis, Ina Yadroitsava, and Igor Yadroitsev. Effects of defects on mechanical properties in metal additive manufacturing: A review focusing on X-ray tomography insights. *Materials & Design*, 187:108385, February 2020.

[10] Ugur M. Dilberoglu, Bahar Gharehpapagh, Ulas Yaman, and Melik Dolen. The Role of Additive Manufacturing in the Era of Industry 4.0. *Procedia Manufacturing*, 11:545, June 2017.

[11] Peyman Ansari, Asif Ur Rehman, Fatih Pitir, Salih Veziroglu, Yogendra Kumar Mishra, Oral Cenk Aktas, and Metin U. Salamci. Selective Laser Melting of 316L Austenitic Stainless Steel: Detailed Process Understanding Using Multiphysics Simulation and Experimentation. *Metals*, 11(7):1076, July 2021.

[12] Naying An, Sansan Shuai, Tao Hu, Chaoyue Chen, Jiang Wang, and Zhongming Ren. Application of Synchrotron X-Ray Imaging and Diffraction in Additive Manufacturing: A Review. *Acta Metallurgica Sinica (English Letters)*, October 2021.

[13] Jian Qin, Fu Hu, Ying Liu, Paul Witherell, Charlie C. L. Wang, David W. Rosen, Timothy W. Simpson, Yan Lu, and Qian Tang. Research and application of machine learning for additive manufacturing. *Additive Manufacturing*, 52:102691, April 2022.

[14] Michael Rüßmann, Markus Lorenz, Philipp Gerbert, Manuela Waldner, Jan Justus, Pascal Engel, and Michael Harnisch. Industry 4.0: The Future of Productivity and Growth in Manufacturing, April 2015.

[15] ISO/ASTM. ISO/ASTM 52900:2021(en), Additive manufacturing — General principles — Fundamentals and vocabulary, 2021.

[16] Dominik Morar, Hans-Georg Kemper, and Heiner Lasi. Challenges in Processing Digital and Physical Parts in Additive Manufacturing: An Exploration. In *2017 Portland International Conference on Management of Engineering and Technology (PICMET)*, pages 1–9, July 2017.

[17] Kazimierz T. Kosmowski. Fourth industrial revolution and new challenges in post-pandemic world. *Safety and Reliability of Systems and Processes*, Summer Safety and Reliability Seminar 2021, October 2021.

[18] Mohit Dharnidharka, Utkarsh Chadha, Lohitha Manya Dasari, Aarunya Paliwal, Yash Surya, and Senthil Kumaran Selvaraj. Optical tomography in additive manufacturing: a review, processes, open problems, and new opportunities. *The European Physical Journal Plus*, 136(11):1133, November 2021.

[19] Daniel Moreno Nieto and Daniel Moreno Sánchez. Design for Additive Manufacturing: Tool Review and a Case Study. *Applied Sciences*, 11(4):1571, February 2021.

[20] Xiaoji Zhang, Yuan-hui Chueh, Chao Wei, Zhe Sun, Jiwang Yan, and Lin Li. Additive manufacturing of three-dimensional metal-glass functionally gradient material

components by laser powder bed fusion with in situ powder mixing. *Additive Manufacturing*, 33:101113, May 2020.

[21] Hong Wei Tan and Yu Ying Clarrisa Choong. Additive manufacturing in COVID-19: recognising the challenges and driving for assurance. *Virtual and Physical Prototyping*, 16(4):498–503, July 2021. Publisher: Taylor & Francis _eprint: https://doi.org/10.1080/17452759.2021.1975882.

[22] Xing Peng, Lingbao Kong, Jerry Ying Hsi Fuh, and Hao Wang. A Review of Post-Processing Technologies in Additive Manufacturing. *Journal of Manufacturing and Materials Processing*, 5(2):38, June 2021. Number: 2 Publisher: Multidisciplinary Digital Publishing Institute.

[23] 'Rapid Prototyping with 3D Printing and Additive Manufacturing'. https://www.ennomotive.com/beyond-rapid-prototyping-with-3d-printing (accessed Aug. 10, 2022).

[24] Jigar Patadiya, Adwait Gawande, Ganapati Joshi, and Balasubramanian Kandasubramanian. Additive Manufacturing of Shape Memory Polymer Composites for Futuristic Technology. *Industrial & Engineering Chemistry Research*, 60(44):15885–15912, November 2021. Publisher: American Chemical Society.

[25] J A Manriquez-Frayre and D L Bourell. Selective Laser Sintering of Binary Metallic Powder. In *SFF Symposium Proceedings*, page 8, Texas, USA, July 1990. University of Texas.

[26] Martin Malý, Daniel Koutný, Libor Pantělejev, Laurent Pambaguian, and David Paloušek. Effect of high-temperature preheating on pure copper thick-walled samples processed by laser powder bed fusion. *Journal of Manufacturing Processes*, 73:924–938, January 2022.

[27] Anketa Jandyal, Ikshita Chaturvedi, Ishika Wazir, Ankush Raina, and Mir Irfan Ul Haq. 3D printing – A review of processes, materials and applications in industry 4.0. *Sustainable Operations and Computers*, 3:33–42, January 2022.

[28] Pascal Schmitt, Stefan Zorn, and Kilian Gericke. Additive Manufacturing Research Landscape: A Literature Review. *Proceedings of the Design Society*, 1:333–344, August 2021.

[29] Byron Blakey-Milner, Paul Gradl, Glen Snedden, Michael Brooks, Jean Pitot, Elena Lopez, Martin Leary, Filippo Berto, and Anton du Plessis. Metal additive manufacturing in aerospace: A review. *Materials & Design*, 209:110008, November 2021.

[30] Haijun Gong, Dean Snelling, Kamran Kardel, and Andres Carrano. Comparison of Stainless Steel 316L Parts Made by FDM- and SLM-Based Additive Manufacturing Processes. *JOM*, 71(3):880, November 2018.

[31] J. V. Ecker, K. Dobrezberger, J. Gonzalez-Gutierrez, M Spoerk, Ch. Gierl-Mayer, and H. Danninger. Additive Manufacturing of Steel and Copper Using Fused Layer Modelling: Material and Process Development. *Powder Metallurgy Progress*, 19(2):63–81, December 2019.

[32] Prof Dr-Ing Christian Seidel. Metal Additive Manufacturing:Why standards lay the foundation for continued industry growth, April 2021.

[33] Ze Chen, Changjun Han, Ming Gao, Sastry Yagnanna Kandukuri, and Kun Zhou. A review on qualification and certification for metal additive manufacturing. *Virtual and Physical Prototyping*, 17(2):382–405, April 2022. Publisher: Taylor & Francis _eprint: https://doi.org/10.1080/17452759.2021.2018938.

[34] Ghasemi Tabasi. *Understanding Thermomechanical Treatments Induced by Laser Powder Bed Fusion Process*. PhD Thesis, École Polytechnique Fédérale de Lausanne, Lausanne, France, October 2021.

[35] Paramjot Singh, Qasim Shaikh, Vamsi K. Balla, Sundar V. Atre, and Kunal H. Kate. Estimating Powder-Polymer Material Properties Used in Design for Metal Fused Filament Fabrication (DfMF3). *JOM*, 72(1):485–495, January 2020.

[36] Mehrdad Mousapour, Mika Salmi, Lassi Klemettinen, and Jouni Partanen. Feasibility study of producing multi-metal parts by Fused Filament Fabrication (FFF) technique. *Journal of Manufacturing Processes*, 67:438–446, July 2021.

[37] Santiago Cano, Joamin Gonzalez-Gutierrez, Janak Sapkota, Martin Spoerk, Florian Arbeiter, Stephan Schuschnigg, Clemens Holzer, and Christian Kukla. Additive manufacturing of zirconia parts by fused filament fabrication and solvent debinding: Selection of binder formulation. *Additive Manufacturing*, 26:117–128, March 2019.

[38] Paramjot Singh, Vamsi K. Balla, Azim Gokce, Sundar V. Atre, and Kunal H. Kate. Additive manufacturing of Ti-6Al-4V alloy by metal fused filament fabrication (MF3): producing parts comparable to that of metal injection molding. *Progress in Additive Manufacturing*, February 2021.

[39] Aghnia Ilmiah Nurhudan, Sugeng Supriadi, Yudan Whulanza, and Agung Shamsuddin Saragih. Additive manufacturing of metallic based on extrusion process: A review. *Journal of Manufacturing Processes*, 66:228–237, June 2021.

[40] PR. Selvakannan, Maciej Mazur, and Xiaochen Sun. Material Extrusion and Vat Photopolymerization—Principles, Opportunities and Challenges. In Suresh K. Bhargava, Seeram Ramakrishna, Milan Brandt, and PR. Selvakannan, editors, *Additive Manufacturing for Chemical Sciences and Engineering*, pages 53–76. Springer Nature, Singapore, September 2022.

[41] Anirudh Kasha, Solomon O. Obadimu, and Kyriakos I. Kourousis. Flexural characteristics of material extrusion steel 316L: Influence of manufacturing parameters. *Additive Manufacturing Letters*, 3:100087, December 2022.

[42] Fábio Cerejo, Daniel Gatões, and M. T. Vieira. Optimization of metallic powder filaments for additive manufacturing extrusion (MEX). *The International Journal of Advanced Manufacturing Technology*, 115(7-8):2449–2464, August 2021.

[43] Haidar Ramazani and Abdolvahed Kami. Metal FDM, a new extrusion-based additive manufacturing technology for manufacturing of metallic parts: a review. *Progress in Additive Manufacturing*, January 2022.

[44] M K Agarwala, Weeren, R. van, Bandyopadhyay, A., Whalen, P.J., Safari, A., and Danforth, S.C. Fused Deposition of Ceramics and Metals: An Overview. In *SFF Symposium Proceedings*, page 8, Texas, USA, July 1996.

[45] Stephen C. Danforth, Mukesh Agarwala, Amit Bandyopadghyay, Noshir Langrana, Vikram R. Jamalabad, Ahmad Safari, and Remco van Weeren. Solid freeform fabrication methods, April 1998.

[46] Takashi Kurose, Yoshifumi Abe, Marcelo V. A. Santos, Yota Kanaya, Akira Ishigami, Shigeo Tanaka, and Hiroshi Ito. Influence of the Layer Directions on the Properties of 316L Stainless Steel Parts Fabricated through Fused Deposition of Metals. *Materials*, 13(11):2493, May 2020.

[47] Joamin Gonzalez-Gutierrez, Santiago Cano, Stephan Schuschnigg, Clemens Holzer, and Christian Kukla. Highly-filled Polymers for Fused Filament Fabrication. In *Proceedings of the 27th Leobener Polymer Colloquium*, Leoben, Austria, April 2018. Kunststogg Technik Leoben.

[48] Ian Gibson, David Rosen, Brent Stucker, and Mahyar Khorasani. Material Extrusion. In *Additive Manufacturing Technologies*, pages 171–201. Springer International Publishing, Cham, November 2020.

[49] Joaquim Manoel Justino Netto, Amir Ilkiu Sarout, Andre Luiz Grando Santos, Alessandra de Almeida Lucas, Marcelo Aparecido Chinelatto, Jorge Lino Alves, António Gaspar-Cunha, José António Covas, and Zilda de Castro Silveira. Design and validation of an innovative 3D printer containing a co-rotating twin screw extrusion unit. *Additive Manufacturing*, 59:103192, November 2022.

[50] Sadettin Cem Altıparmak, Victoria A. Yardley, Zhusheng Shi, and Jianguo Lin. Extrusion-based additive manufacturing technologies: State of the art and future perspectives. *Journal of Manufacturing Processes*, 83:607–636, November 2022.

[51] Joamin Gonzalez-Gutierrez, Santiago Cano, Stephan Schuschnigg, Christian Kukla, Janak Sapkota, and Clemens Holzer. Additive Manufacturing of Metallic and Ceramic Components by the Material Extrusion of Highly-Filled Polymers: A Review and Future Perspectives. *Materials*, 11(5):840, May 2018.

[52] Daniel Moreno Nieto, Victor Casal López, and Sergio Ignacio Molina. Large-format polymeric pellet-based additive manufacturing for the naval industry. *Additive Manufacturing*, 23:79, July 2018.

[53] Timothy W. Womer. 'Single Screw Micro-extruder for 3D Printing', US 2017/0291364 A1, October 2017.

[54] Sunidhi Dayam, Puneet Tandon, and Satwik Priyadarshi. Development of paste extrusion-based metal additive manufacturing process. *Rapid Prototyping Journal*, 28(10):1920–1932, January 2022. Publisher: Emerald Publishing Limited.

[55] Chanun Suwanpreecha and Anchalee Manonukul. A Review on Material Extrusion Additive Manufacturing of Metal and How It Compares with Metal Injection Moulding. *Metals*, 12(3):429, February 2022.

[56] Joamin Gonzalez-Gutierrez, Florian Arbeiter, Thomas Schlauf, Christian Kukla, and Clemens Holzer. Tensile properties of sintered 17-4PH stainless steel fabricated by material extrusion additive manufacturing. *Materials Letters*, 248:165, 2019.

[57] Massimiliano Annoni, Hermes Giberti, and Matteo Strano. Feasibility Study of an Extrusion-based Direct Metal Additive Manufacturing Technique. *44th Proceedings of the North American Manufacturing Research Institution of SME*, 5:916, June 2016.

[58] Fábio José Silva Cerejo. Development of Filaments for 3D Printing of Steel Parts. Master's thesis, University of Coimbra, Portugal, July 2018.

[59] Luquan Ren, Xueli Zhou, Zhengyi Song, Che Zhao, Qingping Liu, Jingze Xue, and Xiujuan Li. Process Parameter Optimization of Extrusion-Based 3D Metal Printing Utilizing PW–LDPE–SA Binder System. *Materials*, 10(3):305, March 2017.

[60] Hermes Giberti, Enrico Fiore, and Luca Sbaglia. Kinematic synthesis of a new 3D printing solution. *MATEC Web of Conferences*, 45:04013, March 2016.

[61] Paolo Parenti, Salvatore Cataldo, and Massimiliano Annoni. Shape deposition manufacturing of 316L parts via feedstock extrusion and green-state milling. *Manufacturing Letters*, 18:6, September 2018.

[62] Jovan Radulovic. Powder injection moulding technology: Properties, possibilities and starting activities. *Scientific Technical Review*, 65(2):20, March 2015.

[63] Mahrukh Sadaf, Santiago Cano, Joamin Gonzalez-Gutierrez, Mario Bragaglia, Stephan Schuschnigg, Christian Kukla, Clemens Holzer, Lilla Vály, Michael Kitzmantel, and Francesca Nanni. Influence of Binder Composition and Material Extrusion (MEX) Parameters on the 3D Printing of Highly Filled Copper Feedstocks. *Polymers*, 14(22):4962, January 2022. Number: 22 Publisher: Multidisciplinary Digital Publishing Institute.

[64] Berenika Hausnerova, Bhimasena Nagaraj Mukund, and Daniel Sanetrnik. Rheological properties of gas and water atomized 17-4PH stainless steel MIM feedstocks: Effect of powder shape and size. *Powder Technology*, 312:152–158, May 2017.

[65] René Wick-Joliat, Martina Schroffenegger, and Dirk Penner. Multi-material ceramic material extrusion 3D printing with granulated injection molding feedstocks. *Ceramics International*, October 2022.

[66] Santiago Cano. *Development of Ceramic Feedstocks for Fused Filament Fabrication*. PhD thesis, University of Leoben, July 2020.

[67] Dayue Jiang and Fuda Ning. Additive Manufacturing of 316L Stainless Steel by a Printing-Debinding-Sintering Method: Effects of Microstructure on Fatigue Property. *Journal of Manufacturing Science and Engineering*, 143(9), April 2021.

[68] Luigi Maria Galantucci, Alessandro Pellegrini, Maria Grazia Guerra, and Fulvio Lavecchia. 3D Printing of parts using metal extrusion: an overview of shaping debinding and sintering technology. *Advanced Technologies & Materials*, 47(1):8, May 2022.

[69] Barreiros, F. M., Vieira, M. T., and Terpstra, R. A. Optimising ceramic feedstock to injection moulding. In *Key Engineering Materials*, volume 206-213, pages 281–284, Bruge, Belgium, September 2001.

[70] Xinfeng Kan, Dengcui Yang, Zhengzhi Zhao, and Jiquan Sun. 316L FFF binder development and debinding optimization. *Materials Research Express*, November 2021.

[71] Amm G. Hasib, Stanislau Niauzorau, Weiheng Xu, Sridhar Niverty, Natalya Kublik, Jason Williams, Nikhilesh Chawla, Kenan Song, and Bruno Azeredo. Rheology scaling of spherical metal powders dispersed in thermoplastics and its correlation to the extrudability of filaments for 3D printing. *Additive Manufacturing*, 41:101967, May 2021.

[72] Fulvio Lavecchia, Alessandro Pellegrini, and Luigi Maria Galantucci. Comparative study on the properties of 17-4 PH stainless steel parts made by metal fused filament fabrication process and atomic diffusion additive manufacturing. *Rapid Prototyping Journal*, ahead-of-print(ahead-of-print), January 2022.

[73] Ian Gibson, David Rosen, Brent Stucker, and Mahyar Khorasani. Materials for Additive Manufacturing. In *Additive Manufacturing Technologies*, pages 379–428. Springer International Publishing, Cham, November 2020.

[74] Telma Joana Jesus Ferreira. *Microinjection Moulding of Austenitic Stainless Steel Reinforced with Carbon Nanotubes*. PhD Thesis, University of Coimbra, Portugal, February 2018.

[75] F.M. Barreiros and M.T. Vieira. PIM of non-conventional particles. *Ceramics International*, 32(3):297–302, January 2006.

[76] Kedarnath Rane and Matteo Strano. A comprehensive review of extrusion-based additive manufacturing processes for rapid production of metallic and ceramic parts. *Advances in Manufacturing*, 7(2):155, April 2019.

[77] 'Profiles & Filaments Extrusion | NUREL Biopolymers'. https://biopolymers.nurel.com/en/products/extrusion/profiles-filaments (accessed Aug. 11, 2022).

[78] Paramjot Singh, Vamsi K. Balla, Sundar V. Atre, Randall M. German, and Kunal H. Kate. Factors affecting properties of Ti-6Al-4V alloy additive manufactured by metal fused filament fabrication. *Powder Technology*, 386:9–19, July 2021.

[79] Yvonne Thompson, Markus Polzer, Joamin Gonzalez-Gutierrez, Olga Kasian, Johannes P. Heckl, Valentin Dalbauer, Christian Kukla, and Peter J. Felfer. Fused Filament Fabrication-Based Additive Manufacturing of Commercially Pure Titanium. *Advanced Engineering Materials*, page 2100380, September 2021.

[80] Ming-Wei Wu, Zeng-Kai Huang, Chun-Feng Tseng, and Kuen-Shyang Hwang. Microstructures, mechanical properties, and fracture behaviors of metal-injection molded 17-4PH stainless steel. *Metals and Materials International*, 21(3):531–537, May 2015.

[81] Anchalee Manonukul, Sukrit Songkuea, Pongporn Moonchaleanporn, and Makiko Tange. Effect of weld line positions on the tensile deformation of two-component metal injection moulding. *International Journal of Minerals, Metallurgy, and Materials*, 24(12):1384–1393, December 2017.

[82] M. K. Agarwala, R. van Weeren, A. Bandyopadhyay, A. Safari, S. C. Danforth, and W. R. Priedeman. Filament Feed Materials for Fused Deposition Processing of Ceramics and Metals. In *SFF Symposium Proceedings*, July 1996. Accepted: 2018-11-15T20:31:27Z.

[83] Guohua Wu, Noshir A. Langrana, Rajendra Sadanji, and Stephen Danforth. Solid freeform fabrication of metal components using fused deposition of metals. *Materials & Design*, 23(1):97, September 2001.

[84] Joamin Gonzalez-Gutierrez, Damir Godec, Christian Kukla, Thomas Schlauf, Carlo Burkhardt, and Clemens Holzer. Shaping, Debinding and Sintering of Steel Components via Fused Filament Fabrication. In *Proceedings of the 16th International Scientific Conference on Production Engineering 2017*, page 6, Zagreb, Croatia, June 2017. Croatian Association of Production Engineering.

[85] Yoshifumi Abe, Takashi Kurose, Marcelo Santos, Yota Kanaya, Akira Ishigami, Shigeo Tanaka, and Hiroshi Ito. Effect of Layer Directions on Internal Structures and Tensile Properties of 17-4PH Stainless Steel Parts Fabricated by Fused Deposition of Metals. *Materials*, 14(2):243, January 2021.

[86] Chanun Suwanpreecha, Phanuphak Seensattayawong, Vorawat Vadhanakovint, and Anchalee Manonukul. Influence of Specimen Layout on 17-4PH (AISI 630) Alloys Fabricated by Low-Cost Additive Manufacturing. *Metallurgical and Materials Transactions A*, 52(5):1999–2009, May 2021.

[87] Chanun Suwanpreecha and Anchalee Manonukul. On the build orientation effect in as-printed and as-sintered bending properties of 17-4PH alloy fabricated by metal fused filament fabrication. *Rapid Prototyping Journal*, ahead-of-print(ahead-of-print), January 2022.

[88] L Castro, S Merino, B Levenfeld, A Várez, and J. M Torralba. Mechanical properties and pitting corrosion behaviour of 316L stainless steel parts obtained by a modified metal injection moulding process. *Journal of Materials Processing Technology*, 143-144:397–402, December 2003.

[89] D. F. Heaney, T. W. Mueller, and P. A. Davies. Mechanical properties of metal injection moulded 316L stainless steel using both prealloy and master alloy techniques. *Powder Metallurgy*, 47(4):367–373, December 2004. Publisher: Taylor & Francis _eprint: https://doi.org/10.1179/003258904225020855.

[90] Ming-Shyan Huang and Hung-Chuan Hsu. Effect of backbone polymer on properties of 316L stainless steel MIM compact. *Journal of Materials Processing Technology*, 209(15):5527–5535, August 2009.

[91] Ji Bin Li, Zhan Gong Xie, Xiao Hui Zhang, Qi Gao Zeng, and Hai Jun Liu. Study of Metal Powder Extrusion and Accumulating Rapid Prototyping. *Key Engineering Materials*, 443:81, June 2010.

[92] Karthikesh Gante Lokesha Renukaradhya. *Metal Filament 3D Printing of SS316L : Focusing on the printing process*. PhD thesis, KTH Royal Institute of Technology, September 2019.

[93] James Damon, Stefan Dietrich, Sasidhar Gorantla, Uwe Popp, Brando Okolo, and Volker Schulze. Process porosity and mechanical performance of fused filament fabricated 316L stainless steel. *Rapid Prototyping Journal*, 25(7):1319–1327, August 2019.

[94] Ilies Ait-Mansour, Niklas Kretzschmar, Sergei Chekurov, Mika Salmi, and Joel Rech. Design-dependent shrinkage compensation modeling and mechanical property targeting of metal FFF. *Progress in Additive Manufacturing*, 5(1):51–57, March 2020.

[95] Bin Liu, Yuxiang Wang, Ziwei Lin, and Tao Zhang. Creating metal parts by Fused Deposition Modeling and Sintering. *Materials Letters*, 263:127252, March 2020.

[96] Yun Wang, Li Zhang, Xun Li, and Zhao Yan. On hot isostatic pressing sintering of fused filament fabricated 316L stainless steel – Evaluation of microstructure, porosity, and tensile properties. *Materials Letters*, 296:129854, August 2021.

[97] Miguel Ángel Caminero, Ana Romero, Jesús Miguel Chacón, Pedro José Núñez, Eustaquio García-Plaza, and Gloria Patricia Rodríguez. Additive manufacturing of 316L stainless-steel structures using fused filament fabrication technology: mechanical and geometric properties. *Rapid Prototyping Journal*, 27(3):583–591, January 2021. Publisher: Emerald Publishing Limited.

[98] Mariangela Quarto, Mattia Carminati, and Gianluca D'Urso. Density and shrinkage evaluation of AISI 316L parts printed via FDM process. *Materials and Manufacturing Processes*, 36(13):1535–1543, October 2021. Publisher: Taylor & Francis _eprint: https://doi.org/10.1080/10426914.2021.1905830.

[99] Tobias Rosnitschek, Andressa Seefeldt, Bettina Alber-Laukant, Thomas Neumeyer, Volker Altstädt, and Stephan Tremmel. Correlations of Geometry and Infill Degree of Extrusion Additively Manufactured 316L Stainless Steel Components. *Materials*, 14(18):5173, January 2021. Number: 18 Publisher: Multidisciplinary Digital Publishing Institute.

[100] Dayue Jiang and Fuda Ning. Anisotropic deformation of 316L stainless steel overhang structures built by material extrusion based additive manufacturing. *Additive Manufacturing*, 50:102545, February 2022.

[101] S. Riecker, J. Clouse, T. Studnitzky, O. Andersen, and B. Kieback. Fused Deposition Modeling-Opportunities for cheap metal AM. In *European Congress and Exhibition on Powder Metallurgy. European PM Conference Proceedings*, Hamburg, Germany, October 2016. EPMA.

[102] Carlo Burkhardt, Peter Freigassner, Oxana Weber, Philipp Imgrund, and Stefan Hampel. Fused Filament Fabrication (FFF) of 316L Green Parts for the MIM process. In *Proceedings of the World PM2016 Congress & Exhibition*, pages 1–7, Hamburg, Germany, October 2016. EPMA.

[103] Christian Kukla, Ivica Duretek, Stephan Schuschnigg, Joamin Gonzalez-Gutierrez, and Clemens Holzer. Properties for PIM Feedstocks Used in Fused Filament Fabrication. In *Proceedings of the World PM 2016*, Hamburg, Germany, October 2016.

[104] Nestle, Nikolaus, Hermant, Marie-Claire, and Schmidt, Kris. Mixture for use in a fused filament fabrication process, January 2016.

[105] Christian Kukla, Joamin Gonzalez-Gutierrez, Santiago Cano, Stefan Hampel, Carlo Burkhardt, Tassilo Moritz, and Clemens Holzer. Fused Filament Fabrication (FFF) of PIM Feedstocks. In *Proceedings of the VI Congreso Nacional de Pulvimetalurgia y I Congreso Iberoamericano de Pulvimetalurgia*, Ciudad Real, Spain, June 2017.

[106] Christian Kukla, Joamin Gonzalez-Gutierrez, Carlo Burkhardt, Oxana Weber, and Clemens Holzer. The Production of Magnets by FFF - Fused Filament Fabrication. In *Proceedings of the EuroPM2017 - AM - Printing Technologies*, Milan, Italy, October 2017.

[107] Yvonne Thompson, Joamin Gonzalez-Gutierrez, Christian Kukla, and Peter Felfer. Fused filament fabrication, debinding and sintering as a low cost additive manufacturing method of 316L stainless steel. *Additive Manufacturing*, 30:100861, December 2019.

[108] Marius A. Wagner, Amir Hadian, Tutu Sebastian, Frank Clemens, Thomas Schweizer, Mikel Rodriguez-Arbaizar, Efrain Carreño-Morelli, and Ralph Spolenak. Fused filament fabrication of stainless steel structures - from binder development to sintered properties. *Additive Manufacturing*, page 102472, November 2021.

[109] M. Sadaf, M. Bragaglia, and F. Nanni. A simple route for additive manufacturing of 316L stainless steel via Fused Filament Fabrication. *Journal of Manufacturing Processes*, 67:141–150, July 2021.

[110] Chenming Wu, Chengkai Dai, Guoxin Fang, Yong-Jin Liu, and Charlie C.L. Wang. RoboFDM: A robotic system for support-free fabrication using FDM. In *2017 IEEE International Conference on Robotics and Automation (ICRA)*, page 1175, Singapore, Singapore, May 2017. IEEE.

[111] Diana Popescu, Aurelian Zapciu, Catalin Amza, Florin Baciu, and Rodica Marinescu. FDM process parameters influence over the mechanical properties of polymer specimens: A review. *Polymer Testing*, 69:157–166, August 2018.

[112] Claudio Tosto, Jacopo Tirillò, Fabrizio Sarasini, and Gianluca Cicala. Hybrid Metal/Polymer Filaments for Fused Filament Fabrication (FFF) to Print Metal Parts. *Applied Sciences*, 11(4):1444, February 2021.

[113] Gulshan Kaur, Ranganath M. Singari, and Harish Kumar. A review of fused filament fabrication (FFF): Process parameters and their impact on the tribological behavior of polymers (ABS). *Materials Today: Proceedings*, 51:854–860, January 2022.

[114] R. Paetzold, F. B. Coulter, G. Singh, D. J. Kelly, and E. D. O'Cearbhaill. Fused filament fabrication of polycaprolactone bioscaffolds: Influence of fabrication parameters and thermal environment on geometric fidelity and mechanical properties. *Bioprinting*, 27:e00206, August 2022.

[115] Muhammad Salman Mustafa, Muhammad Arslan Muneer, Muhammad Qasim Zafar, Muhammad Arif, Ghulam Hussain, and Farrukh Arsalan Siddiqui. Process parameter optimization for Fused Filament Fabrication additive manufacturing of PLA/PHA biodegradable polymer blend. *International Polymer Processing*, 37(1):1–14, March 2022. Publisher: De Gruyter.

[116] Armin Yousefi Kanani and Andrew Kennedy. Effect of the Material Extrusion Process Parameters on the Compressive Properties of Additively Manufactured Foamed and Nonfoamed Polylactic Acid Structures. *3D Printing and Additive Manufacturing*, July 2022. Publisher: Mary Ann Liebert, Inc., publishers.

[117] Matt Schmitt and Il Yong Kim. Topology optimization for infill in MEx. *Rapid Prototyping Journal*, 27(8):1580–1590, January 2021. Publisher: Emerald Publishing Limited.

[118] Luca Grigolato, Stefano Rosso, Roberto Meneghello, Gianmaria Concheri, and Gianpaolo Savio. Design and manufacturing of graded density components by material extrusion technologies. *Additive Manufacturing*, 57:102950, September 2022.

[119] Raphaël Comminal, Marcin P. Serdeczny, David B. Pedersen, and Jon Spangenberg. Numerical modeling of the strand deposition flow in extrusion-based additive manufacturing. *Additive Manufacturing*, 20:68–76, March 2018.

[120] Chelsea S. Davis, Kaitlyn E. Hillgartner, Seung Hoon Han, and Jonathan E. Seppala. Mechanical strength of welding zones produced by polymer extrusion additive manufacturing. *Additive Manufacturing*, 16:162, June 2017.

[121] Mercedes Pérez, Gustavo Medina-Sánchez, Alberto García-Collado, Munish Gupta, and Diego Carou. Surface Quality Enhancement of Fused Deposition Modeling (FDM) Printed Samples Based on the Selection of Critical Printing Parameters. *Materials*, 11(8):1382, August 2018.

[122] Francisco Rafael dos Reis Cruz. Additive Manufacturing and Copper. Master's thesis, University of Coimbra, Portugal, July 2019.

[123] Sandeep Kuriakose, Paolo Parenti, Salvatore Cataldo, and Massimiliano Annoni. Green-State Micromilling of Additive Manufactured AISI316 L. *Journal of Micro and Nano-Manufacturing*, 7(1):10, March 2019.

[124] S. Banerjee and C.J. Joens. Debinding and sintering of metal injection molding (MIM) components. In Donald F. Heaney, editor, *Handbook of Metal Injection Molding (Second Edition)*, pages 129–171. Woodhead Publishing, March 2019.

[125] R.M. German. Thermodynamics of sintering. In *Sintering of Advanced Materials*, pages 3–483. Elsevier, March 2010.

[126] Marius A. Wagner, Jona Engel, Amir Hadian, Frank Clemens, Mikel Rodriguez-Arbaizar, Efrain Carreño-Morelli, Jeffrey M. Wheeler, and Ralph Spolenak. Filament extrusion-based additive manufacturing of 316L stainless steel: Effects of sintering conditions on the microstructure and mechanical properties. *Additive Manufacturing*, 59:103147, November 2022.

[127] Zhigang Zak Fang. *Sintering of Advanced Materials*. Woodhead Publishing Limited, March 2010.

[128] Anchalee Manonukul, Warakij Likityingwara, Phataraporn Rungkiatnawin, Nattapol Muenya, Suttha Amoranan, Witoo Kittinantapol, and Suphachai Surapunt. Study of Recycled and Virgin Compounded Metal Injection Moulded Feedstock for Stainless Steel 630. *Journal of Solid Mechanics and Materials Engineering*, 1(4):411–420, January 2007.

[129] P.F. Jiang, C.H. Zhang, S. Zhang, J.B. Zhang, J. Chen, and H.T. Chen. Additive manufacturing of novel ferritic stainless steel by selective laser melting: Role of

laser scanning speed on the formability, microstructure and properties. *Optics & Laser Technology*, 140:107055, August 2021.

[130] Andersen, Olaf, Riecker, Sebastian, and Studnitzky, Thomas. Manufacturing and Properties of Metal Parts made by Fused Filament Fabrication. In *Studnitzky*, Bilbao Exhibition Centre (BEC) Bilbao, Spain, October 2018. EPMA.

[131] Ralf Eickhoff, Steffen Antusch, Siegfried Baumgärtner, Dorit Nötzel, and Thomas Hanemann. Feedstock Development for Material Extrusion-Based Printing of Ti6Al4V Parts. *Materials*, 15(18):6442, January 2022. Number: 18 Publisher: Multidisciplinary Digital Publishing Institute.

[132] Dongdong Gu. *Laser Additive Manufacturing of High-Performance Materials*. Springer Berlin Heidelberg, Berlin, 2015.

[133] Jingchang Li, Qi Zhou, Xufeng Huang, Menglei Li, and Longchao Cao. In situ quality inspection with layer-wise visual images based on deep transfer learning during selective laser melting. *Journal of Intelligent Manufacturing*, September 2021.

[134] 'Empa - Coating Competence Center - Selective Laser Melting (SLM)'. https://www.empa.ch/web/coating-competence-center/selective-laser-melting (accessed Oct. 18, 2022).

[135] Atefeh A. Tafti, Vincent Demers, Seyed Mohammad Majdi, Guillem Vachon, and Vladimir Brailovski. Effect of Thermal Debinding Conditions on the Sintered Density of Low-Pressure Powder Injection Molded Iron Parts. *Metals*, 11(2):264, February 2021.

[136] Chong Heng Lim, Hua Li, Manickavasagam Krishnan, Kewei Chen, and Junru Li. Investigation of the transition heat treatment temperature of AlSi10Mg manufactured by selective laser melting and the effect on the compressive strength. *Materials Today: Proceedings*, September 2022.

[137] J. Gunasekaran, P. Sevvel, and I. John Solomon. Metallic materials fabrication by selective laser melting: A review. *Materials Today: Proceedings*, 37:252–256, January 2021.

[138] Andac Ozsoy, Evren Yasa, Mert Keles, and Erkan Bugra Tureyen. Pulsed-mode Selective Laser Melting of 17-4 PH stainless steel: Effect of laser parameters on density and mechanical properties. *Journal of Manufacturing Processes*, 68:910–922, August 2021.

[139] Jae Hyeon Bae, Jong Min Yu, Van Hung Dao, Vanno Lok, and Kee Bong Yoon. Effects of processing parameters on creep behavior of 316L stainless steel produced using selective laser melting. *Journal of Mechanical Science and Technology*, 35(9):3803–3812, September 2021.

[140] Jiaqi Zhang, Minjie Wang, Liuhui Niu, Jianye Liu, Jinhai Wang, Yu Liu, and Zhenwei Shi. Effect of process parameters and heat treatment on the properties of stainless steel CX fabricated by selective laser melting. *Journal of Alloys and Compounds*, 877:160062, October 2021.

[141] Christoph Haberland. 'Additive Manufacturing: Myths, misconceptions and untruths', Metal Additive Manufacturing, Sep. 01, 2018. https://www.metal-am.com/articles/3d-printing-myths-misconceptions-and-untruths/ (accessed Aug. 09, 2022).

[142] Patiparn Ninpetch, Pruet Kowitwarangkul, Sitthipong Mahathanabodee, Prasert Chalermkarnnon, and Phadungsak Rattanadecho. Computational investigation of thermal behavior and molten metal flow with moving laser heat source for selective laser melting process. *Case Studies in Thermal Engineering*, 24:100860, April 2021.

[143] Ângela Cunha, Ana Marques, Mariana Rodrigues Silva, Flávio Bartolomeu, Filipe Samuel Silva, Michael Gasik, Bruno Trindade, and Óscar Carvalho. Laser powder bed fusion of the steels used in the plastic injection mould industry: a review of the influence of processing parameters on the final properties. *The International Journal of Advanced Manufacturing Technology*, 121(7):4255–4287, August 2022.

[144] X. Cui, S. Zhang, C. H. Zhang, J. Chen, J. B. Zhang, and S. Y. Dong. A comparison on microstructure features of 24CrNiMo low alloy steel prepared by selective laser melting and laser melting deposition. *Vacuum*, 191:110394, September 2021.

[145] Wei Yang, Xiaoxun Zhang, Fang Ma, Sensen Dong, and Juze Jiang. Selective laser melting of 1.2738 mold steel: densification, microstructure and microhardness. *Materials Research Express*, 8(1):016525, January 2021. Publisher: IOP Publishing.

[146] Adriel P. Oliveira, Luiz H. Q. R. Lima, Bianca C. A. Felipe, Claudemiro Bolfarini, Reginaldo T. Coelho, and Piter Gargarella. Effect of microstructure and defect formation on the bending properties of additive manufactured H13 tool steel. *Journal of Materials Research and Technology*, 15:3598–3609, November 2021.

[147] Gabriel Awuku Dzukey, Ke Yang, Qiuyu Wang, Bailiang Zhuang, and Wenda Hou. Porosity, Hardness, Friction and Wear Performance Analysis of H13 SLM-Formed Samples. *Journal of Materials Engineering and Performance*, August 2020.

[148] Yap, C. Y., Chua, C. K., Dong, Z. L., Liu, Z. H., Zhang, D. Q., Loh, L. E., and Sing, S. L. Review of selective laser melting: Materials and applications. *Applied Physics Reviews*, 2(4):041101, October 2015.

[149] Jiaxin Li, Zezhou Kuai, Zhonghua Li, Bin Liu, Yanlei Chen, Shengyu Lu, Yunfei Nie, and Zhicheng Yang. Effects of Process Parameters on the Relative Density and Properties of CuCrZr Alloy Produced by Selective Laser Melting. *Metals*,

12(5):701, May 2022. Number: 5 Publisher: Multidisciplinary Digital Publishing Institute.

[150] Roberta Della Gatta, Valerio Lampitella, Marco Trofa, Gaetano D'Avino, Domenico Borrelli, Antonio Caraviello, and Antonello Astarita. Reducing the energy density in Selective Laser Melting of an Al-Si-Mg-Cu alloy through an improved spreading process of the powder bed. *CIRP Journal of Manufacturing Science and Technology*, 38:813–823, August 2022.

[151] Eyob Messele Sefene. State-of-the-art of selective laser melting process: A comprehensive review. *Journal of Manufacturing Systems*, 63:250–274, April 2022.

[152] Suraj Dinkar Jadhav, Louca Raphaël Goossens, Yannis Kinds, Brecht Van Hooreweder, and Kim Vanmeensel. Laser-based powder bed fusion additive manufacturing of pure copper. *Additive Manufacturing*, 42:101990, June 2021.

[153] Xi-Huai Yang, Chong-Ming Jiang, Jeng-Rong Ho, Pi-Cheng Tung, and Chih-Kuang Lin. Effects of Laser Spot Size on the Mechanical Properties of AISI 420 Stainless Steel Fabricated by Selective Laser Melting. *Materials*, 14(16):4593, August 2021.

[154] T. Hassel, A. Beniyash, and G. Klimov. Non-vacuum electron beam welding and cutting of cupper. *IOP Conference Series: Materials Science and Engineering*, 759(1):012003, February 2020. Publisher: IOP Publishing.

[155] Sang-Woo Han, Won-Ik Cho, Lin-Jie Zhang, and Suck-Joo Na. Coupled simulation of thermal-metallurgical-mechanical behavior in laser keyhole welding of AH36 steel. *Materials & Design*, 212:110275, December 2021.

[156] Xuehui Chen, Weihao Mu, Xin Xu, Wei Liu, Lei Huang, and Hao Li. Numerical analysis of double track formation for selective laser melting of 316L stainless steel. *Applied Physics A*, 127(8):586, July 2021.

[157] Taban Larimian, Bandar AlMangour, Dariusz Grzesiak, Ganesh Walunj, and Tushar Borkar. Effect of Laser Spot Size, Scanning Strategy, Scanning Speed, and Laser Power on Microstructure and Mechanical Behavior of 316L Stainless Steel Fabricated via Selective Laser Melting. *Journal of Materials Engineering and Performance*, 31(3):2205–2224, March 2022.

[158] De Wang, Donghai Cheng, Zhangyu Zhou, Wenqin Wang, Bo Hu, Yujiang Xie, Zhenyu Xiong, and Dean Hu. Effect of laser power on the microstructure and properties of additive manufactured 17-4 PH stainless steel in different fabrication atmosphere. *Materials Science and Engineering: A*, 839:142846, April 2022.

[159] Weihao Zhang, Honglin Ma, Qi Zhang, and Shuqian Fan. Prediction of powder bed thickness by spatter detection from coaxial optical images in selective laser melting of 316L stainless steel. *Materials & Design*, 213:110301, January 2022.

[160] Guanyi Jing and Zemin Wang. Defects, densification mechanism and mechanical properties of 300M steel deposited by high power selective laser melting. *Additive Manufacturing*, 38:101831, February 2021.

[161] Dongju Chen, Peng Wang, Ri Pan, Chunqing Zha, Jinwei Fan, Shupei Li, and Kai Cheng. Process optimization of selective laser melting 316L stainless steel by a data-driven nonlinear system. *Welding in the World*, 66(3):409–422, March 2022.

[162] Antonio Collazo, Raúl Figueroa, Carmen Pérez, and Xosé Ramón Nóvoa. Effect of Laser Speed and Hatch Spacing on the Corrosion Behavior of 316L Stainless Steel Produced by Selective Laser Melting. *Materials*, 15(4):1353, January 2022. Number: 4 Publisher: Multidisciplinary Digital Publishing Institute.

[163] Zhengyan Zhang, Shun Wang, Haitao Liu, Lei Wang, and Xinyi Xiao. Effects of Hatch Distance on the Microstructure and Mechanical Anisotropy of 316 L Stainless Steel Fabricated by Laser Powder Bed Fusion. *Journal of Materials Engineering and Performance*, October 2022.

[164] Ayan Bhowmik, Wengang Zhai, Wei Zhou, and Sharon Mui Ling Nai. Characterization of carbide particle-reinforced 316L stainless steel fabricated by selective laser melting. *Materials Characterization*, 179:111360, September 2021.

[165] K. Q. Le, C. Tang, and C. H. Wong. On the study of keyhole-mode melting in selective laser melting process. *International Journal of Thermal Sciences*, 145:105992, November 2019.

[166] Subin Shrestha, Thomas Starr, and Kevin Chou. A Study of Keyhole Porosity in Selective Laser Melting: Single-Track Scanning With Micro-CT Analysis. *Journal of Manufacturing Science and Engineering*, 141(7), May 2019.

[167] Jinge Liu and Peng Wen. Metal vaporization and its influence during laser powder bed fusion process. *Materials & Design*, 215:110505, March 2022.

[168] Chang-Shuo Chang, Kuan-Ta Wu, Chang-Fu Han, Tsung-Wen Tsai, Sung-Ho Liu, and Jen-Fin Lin. Establishment of the Model Widely Valid for the Melting and Vaporization Zones in Selective Laser Melting Printings Via Experimental Verifications. *International Journal of Precision Engineering and Manufacturing-Green Technology*, 9(1):143–162, January 2022.

[169] Guohao Zhang, Jing Chen, Min Zheng, Zhenyu Yan, Xufei Lu, Xin Lin, and Weidong Huang. Element Vaporization of Ti-6Al-4V Alloy during Selective Laser Melting. *Metals*, 10(4):435, April 2020. Number: 4 Publisher: Multidisciplinary Digital Publishing Institute.

[170] Jintao Wang, Shouping Liu, Yunpeng Fang, and Zhongrui He. A short review on selective laser melting of H13 steel. *The International Journal of Advanced Manufacturing Technology*, 108(7):2453–2466, June 2020.

[171] Yuchao Bai, Cuiling Zhao, Di Wang, and Hao Wang. Evolution mechanism of surface morphology and internal hole defect of 18Ni300 maraging steel fabricated by selective laser melting. *Journal of Materials Processing Technology*, 299:117328, January 2022.

[172] S. Cacace, V. Furlan, R. Sorci, Q. Semeraro, and M. Boccadoro. Using recycled material to produce gas-atomized metal powders for additive manufacturing processes. *Journal of Cleaner Production*, page 122218, May 2020.

[173] Zachary Young, Minglei Qu, Meelap Michael Coday, Qilin Guo, Seyed Mohammad H. Hojjatzadeh, Luis I. Escano, Kamel Fezzaa, and Lianyi Chen. Effects of Particle Size Distribution with Efficient Packing on Powder Flowability and Selective Laser Melting Process. *Materials*, 15(3):705, January 2022.

[174] Mitsugu Yamaguchi, Tatsuaki Furumoto, Yuuya Tanabe, Shinnosuke Yamada, Mototsugu Osaki, Yohei Hashimoto, Tomohiro Koyano, and Akira Hosokawa. Effects of the powder morphology, size distribution, and characteristics on the single track formation in selective laser melting of H13 steel. *Journal of Advanced Mechanical Design, Systems, and Manufacturing*, 15(3):1–13, June 2021.

[175] Hang Qi, Xianglin Zhou, Jinghao Li, Yunfei Hu, and Lianghui Xu. Performance Testing and Rapid Solidification Behavior of Stainless Steel Powders Prepared by Gas Atomization. *Materials*, 14(18):5188, January 2021. Number: 18 Publisher: Multidisciplinary Digital Publishing Institute.

[176] M. Chemkhi, J. Marae Djouda, M.A. Bouaziz, J. Kauffmann, F. Hild, and D. Retraint. Effects of Mechanical Post-Treatments on Additive Manufactured 17-4PH Stainless Steel Produced by Bound Powder Extrusion. *Procedia CIRP*, 104:957–961, 2021.

[177] Marius Hilzenthaler, Luca Bifano, Florian Scherm, Gerhard Fischerauer, Andrea Seemann, and Uwe Glatzel. Characterization of recycled AISI 904L superaustenitic steel powder and influence on selective laser melted parts. *Powder Technology*, 391:57–68, October 2021.

[178] Tatiana Fedina, Jesper Sundqvist, and Alexander F. H. Kaplan. Spattering and oxidation phenomena during recycling of low alloy steel powder in Laser Powder Bed Fusion. *Materials Today Communications*, 27:102241, June 2021.

[179] Harikrishnan Ramadas, Sagar Sarkar, Angshuman Chattopadhyay, and Ashish Kumar Nath. Effect of Morphology and Particle Size Distribution on the Reusability of 15-5 Precipitation Hardening Stainless Steel Powder in Laser Powder Bed Fusion Process. In Saroj Kumar Acharya and Dipti Prasad Mishra, editors, *Current Advances in Mechanical Engineering*, Lecture Notes in Mechanical Engineering, pages 817–824, Singapore, 2021. Springer.

[180] Shihua Li, Bo Chen, Caiwang Tan, and Xiaoguo Song. Study on Recyclability of 316L Stainless Steel Powder by Using Laser Directed Energy Deposition. *Journal of Materials Engineering and Performance*, 31(1):400–409, January 2022.

[181] Seyeon Hwang, Sangsup An, Ubaldo Robles, and Raymond C. Rumpf. Process parameter optimization for removable partial denture frameworks manufactured by selective laser melting. *The Journal of Prosthetic Dentistry*, June 2021.

[182] Zafer Cagatay Oter and Mert Coskun. Effect of Building Platform Position on the Surface Quality, Dimensional Accuracy, and Geometrical Precision of Direct Metal Laser Sintering (DMLS) Parts, February 2021.

[183] R. E. Napolitano, S. Jain, C. Sobczak, B. A. Augustine, and E. M. Johnson. Build Optimization for Selective Laser Melting of 316L Stainless Steel and Parameterization for Cross-Material Comparison and Process Design. *Journal of Materials Engineering and Performance*, 30(7):5491–5505, July 2021.

[184] P. Didier, G. Le Coz, G. Robin, P. Lohmuller, B. Piotrowski, A. Moufki, and P. Laheurte. Consideration of SLM additive manufacturing supports on the stability of flexible structures in finish milling. *Journal of Manufacturing Processes*, 62:213–220, February 2021.

[185] Mattia Mele, André Bergmann, Giampaolo Campana, and Tony Pilz. Experimental investigation into the effect of supports and overhangs on accuracy and roughness in laser powder bed fusion. *Optics & Laser Technology*, 140:107024, August 2021.

[186] Haolin Jia, Hua Sun, Hongze Wang, Yi Wu, and Haowei Wang. Scanning strategy in selective laser melting (SLM): a review. *The International Journal of Advanced Manufacturing Technology*, 113(9):2413–2435, April 2021.

[187] Toshi-Taka Ikeshoji, Kazuya Nakamura, Makiko Yonehara, Ken Imai, and Hideki Kyogoku. Selective Laser Melting of Pure Copper. *JOM*, 70(3):396–400, March 2018.

[188] Xingchen Yan, Cheng Chang, Dongdong Dong, Shuohong Gao, Wenyou Ma, Min Liu, Hanlin Liao, and Shuo Yin. Microstructure and mechanical properties of pure copper manufactured by selective laser melting. *Materials Science and Engineering: A*, 789:139615, July 2020.

[189] Jian Huang, Xingchen Yan, Cheng Chang, Yingchun Xie, Wenyou Ma, Renzhong Huang, Ruimin Zhao, Shunhua Li, Min Liu, and Hanlin Liao. Pure copper components fabricated by cold spray (CS) and selective laser melting (SLM) technology. *Surface and Coatings Technology*, 395:125936, August 2020.

[190] Xia Lingqin, Chen Guang, Zheng Luyu, and Lu Pan. Explore the feasibility of fabricating pure copper parts with low-laser energy by selective laser melting. *Materials Research Express*, 7(10):106509, October 2020.

[191] Loic Constantin, Zhipeng Wu, Nan Li, Lisha Fan, Jean-François Silvain, and Yong Feng Lu. Laser 3D printing of complex copper structures. *Additive Manufacturing*, 35:101268, October 2020.

[192] Ken Imai, Toshi-Taka Ikeshoji, Yuji Sugitani, and Hideki Kyogoku. Densification of pure copper by selective laser melting process. *Mechanical Engineering Journal*, 7(2):19–00272–19–00272, 2020.

[193] Peng Yang, Xingye Guo, Dingyong He, Zhen Tan, Wei Shao, and Hanguang Fu. Selective Laser Melting of High Relative Density and High Strength Parts Made of Minor Surface Oxidation Treated Pure Copper Powder. *Metals*, 11(12):1883, November 2021.

[194] Zhibo Ma, Kaifei Zhang, Zhihao Ren, David Z. Zhang, Guibao Tao, and Haisheng Xu. Selective laser melting of Cu–Cr–Zr copper alloy: Parameter optimization, microstructure and mechanical properties. *Journal of Alloys and Compounds*, 828:154350, July 2020.

[195] Zhihao Ren, David Z. Zhang, Guang Fu, Junjie Jiang, and Miao Zhao. High-fidelity modelling of selective laser melting copper alloy: Laser reflection behavior and thermal-fluid dynamics. *Materials & Design*, 207:109857, September 2021.

[196] Gengming Zhang, Chao Chen, Xiaojun Wang, Pengwei Wang, Xiaoyong Zhang, Xueping Gan, and Kechao Zhou. Additive manufacturing of fine-structured copper alloy by selective laser melting of pre-alloyed Cu-15Ni-8Sn powder. *The International Journal of Advanced Manufacturing Technology*, 96(9):4223–4230, June 2018.

[197] I.A. Polozov, E.V. Borisov, V.Sh. Sufiiarov, and A.A. Popovich. Selective laser melting of copper alloy. *Material Physics and Mechanics*, 43:65–71, November 2019. Publisher: Peter the Great St. Petersburg Polytechnic University.

[198] Subrata Deb Nath, Harish Irrinki, Gautam Gupta, Martin Kearns, Ozkan Gulsoy, and Sundar Atre. Microstructure-property relationships of 420 stainless steel fabricated by laser-powder bed fusion. *Powder Technology*, 343:738–746, February 2019.

[199] G. Sander, S. Thomas, V. Cruz, M. Jurg, N. Birbilis, X. Gao, M. Brameld, and C. R. Hutchinson. On The Corrosion and Metastable Pitting Characteristics of 316L Stainless Steel Produced by Selective Laser Melting. *Journal of The Electrochemical Society*, 164(6):C250, March 2017. Publisher: IOP Publishing.

[200] Di Wang, Shibiao Wu, Yongqiang Yang, Wenhao Dou, Shishi Deng, Zhi Wang, and Sheng Li. The Effect of a Scanning Strategy on the Residual Stress of 316L Steel Parts Fabricated by Selective Laser Melting (SLM). *Materials*, 11(10):1821, October 2018. Number: 10 Publisher: Multidisciplinary Digital Publishing Institute.

[201] Decheng Kong, Xiaoqing Ni, Chaofang Dong, Xiaowei Lei, Liang Zhang, Cheng Man, Jizheng Yao, Xuequn Cheng, and Xiaogang Li. Bio-functional and anti-corrosive 3D printing 316L stainless steel fabricated by selective laser melting. *Materials & Design*, 152:88–101, August 2018.

[202] Mostafa Yakout, M. A. Elbestawi, and Stephen C. Veldhuis. A study of thermal expansion coefficients and microstructure during selective laser melting of Invar 36 and stainless steel 316L. *Additive Manufacturing*, 24:405–418, December 2018.

[203] Xue Wang, Liping Zhao, Jerry Ying Hsi Fuh, and Heow Pueh Lee. Experimental characterization and micromechanical-statistical modeling of 316L stainless steel processed by selective laser melting. *Computational Materials Science*, 177:109595, May 2020.

[204] Jacob C. Simmons, Xiaobo Chen, Arad Azizi, Matthias A. Daeumer, Peter Y. Zavalij, Guangwen Zhou, and Scott N. Schiffres. Influence of processing and microstructure on the local and bulk thermal conductivity of selective laser melted 316L stainless steel. *Additive Manufacturing*, 32:100996, March 2020.

[205] Jithin James Marattukalam, Dennis Karlsson, Victor Pacheco, Přemysl Beran, Urban Wiklund, Ulf Jansson, Björgvin Hjörvarsson, and Martin Sahlberg. The effect of laser scanning strategies on texture, mechanical properties, and site-specific grain orientation in selective laser melted 316L SS. *Materials & Design*, 193:108852, August 2020.

[206] Dengcui Yang, Yanjun Yin, Xinfeng Kan, Yan Zhao, Zhengzhi Zhao, and Jiquan Sun. The mechanism of substructure formation and grain growth 316L stainless steel by selective laser melting. *Materials Research Express*, 8(9):096510, September 2021.

[207] Joseph J. Sopcisak, Mingxi Ouyang, Duane A. Macatangay, Brendan P. Croom, Timothy J. Montalbano, David J. Sprouster, Robert G. Kelly, Jason R. Trelewicz, Rengaswamy Srinivasan, and Steven M. Storck. Improving the Pitting Corrosion Performance of Additively Manufactured 316L Steel Via Optimized Selective Laser Melting Processing Parameters. *JOM*, 74(4):1719–1729, April 2022.

[208] Hengfeng Gu, Haijun Gong, Deepankar Pal, Khalid Rafi, Thomas Starr, and Brent Stucker. Influences of Energy Density on Porosity and Microstructure of Selective Laser Melted 17- 4PH Stainless Steel. In *SFF Symposium Proceedings*. University of Texas at Austin, July 2013. Accepted: 2021-10-11T20:40:39Z.

[209] H. Khalid Rafi, Deepankar Pal, Nachiket Patil, Thomas L. Starr, and Brent E. Stucker. Microstructure and Mechanical Behavior of 17-4 Precipitation Hardenable Steel Processed by Selective Laser Melting. *Journal of Materials Engineering and Performance*, 23(12):4421–4428, December 2014.

[210] A. Stashkov, E. Schapova, T. Tsar'kova, E. Sazhina, V. Bychenok, A. Fedorov, A. Kaigorodov, and I. Ezhov. Magnetic, electric properties and hardness of 17-4 PH stainless steel fabricated by selective laser melting. *Journal of Physics: Conference Series*, 1389(1):012124, November 2019. Publisher: IOP Publishing.

[211] Chuanli Yu, Zhiyong Huang, Zian Zhang, Jian Wang, Jiebin Shen, and Zhiping Xu. Effects of sandblasting and HIP on very high cycle fatigue performance of

SLM-fabricated IN718 superalloy. *Journal of Materials Research and Technology*, 18:29–43, May 2022.

[212] Jino Joshy, Allan George, Basil Kuriachen, and Jose Mathew. Influence of post processing on the micro-machinability of selective laser melted AlSi10Mg: an experimental investigation. *Materials and Manufacturing Processes*, 0(0):1–13, May 2022. Publisher: Taylor & Francis _eprint: https://doi.org/10.1080/10426914.2022.2075886.

[213] Johannes Kunz, Simone Herzog, Anke Kaletsch, and Christoph Broeckmann. Influence of initial defect density on mechanical properties of AISI H13 hot-work tool steel produced by laser powder bed fusion and hot isostatic pressing. *Powder Metallurgy*, 65(1):1–12, January 2022. Publisher: Taylor & Francis _eprint: https://doi.org/10.1080/00325899.2021.1934634.

[214] A. du Plessis and E. Macdonald. Hot isostatic pressing in metal additive manufacturing: X-ray tomography reveals details of pore closure. *Additive Manufacturing*, page 101191, April 2020.

[215] M. Åsberg, G. Fredriksson, S. Hatami, W. Fredriksson, and P. Krakhmalev. Influence of post treatment on microstructure, porosity and mechanical properties of additive manufactured H13 tool steel. *Materials Science and Engineering: A*, 742:584–589, January 2019.

[216] M. Krinitcyn, N. Toropkov, A. Pervikov, and M. Lerner. Structure and mechanical properties of Fe-10Cu alloy obtained by material extrusion-based additive manufacturing method with bimodal powder. *Powder Technology*, 406:117593, July 2022.

[217] Paramjot Singh, Vamsi K. Balla, Alireza Tofangchi, Sundar V. Atre, and Kunal H. Kate. Printability studies of Ti-6Al-4V by metal fused filament fabrication (MF3). *International Journal of Refractory Metals and Hard Materials*, 91:105249, September 2020.

[218] Marc-Antoine de Pastre, Yann Quinsat, and Claire Lartigue. Effects of additive manufacturing processes on part defects and properties: a classification review. *International Journal on Interactive Design and Manufacturing (IJIDeM)*, February 2022.

[219] Youssef AbouelNour and Nikhil Gupta. In-situ monitoring of sub-surface and internal defects in additive manufacturing: A review. *Materials & Design*, 222:111063, October 2022.

[220] Saveria Spiller, Filippo Berto, and Seyed Mohammad Javad Razavi. Mechanical behavior of Material Extrusion Additive Manufactured components: an overview. *Procedia Structural Integrity*, 41:158–174, 2022.

[221] Yubo Tao, Fangong Kong, Zelong Li, Jingfa Zhang, Xin Zhao, Qing Yin, Dan Xing, and Peng Li. A review on voids of 3D printed parts by fused filament fabrication. *Journal of Materials Research and Technology*, page S2238785421012448, October 2021.

[222] Weiheng Xu, Sayli Jambhulkar, Yuxiang Zhu, Dharneedar Ravichandran, Mounika Kakarla, Brent Vernon, David G. Lott, Jeffrey L. Cornella, Orit Shefi, Guillaume Miquelard-Garnier, Yang Yang, and Kenan Song. 3D printing for polymer/particle-based processing: A review. *Composites Part B: Engineering*, 223:109102, October 2021.

[223] Joamin Gonzalez-Gutierrez, Santiago Cano, Josef Valentin Ecker, Michael Kitzmantel, Florian Arbeiter, Christian Kukla, and Clemens Holzer. Bending Properties of Lightweight Copper Specimens with Different Infill Patterns Produced by Material Extrusion Additive Manufacturing, Solvent Debinding and Sintering. *Applied Sciences*, 11(16):7262, January 2021. Number: 16 Publisher: Multidisciplinary Digital Publishing Institute.

[224] Slawomir Kedziora, Thierry Decker, Elvin Museyibov, Julian Morbach, Steven Hohmann, Adrian Huwer, and Michael Wahl. Strength Properties of 316L and 17-4 PH Stainless Steel Produced with Additive Manufacturing. *Materials*, 15(18):6278, January 2022. Number: 18 Publisher: Multidisciplinary Digital Publishing Institute.

[225] Lennart Waalkes, Jan Längerich, Philipp Imgrund, and Claus Emmelmann. Piston-Based Material Extrusion of Ti-6Al-4V Feedstock for Complementary Use in Metal Injection Molding. *Materials*, 15(1):351, January 2022. Number: 1 Publisher: Multidisciplinary Digital Publishing Institute.

[226] Paolo Parenti, Dario Puccio, Bianca Maria Colosimo, and Quirico Semeraro. A new solution for assessing the printability of 17-4 PH gyroids produced via extrusion-based metal AM. *Journal of Manufacturing Processes*, 74:557–572, February 2022.

[227] Vahid Momeni, Zahra Shahroodi, Christian Kukla, and Clemens Holzer. Developing a Feedstock for the Fused Filament Fabrication (FFF) of Aluminium. *Conference: 2nd International Conference on Polymer Process Innovation*, September 2022.

[228] Amir Hadian, Leonard Koch, Philipp Koberg, Fateme Sarraf, Antje Liersch, Tutu Sebastian, and Frank Clemens. Material extrusion based additive manufacturing of large zirconia structures using filaments with ethylene vinyl acetate based binder composition. *Additive Manufacturing*, 47:102227, November 2021.

[229] Gurminder Singh, Jean-Michel Missiaen, Didier Bouvard, and Jean-Marc Chaix. Additive manufacturing of 17–4 PH steel using metal injection molding feedstock: Analysis of 3D extrusion printing, debinding and sintering. *Additive Manufacturing*, 47:102287, November 2021.

[230] J. Vetter, F. Huber, S. Wachter, C. Körner, and M. Schmidt. Development of a Material Extrusion Additive Manufacturing Process of 1.2083 steel comprising FFF Printing, Solvent and Thermal Debinding and Sintering. *Procedia CIRP*, 113:341–346, 2022.

[231] Antonio Cañadilla, Ana Romero, Gloria P. Rodríguez, Miguel Á Caminero, and Óscar J. Dura. Mechanical, Electrical, and Thermal Characterization of Pure Copper Parts Manufactured via Material Extrusion Additive Manufacturing. *Materials*, 15(13):4644, January 2022. Number: 13 Publisher: Multidisciplinary Digital Publishing Institute.

[232] Sara Nasiri and Mohammad Reza Khosravani. Machine learning in predicting mechanical behavior of additively manufactured parts. *Journal of Materials Research and Technology*, 14:1137–1153, September 2021.

[233] Gowtham Soundarapandiyan, Carol Johnston, Raja H.U. Khan, Bo Chen, and Michael E. Fitzpatrick. A technical review of the challenges of powder recycling in the laser powder bed fusion additive manufacturing process. *The Journal of Engineering*, 2021(2):97–103, February 2021.

[234] Austin T. Sutton, Caitlin S. Kriewall, Sreekar Karnati, Ming C. Leu, and Joseph W. Newkirk. Characterization of AISI 304L stainless steel powder recycled in the laser powder-bed fusion process. *Additive Manufacturing*, 32:100981, March 2020.

[235] J. Boes, A. Röttger, W. Theisen, C. Cui, V. Uhlenwinkel, A. Schulz, H.-W. Zoch, F. Stern, J. Tenkamp, and F. Walther. Gas atomization and laser additive manufacturing of nitrogen-alloyed martensitic stainless steel. *Additive Manufacturing*, 34:101379, August 2020.

[236] F.C. Pinto, I.R. Souza Filho, M.J.R. Sandim, and H.R.Z. Sandim. Defects in parts manufactured by selective laser melting caused by δ-ferrite in reused 316L steel powder feedstock. *Additive Manufacturing*, 31:100979, January 2020.

[237] Laura Cordova, Mónica Campos, and Tiedo Tinga. Revealing the Effects of Powder Reuse for Selective Laser Melting by Powder Characterization. *JOM*, 71(3):1062–1072, March 2019.

[238] V. B. Vukkum and R. K. Gupta. Review on corrosion performance of laser powder-bed fusion printed 316L stainless steel: Effect of processing parameters, manufacturing defects, post-processing, feedstock, and microstructure. *Materials & Design*, 221:110874, September 2022.

[239] Daniel Powell, Allan Rennie, Louise Geekie, and Neil Burns. Understanding powder degradation in metal additive manufacturing to allow the upcycling of recycled powders. *Journal of Cleaner Production*, page 122077, May 2020.

[240] Zahraa Lotfi, Amir Mostafapur, and Ahmad Barari. Properties of Metal Extrusion Additive Manufacturing and Its Application in Digital Supply Chain Management. *IFAC-PapersOnLine*, 54(1):199–204, 2021.

[241] Konrad Gruber, Irina Smolina, Marcin Kasprowicz, and Tomasz Kurzynowski. Evaluation of Inconel 718 Metallic Powder to Optimize the Reuse of Powder and to Improve the Performance and Sustainability of the Laser Powder Bed Fusion (LPBF) Process. *Materials*, 14(6):1538, March 2021.

[242] Shihua Wang and Baoxi Xu. Calibrated X-ray computed tomography for testing micro-scale pore defect in metallic powder particles for additive manufacturing. *Measurement: Sensors*, 18:100110, December 2021.

[243] Debomita Basu, Ziheng Wu, John L. L. Meyer, Elizabeth Larson, Robin Kuo, and Anthony Rollett. Entrapped Gas and Process Parameter-Induced Porosity Formation in Additively Manufactured 17-4 PH Stainless Steel. *Journal of Materials Engineering and Performance*, 30(7):5195–5202, July 2021.

[244] Muhannad Ahmed Obeidi, Andre Mussatto, Robert Groarke, Rajani K. Vijayaraghavan, Alex Conway, Frederico Rossi Kaschel, Eanna McCarthy, Owen Clarkin, Robert O'Connor, and Dermot Brabazon. Comprehensive assessment of spatter material generated during selective laser melting of stainless steel. *Materials Today Communications*, 25:101294, December 2020.

[245] Michael Katancik, Saereh Mirzababaei, Milad Ghayoor, and Somayeh Pasebani. Selective laser melting and tempering of H13 tool steel for rapid tooling applications. *Journal of Alloys and Compounds*, 849:156319, December 2020.

[246] Majid Laleh, Anthony E. Hughes, Sam Yang, Jiangting Wang, Jianli Li, A. Matt Glenn, Wei Xu, and Mike Y. Tan. A critical insight into lack-of-fusion pore structures in additively manufactured stainless steel. *Additive Manufacturing*, 38:101762, February 2021.

[247] Ankur K. Agrawal and Dan J. Thoma. High-throughput surface characterization to identify porosity defects in additively manufactured 316L stainless steel. *Additive Manufacturing Letters*, 3:100093, December 2022.

[248] Elliott Jost, John Miers, Aron Robinsont, David Mooret, and Christopher Sa. Effects of Spatial Energy Distribution-Induced Porosity on Mechanical Properties of Laser Powder Bed Fusion 316 L Stainless Steel. In *SFF Symposium Proceedings*, volume 39, page 15, August 2021.

[249] Chenghong Duan, Minghuang Zhao, and Xiangpeng Luo. Study on typical defects and cracking characteristics of tool steel fabricated by laser 3D printing. *IOP Conference Series: Earth and Environmental Science*, 714(3):032026, March 2021.

[250] Olivier Andreau, Etienne Pessard, Imade Koutiri, Patrice Peyre, and Nicolas Saintier. Influence of the position and size of various deterministic defects on the high cycle fatigue resistance of a 316L steel manufactured by laser powder bed fusion. *International Journal of Fatigue*, 143:105930, February 2021.

[251] Yingyu Wang and Zhenli Su. Effect of micro-defects on fatigue lifetime of additive manufactured 316L stainless steel under multiaxial loading. *Theoretical and Applied Fracture Mechanics*, 111:102849, February 2021.

[252] Hua-Zhen Jiang, Zheng-Yang Li, Tao Feng, Peng-Yue Wu, Qi-Sheng Chen, Yun-Long Feng, Long-Fei Chen, Jing-Yu Hou, and He-Jian Xu. Effect of Process Parameters on Defects, Melt Pool Shape, Microstructure, and Tensile Behavior of 316L Stainless Steel Produced by Selective Laser Melting. *Acta Metallurgica Sinica (English Letters)*, 34(4):495–510, April 2021.

[253] Zeki Azakli and Recep Gümrük. Particle Erosion Performance of Additive Manufactured 316L Stainless Steel Materials. *Tribology Letters*, 69(4):130, December 2021.

[254] Aniket K. Dutt, G. K. Bansal, S. Tripathy, K. Gopala Krishna, V. C. Srivastava, and S. Ghosh Chowdhury. Optimization of Selective Laser Melting (SLM) Additive Manufacturing Process Parameters of 316L Austenitic Stainless Steel. *Transactions of the Indian Institute of Metals*, July 2022.

[255] Filip Véle, Michal Ackermann, Václav Bittner, and Jiří Šafka. Influence of Selective Laser Melting Technology Process Parameters on Porosity and Hardness of AISI H13 Tool Steel: Statistical Approach. *Materials*, 14(20):6052, October 2021.

[256] Ruidi Li, Jinhui Liu, Yusheng Shi, Li Wang, and Wei Jiang. Balling behavior of stainless steel and nickel powder during selective laser melting process. *The International Journal of Advanced Manufacturing Technology*, 59(9-12):1025–1035, April 2012.

[257] Andelle D. Kudzal, Brandon A. McWilliams, Josh Taggart-Scarff, and Marko Knezevic. Fabrication of a low alloy ultra-high strength (>1500 MPa yield) steel using powder bed fusion additive manufacturing. *Materials Science and Engineering: A*, 770:138512, January 2020.

[258] A. Damiens, H. Bonnefoy, and I. Titeux. Influence of processing parameters on mechanical and fatigue properties of 316 L steel manufactured by selective laser melting. *Welding in the World*, 64(8):1321–1328, August 2020.

[259] Aeriel D. Murphy-Leonard, Darren C. Pagan, Patrick G. Callahan, Zach K. Heinkel, Christopher E. Jasien, and David J. Rowenhorst. Investigation of porosity, texture, and deformation behavior using high energy X-rays during in-situ tensile loading in additively manufactured 316L stainless steel. *Materials Science and Engineering: A*, 810:141034, April 2021.

[260] Greg N. Nigon, O. Burkan Isgor, and Somayeh Pasebani. The effect of annealing on the selective laser melting of 2205 duplex stainless steel: Microstructure, grain orientation, and manufacturing challenges. *Optics & Laser Technology*, 134:106643, February 2021.

[261] Haijun Gong, Hengfeng Gu, Kai Zeng, J.j.s Dilip, Deepankar Pal, Brent Stucker, Daniel Christiansen, Jack Beuth, and John Lewandowski. Melt Pool Characterization for Selective Laser Melting of Ti-6Al-4V Pre-alloyed Powder. In *SFF Symposium Proceedings*, July 2014.

[262] Tomasz Kozior, Jerzy Bochnia, Paweł Zmarzły, Damian Gogolewski, and Thomas G. Mathia. Waviness of Freeform Surface Characterizations from Austenitic Stainless Steel (316L) Manufactured by 3D Printing-Selective Laser Melting (SLM) Technology. *Materials*, 13(19):4372, September 2020.

[263] Christian Weingarten, Damien Buchbinder, Norbert Pirch, Wilhelm Meiners, Konrad Wissenbach, and Reinhart Poprawe. Formation and reduction of hydrogen porosity during selective laser melting of AlSi10Mg. *Journal of Materials Processing Technology*, 221:112–120, July 2015.

[264] Gyung Bae Bang, Young Jae Hwang, Won Rae Kim, Yeong Hwan Song, Gun Hee Kim, Soong-Keun Hyun, Sung Chul Cha, Heon Joon Park, Taeg Woo Lee, and Hyung Giun Kim. Microstructural and mechanical properties of AISI 440C stainless steel fabricated using selective laser melting. *Materials Science and Engineering: A*, 860:144259, December 2022.

[265] Sara Giganto, Susana Martínez-Pellitero, Joaquín Barreiro, Paola Leo, and Mª Ángeles Castro-Sastre. Impact of the laser scanning strategy on the quality of 17-4PH stainless steel parts manufactured by selective laser melting. *Journal of Materials Research and Technology*, 20:2734–2747, September 2022.

[266] Saad Waqar, Kai Guo, and Jie Sun. Evolution of residual stress behavior in selective laser melting (SLM) of 316L stainless steel through preheating and in-situ re-scanning techniques. *Optics & Laser Technology*, 149:107806, May 2022.

[267] Zhen Zhang, Zhanyong Zhao, Xiaofeng Li, Liqing Wang, Bin Liu, and Peikang Bai. Effect of heat treatments on metastable pitting of 316L stainless steel fabricated by selective laser melting. *Journal of Materials Research and Technology*, 21:1903–1914, November 2022.

[268] Xin Yang, Wen-jun Ma, Yao-jia Ren, Shi-feng Liu, Yan Wang, Wan-lin Wang, and Hui-ping Tang. Subgrain microstructures and tensile properties of 316L stainless steel manufactured by selective laser melting. *Journal of Iron and Steel Research International*, 28(9):1159–1167, September 2021.

[269] Qi Shi, Feng Qin, Kefeng Li, Xin Liu, and Ge Zhou. Effect of hot isostatic pressing on the microstructure and mechanical properties of 17-4PH stainless steel parts fabricated by selective laser melting. *Materials Science and Engineering: A*, 810:141035, April 2021.

[270] Alcide Bertocco, Gianluca Iannitti, Antonio Caraviello, and Luca Esposito. Lattice structures in stainless steel 17-4PH manufactured via selective laser melting (SLM) process: dimensional accuracy, satellites formation, compressive response

and printing parameters optimization. *The International Journal of Advanced Manufacturing Technology*, 120(7):4935–4949, June 2022.

[271] Tianlin Zhong, Ketai He, Huaixue Li, and Lechang Yang. Mechanical properties of lightweight 316L stainless steel lattice structures fabricated by selective laser melting. *Materials & Design*, 181:108076, November 2019.

[272] Tatsuaki Furumoto, Kyota Egashira, Kazushi Oishi, Satoshi Abe, Mitsugu Yamaguchi, Yohei Hashimoto, Tomohiro Koyano, and Akira Hosokawa. Experimental investigation into the spatter particle behavior of maraging steel during selective laser melting. *Journal of Advanced Mechanical Design, Systems, and Manufacturing*, 15(4):JAMDSM0039–JAMDSM0039, 2021.

[273] Dongdong Dong, Cheng Chang, Hao Wang, Xingchen Yan, Wenyou Ma, Min Liu, Sihao Deng, Julien Gardan, Rodolphe Bolot, and Hanlin Liao. Selective laser melting (SLM) of CX stainless steel: Theoretical calculation, process optimization and strengthening mechanism. *Journal of Materials Science & Technology*, 73:151–164, May 2021.

[274] A. Toma, R. Condruz, R. Carlanescu, and I. Daniel. A mini-review on non-destructive techniques for additive manufactured metal parts. *AIP Conference Proceedings*, 2302(1):060017, December 2020. Publisher: American Institute of Physics.

[275] ASTM, 'Nondestructive Testing Standards - Standards Products - Standards & Publications - Products & Services'. https://www.astm.org/products-services/standards-and-publications/standards/nondestructive-testing-standards.html (accessed Nov. 09, 2022).

[276] Andrzej Pacana and Karolina Czerwińska. Model of Diagnosing and Searching for Incompatibilities in Aluminium Castings. *Materials*, 14(21):6497, January 2021. Number: 21 Publisher: Multidisciplinary Digital Publishing Institute.

[277] P. S. Gowthaman and S. Jeyakumar. A critical review on non-destructive evaluation on additive manufacturing components. *AIP Conference Proceedings*, 2460(1):020008, August 2022. Publisher: American Institute of Physics.

[278] Alessandro Pellegrini, Maria Emanuela Palmieri, and Maria Grazia Guerra. Evaluation of anisotropic mechanical behaviour of 316L parts realized by metal fused filament fabrication using digital image correlation. *The International Journal of Advanced Manufacturing Technology*, 120(11-12):7951–7965, June 2022.

[279] Valdemar R. Duarte, Tiago A. Rodrigues, Miguel A. Machado, João P.M. Pragana, Pedro Pombinha, Luísa Coutinho, Carlos M.A. Silva, Rosa M. Miranda, Carley Goodwin, Daniel E. Huber, Joao P. Oliveira, and Telmo G. Santos. Benchmarking of Nondestructive Testing for Additive Manufacturing. *3D Printing and Additive Manufacturing*, 8(4):263–270, August 2021. Publisher: Mary Ann Liebert, Inc., publishers.

[280] Masoud Shaloo, Martin Schnall, Thomas Klein, Norbert Huber, and Bernhard Reitinger. A Review of Non-Destructive Testing (NDT) Techniques for Defect Detection: Application to Fusion Welding and Future Wire Arc Additive Manufacturing Processes. *Materials*, 15(10):3697, January 2022. Number: 10 Publisher: Multidisciplinary Digital Publishing Institute.

[281] Andreea Ioana Sacarea, Gheorghe Oancea, and Luminita Parv. Magnetic Particle Inspection Optimization Solution within the Frame of NDT 4.0. *Processes*, 9(6):1067, June 2021. Number: 6 Publisher: Multidisciplinary Digital Publishing Institute.

[282] Marvin A. Spurek, Adriaan B. Spierings, Marc Lany, Bernard Revaz, Gilles Santi, Jonatan Wicht, and Konrad Wegener. In-situ monitoring of powder bed fusion of metals using eddy current testing. *Additive Manufacturing*, page 103259, November 2022.

[283] Philipp Stoll, Enrico Gasparin, Adriaan Spierings, and Konrad Wegener. Embedding eddy current sensors into LPBF components for structural health monitoring. *Progress in Additive Manufacturing*, 6(3):445–453, August 2021.

[284] Heba E. Farag, Ehsan Toyserkani, and Mir Behrad Khamesee. Non-Destructive Testing Using Eddy Current Sensors for Defect Detection in Additively Manufactured Titanium and Stainless-Steel Parts. *Sensors*, 22(14):5440, January 2022. Number: 14 Publisher: Multidisciplinary Digital Publishing Institute.

[285] Juan Carlos Pereira, Fidel Zubiri, Maria Jose Garmendia, Mikel Tena, Haizea Gonzalez, and Luis Norberto López de Lacalle. Study of laser metal deposition additive manufacturing, CNC milling, and NDT ultrasonic inspection of IN718 alloy preforms. *The International Journal of Advanced Manufacturing Technology*, 120(3):2385–2406, May 2022.

[286] Kazufumi Nomura, Taketo Matsuida, Satoshi Otaki, and Satoru Asai. Fundamental study of the quality measurement for wire arc additive manufacturing process by laser ultrasonic technique. *Welding in the World*, 66(11):2271–2280, November 2022.

[287] Jun Zhang, Xin Zhao, Bing Yang, Jingyu Li, Yan Liu, Guanbing Ma, Shuxian Yuan, and Jinfeng Wu. Nondestructive evaluation of porosity in additive manufacturing by laser ultrasonic surface wave. *Measurement*, 193:110944, April 2022.

[288] A.-F. Obaton, Y. Wang, B. Butsch, and Q. Huang. A non-destructive resonant acoustic testing and defect classification of additively manufactured lattice structures. *Welding in the World*, 65(3):361–371, March 2021.

[289] Matthias Heinrich, Bernd Valeske, and Ute Rabe. Efficient Detection of Defective Parts with Acoustic Resonance Testing Using Synthetic Training Data. *Applied Sciences*, 12(15):7648, January 2022. Number: 15 Publisher: Multidisciplinary Digital Publishing Institute.

[290] Rui Li Zu, Dong Liang Wu, Jiang Fan Zhou, Zhan Wei Liu, Hui Min Xie, and Sheng Liu. Advances in Online Detection Technology for Laser Additive Manufacturing: A Review. *3D Printing and Additive Manufacturing*, October 2021. Publisher: Mary Ann Liebert, Inc., publishers.

[291] Bin Shen, Jun Lu, Yiming Wang, Dongli Chen, Jing Han, Yi Zhang, and Zhuang Zhao. Multimodal-based weld reinforcement monitoring system for wire arc additive manufacturing. *Journal of Materials Research and Technology*, 20:561–571, September 2022.

[292] Ézio Carvalho de Santana, Wellington Francisco da Silva, Marcella Grosso Lima, Gabriela Ribeiro Pereira, and Douglas Bressan Riffel. Three-Dimensional Printed Subsurface Defect Detection by Active Thermography Data-Processing Algorithm. *3D Printing and Additive Manufacturing*, November 2021. Publisher: Mary Ann Liebert, Inc., publishers.

[293] J. J. Valdiande, M. Martínez-Minchero, A. Cobo, J. M. Lopez-Higuera, and J. Mirapeix. On-line monitoring and defect detection of arc-welding via plasma optical spectroscopy and LIBS. *Spectrochimica Acta Part B: Atomic Spectroscopy*, 194:106474, August 2022.

[294] Md Shahjahan Hossain, Ashley Pliego, Jinsun Lee, and Hossein Taheri. Characterization of Wire-Arc Additively Manufactured (WAAM) of Titanium Alloy (Ti-6Al-4V) for Nanomechanical Properties. In *ASME 2021 International Mechanical Engineering Congress and Exposition Proceedings*. American Society of Mechanical Engineers Digital Collection, January 2022.

[295] Felix H. Kim, Adam Pintar, Anne-Françoise Obaton, Jason Fox, Jared Tarr, and Alkan Donmez. Merging experiments and computer simulations in X-ray Computed Tomography probability of detection analysis of additive manufacturing flaws. *NDT & E International*, 119:102416, April 2021.

[296] Mohd Javaid, Abid Haleem, Ravi Pratap Singh, Rajiv Suman, Baharul Hussain, and Shanay Rab. Extensive Capabilities of Additive Manufacturing and Its Metrological Aspects. *MAPAN*, June 2022.

[297] Lening Wang, Xiaoyu Chen, Daniel Henkel, and Ran Jin. Pyramid Ensemble Convolutional Neural Network for Virtual Computed Tomography Image Prediction in a Selective Laser Melting Process. *Journal of Manufacturing Science and Engineering*, 143(12), June 2021.

[298] Wenjie Niu, HuaZhi Xiao, Hao Ying, Ying Xu, and YanFang Zhang. Micro-Computed Tomography to Assess the Processing Quality of the Additive Manufacturing of Spiral Microcoils. *3D Printing and Additive Manufacturing*, 7(2):70–77, April 2020. Publisher: Mary Ann Liebert, Inc., publishers.

[299] Anton du Plessis. Effects of process parameters on porosity in laser powder bed fusion revealed by X-ray tomography. *Additive Manufacturing*, 30:100871, December 2019.

[300] A Thompson, I Maskery, and R K Leach. X-ray computed tomography for additive manufacturing: a review. *Measurement Science and Technology*, 27(7):072001, July 2016.

[301] Ricardo Santamaria, Mobin Salasi, Sam Bakhtiari, Garry Leadbeater, Mariano Iannuzzi, and Md Zakaria Quadir. Microstructure and mechanical behaviour of 316L stainless steel produced using sinter-based extrusion additive manufacturing. *Journal of Materials Science*, January 2022.

[302] Gurminder Singh, Jean-Michel Missiaen, Didier Bouvard, and Jean-Marc Chaix. Copper additive manufacturing using MIM feedstock: adjustment of printing, debinding, and sintering parameters for processing dense and defectless parts. *The International Journal of Advanced Manufacturing Technology*, May 2021.

[303] Mohammad Reza Khosravani and Tamara Reinicke. On the Use of X-ray Computed Tomography in Assessment of 3D-Printed Components. *Journal of Nondestructive Evaluation*, 39(4):75, September 2020.

[304] Paschalis Charalampous, Ioannis Kostavelis, and Dimitrios Tzovaras. Non-destructive quality control methods in additive manufacturing: a survey. *Rapid Prototyping Journal*, 26(4):777–790, March 2020.

[305] Anton du Plessis, Igor Yadroitsev, Ina Yadroitsava, and Stephan G. Le Roux. X-Ray Microcomputed Tomography in Additive Manufacturing: A Review of the Current Technology and Applications. *3D Printing and Additive Manufacturing*, 5(3):227–247, September 2018.

[306] Denghao Yi, Xiaofeng Li, Congwei Wang, Jinfang Zhang, Xiaohui Yang, and Dongyun Zhang. Formation and influence of graphene in Inconel 625 prepared by selective laser melting. *Journal of Alloys and Compounds*, 878:160310, October 2021.

[307] Radek Vrána, Daniel Koutný, David Paloušek, Libor Pantělejev, Jan Jaroš, Tomáš Zikmund, and Jozef Kaiser. Selective Laser Melting Strategy for Fabrication of Thin Struts Usable in Lattice Structures. *Materials*, 11(9):1763, September 2018. Number: 9 Publisher: Multidisciplinary Digital Publishing Institute.

[308] Jan Suchy, Libor Pantelejev, David Palousek, Daniel Koutny, and Jozef Kaiser. Processing of AlSi9Cu3 alloy by selective laser melting. *Powder Metallurgy*, 63(3):197–211, May 2020. Publisher: Taylor & Francis _eprint: https://doi.org/10.1080/00325899.2020.1792675.

[309] Yasin Amani, Sylvain Dancette, Pauline Delroisse, Aude Simar, and Eric Maire. Compression behavior of lattice structures produced by selective laser melting: X-ray tomography based experimental and finite element approaches. *Acta Materialia*, 159:395–407, October 2018.

[310] S. L. Campanelli, L. Santoro, L. Lamberti, F. Caiazzo, and V. Alfieri. Nonlinear analysis of compressive behavior of 17-4PH steel structures with large spherical

pores built by selective laser melting. *Journal of Materials Science*, 57(5):3777–3806, February 2022.

[311] M. Dallago, B. Winiarski, F. Zanini, S. Carmignato, and M. Benedetti. On the effect of geometrical imperfections and defects on the fatigue strength of cellular lattice structures additively manufactured via Selective Laser Melting. *International Journal of Fatigue*, 124:348–360, July 2019.

[312] Hao Zhou, Heran Jia, Huizhong Zeng, Yonggang Tu, Linli Li, Xiaoyu Zhang, and Hongshuai Lei. Resonance frequency prediction approach of lattice structure fabricated by selective laser melting. *Advances in Astronautics Science and Technology*, May 2022.

[313] Ondřej Červinek, Benjamin Werner, Daniel Koutný, Ondřej Vaverka, Libor Pantělejev, and David Paloušek. Computational Approaches of Quasi-Static Compression Loading of SS316L Lattice Structures Made by Selective Laser Melting. *Materials*, 14(9):2462, January 2021. Number: 9 Publisher: Multidisciplinary Digital Publishing Institute.

[314] N. Ahmed, I. Barsoum, G. Haidemenopoulos, and R. K. Abu Al-Rub. Process parameter selection and optimization of laser powder bed fusion for 316L stainless steel: A review. *Journal of Manufacturing Processes*, 75:415–434, March 2022.

[315] Yaozhong Zhang and Aljoscha Roch. Fused filament fabrication and sintering of 17-4PH stainless steel. *Manufacturing Letters*, 33:29–32, August 2022.

[316] X. Zhao, Q. S. Wei, N. Gao, E. L. Zheng, Y. S. Shi, and S. F. Yang. Rapid fabrication of TiN/AISI 420 stainless steel composite by selective laser melting additive manufacturing. *Journal of Materials Processing Technology*, 270:8–19, August 2019.

[317] Yubao Huang, Shanglei Yang, Jiaxing Gu, Qi Xiong, Chenfeng Duan, Xuan Meng, and Yu Fang. Microstructure and wear properties of selective laser melting 316L. *Materials Chemistry and Physics*, 254:123487, November 2020.

[318] Sebastian Greco, Kevin Gutzeit, Hendrik Hotz, Benjamin Kirsch, and Jan C. Aurich. Selective laser melting (SLM) of AISI 316L—impact of laser power, layer thickness, and hatch spacing on roughness, density, and microhardness at constant input energy density. *The International Journal of Advanced Manufacturing Technology*, 108(5):1551–1562, May 2020.

[319] Swathi Vunnam, Abhinav Saboo, Chantal Sudbrack, and Thomas L. Starr. Effect of powder chemical composition on the as-built microstructure of 17-4 PH stainless steel processed by selective laser melting. *Additive Manufacturing*, 30:100876, December 2019.

[320] P. Ponnusamy, Basant Sharma, S. H. Masood, R. A. Rahman Rashid, Riyan Rashid, S. Palanisamy, and D. Ruan. A study of tensile behavior of SLM processed 17-4 PH stainless steel. *Materials Today: Proceedings*, 45:4531–4534, January 2021.

[321] Usman Ali, Reza Esmaeilizadeh, Farid Ahmed, Dyuti Sarker, Waqas Muhammad, Ali Keshavarzkermani, Yahya Mahmoodkhani, Ehsan Marzbanrad, and Ehsan Toyserkani. Identification and characterization of spatter particles and their effect on surface roughness, density and mechanical response of 17-4PH stainless steel laser powder-bed fusion parts. *Materials Science and Engineering: A*, 756:98–107, May 2019.

[322] Chong-Ming Jiang, Jeng-Rong Ho, Pi-Cheng Tung, and Chih-Kuang Lin. Tempering Effect on the Anisotropic Mechanical Properties of Selective Laser Melted 420 Stainless Steel. *Journal of Materials Engineering and Performance*, September 2022.

[323] Matti Kultamaa, Kari Mönkkönen, Jarkko J. Saarinen, and Mika Suvanto. Corrosion Protection of Injection Molded Porous 440C Stainless Steel by Electroplated Zinc Coating. *Coatings*, 11(8):949, August 2021. Number: 8 Publisher: Multidisciplinary Digital Publishing Institute.

[324] Cyril Santos, Daniel Gatões, Fábio Cerejo, and Maria Teresa Vieira. Influence of Metallic Powder Characteristics on Extruded Feedstock Performance for Indirect Additive Manufacturing. *Materials*, 14(23):7136, November 2021.

[325] Ansys. Ansys, 'The CES Edupack 2013'. Granta's Design Ltd, UK, 2013.

[326] S. D. Jadhav, S. Dadbakhsh, L. Goossens, J-P Kruth, J. Van Humbeeck, and K. Vanmeensel. Influence of selective laser melting process parameters on texture evolution in pure copper. *Journal of Materials Processing Technology*, 270:47–58, August 2019.

[327] Xingchen Yan, Chaoyue Chen, Cheng Chang, Dongdong Dong, Ruixin Zhao, Richard Jenkins, Jiang Wang, Zhongming Ren, Min Liu, Hanlin Liao, Rocco Lupoi, and Shuo Yin. Study of the microstructure and mechanical performance of C-X stainless steel processed by selective laser melting (SLM). *Materials Science and Engineering: A*, 781:139227, April 2020.

[328] A R Farinha, C Batista, L F Dias, E W Sequeiros, and M T Vieira. Modification of H13 (AISI) Tool Steel Powders to Manufacture Inserts and Cooling Systems for Moulds by SLM. In *European Congress and Exhibition on Powder Metallurgy. European PM Conference Proceedings*, page 1, Reims, France, November 2015.

[329] Zhongji Sun, Xipeng Tan, Shu Beng Tor, and Chee Kai Chua. Simultaneously enhanced strength and ductility for 3D-printed stainless steel 316L by selective laser melting. *NPG Asia Materials*, 10(4):127–136, April 2018.

[330] P. Bajaj, A. Hariharan, A. Kini, P. Kürnsteiner, D. Raabe, and E.A. Jägle. Steels in additive manufacturing: A review of their microstructure and properties. *Materials Science and Engineering: A*, 772:138633, January 2020.

Appendices

Appendix A

Optimization of metallic powder filaments for additive manufacturing extrusion

materials MDPI

Article

Selective Laser Melting and Mechanical Properties of Stainless Steels

Daniel Gatões *, Ricardo Alves, Bernardo Alves and Maria Teresa Vieira

CEMMPRE—Centre for Mechanical Engineering Materials and Processes, Department of Mechanical Engineering, University of Coimbra, Rua Luís Reis Santos, 3030-788 Coimbra, Portugal
* Correspondence: daniel.gatoes@uc.pt; Tel.: +351-239790765

Abstract: Metal additive manufacturing (AM) has been evolving in response to industrial and social challenges. However, new materials are hindered in these technologies due to the complexity of direct additive manufacturing technologies, particularly selective laser melting (SLM). Stainless steel (SS) 316L, due to its very low carbon content, has been used as a standard powder in SLM, highlighting the role of alloying elements present in steels. However, reliable research on the chemical impact of carbon content in steel alloys has been rarely conducted, despite being the most prevalent element in steel. Considering the temperatures involved in the SLM process, the laser–powder interaction can lead to a significant carbon decrease, whatever the processing atmosphere. In the present study, four stainless steels with increasing carbon content—AISI 316L, 630 (17-4PH), 420 and 440C—were processed under the same SLM parameters. In addition to roughness and surface topography, the relationship with the microstructure (including grain size and orientation), defects and mechanical properties (hardness and tensile strength) were established, highlighting the role of carbon. It was shown that the production by SLM of stainless steels with similar packing densities and different carbon contents does not oblige the changing of processing parameters. Moreover, alterations in material response in stainless steels produced under the same volumetric energy density mainly result from microstructural evolution during the process.

Keywords: additive manufacturing; selective laser melting; stainless steel; AISI 316L; AISI 630 (17-4PH); AISI 420; AISI 440C; carbon content

Citation: Gatões, D.; Alves, R.; Alves, B.; Vieira, M.T. Selective Laser Melting and Mechanical Properties of Stainless Steels. *Materials* **2022**, *15*, 7575. https://doi.org/10.3390/ma15217575

Academic Editors: Wai Yee Yeong and Swee Leong Sing

Received: 17 September 2022
Accepted: 17 October 2022
Published: 28 October 2022

1. Introduction

Metal additive manufacturing (MAM), and particularly selective laser melting (SLM), is an effective way of producing steel metal parts [1]. In SLM, a laser is used to melt and fuse metallic powder particles, layer by layer, to build the desired three-dimensional shape (3D object) [2]. SLM was shown to be able to produce low-carbon stainless steel with good quality and reliability [3]. However, some properties in SLM are primarily dependent on the processing step, since a large number of variables affect the quality of final parts, such as powder characteristics, atmosphere, the response of the material to the volumetric energy density (VED) and the rapid heating and cooling cycles [4,5]. As a result, the complex physical and chemical behavior in the melting pool leads to an anisotropic microstructure and the appearance of voids, affecting the final properties [6,7]. The carbon content must be carefully controlled during the manufacturing process, since its presence and quantity can significantly impact the properties of the resulting steel. While the carbon content of SLM-produced stainless steels can be controlled to some degree and generally leads to better mechanical properties, typically associated with less corrosion resistance [8], these steels have a tendency to form cracks and pores during the SLM process [9,10].

Besides porosity, which has a significant impact on mechanical properties, interstitial defects (chemical composition of powder, processing atmosphere, etc.) during SLM and microstructures can also contribute to substantial variations in the properties of the stainless

steels. Thus, it is essential to carefully consider the properties of an SLM-produced alloy before selecting it for application [11–13].

Stainless steel 316L has been the subject of many studies since the dawn of SLM [14]. The ease of production associated with the low carbon content, no phase transformation (austenitic matrix) in the SLM process, and good mechanical properties make it a standard material in SLM [15,16], and it was used as a standard stainless steel in this study. SS 630 studies have been growing in the last few years due to its excellent mechanical properties [17]. Note that 420 martensitic stainless steel has also been of significant interest in SLM, since its properties are suitable for specific applications, due to its high strength and corrosion resistance [18]. Consequently, many studies have been published concerning the microstructure, mechanical properties, and roughness of these stainless steels, produced by SLM ([19–21] −316L, [22–24] −630, [25–27] −420). SS 440C is also a martensitic stainless steel, but has high carbon content; it is used in applications where high hardness and corrosion resistance are necessary, such as bearings, knives and automotive parts [28]. As far as the authors are aware, this steel has not been subject to any studies regarding SLM technology. Moreover, a detailed study comparing various stainless steels produced with the same parameters in SLM is not available.

In addition to 316L, the standard, in the present study, three stainless steels with similar chromium contents and various levels of carbon content were processed through SLM, using the same atmosphere and set of SLM parameters, as a way to highlight the role of carbon content in AM mechanical properties. A detailed study of the microstructures of these steels compared with the powder was performed. It is worth noting that powder production was also attained in the same atmosphere. The occurrence of defects and their consequences on the mechanical properties can be highlighted by microcomputed tomography (µCT). This non-destructive technique can be useful to study 3D objects pores, voids and impurities distribution, whatever the material [29–31].

2. Materials and Methods

Four stainless steel powders with increasing carbon content were selected for this study, attained by gas atomization. The 316L and 630 (17-4PH) stainless steels powder were from SLM Solutions GmbH (SLM Solutions Group AG, Lübeck, Germany), and 420 and 440C powders were from Sandvik Osprey Ltd. (Sandvik AB, Sandviken, Sweden). The powders' chemical compositions are summarized in Table 1. Particle size and particle size distribution (PSD) were evaluated by laser diffraction spectrometry LDS, Malvern Mastersizer 3000 (Malvern Panalytical, Egham, UK). SEM Quanta 400 FEG STEM (FEI Company, Hillsboro, OR, USA) was used for powder shape-factor evaluation. Powder density was measured (5 measurements per steel) by helium pycnometry with Accupyc 1330 (Micrometrics, Norcross, GA, USA).

Table 1. Chemical compositions of the different stainless steels (wt.%).

Element	C	Cr	Ni	Cu	Mo	Nb + Ta	Si	Mn	N	P	S	O
316L	0.030	16–18	10–14	-	2–3	-	1	2	0.100	0.045	0.030	0.100
630	0.070	15–17	3–5	3–5	-	0.150–0.450	1	1	0.100	-	0.030	0.100
420	min 0.150	12–14	-	-	-	-	1	1	-	0.040	0.030	-
440C	0.950–1.200	16–18	-	-	0.750	-	1	1	-	0.040	0.030	0.100

X-ray diffraction to evaluate types of phases involved a Philips X'Pert diffractometer (Philips, Egham, UK) at 40 kV, Bragg–Brentano geometry (θ–2θ), cobalt anticathode (λ(kα1) = 0.178897 nm and λ(kα2) = 0.179285 nm) and a current intensity of 35 mA. The X-ray diffraction scans were carried out from 40 to 100° in steps of 0.025°, with an acquisition time of 1 s per step.

Materials **2022**, *15*, 7575

The SLM equipment was an EOS M290 system (EOS GmbH, Krailling, Germany) equipped with a Yb-fiber laser (λ = 1064 nm) with a maximum power of 400 W and a spot size of 100 µm. The SLM processing was undertaken with an oxygen content below 0.1% in the working chamber using a continuous flow of nitrogen. The laser power was set to 260 W, scanning speed was 1060 mm/s, hatch space was 100 µm and layer thickness was 30 µm (VED = 82 $\frac{J}{mm^3}$). The scanning strategy was a zigzag pattern with a rotation angle of 67° between adjacent layers. Each batch included density cubes (10 × 10 × 10 mm^3) and tensile test specimens. Additionally, a 10° rotation relative to the substrate position (Figure 1) was added to avoid contamination by spattering. All 3D objects were studied as SLMed, without post-processing treatment.

Figure 1. Positions of the specimens on the SLM bed.

The final density was evaluated through the Archimedes method and averaged for 10 specimens (density cubes).

Surface and inside defects on tensile specimens were evaluated by X-ray micro-computed tomography using a Bruker SkyScan 1275 (Bruker, Kontich, Belgium). Specimens were polished on both the top and bottom surfaces of tensile test specimens until a thickness of 2 mm was achieved. An acceleration voltage of 100 kV and a beam current of 100 µA were set using a 1 mm copper filter with step-and-shoot mode. Pixel size was set to 10 µm, and the random mode was used. The images were acquired at a 0.4° angular step with 10 frames on average per step using an exposure time of 245 ms. The µCT images were reconstructed with the dedicated manufacturer software.

Optical microscopy was done using a Leica DM 4000 M LED (Leica Microsystems AG, Wetzlar, Germany) with a Leica camera, model MC 120 HD.

For 316L, 630 and 420 steels, etching used a Vilella solution (2 g of picric acid, 5 mL of HCl and 100 mL of ethanol). For 440C, Kalling solution etching (5 g of $CuCl_2$, 100 mL of HCl and 100 mL of ethanol) was selected.

Surface roughness was evaluated using focus variation microscopy Alicona Infinite Focus (Bruker, Kontich, Belgium) following ISO 4287 and 4288.

Microhardness measurements were performed on a Fisherscope H100 (Fischer Instrumentation LTD, Pershore, UK), equipped with a Vickers indentor (10 measurements per sample, maximum load of 1000 mN, holding time of 30 s).

Tensile tests were performed on a SHIMADZU Autograph (Shimadzu, Kyoto, Japan), with a 100 kN load cell, according to ISO 6892, at room temperature, at a strain rate of 10 MPa per second. Tensile specimens' dimensions were in accordance with Figure 2.

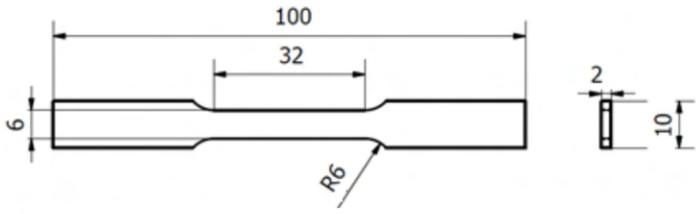

Figure 2. Tensile test specimen measurements, in mm (ISO 6892).

3. Results

3.1. Powder

All four studied stainless steel powders showed symmetric and narrow normal particle size distributions. Table 2 summarizes the d_{10}, d_{50} and d_{90} powder particle size and density.

Table 2. Powder size distribution and density of each stainless steel powder.

Powder	d_{10} (µm)	d_{50} (µm)	d_{90} (µm)	$\rho\left(\frac{Kg}{m^3}\right)$
316L	22.7	32.4	45.2	7880
630	17.8	26.2	37.6	7880
420	17.0	24.3	34.3	7820
440C	18.1	26.4	37.9	7940

Powder shape was almost spherical for all powders; there were some satellites, particularly in 316L and 420 steel powders (Figure 3).

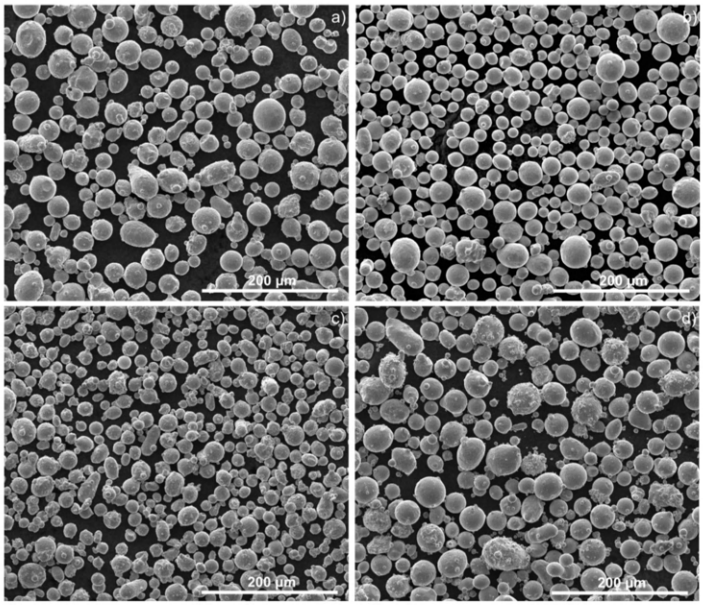

Figure 3. Particle shapes of the 316L (**a**), 630 (**b**), 420 (**c**) and 440C (**d**) powders (SEM).

The selected stainless steels presented martensitic and austenitic phases (Figure 4).

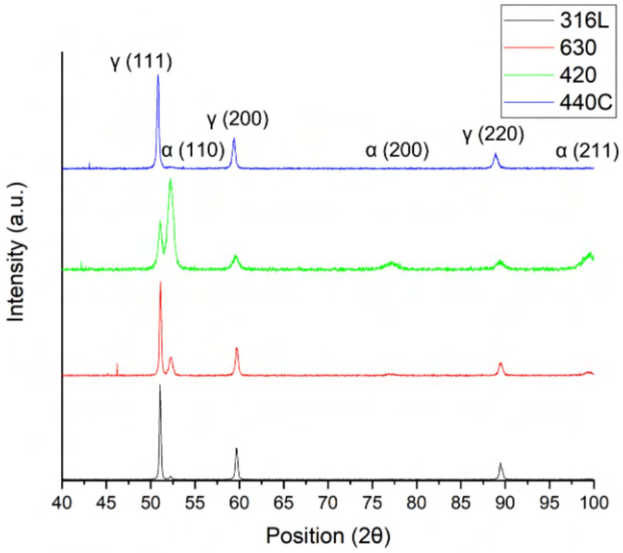

Figure 4. X-ray diffractograms of the 316L, 630, 420 and 440C powders (from bottom to top, respectively).

3.2. 3D Object

3.2.1. Porosity Evaluation

Porosity is directly related to density. However, the measured values for the four steels are not only related to the porosity, but mainly to the phase difference between the 3D object and starting powder.

The reduced section (cross-section) of the tensile specimen can be observed in Figure 5. Figure 6 shows a rendering of the pore distribution within the reduced section of the tensile specimen. It is noteworthy that only defects bigger than the pixel size (10 µm) were observable in this case.

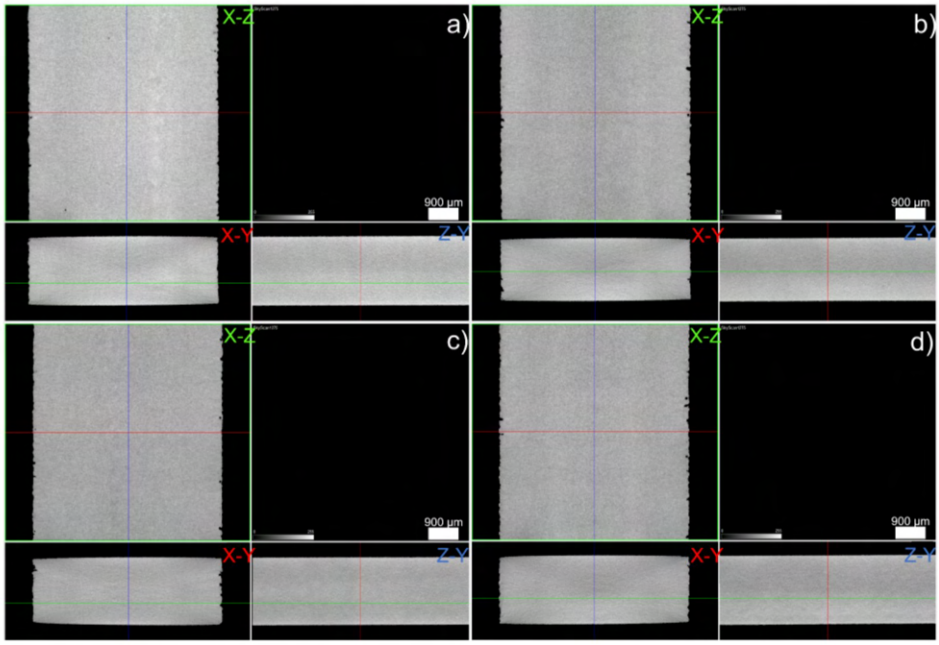

Figure 5. 2D visualization of the pores location in cross-section for 316L (**a**), 630 (**b**), 420 (**c**) and 440C (**d**).

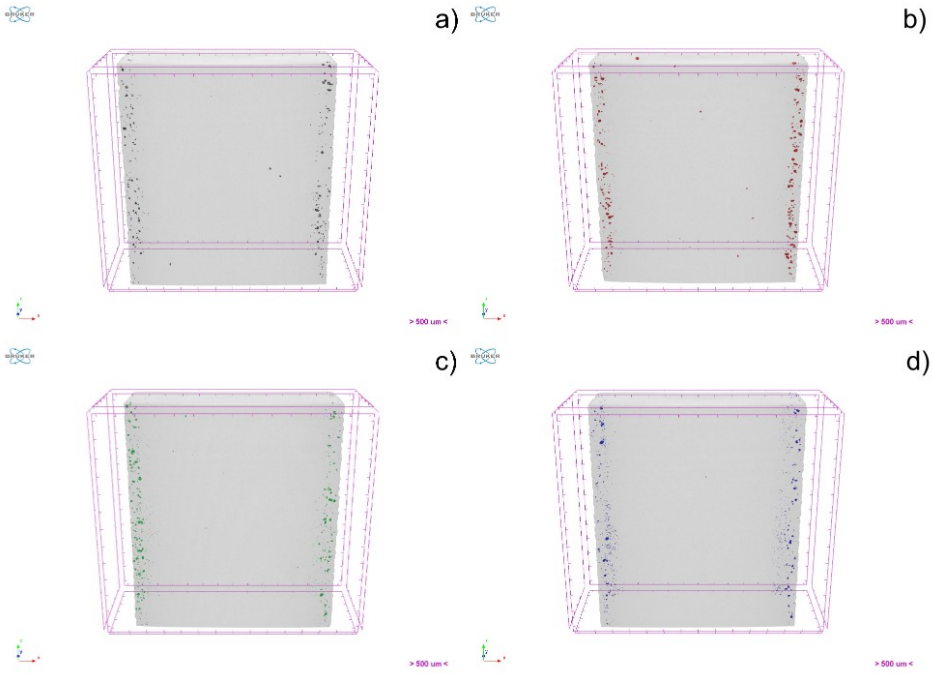

Figure 6. 3D visualization of the pores location within the 3D object volume for 316L (**a**), 630 (**b**), 420 (**c**) and 440C (**d**).

Table 3 summarizes the values of density of the 3D object and the relative porosity, compared to powder density.

Table 3. Density comparison between powder and 3D object.

Type	Powder Density $\left(\frac{Kg}{m^3}\right)$	3D Object Density $\left(\frac{Kg}{m^3}\right)$
316L	7880	7790
630	7880	7660
420	7820	7590
440C	7940	7490

3.2.2. Microstructure

X-ray diffractions of the 3D objects are shown in Figure 7. Stainless steel 316L showed only an austenitic phase but a strong orientation in [220]. The texture corresponds to <011> direction, which has a major influence on mechanical properties [32]. SS 630 showed an increase in martensite, and 420 showed a shift in the austenite phase when compared to the powder.

All observed stainless steels, besides SS 316L, tended to form elongated grains in the scanning direction, which is common in metals processed by SLM (Figure 8). It was possible to distinguish narrower elongated grains in 630, 420 and 440C, which allowed the distinction between the previous layer (rotated 90°) and the current layer.

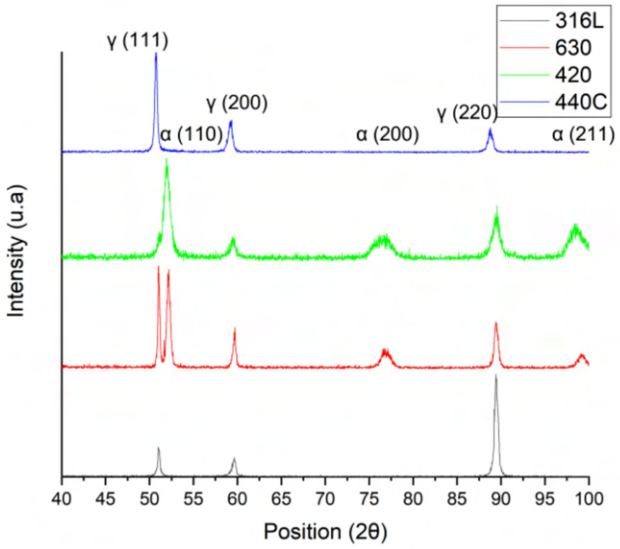

Figure 7. X-ray diffractograms of the 316L, 630, 420 and 440C 3D objects (from bottom to top, respectively).

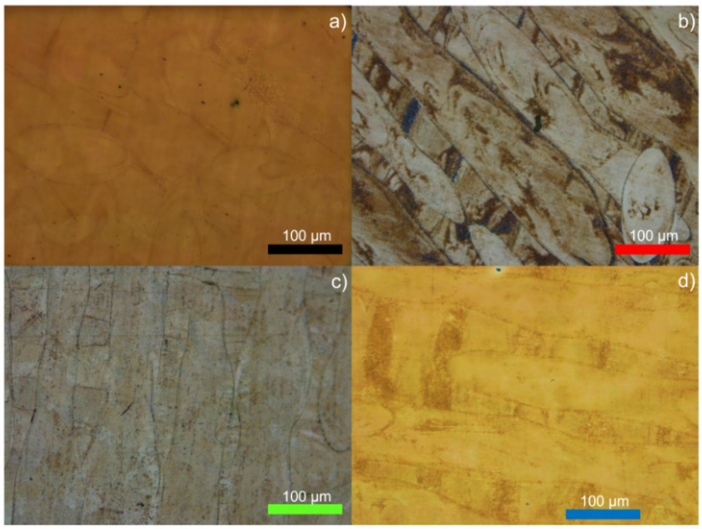

Figure 8. Micrographies of the etched surfaces of 316L (**a**), 630 (**b**), 420 (**c**) and 440C (**d**) stainless steels.

3.2.3. Roughness, Topography and Geometrical Evaluation

Table 4 shows the attained roughness values of each specimen.

In what concerns the surface topography, a group of beads corresponding to the scanning direction could be observed in Figure 9. Moreover, the not-fully melted powder could be observed scattered throughout the surface.

Produced tensile specimens were measured in order to ensure the adequacy of mechanical tests. Table 5 summarizes the size comparison between CAD and 3D objects.

Table 4. Roughness measurements of the tensile test specimens, for each stainless steel.

Type	Ra (µm)	Rq (µm)	Rz (µm)
316L	16.204	19.864	94.401
630	12.988	16.030	79.347
420	7.669	9.440	53.783
440C	6.369	8.093	46.391

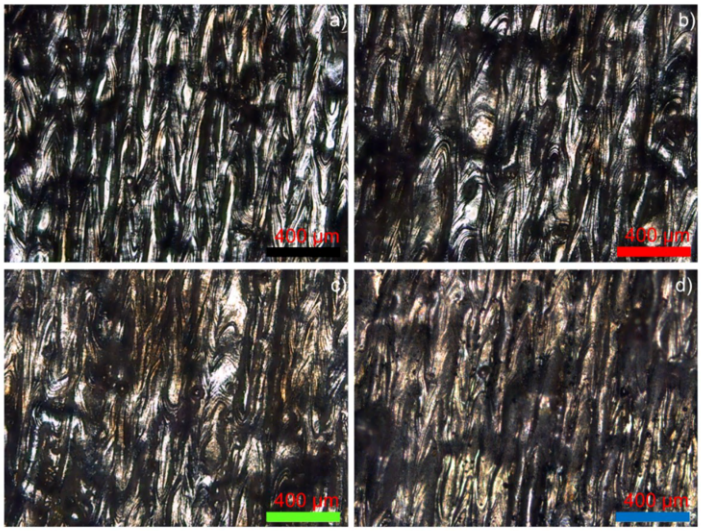

Figure 9. Micrographies of the 316L (**a**), 630 (**b**), 420 (**c**) and 440C (**d**) surfaces.

Table 5. Comparison between CAD and final 3D object sizes of tensile test specimens, for each material type.

Type	Width at Grip (%)	Width at Reduced Section (%)	Length (%)
316L	99.40 ± 0.24	98.50 ± 0.32	99.70 ± 0.03
630	99.60 ± 0.19	99.00 ± 0.27	99.81 ± 0.05
420	99.70 ± 0.25	98.67 ± 0.27	100.00 ± 0.06
440C	99.20 ± 0.03	98.83 ± 0.25	99.58 ± 0.05

3.2.4. Mechanical Properties

Microhardness

Table 6 summarizes the measured hardness ($HV_{0.1}$) for the different stainless steels and compares it to the bulk.

Table 6. Microhardness levels of the selected stainless steel 3D objects, compared to the bulk [33].

Type	3D Object $HV_{0.1}$	Bulk $HV_{0.1}$
316L	133 ± 17	170–220
630	306 ± 11	250–460
420	647 ± 27	260–641
440C	803 ± 26	510–760

Tensile Tests

Figure 10 shows the stress–strain results for five tensile test specimens per stainless steel type.

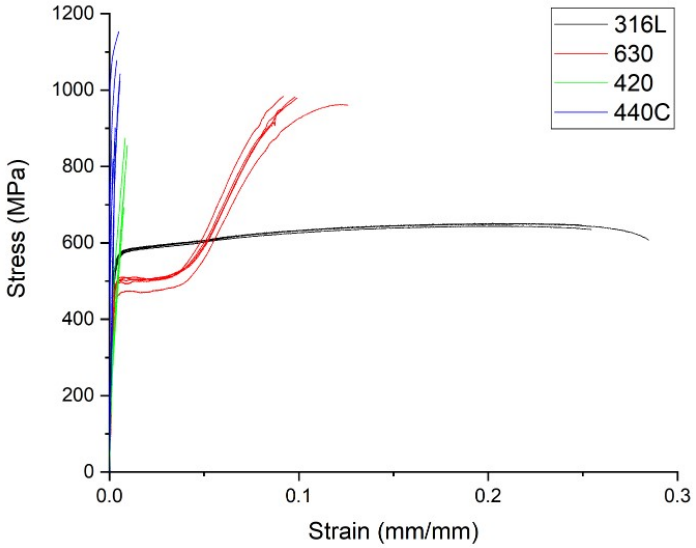

Figure 10. Strain–stress curves for the 316L (black), 630 (red), 420 (green) and 440C (blue) steels.

Table 7 summarizes the elongation and ultimate tensile strength (UTS) of the stainless steel tensile specimens.

Table 7. Elongation and ultimate tensile strength for each steel-type 3D object, compared to bulk [34].

Type	3D Object ϵ (%)	Bulk ϵ (%)	3D Object UTS (MPa)	Bulk UTS (MPa)
316L	25.4 ± 2.4	30–50	645 ± 10	550
630	10.0 ± 1.3	4–6	1020 ± 33	943
420	0.7 ± 0.2	5–11	814 ± 74	655
440C	0.4 ± 0.1	0.5–4	1164 ± 13	760

4. Discussion

4.1. Powder

All selected powder particles had similar particle sizes, particle size distributions and shape factors. However, some satellites were observed for 316L and 420 steel powders. These characteristics did not contribute to a significant discrepancy in the powder flowability, and consequently, packing behavior in the powder bed. The difference in measured powder density was mainly related to the phase composition of the steel and its atomization atmosphere. Thus, the austenite phase is always present, resulting from the atomization atmosphere—nitrogen. This is supported by the X-ray diffraction (Figure 4). The SS 440C powder presented mainly the austenite phase and the highest powder density. In opposition, the 420 powder showed the highest martensite content of all selected powder, and therefore, the lowest density.

4.2. 3D Object

4.2.1. Density and Microstructure

A representative area of defects (Figure 6) shows that the main pores in all stainless steel 3D objects were relatively similar, independently of carbon content. Surface finishing is mostly obligatory in SLM, since close-to-surface defects can be the main driving force for crack initiation, if not removed. Thus, the presence of these defects is not relevant in real-world applications. However, due to µCT resolution, it can be concluded that microporosity (<10 µm) could also have been present. Nevertheless, this is not enough to justify the measured 3D object's density.

Considering that the nitrogen atmosphere was similar for powder and 3D objects, and the fact that the carbon content's effects on the porosity distribution and percentage were negligible, the density must be justified by taking into account the microstructure of the steel (before and after SLM). This means that the density modification can be attributed mainly to the content of the prevalent austenitic phase and the presence of carbide phases, particularly in high-carbon content steels.

SLM processing of the 3D objects, despite 440C not sustaining a phase alteration, affected the phase compositions of 316L, 630 and 420 steels. Particularly, 316L and 420 suffered a shift in the crystallographic orientation, and 630 had an increase in the martensitic phase. This deviation in crystallographic texture resulted from short, deep melt pools, resulting from higher laser power, as shown by [32].

As is common in metals processed by SLM, the microstructure is oriented toward the scanning strategy. This is due to the heating and cooling rates involved in the SLM process, which are the main drivers of microstructure growth. However, high carbon presence in the melt pool was shown to have a particular effect on microstructure due to the carbon movement in the direction of the melt pool frontier, resulting from Marangoni convection [35,36]. Moreover, carbon is a significant element of austenite stabilization. Thus, the carbon depletion of 630 may have been the driver for the increase in martensitic content when compared to the same material powder.

Figure 8 displays apparent grain anisotropy in the 3D objects, whatever the steel. SS 316L's clear etched surface was consistent with the fact that little-to-no martensite was present in the steel, but grain orientation along the scanning direction was still visible. SS 630 presented a microstructure close to that of dual-phase steel, with austenite and martensite distributed almost equally within the steel and strong processed-caused anisotropy. SS 420 had a dominant martensitic phase with residual austenite. Martensite grew alongside austenite in these steels, as a virtue of the complex melt pool temperature dynamics that occur in the SLM production.

4.2.2. Roughness, Geometry and Topography

Melt pool beads could be seen all over the surfaces. However, it is possible to relate the reduced z-growth of the melt pool with increased carbon content, resulting in lower roughness for higher carbon steels. All steels presented fused powders on their surface, which is detrimental to roughness but can usually be mitigated by shot-peening [37].

The geometrical deviation between the steels, after SLM, was low and consistent, which can mean that the selected VED is indicated for all the steels. VED has a significant effect on melt pool width. If too low, a clear frontier within adjacent melt pools should be observed, along with oriented porosity along the scanning direction. If too high, an uncontrolled melt pool with varying lengths is achieved, and growth in XY direction is expected. Consequently, VED must be considered to be within the optimal range for all the studied stainless steels, corroborating the previous statements.

4.2.3. Mechanical Properties

The microhardness values of the SLM 3D objects produced from the powders of 630, 420 and 440C stainless steels were higher than the maximum hardness of the bulk steels processed by conventional approaches, including heat treatment. Nevertheless, SS 316L showed a slight decrease in hardness compared to the bulk due to the texture assumed during SLM processing. In concomitance with hardness, UTS values for all stainless steels studied, processed by SLM, show a tendency to be higher than the values of conventional processing. It must be highlighted that SS 630 had hardness within the range of the values assumed, considering the various heat treatments that can be used. However, the tensile test showed a particular behavior consistent with the strain-induced martensite formation (TRIP) effect observed by [1,23,24], resulting from a high retained austenite content. This effect led to higher ductility than conventionally heat-treated SS 630. SS 420 and 440C have higher hardness, and the UTS values are outstanding.

Nevertheless, SS 420 processed by SLM is a brittle material with negligible elongation due to an unconventional microstructure.

5. Conclusions

Whatever the carbon composition, the SLM parameters generally used for 316L induce in other stainless steels with low nickel and higher carbon content low porosity and high densification. The microstructures resulting from SLM without post-processing treatments are mandatory for assessing the mechanical behavior of 3D objects. The hardness and UTS of SLM 3D objects are higher than those of bulk stainless steels with the same compositions, after heat treatment. This is due to a direct relationship between carbon and elements with high affinity to it (e.g., chromium, iron, and molybdenum); however, the content of other elements of selected stainless steels is insufficient for carbide formation. Moreover, it must be highlighted that the stabilization of residual austenite present in the steels with higher carbon content can result from the processing atmosphere; nitrogen is more effective than other elements in the matrix. Furthermore, the strong anisotropy observed in all stainless steels resulted from the selected scanning strategy and VED values. In the studied stainless steels, the microstructural difference, when compared to conventionally processed bulk materials, is mainly due to the processing atmosphere, so a constant VED can be used to process different stainless steels with varying carbon compositions. Future studies regarding the influence of carbon content in indirect additive manufacturing will be compared to the results reported here.

Author Contributions: Conceptualization, D.G. and M.T.V.; methodology, D.G.; validation, M.T.V.; formal analysis, D.G. and M.T.V.; investigation, D.G., B.A. and R.A.; resources, M.T.V.; data curation, D.G. and B.A.; writing—original draft preparation, D.G. and R.A.; writing—review and editing, D.G., B.A. and M.T.V.; visualization, D.G.; supervision, M.T.V.; project administration, M.T.V.; funding acquisition, M.T.V. All authors have read and agreed to the published version of the manuscript.

Funding: This work was supported by the European Regional Development Fund (ERDF) under the Portuguese program Programa Operacional Factores de Competitividade (COMPETE) (grant agreement number POCI-01-0247-FEDER-039910). This research is sponsored by national funds through FCT—Fundação para a Ciência e a Tecnologia—under the project UIDB/00285/2020 and LA/P/0112/2020.

Informed Consent Statement: Not applicable.

Data Availability Statement: Data sharing not applicable to this article.

Conflicts of Interest: The authors declare no conflict of interest.

References

1. Bajaj, P.; Hariharan, A.; Kini, A.; Kürnsteiner, P.; Raabe, D.; Jägle, E. Steels in additive manufacturing: A review of their microstructure and properties. *Mater. Sci. Eng. A* **2020**, *772*, 138633. [CrossRef]
2. *ISO/ASTM 52900:2021(en)*; Additive Manufacturing—General Principles—Fundamentals and Vocabulary. ISO/ASTM: Geneva, Switzerland, 2021.
3. Sun, H.; Chu, X.; Liu, Z.; Gisele, A.; Zou, Y. Selective Laser Melting of Maraging Steels Using Recycled Powders: A Comprehensive Microstructural and Mechanical Investigation. *Metall. Mater. Trans. A* **2021**, *52*, 1714–1722. [CrossRef]
4. Wang, Y.; Luo, L.; Liu, T.; Wang, B.; Luo, L.; Zhao, J.; Wang, L.; Su, Y.; Guo, J.; Fu, H. Tuning process parameters to optimize microstructure and mechanical properties of novel maraging steel fabricated by selective laser melting. *Mater. Sci. Eng. A* **2021**, *823*, 141740. [CrossRef]
5. Waqar, S.; Guo, K.; Sun, J. FEM analysis of thermal and residual stress profile in selective laser melting of 316L stainless steel. *J. Manuf. Process.* **2021**, *66*, 81–100. [CrossRef]
6. Ansari, P.; Rehman, A.U.; Pitir, F.; Veziroglu, S.; Mishra, Y.K.; Aktas, O.C.; Salamci, M.U. Selective Laser Melting of 316L Austenitic Stainless Steel: Detailed Process Understanding Using Multiphysics Simulation and Experimentation. *Metals* **2021**, *11*, 1076. [CrossRef]
7. Trejos-Taborda, J.; Reyes-Osorio, L.; Garza, C.; del Carmen Zambrano-Robledo, P.; Lopez-Botello, O. Finite element modeling of melt pool dynamics in laser powder bed fusion of 316L stainless steel. *Int. J. Adv. Manuf. Technol.* **2022**, *120*, 3947–3961. [CrossRef]
8. Adeyemi, A.; Akinlabi, E.T.; Mahamood, R.M. Powder Bed Based Laser Additive Manufacturing Process of Stainless Steel A Review. *Mater. Today: Proc.* **2018**, *5*, 18510–18517. [CrossRef]

9. Chang, C.; Yan, X.; Deng, Z.; Lu, B.; Bolot, R.; Gardan, J.; Deng, S.; Chemkhi, M.; Liu, M.; Liao, H. Heat treatment induced microstructural evolution, oxidation behavior and tribological properties of Fe-12Cr-9Ni-2Al steel (CX steel) prepared using selective laser melting. *Surf. Coatings Technol.* **2022**, *429*, 127982. [CrossRef]
10. Saewe, J.; Gayer, C.; Vogelpoth, A.; Schleifenbaum, J.H. Feasability Investigation for Laser Powder Bed Fusion of High-Speed Steel AISI M50 with Base Preheating System. *BHM Berg-Und Hüttenmännische Monatshefte* **2019**, *164*, 101–107. [CrossRef]
11. Ronneberg, T.; Davies, C.M.; Hooper, P.A. Revealing relationships between porosity, microstructure and mechanical properties of laser powder bed fusion 316L stainless steel through heat treatment. *Mater. Des.* **2020**, *189*, 108481. [CrossRef]
12. Pasebani, S.; Ghayoor, M.; Badwe, S.; Irrinki, H.; Atre, S.V. Effects of atomizing media and post processing on mechanical properties of 17-4 PH stainless steel manufactured via selective laser melting. *Addit. Manuf.* **2018**, *22*, 127–137. [CrossRef]
13. Maharjan, N.; Zhou, W.; Zhou, Y.; Wu, N. Decarburization during laser surface processing of steel. *Appl. Phys. A* **2018**, *124*, 682. [CrossRef]
14. Ahmed, N.; Barsoum, I.; Haidemenopoulos, G.; Al-Rub, R.K.A. Process parameter selection and optimization of laser powder bed fusion for 316L stainless steel: A review. *J. Manuf. Process.* **2022**, *75*, 415–434. [CrossRef]
15. Yang, X.; Ma, W.J.; Ren, Y.J.; Liu, S.F.; Wang, Y.; Wang, W.L.; Tang, H.P. Subgrain microstructures and tensile properties of 316L stainless steel manufactured by selective laser melting. *J. Iron Steel Res. Int.* **2021**, *28*, 1159–1167. [CrossRef]
16. Zhai, W.; Zhou, W.; Zhu, Z.; Nai, S.M.L. Selective Laser Melting of 304L and 316L Stainless Steels: A Comparative Study of Microstructures and Mechanical Properties. *Steel Res. Int.* **2022**, *93*, 2100664. [CrossRef]
17. Zhang, Y.; Roch, A. Fused filament fabrication and sintering of 17-4PH stainless steel. *Manuf. Lett.* **2022**, *33*, 29–32. [CrossRef]
18. Zhao, X.; Wei, Q.S.; Gao, N.; Zheng, E.L.; Shi, Y.S.; Yang, S.F. Rapid fabrication of TiN/AISI 420 stainless steel composite by selective laser melting additive manufacturing. *J. Mater. Process. Technol.* **2019**, *270*, 8–19. [CrossRef]
19. Huang, Y.; Yang, S.; Gu, J.; Xiong, Q.; Duan, C.; Meng, X.; Fang, Y. Microstructure and wear properties of selective laser melting 316L. *Mater. Chem. Phys.* **2020**, *254*, 123487. [CrossRef]
20. Jiang, H.Z.; Li, Z.Y.; Feng, T.; Wu, P.Y.; Chen, Q.S.; Feng, Y.L.; Chen, L.F.; Hou, J.Y.; Xu, H.J. Effect of Process Parameters on Defects, Melt Pool Shape, Microstructure, and Tensile Behavior of 316L Stainless Steel Produced by Selective Laser Melting. *Acta Metall. Sin. (Engl. Lett.)* **2021**, *34*, 495–510. [CrossRef]
21. Greco, S.; Gutzeit, K.; Hotz, H.; Kirsch, B.; Aurich, J.C. Selective laser melting (SLM) of AISI 316L—impact of laser power, layer thickness, and hatch spacing on roughness, density, and microhardness at constant input energy density. *Int. J. Adv. Manuf. Technol.* **2020**, *108*, 1551–1562. [CrossRef]
22. Vunnam, S.; Saboo, A.; Sudbrack, C.; Starr, T.L. Effect of powder chemical composition on the as-built microstructure of 17-4 PH stainless steel processed by selective laser melting. *Addit. Manuf.* **2019**, *30*, 100876. [CrossRef]
23. Ponnusamy, P.; Sharma, B.; Masood, S.H.; Rahman Rashid, R.A.; Rashid, R.; Palanisamy, S.; Ruan, D. A study of tensile behavior of SLM processed 17-4 PH stainless steel. *Mater. Today Proc.* **2021**, *45*, 4531–4534. [CrossRef]
24. Ali, U.; Esmaeilizadeh, R.; Ahmed, F.; Sarker, D.; Muhammad, W.; Keshavarzkermani, A.; Mahmoodkhani, Y.; Marzbanrad, E.; Toyserkani, E. Identification and characterization of spatter particles and their effect on surface roughness, density and mechanical response of 17-4 PH stainless steel laser powder-bed fusion parts. *Mater. Sci. Eng. A* **2019**, *756*, 98–107. [CrossRef]
25. Nath, S.D.; Irrinki, H.; Gupta, G.; Kearns, M.; Gulsoy, O.; Atre, S. Microstructure-property relationships of 420 stainless steel fabricated by laser-powder bed fusion. *Powder Technol.* **2019**, *343*, 738–746. [CrossRef]
26. Yang, X.H.; Jiang, C.M.; Ho, J.R.; Tung, P.C.; Lin, C.K. Effects of Laser Spot Size on the Mechanical Properties of AISI 420 Stainless Steel Fabricated by Selective Laser Melting. *Materials* **2021**, *14*, 4593. [CrossRef]
27. Jiang, C.M.; Ho, J.R.; Tung, P.C.; Lin, C.K. Tempering Effect on the Anisotropic Mechanical Properties of Selective Laser Melted 420 Stainless Steel. *J. Mater. Eng. Perform.* **2022**. [CrossRef]
28. Kultamaa, M.; Mönkkönen, K.; Saarinen, J.J.; Suvanto, M. Corrosion Protection of Injection Molded Porous 440C Stainless Steel by Electroplated Zinc Coating. *Coatings* **2021**, *11*, 949. [CrossRef]
29. Wang, X.; Zhao, L.; Fuh, J.Y.H.; Lee, H.P. Effects of statistical pore characteristics on mechanical performance of selective laser melted parts: X-ray computed tomography and micromechanical modeling. *Mater. Sci. Eng. A* **2022**, *834*, 142515. [CrossRef]
30. Zheng, Z.; Peng, L.; Wang, D. Defect Analysis of 316 L Stainless Steel Prepared by LPBF Additive Manufacturing Processes. *Coatings* **2021**, *11*, 1562. [CrossRef]
31. Liverani, E.; Fortunato, A. Additive manufacturing of AISI 420 stainless steel: Process validation, defect analysis and mechanical characterization in different process and post-process conditions. *Int. J. Adv. Manuf. Technol.* **2021**, *117*, 809–821. [CrossRef]
32. Sun, Z.; Tan, X.; Tor, S.B.; Chua, C.K. Simultaneously enhanced strength and ductility for 3D-printed stainless steel 316L by selective laser melting. *NPG Asia Mater.* **2018**, *10*, 127–136. [CrossRef]
33. *The CES Edupack 2013*; Granta's Design Ltd.: Cambridge, UK, 2013.
34. Online Materials Information Resource—MatWeb. Available online: https://www.matweb.com/ (accessed on 8 September 2022).
35. Zhao, X.; Song, B.; Zhang, Y.; Zhu, X.; Wei, Q.; Shi, Y. Decarburization of stainless steel during selective laser melting and its influence on Young's modulus, hardness and tensile strength. *Mater. Sci. Eng. A* **2015**, *647*, 58–61. [CrossRef]
36. Karthik, G.M.; Kim, H.S. Heterogeneous Aspects of Additive Manufactured Metallic Parts: A Review. *Met. Mater. Int.* **2021**, *27*, 1–39. [CrossRef]
37. Aqilah, D.N.; Sayuti, A.K.M.; Farazila, Y.; Suleiman, D.Y.; Amirah, M.A.N.; Izzati, W.B.W.N. Effects of Process Parameters on the Surface Roughness of Stainless Steel 316L Parts Produced by Selective Laser Melting. *J. Test. Eval.* **2018**, *46*, 20170140. [CrossRef]

Appendix B

Optimization of metallic powder filaments for additive manufacturing extrusion

The International Journal of Advanced Manufacturing Technology (2021) 115:2449–2464
https://doi.org/10.1007/s00170-021-07043-0

ORIGINAL ARTICLE

Optimization of metallic powder filaments for additive manufacturing extrusion (MEX)

Fábio Cerejo [1,2] · Daniel Gatões [2] · M. T. Vieira [2]

Received: 26 January 2021 / Accepted: 1 April 2021 / Published online: 25 May 2021

Abstract
Additive manufacturing (AM) of metallic powder particles has been establishing itself as sustainable, whatever the technology selected. Material extrusion (MEX) integrates the ongoing effort to improve AM sustainability, in which low-cost equipment is associated with a decrease of powder waste during manufacturing. MEX has been gaining increasing interest for building 3D functional/structural metallic parts because it incorporates the consolidated knowledge from powder injection moulding/extrusion feedstocks into the AM scope—filament extrusion layer-by-layer. Moreover, MEX as an indirect process can overcome some of the technical limitations of direct AM processes (laser/electron-beam-based) regarding energy-matter interactions. The present study reveals an optimal methodology to produce MEX filament feedstocks (metallic powder, binder, and additives), having in mind to attain the highest metallic powder content. Nevertheless, the main challenges are also to achieve high extrudability and a suitable ratio between stiffness and flexibility. The metallic powder volume content (vol.%) in the feedstocks was evaluated by the critical powder volume concentration (CPVC). Subsequently, the rheology of the feedstocks was established by means of the mixing torque value, which is related to the filament extrudability performance.

Keywords MEX · Filament · Additive manufacturing · Mixing torque · Austenitic stainless steel (316L)

1 Introduction

Additive manufacturing (AM) of powder metals and metal alloys is an unavoidable area for Industry 4.0 owing to its potential to address some of the most significant industrial challenges in the twenty-first century concerning parts/system/devices processing [1]. The rising trend to select AM processes is based on new design approaches, the ability to create near net shape 3D objects, cloud access to manufacturing, shorter time-to-market, product customization, and circular economy [2]. Among other factors, the possibility of merging cost savings and new part properties and features that are impossible to obtain using traditional manufacturing technologies is the largest benefit of AM. This manufacturing paradigm, concerning powder metal AM, has attracted significant interest over the past few years, where AM direct methods (e.g. Selective Laser Melting, Electron Beam Melting, etc.) established themselves as technologies for functional/structural metallic parts, with several components approved by ISO and ASTM standards in industries such as aerospace and automotive [3]. However, these processes have several drawbacks, the high-power source that can promote micro- and macroscopic defects in metallic parts due to the multiple thermal treatments of the deposited layers; material range, due to the energy-matter interaction that limits the powder characteristics, like reflectivity and conductivity; and significant powder wastes during manufacturing and handling hazard. Besides, the high cost of direct AM equipment is one of the major obstacles [4–10].

Material extrusion (MEX) and binder jetting (BJ) [11] are already well-established technologies with market acceptance for the AM. Based on this successful background, MEX and BJ have been investigated with the aim to produce metallic and ceramic functional/structural components through shaping, debinding, and sintering (SDS). In these indirect AM processes,

✉ Fábio Cerejo
fcerejo@ipn.pt

✉ Daniel Gatões
daniel.gatoes@uc.pt

[1] IPN - LED&MAT - Instituto Pedro Nunes, Laboratório de Ensaios, Desgaste e Materiais, Rua Pedro Nunes, 3030-199 Coimbra, Portugal

[2] University of Coimbra, CEMMPRE - Centre for Mechanical Engineering, Materials and Processes, Department of Mechanical Engineering, Rua Luís Reis Santos, 3030-788 Coimbra, Portugal

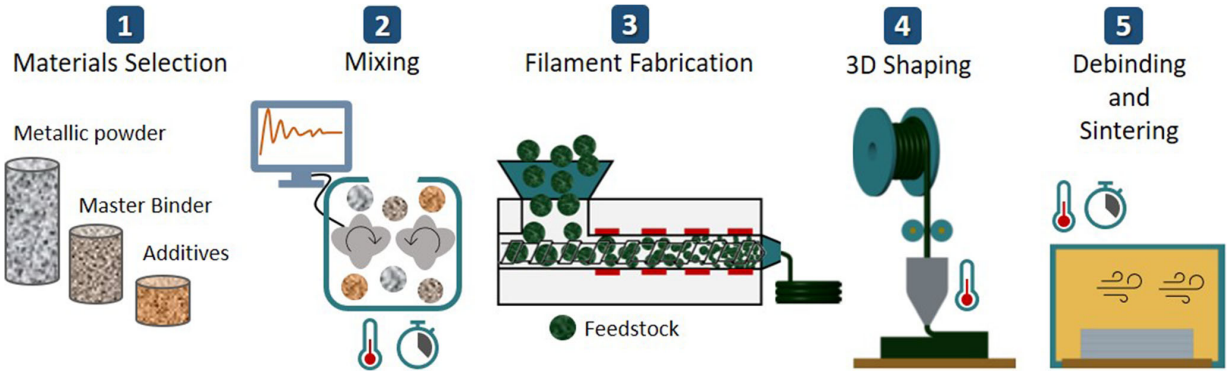

Fig. 1 MEX manufacturing route through the shaping, debinding, and sintering (SDS) process

unlike direct methods, the material processability is independent of the power source, which makes the production of functionally graded materials feasible [12]. Regarding shaping, BJ and MEX differ from each other and are often complementary technologies, since resolution, the optimal number of parts per production, the necessity of supports, material, and equipment costs are unique for each process. In BJ, the binder droplets are selectively deposited to interact with powder particles, which present new challenges not associated with MEX, such as powder/binder wettability; binder vertical migration, since layer height affects the penetration depth of the binder, through time and capillary force; and binder saturation that must be fine-tuned, as well as droplet size and dispensing frequency. However, the metallic powder is fed independently of the binder, which makes the rheological properties not as hard to control as it happens with MEX, which is beneficial to achieve the highest vol.% of metallic powder and less binder content in the shaped 3D object [12, 13]. Even though both technologies differ in what concerns the powder-binder processability, they also face the same challenges, such as optimizing debinding heating profiles to degrade the polymer is time-consuming; possible undesired reactions from residual polymer ash that could affect the final properties; and porosity, since both technologies do not have high pressures that promote the highest final part densification [12, 14].

The present study is focused on the MEX technology, which was initially referred to as the fused deposition of metals (FDMet), and then as Fused Filament Fabrication (FFF) or as Metallic Fused Filament Fabrication (MF^3) [15]. MEX is based on the fused deposition modelling (FDM^{TM}) technology commercialized by Stratasys Inc. for polymers and waxes, where the filament is composed of a mixture of a high volume content (vol.%) of metallic powders with organic constituents [16]. MEX is suitable for manufacturing geometrical complex metal parts in conjunction with post-shaping steps, such as debinding and sintering [17].

The processing by MEX technology consists of 5 stages (Fig. 1), as follows: Stage 1, materials selection; Stage 2, mixing (1+2=powder material extrusion feedstocks fabrication); Stage 3, feedstock extrusion (filament); Stage 4, 3D part/device built layer-by-layer (green) from extruded filament; and Stage 5, binder removal (debinding) and subsequent consolidation of metallic powder particles (sintering). The first two stages are fundamental to attain an appropriate viscosity and an excellent balance between flexibility and stiffness of the filament associated with the highest content

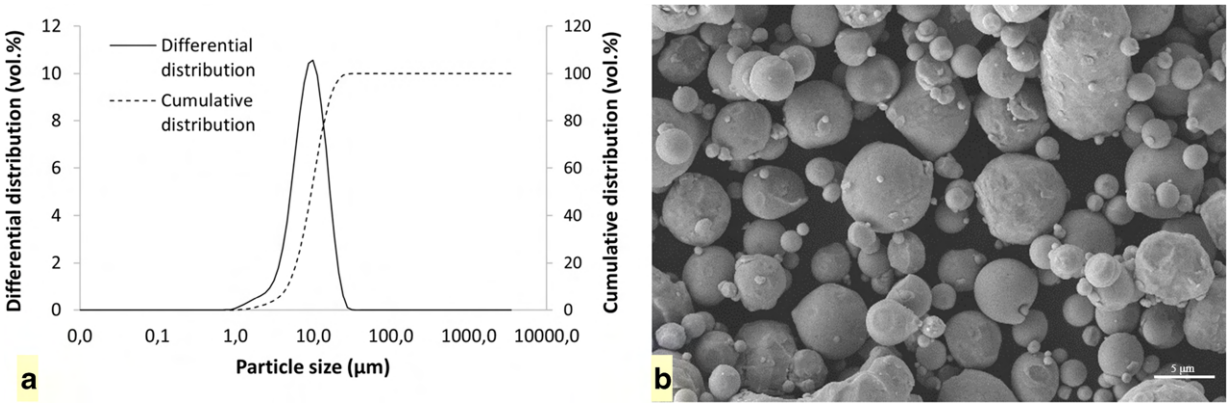

Fig. 2 **a** Particle size distribution (Malvern Mastersizer 2000) and **b** powder shape (SEM analysis, SE) of the SS 316L powder

(%vol) of metallic powders and a subsequent homogeneity (chemical and dimensional) needed to attain low porosity and excellent quality of the parts/devices.

High-quality structural/functional parts/systems/devices through an SDS process must include efforts to achieve the highest content (vol.%) of the metallic powder particles possible in the feedstock within the steady-state regime but always taking into account the final mixing torque value. This becomes a significant challenge in MEX because the mixture must be manufactured in a filament form. Based on these assumptions, there are a few available studies in the bibliography. Agarwala et al. obtained stiff and straight filaments from feedstocks with 60 vol.% 17-4PH grade stainless steel (SS) [18]. Kukla and Gutierrez et al. [19, 20] used 55 vol.% SS 316L and 17-4PH; Godec et al. [10] also selected 55 vol.% SS 316L, as well as Burkhardt et al. [21]. Anderson et al. [22] produced SS 316L grade filaments with 55 vol.%; Kurose et al. [23] used SS 316L grade filaments with 60 vol.%. Gloeckle et al. [24] performed an extensive study on the printability of Ti-6Al-4V filaments with up to 60 vol.% of inorganic material, and Singh et al. [15] used the same Ti-6Al-4V with 59 vol.%. BASF SE® has a commercially available SS 316L filament with a metallic powder content lower than 60 vol.% [25].

The mechanical performance of MEX metallic filaments has been a major limitation for increasing the ratio between inorganic and organic constituents since high powder concentration can lead to poor extrudability, where the filament becomes too brittle to be handled. A balance between stiffness and flexibility must be guaranteed to promote filament printability [15, 19].

The focus of the present study is to develop filaments with the highest metallic powder volume content (>50 vol.%) that link the primary MEX filament requirements to a suitable viscosity and mechanical behaviour. The selection of the highest content of metallic powder was evaluated by critical powder volume concentration (CPVC) methodology [26–28]. This procedure aims to promote the highest part green density, which is essential for maintaining the part shape integrity after debinding and sintering.

The present study aims to contribute, whatever the powder selected, to high-quality filaments for MEX technology, that is in conjunction with binder jetting technology, the future of AM of functional/structural 3D metallic objects.

Table 1 SS 316L powder characteristics

d_{10} [μm]	d_{50} [μm]	d_{90} [μm]	SSA* [kg/m^2]	ρ [kg/m^3] **
4.63	9.43	16.60	786	7896 ± 30.2

*Specific surface area

**Density

2 Materials and methods

2.1 Characterization techniques

The characterizations of the powders, feedstocks, and filaments were performed through the following techniques: laser diffraction to measure the particle size (Malvern Mastersizer 2000, Malvern Instruments Ltd, Worcestershire, UK) according to ISO 13320:2009(E); helium pycnometry to measure the density, based on the mean of five runs for each specimen (Micromeritics AccuPyc 1330, Micromeritics Instrument Corporation, Norcross, GA, USA); scanning electron microscopy (SEM) to analyse the morphology and shape factor (FEI Quanta 400FEG, FEI Europe BV, Eindhoven, The Netherlands) x-ray diffraction (XRD) according to EN 13925:2003, to identify the phases (Philips X'Pert, cobalt radiation $\lambda_{k\alpha1}$= 0.1789 nm and $\lambda_{k\alpha2}$= 0.1793 nm, Bragg-Brentano geometry, Philips, Eindhoven, Netherlands); and TGA to analyse the weight variation kinetics (TGA Q500 V20.13, TA Instruments, DE, USA). The filament was micro-CT (X-ray micro computed tomography) scanned using a Bruker SkyScan 1275 (Bruker, Kontich, Belgium). An acceleration voltage of 80 kV and a beam current of 125 μA was set while using a 1-mm aluminium filter and step-and-shoot mode. Pixel size was set to 6 μm, and random mode was used. In total, 1056 projection images were acquired at 0.2° angular step with 5 frames average per step using an exposure time of 46 ms. The micro-CT images were reconstructed with the dedicated manufacturer software.

A three-point flexural test of each filament was performed five times using SHIMADZU-EZ-LX (Shimadzu Corp., Kyoto, Japan) equipment with a load capacity of 500 N. The load was applied to the specimen at a rate of 0.5 mm/min with a span length of 20 mm.

3D prototype geometries were measured with Focus Variation Microscopy (FVM) using Alicona InfiniteFocusG4 (Alicona Imaging; Graz, Austria). Hardness measurements, according to ISO 6507-2:2018, were performed with a Shimadzu

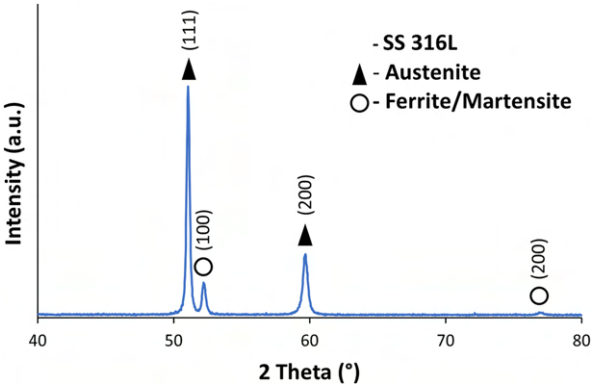

Fig. 3 SS 316L XRD diffractogram; λ Co = 0.1789 nm (Philips X'Pert)

Table 2 Densities of the binder and additives measured with a helium pycnometer (Micromeritics AccuPyc 1330)

	M1	TPE	ULD-PE	S†	P✕
Density [kg/m^3]	970 ± 1	1028 ± 12.2	9144 ± 1.5	983 ± 1	965 ± 0.6

S† Surfactant

P✕ Plasticizer

HMV microhardness tester (Shimadzu Corp., Kyoto, Japan). For each measurement, a load of 9.8 N was applied for 15 s by a Vickers indenter.

2.2 Metallic powder, binder, and additives

The set material for this study was austenitic stainless steel 316L (SS 316L) since it is one of the most studied materials in AM. This material can be a good standard for the methodology to be established by the present work and extrapolated to other metallic alloys [29].

The characteristics of the selected powders were studied using the 4S's methodology (size and size distribution, shape, and structure). The particle size is d_{50} = 9.43 μm. Figure 2 shows the particle size distribution (a) and particle shape factor (b). Shape factor was close to 1 for the nitrogen-atomized SS 316L powders (Sandvik Osprey Ltd., Neath, UK).

Table 1 summarizes the powder characteristics.

The X-ray diffractogram (Fig. 3) of the SS 316L powder exhibited a biphasic character, where the major phase was austenite (ICDD 33-0397). However, other peaks with low I/I_0 were present, which can be indexed as (100), (200) that are typical of ferrite/martensite (ICDD 87-0722). The cooling stress could contribute to the evolution of the austenite phase into martensite. Nevertheless, nitrogen atomizing results in lower stress in the particles than those from water atomizing, where martensite is more prevalent for a similar powder [30].

In the present study, the organic constituents of the feedstocks were divided into two primary groups: master binder and additives; the last one includes the backbone and surfactant/plasticiser. The selected master binder (M1) was a commercial-grade (Atect Corp., Shiga, Japan) that is a mixture of polyolefin waxes and > 60 wt. % of polyoxymethylene (POM). Although POM is included, this binder is commercialized as a thermal-only debinding and previous studies with this binder shown that no carbonaceous residues remained on the final parts. The thermoplastic elastomer (TPE), as well as an ultra-low density polyethylene (ULD-PE), was used for the backbone, and a surfactant (stearic acid (S †)) and an external plasticizer (P ✕) were used as additives. Density of master binder and additives (Table 2) was performed to support the theoretical calculations of the volume of these constituents in the feedstock, which is further compared with the practical results (TGA analysis).

2.3 Filament production

The vol.% of each organic component in the feedstock was tailored to achieve the proper filament properties for MEX (rheology and flexibility/stiffness balance). The CPVC and

Table 3 Filament feedstocks

Feedstock	Master binder	Additives				Powder	
		Backbone	Backbone content (vol.%)*	S† or P✕	S† or P✕ (vol.%)	SS 316 L content (vol.%)	Particle size d_{50} (μm)
F01	M1	-	-	-	-	60	6.85
F02	M1	TPE	*Y*	-	-	60	6.85
F03	M1	TPE	*X*	S†	5	60	6.85
F04	M1	TPE	*X* + 5	S†	5	60	6.85
F05	M1	TPE	*X* + 10	S†	5	60	6.85
F06	M1	TPE	*X*	P✕	5	60	6.85
F07	M1	TPE	*W*	P✕	10	60	6.85
F08	M1	ULD-PE	*X*	P✕	5	60	6.85

*The exact ratio of master binder/backbone in the feedstock will be kept confidential. *Y*, *X*, and *W* represent the different amounts of backbone (vol.%).

X = *Y* – 2.5 vol.%; (½ of S/P content: 5 vol.%).

W = *Y* – 5 vol.%; (½ of F07 plasticiser (P) content: 10 vol.%).

S†, Surfactant

P✕, Plasticiser

Int J Adv Manuf Technol (2021) 115:2449–2464 2453

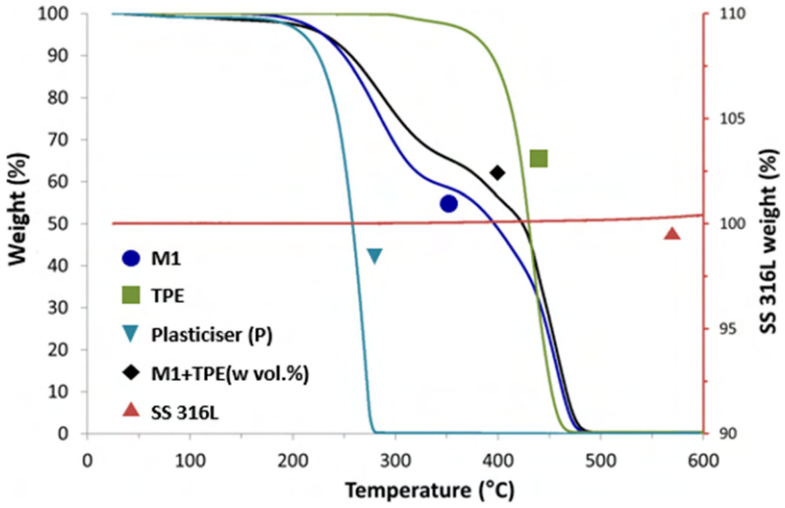

Fig. 4 TGA curves of the SS 316L, M1, TPE, and M1 + TPE under an N_2 atmosphere

feedstock optimization was performed with a torque rheometer (Plastograph® Brabender W 50, Brabender GmbH & Co. KG, Duisburg, Germany) that evaluates the torque variation as a function of the powder composition. The temperature inside the 38.5 cm^3 mixing chamber of 180 °C was selected together with 30 rpm blades rotation speed, taking into account previous work with the same master binder [31]. For the CPVC evaluation, an increment of 1 vol.% powder content was made approximately every 10 min or after reaching a steady state. The backbone percentage was not higher than 30% of the total organic portion. Table 3 summarizes the different feedstock compositions (F01–F08, F03A, and F03B). Each formulation mixing torque value was evaluated from six independent measurements and done until a steady-state regime was achieved.

Small pellets of feedstocks were extruded into a filament form. Filament fabrication was performed in a single screw extruder (Brabender GmbH & Co., Duisburg, Germany) with 5 heating zones. The temperature of the zones, from feeder to nozzle (ø 1.75 mm), was set at 160, 165, 170, 175, and 180 °C. The screw rotation speed was set at 5 rpm. The filament was measured at multiple points to guarantee its dimensional accuracy throughout the filament fabrication process.

Instead of using catalytic debinding, thermal debinding was selected, which shows no carbonaceous residues present during sintering, consistent with previous studies with low-pressure injection moulding [31], thus voiding the nitric acid used for catalytic debinding. The thermogravimetric analysis highlights that all of the organic constituents of the feedstock fully degrade, during the debinding stage (Fig. 4).

The thermal cycles in this work were selected based on thermogravimetric analysis (TGA). The primary events in the master binder and backbone weight loss curves up to 600 °C (Fig. 4 and Table 4) were the isothermal plateaus during the debinding stage. The beginning and ending values were evaluated from the first derivative (DTG) of the respective curve. At 495 °C, the carbonaceous residue was close to 0 wt.%.

Concerning the thermal oxidation of the as-received SS 316L powder, TGA showed that it was quite stable up to 600 °C in an N_2 atmosphere. An insignificant increase in the weight of the powder was noticeable above 500 °C. This is not

Table 4 Weight loss and degradation temperatures of the M1, TPE, and M1 + TPE

Binder component	Degradation stage	Weight loss [%]	Onset [°C]	End [°C]
M1	1st	41	232	314
	2nd	13	378	437
	3rd	46	437	472
TPE	1st	2	300	327
	2nd	98	408	454
M1 + TPE	1st	35	238	320
	2nd	11	375	398
	3rd	23	427	441
	4th	31	450	475
Plasticizer	1st	100	242	276

2454 Int J Adv Manuf Technol (2021) 115:2449–2464

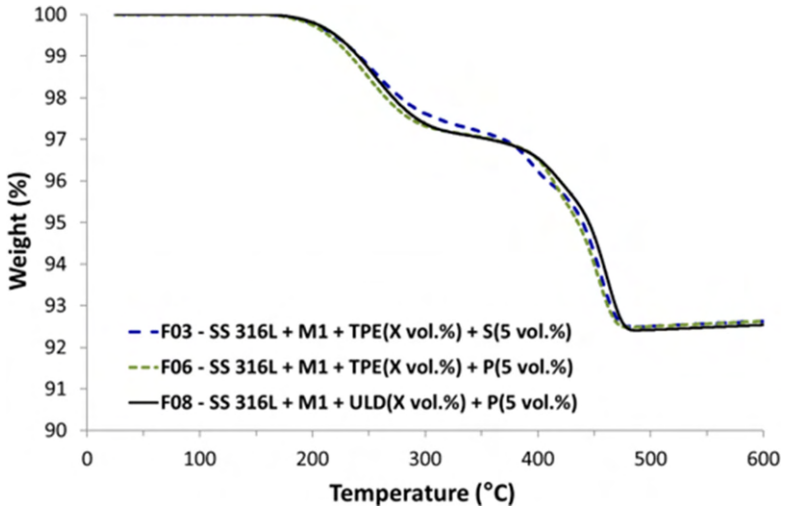

Fig. 5 TGA curves of the filaments F03, F06, and F08 with 60 vol.% of SS 316L powder under an N_2 atmosphere

exclusively attributed to the TGA protective atmosphere type (N_2) because other studies show the same behaviour under an Ar + H_2(5%) atmosphere [30, 32].

A significant difference was not detected in the debinding kinetics of the M1 and TPE as raw materials (Fig. 4) and as feedstocks constituents (Fig. 5) when mixed with 60 vol.% of metallic powder. This is an indication that there are no undesired reactions among the feedstock constituents that could interfere in the debinding cycle.

Table 5 shows a comparison of the theoretical values against the final experimental values (wt.%) of the feedstock filaments at 600 °C in order to illustrate the expected SS 316L weight (%) after binder degradation based on the SS 316L vol.% in the feedstock. The small deviation between theoretical and experimental values can be attributed to the experimental evaluation of the densities and can be assumed that the binder degradation was total.

2.4 Printability

Green specimens were built on a BQ Prusa I3 Hephestos 3D printer. Extruder nozzle temperature was maintained at 210°C, extrusion speed was limited to 10 mm/s, and extrusion multiplier was set at 1.4. Layer height was set at 0.20 mm, and the selected nozzle diameter was 0.40 mm. A glass platform with a layer of glue was used, to promote part adhesion, since this 3D printer has no heated build plate feature.

Table 5 TGA experimental vs theoretical weight reduction of filaments F03, F06, and F08

Feedstock	Metallic powder [wt.%]	
	Experimental	Theoretical*
F03	92.5±0.1	92.4
F06	92.5±0.1	92.4
F08	92.4±0.1	92.4

*Conversion from SS 316L 60 vol.%

2.5 Debinding and sintering

The heating rates for debinding and sintering were 1 °C/min and 10 °C/min up to the maximum temperatures of 600 °C and 1250 °C, respectively, including several debinding isothermal holding times, based on the TGA results. The filaments and parts were debinded and sintered under H_2 atmosphere at 4×10^{-2} MPa.

3 Results and discussion

3.1 Feedstock optimization

3.1.1 Evaluation of the critical powder volume concentration

The evaluation of the CPVC in each feedstock was performed by recording the mixing torque to maximize the metal powder content (vol.%), to promote higher green densities. Nevertheless, MEX feedstocks require overcoming new challenges (rheology and flexibility/stiffness balance) because the filament must be spooled, handled, and extruded through a small-diameter nozzle. Therefore, PIM feedstocks must be modified to be suitable for MEX, and the rheological behaviour of the new feedstock must be studied.

Torque values were recorded for the initial mixture of the master binder and additives F06 (M1 + TPE + P) with 50 vol.% SS 316L powder. The effect of

Int J Adv Manuf Technol (2021) 115:2449–2464 2455

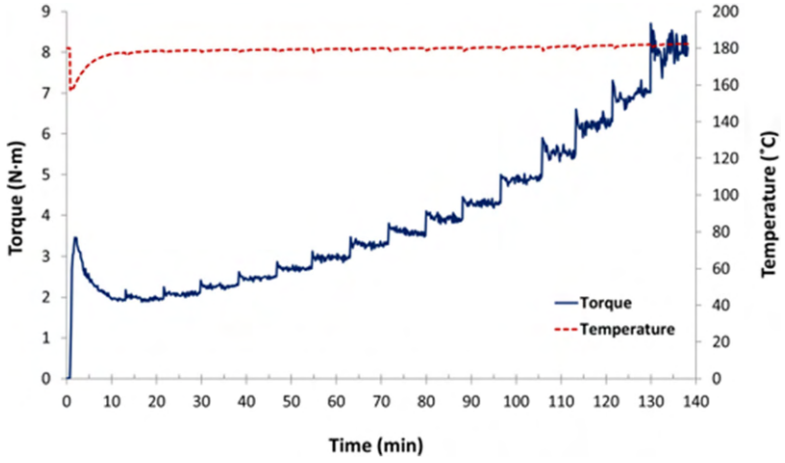

Fig. 6 Torque as a function of time of the F06 feedstock at 180 °C with the incremental addition of 1 vol.% of SS 316L

subsequent additions of metallic powder (1 vol.%) on the torque value, shown at every peak from the 10-min mark, was measured after attaining a steady-state regime for each percentage (Fig. 6). Based on this evaluation, the defined ratio of inorganic/organic vol.% among all studied feedstocks was maintained.

Figure 7 shows the torque values for the incremental additions of 1 vol.% of SS 316L powder (50–65 vol.%). Three linear regimes can be observed:

- The first regime includes up to 58 vol.% of SS 316L powder, and the torque variation between each addition is between 1.9 (50 vol.%) and 3.5 N·m (58 vol.%).
- In the second regime, at up to 62 vol.% of SS 316L powder, the mixture rheology changes, which corresponds to a slightly higher slope than the first regime, and the maximum torque is 5.4 N·m.
- The third regime, where the most significant variation occurs (62–65 vol.%), reaches the highest mixing torque value (8.1 N·m). In this range, the mixing torque behaviour clearly becomes more unstable (cf. Fig. 7).

The CPVC should correspond to the interface torque value between the second and third regimes (point of intersection), which in the present study was 62 vol.%. However, a great number of studies performed concerning the optimization of powder and binder feedstocks show that the torque value should not exceed 5 N.m for this specific torque rheometer (Plastograph® W 50), to attain the best rheological properties, in order to guarantee optimal processability [28, 33, 34].

Based on the CPVC evaluations (Figs. 6 and 7) and keeping in mind that the feedstock flowability to build the green part, through a 3D printer with a 0.4-mm nozzle, is promoted by the filament (it acts like a piston through the 3D printer pull system) and not by a screw (high pressures), 60 vol.% (torque value of 4.3 N.m) was selected as the metallic load for all studied feedstocks.

3.1.2 Effect of additives in the feedstock

In PIM, the binder generally promotes the best compromise between green integrity and flowability.

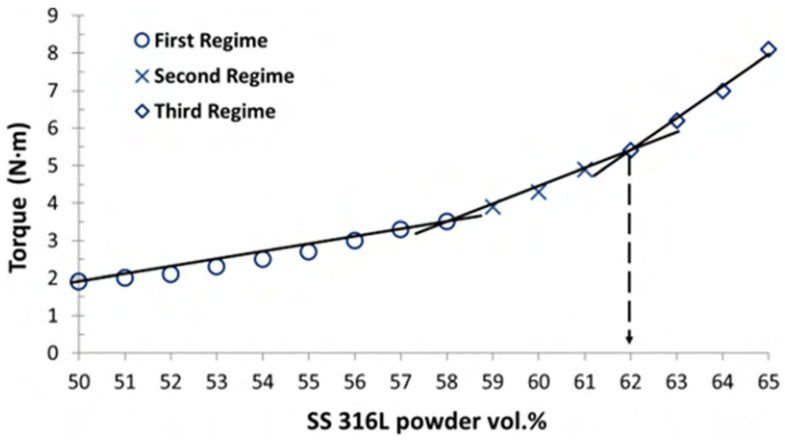

Fig. 7 Three different regimes of torque as a function of powder volume concentration (feedstock F06)

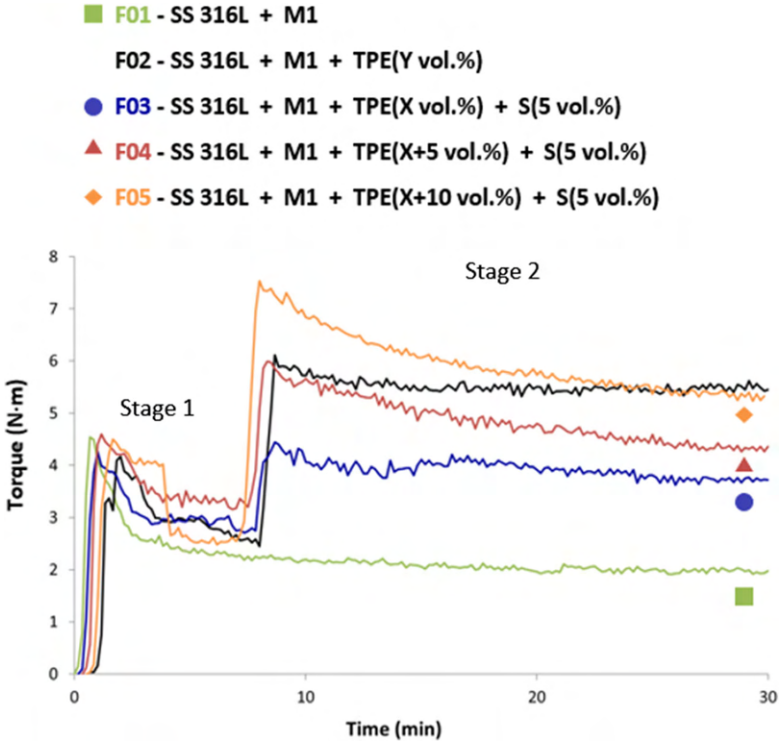

Fig. 8 Mixing torques (F01-F05) as a function of time ($Y < X$ vol.%.); Stage 1, only binder addition; Stage 2, feedstock with additive addition. F01 is the standard feedstock without additives

However, as previously mentioned, flexibility is one of the major characteristics of MEX filaments. For this reason, the backbone, surfactant, and plasticizer content were optimized. To select the best feedstock composition, two different approaches were considered: the addition of TPE + surfactant (S) and the addition of TPE + plasticizer (P).

Figure 8 shows the impact of the additive composition on the final torque value at the end of 30 min. F01 is a feedstock

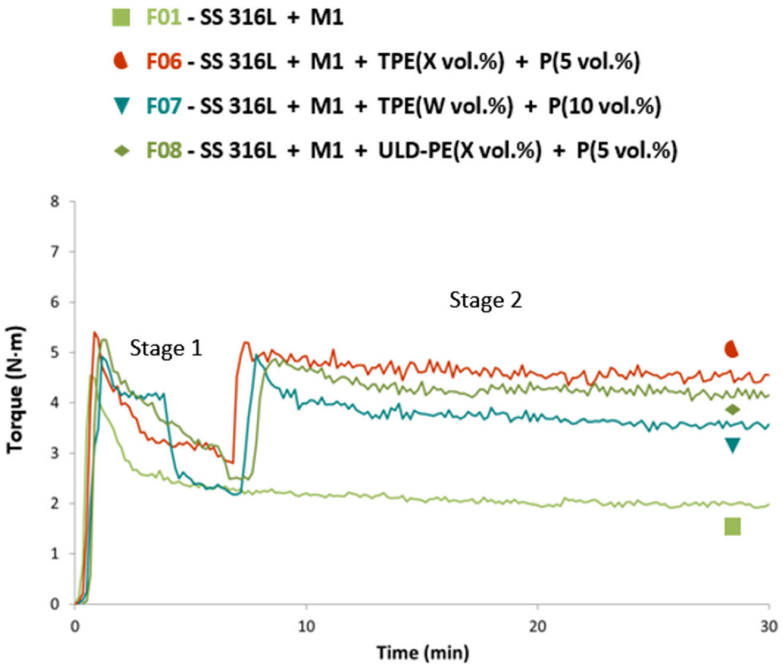

Fig. 9 F01 and F06–F08 mixing torques as a function of time ($W < X$ vol.%); Stage 1, only binder addition; Stage 2, feedstock with additive addition. F01 is the standard feedstock without additives

Int J Adv Manuf Technol (2021) 115:2449–2464 2457

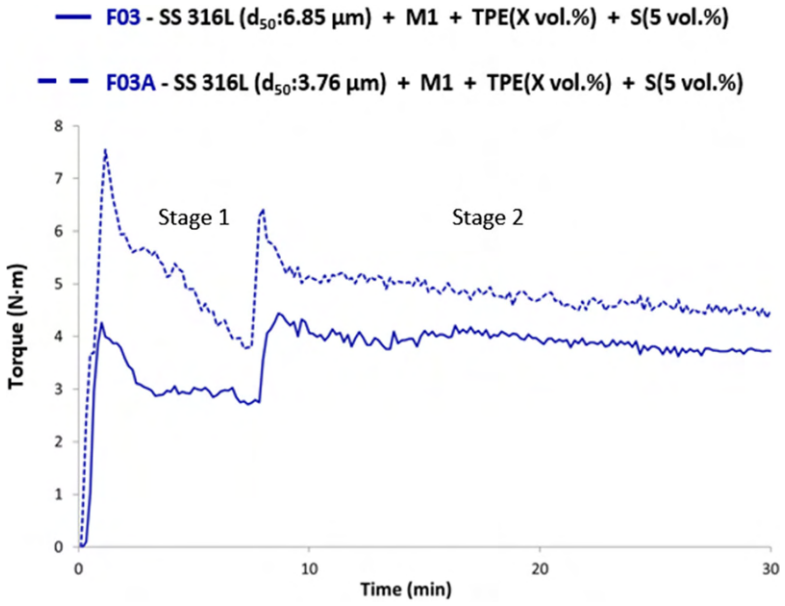

Fig. 10 Torque of the F03A and F03 mixtures as a function of time; Stage 1, only binder addition; Stage 2, feedstock with additive addition

used in PIM, where there are no concerns about flexibility. In addition to promoting filament flexibility, TPE has a negative impact on the rheological behaviour of the feedstock. To overcome this issue, a surfactant (S) was added. Among the feedstocks in Fig. 8, F03 (blue curve) showed the most promising behaviour (close to 4 N.m).

Although the selected surfactant, stearic acid (SA), clearly reduced the feedstock torque, other mixtures were studied to possibly replace it owing to the difficulty of fully removing it during debinding. Other work reported that SA requires raising the debinding temperature from 600 to 700 °C [30]. Thus, SA was replaced with a plasticizer (P), which also acts as a rheological modifier with the advantage that it promotes filament flexibility.

Figure 9 shows the different torque values for the remaining studied feedstocks (F06–F08). F06 had a final torque (4.6 N·m) that was higher than that of F07 (3.6 N·m) due to its high TPE content. Comparing the feedstocks with the same vol.% of all constituents (F03, F06, and F08), the addition of the surfactant (F03) had a larger influence on the final torque value than a plasticizer (F06 and F08), as expected. However, the plasticizer boosts filament flexibility, which is a very important requirement.

The feedstock F08, which had the composition as F06 except the TPE was replaced by ULD-PE, had a lower torque value, but it was still higher than the feedstock with SA (F03). Based on torque values of the feedstocks, F06–F08 seem to be suitable for use in MEX.

3.1.3 Influence of metal powder particle size

To evaluate the influence of the SS 316L powder particle size on the rheological behaviour of the feedstock, two mixtures with the same vol.% of SS 316 and additives but different particle sizes were compared: F03A and F03 with d_{50} = 3.76 µm and d_{50} = 6.85 µm, respectively (Fig. 10). The finer particle size led to a higher final mixing torque compared with that of F03. For this reason, powder with d_{50} = 3.76 µm was not selected for the studied feedstocks. This is an expected behaviour as small particles have a high specific surface area of contact, which promotes high interparticle friction [35].

Table 6 summarizes the average of ten torque values for each of the different feedstocks.

Table 6 Torque values of different feedstocks

	F01	F02	F03	F04	F05	F06	F07	F08	F03A
Torque [N.m]	2.0±0.04	5.5±0.07	3.7±0.03	4.3±0.04	5.3±0.06	4.5±0.07	3.6±0.05	4.2±0.07	4.6±0.07
Backbone content	-	*Y*	*X*	*X*+5	*X*+10	*X*	*W*	*X*	*X*
$S^{\dagger}$ or $P^{\divideontimes}$ (vol.%)	-	-	5	5	5	5	10	5	5

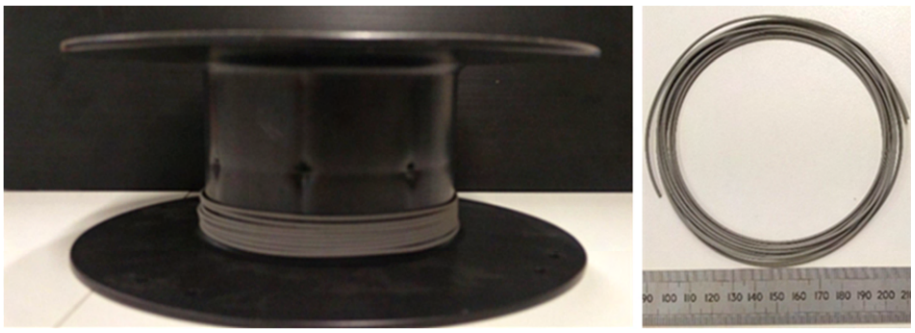

Fig. 11 Spooled filament from feedstock F06

3.2 Filaments

3.2.1 Green filament production

In this study, the filament was not spooled by an automatic system. To avoid filament diameter deviations due to gravity action, a constant height between the extruder nozzle and the table was preserved for all formulations.

Standard filament (powder and binder, F01) was too brittle to spool. TPE addition resulted in the highest final torque value (5.5 N.m) in mixture F02 curve. Also, the torque profile is the most unstable, because the dispersion of powder

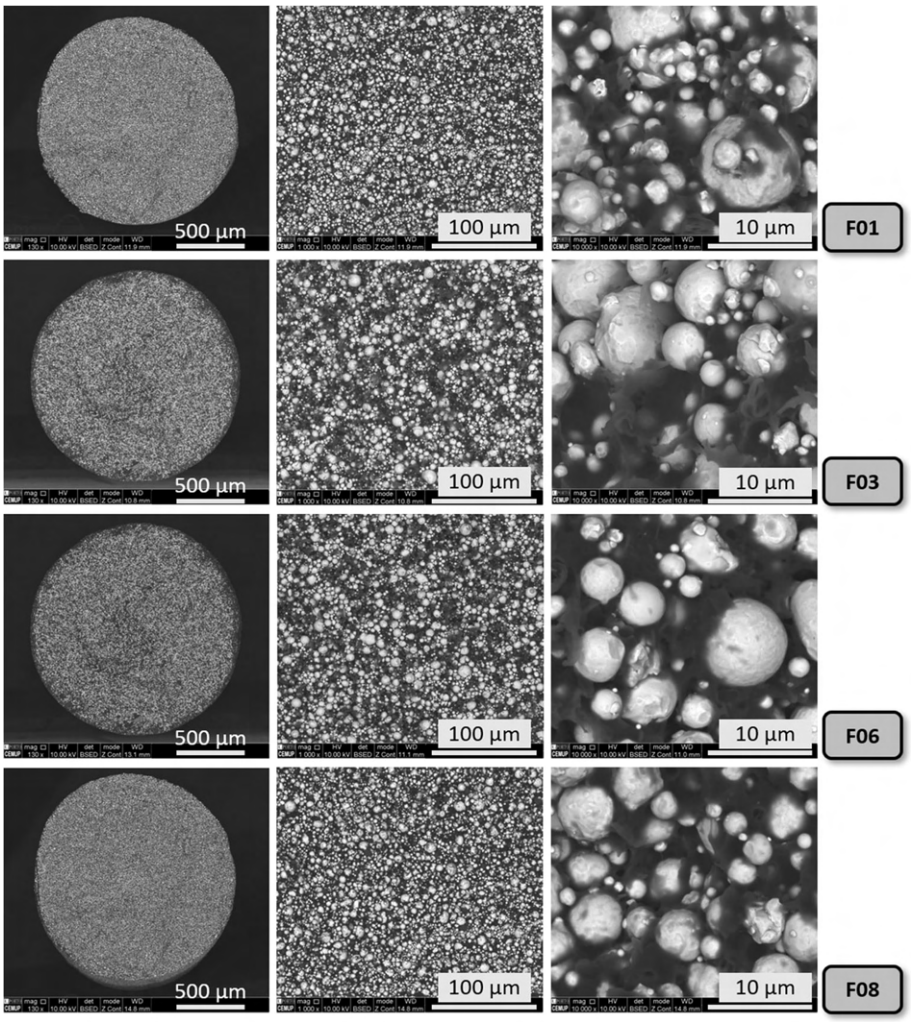

Fig. 12 Cross-section fracture surfaces of filaments F01, F03, F06, and F08

Int J Adv Manuf Technol (2021) 115:2449–2464 2459

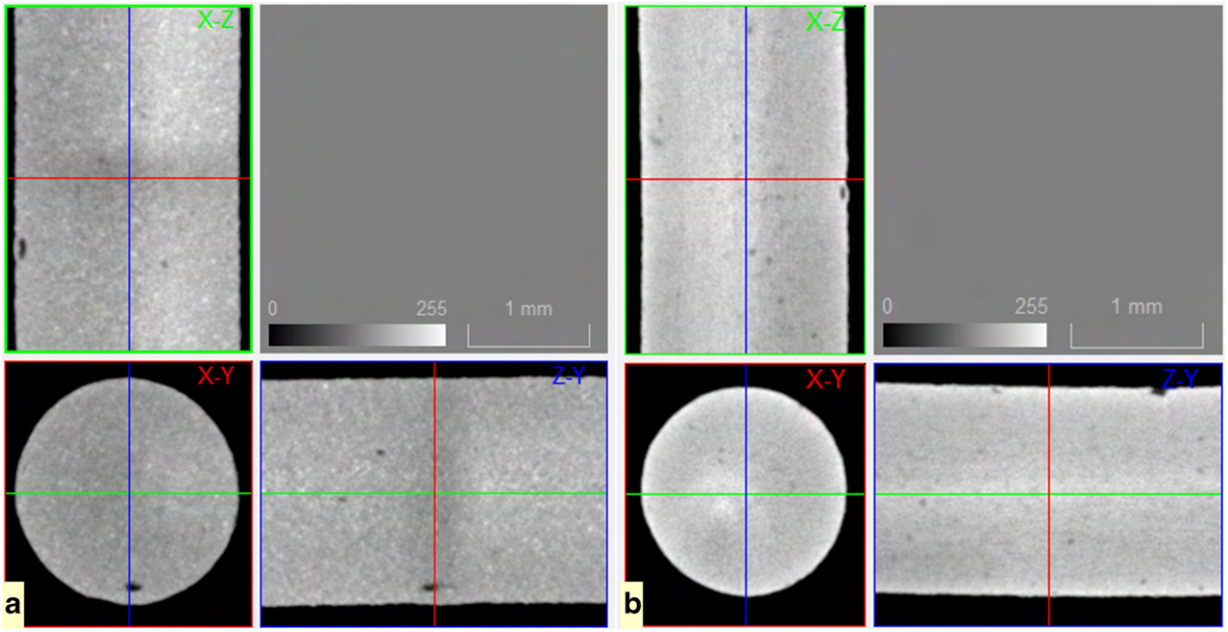

Fig. 13 Micro-CT of the **a** green filament F06 and **b** sintered filament F06 – green filament with the highest homogeneity

particles is more problematic in this binder. Thus, F02 was not extruded in a filament form. The other feedstocks (powder, binder, and additives) could be spooled (F03, F04, F05, and F08) but with a higher curvature than those of F06 and F07 (Fig. 11). It must be emphasized that the best filaments were those resulting from feedstocks with plasticizer and torque close to 5.0 N·m.

3.2.2 Characterization

3.2.2.1 Homogeneity SEM observations of the filament cross-section shown that filament feedstocks without TPE (F01 and F08) appeared to be more homogeneous than the others (F03 and F06, Fig. 12), but their flexibility was poor. F03 and F06 (= M1 + TPE + S/P vol.%) were quite similar regarding the homogeneity of the distribution of metallic powder. A large powder particle distance in the feedstocks improves flexibility but decreases density. Thus, considering these two features (filament flexibly and interparticle distance), a homogenous powder distribution is crucial, and a suitable balance between these features is required for the success of MEX.

Micro-CT analysis can be an effective solution for assessing filament homogeneity without fracture, which can modify the defect distribution on the observed volumes. Micro-CT was performed in a representative cross-section of filament F06 in the green and sintered states (Fig. 13 a and b, respectively). It can be noted that the green filament (extruded feedstock in filament form, not subject to any subsequent processing step) presents a high density and consistent diameter throughout its section, reiterating the mechanical behaviour results (cf. 3.2.2.3). The observed residual pores seem to follow the extrusion direction (Fig. 13a, *X-Z* and *Z-Y* section), suggesting that the defects may occur in the extrusion process, resulting in elongated pore geometry. Nevertheless, the sintered filament shows that a sintered part with consistent density, with no persistent porosity caused by debinding, is still achievable, indicating that resulting porosity in final parts may be connected to printing parameters.

3.2.2.2 Structure The X-ray diffractograms (Fig. 14) show the evolution from SS 316L powder to the green and sintered filament. As referred, the austenitic powder, owing to its preparation technique, besides austenite (ICDD 33-0397), presents a ferrite/martensite phase (ICDD 87-0722—Fig. 3). This one increases, as expected, due to the deformation of powders

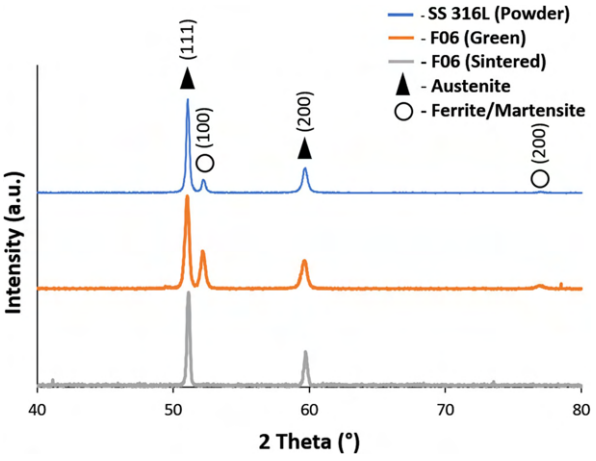

Fig. 14 X-ray diffraction of the sintered filament F06

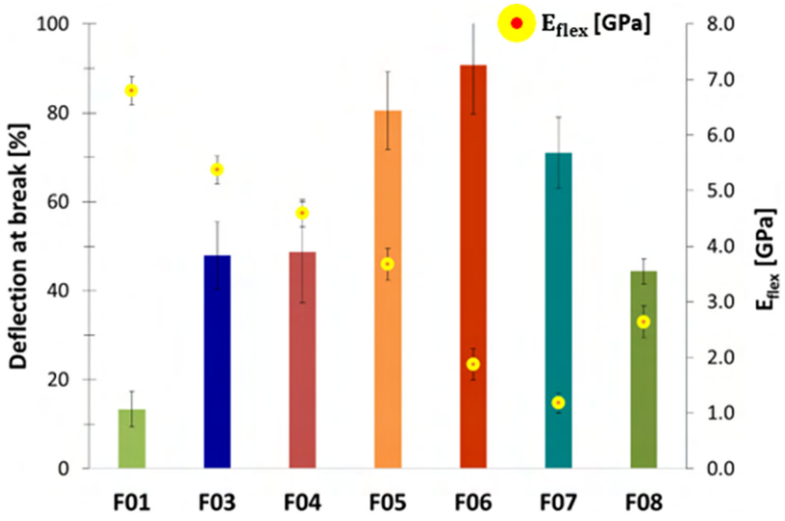

Fig. 15 Deflection at break (%) and E_{flex} of filaments F01 and F03–F08

during its extrusion (Fig. 14) [36]. However, after sintering, the X-ray diffractogram shows only constituted by the austenitic phase, avoiding a post heat treatment, required in other additive processes.

3.2.2.3 Mechanical behaviour The deflection at rupture (%) and flexural modulus of elasticity (E_{flex}) was measured by three-point bending tests (Fig. 15). Each value in the figure is the average of five tests. These results, together with the previous torque rheometry study, allowed for selecting the most promising filament feedstocks regarding green processability.

The filament from feedstock F01, without additives, was the most brittle (13%). With the incremental addition of TPE to feedstocks F03–F05, the maximum deflection of the filaments increased. Comparing filaments F03 and F06 (equal vol.% of organic constituents), the replacement of the surfactant with a plasticizer improved the flexibility. A reduction in deflection from F06 (91%) to F07 (71%) was noticeable. F07

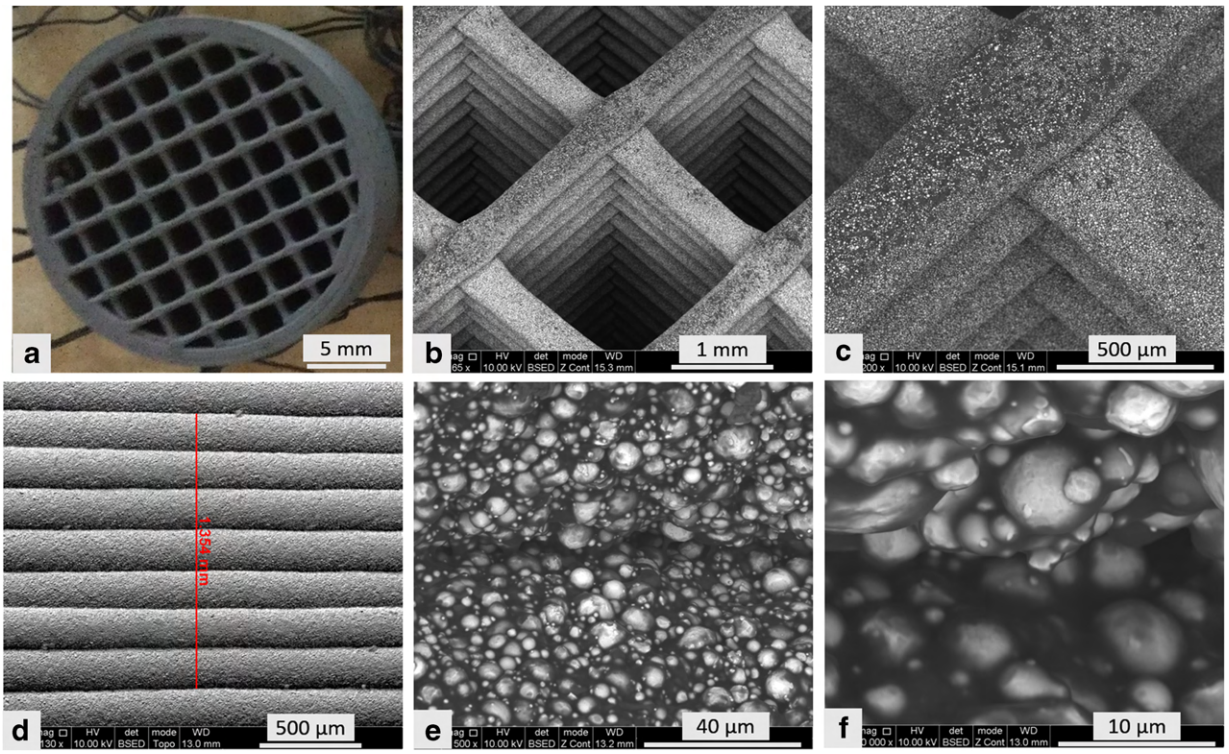

Fig. 16 Morphological analysis of the F06 green part: **a**, **b**, and **c** top views; **d**, **e**, and **f** side views

Int J Adv Manuf Technol (2021) 115:2449–2464 2461

Table 7 FVM part dimensions (before and after sintering)

	Height (mm)		Diameter (mm)	
	Green	Final part	Green	Final part
Measurement 1	7.2	6.2	19.7	16.5
Measurement 2	7.2	6.2	19.7	16.5
Mean	7.2	6.2	19.7	16.5
Shrinkage (%)	13		16	

Table 8 FVM part infill evaluation (before and after sintering)

	Measurement	Distance (mm)					
		1	2	3	4	5	6
Green	Direction 1	1.6	1.6	1.6	1.6	1.6	1.6
	Direction 2	1.6	1.6	1.6	1.6	1.5	1.7
Final	Direction 1	1.3	1.3	1.3	1.3	1.3	1.3
	Direction 2	1.3	1.3	1.3	1.3	1.2	1.4
Shrinkage (%)		19	18	19	19	19	19

had the highest additive content and, consequently, less TPE in the feedstock. F08 had ULD-PE instead of TPE. The reduction in the F08 filament flexibility (44%) is more obvious compared to that of F06, which had the same additive, a plasticizer. In fact, filament from feedstock F08 was not used to produce the green parts because it was brittle, despite its promising mixing torque (4.2 N·m).

The E_{flex} results of F07 and F08 were not expected, taking into account the relationship between the maximum deflection at break and the E_{flex} of the remaining filaments. This can be attributed to several factors, including porosity and the non-homogeneous feedstock mixture. Similar behaviour was also reported by another study [19].

3.3 Proof of concept

The printability of the spoolable filaments (F03-F08) was studied. Filaments with the same surfactant (SA) but different TPE content (F03 and F04) were successfully printed. F05 was not printable owing to its high torque value, which was promoted by the high amount of TPE (vol.%). F08 was too brittle to be printable, although within optimal mixture torque range. F06 and F07 shown the best printing behaviour.

The filament with the best mechanical characteristics (F06) was used to produce a part consisting of an infill pattern extrusion lines (0.4 mm) in a grid form and a two-perimeter exterior. Figure 16 shows different details of the green part (top and side views) built from the selected filament. Figure 16b shows that a single extrusion line is geometrically reliable (not considering the flat zones due to superposition of lines), indicating that a filament with consistent diameter and no relevant ovality was achieved, since this would otherwise affect the extrusion behaviour. Figure 16d shows that the post-deposited layer thickness was almost the same as the 3D design (0.2 mm).

For the highest magnifications (Fig. 16e and f), it is obvious that a critical zone exists: interface layers. These bonding zones could have a significant role in the occurrence of defects in the final parts. For this reason, further detailed studies must be performed to understand their influence on the properties of the final metallic part.

The green shrinkage and warpage were evaluated by FVM. The measurements of the external diameter and height were performed in two opposite locations. From the results (Table 7), a slight variation in the green dimensions was noticeable when compared with the 3D model (ø 20 mm and a height of 7.0 mm).

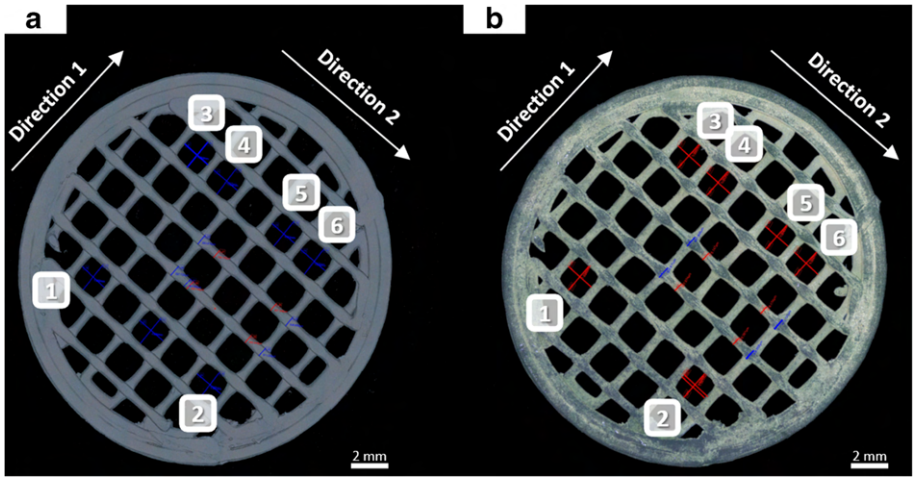

Fig. 17 FVM part B infill evaluation: **a** green and **b** sintered part

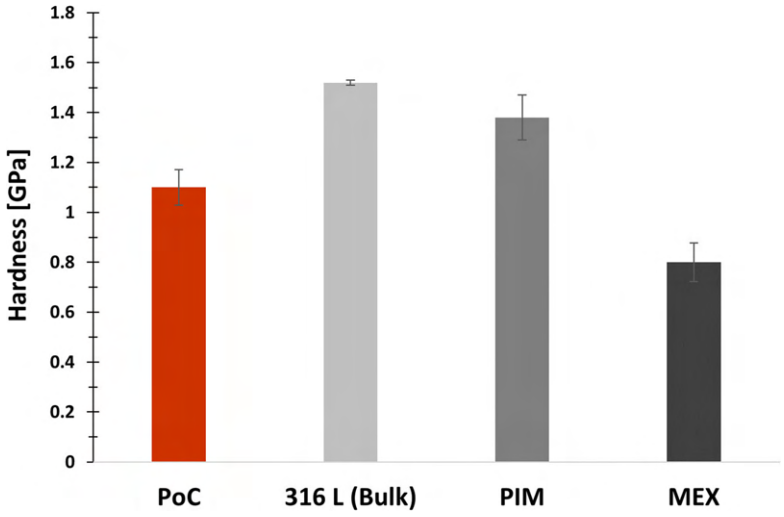

Fig. 18 Microhardness of the proof of concept (PoC) part in comparison with other data [30, 37, 38]

There was a slight variation in the shrinkage between the *XY* plane and the *Z*-axis. This deviation was also reported in other studies and can be associated with the build strategy (orientation of the layers) [4, 17]. The diameter shrinkage was, on average, 2.5% higher than in the build direction. Because the amount of shrinkage is affected by processing parameters and feedstock characteristics, a detailed comparison must be avoided without further investigation.

The geometry of the green infill (40%) and shrinkage was also evaluated by FVM (Fig. 17). Green part infill was printed with high accuracy because the interlayer distance (measurement 1 to 6) was constant in both measured directions (0° and 90°) (Fig. 17a and Table 8). After sintering, accuracy was not affected (Fig. 18b and Table 8).

In comparison with the previous FVM measurements, the part infill (width = nozzle ø, 0.4 mm) shrinkage was higher (~19%, Table 8) than in the other directions (13–17%, Table 7). The 40% infill configuration can largely affect the shrinkage of the part relative to the *XY* directions. This is similar to what occurs in PIM parts for different thicknesses.

The microhardness value of the part developed as a proof of concept (PoC, Fig. 18) was 1.1 GPa, which is higher than those of other studies for the same material on MEX [37]. Nevertheless, the microhardness values are lower than those measured in a PIM made from SS 316L and a bulk steel part [30, 38].

4 Conclusions

High-quality filaments for metallic MEX can be attained by optimization of different manufacturing steps: feedstocks production (metallic powder, binder, and additives), evaluation of extrudability (torque <4.0–4.5 N·m, supported by other rheological studies), debinding, and sintering. In the filament feedstocks, the main challenges are to reach the highest metallic powder content with good extrudability and a suitable ratio between stiffness and flexibility. Some filaments, without surfactant/plasticizer or with different additive contents, are unsuitable due to the difficulty to be extruded, owing to their high mixing torque.

From the extruded feedstocks, the selected case study shows that, for the filament constituted by SS 316L + M1 + TPE + P, the best green mechanical characteristics are attained due to the excellent homogenization of the mixing, demonstrated by micro-CT. Moreover, the best filament, after debinding and sintering, continues to show excellent performance, concerning defects (porosity) and consequently, the best flexural modulus, and deflection at break, assuring an excellent MEX processability. In the case of austenitic steel powders, the austenite phase is the only phase present, avoiding other costly post heat treatments. In conclusion, this study promotes a supported methodology for producing filaments for MEX and promotes the possibility to make 3D parts/systems or devices whatever the metallic powders selected, without commercial market offer dependence.

Author contribution Fábio Cerejo: investigation, conceptualization, methodology, visualization, and writing—original draft preparation. Daniel Gatões: Micro-CT investigation and methodology, writing, and review. Teresa Vieira: supervision, conceptualization, and review and editing.

Funding This work was supported by the European Regional Development Fund (ERDF) under the Portuguese program, Programa Operacional Factores de Competitividade (COMPETE) [grant agreement No. POCI-01-0247-FEDER-024533]; and this research is sponsored by

FEDER funds through the program COMPETE—Programa Operacional Factores de Competitividade—and by national funds through FCT, Fundação para a Ciência e a Tecnologia, under the project UIDB/00285/2020.

Data availability Data will be available upon request.

Declarations

Ethical approval Not applicable.

Consent to participate Not applicable.

Consent for publication Not applicable.

Conflict of interest The authors declare no competing interests.

References

1. Alcácer V, Cruz-Machado V (2019) Scanning the Industry 4.0: a literature review on technologies for manufacturing systems. Eng Sci Technol Int J 22:899. https://doi.org/10.1016/j.jestch.2019.01.006
2. Dilberoglu UM, Gharehpapagh B, Yaman U, Dolen M (2017) The role of additive manufacturing in the era of Industry 4.0. Proc Manufact 11:545. https://doi.org/10.1016/j.promfg.2017.07.148
3. Additive Manufacturing Wohlers Report 2018 shows rise in metal additive manufacturing. https://www.additivemanufacturing.media/news/wohlers-report-2018-shows-rise-in-metal-additive-manufacturing.
4. Lieberwirth C, Harder A, Seitz H (2017) Extrusion based additive manufacturing of metal parts. JMEA 7. https://doi.org/10.17265/2159-5275/2017.02.004
5. Gong H, Crater C, Ordonez A, Ward C, Waller M, Ginn C (2018) Material properties and shrinkage of 3D printing parts using Ultrafuse Stainless Steel 316LX Filament. MATEC Web Conf 249:01001. https://doi.org/10.1051/matecconf/201824901001
6. Thompson Y, Gonzalez-Gutierrez J, Kukla C, Felfer P (2019) Fused filament fabrication, debinding and sintering as a low cost additive manufacturing method of 316L stainless steel. Addit Manufact 30:100861. https://doi.org/10.1016/j.addma.2019.100861
7. (2020) Making additive manufacturing sustainable: ask the right question. tct MAG 28:24–25
8. Lingqin X, Guang C, Luyu Z, Pan L (2020) Explore the feasibility of fabricating pure copper parts with low-laser energy by selective laser melting. Mater Res Express 7:106509. https://doi.org/10.1088/2053-1591/abbd08
9. Ikeshoji T-T, Nakamura K, Yonehara M, Imai K, Kyogoku H (2018) Selective laser melting of pure copper. JOM 70:396–400. https://doi.org/10.1007/s11837-017-2695-x
10. Godec D, Cano S, Holzer C, Gonzalez-Gutierrez J (2020) Optimization of the 3D printing parameters for tensile properties of specimens produced by fused filament fabrication of 17-4PH Stainless Steel. Materials 13:774. https://doi.org/10.3390/ma13030774
11. ISO/ASTM Additive manufacturing - General principles - terminology (ISO/ASTM DIS 52900:2018)
12. Ziaee M, Crane NB (2019) Binder jetting: a review of process, materials, and methods. Addit Manufact 28:781–801. https://doi.org/10.1016/j.addma.2019.05.031
13. Bai Y, Williams CB (2018) Binder jetting additive manufacturing with a particle-free metal ink as a binder precursor. Mater Des 11
14. Bai Y, Wagner G, Williams CB (2017) Effect of particle size distribution on powder packing and sintering in binder jetting additive manufacturing of metals. J Manuf Sci Eng 139:081019. https://doi.org/10.1115/1.4036640
15. Singh P, Balla VK, Tofangchi A, Atre SV, Kate KH (2020) Printability studies of Ti-6Al-4V by metal fused filament fabrication (MF3). Int J Refract Met Hard Mater 91:105249. https://doi.org/10.1016/j.ijrmhm.2020.105249
16. Danforth SC, Agarwala M, Bandyopadghyay A et al (1998) Solid freeform fabrication methods. 17
17. Gonzalez-Gutierrez J, Cano S, Schuschnigg S, Kukla C, Sapkota J, Holzer C (2018) Additive manufacturing of metallic and ceramic components by the material extrusion of highly-filled polymers: a review and future perspectives. Materials 11:840. https://doi.org/10.3390/ma11050840
18. M K Agarwala, Weeren, R. van, Bandyopadhyay, A., et al (1996) Fused deposition of ceramics and metals: an overview. In: International Solid Freeform Fabrication Symposium. Texas, USA, p 8
19. Kukla C, Duretek I, Schuschnigg S, Gonzalez-Gutierrez J (2016) Properties for PIM feedstocks used in fused filament fabrication. In: Proceedings of the World PM2016 Congress & Exhibition. Hamburg, Germany, 9–13 October 2016, p 5
20. Gonzalez-Gutierrez J, Godec D, Kukla C et al (2017) Shaping, debinding and sintering of steel components via fused filament fabrication. Croatian Association of Production Engineering, Zagreb, pp 99–104
21. Burkhardt C, Freigassner P, Weber O et al (2016) Fused filament fabrication (FFF) of 316L Green parts for the MIM process. In: Proceedings of the World PM2016 Congress & Exhibition. EPMA, Hamburg, pp 9–13 October 2016
22. Andersen O, Riecker S, Studnitzky T et al (2018) Manufacturing and properties of metal parts made by fused filament fabrication. In: Euro PM2018 Proceedings. EPMA, Bilbao, Spain, 14 – 18 October 2018, pp 1–6
23. Kurose T, Abe Y, Santos MVA, Kanaya Y, Ishigami A, Tanaka S, Ito H (2020) Influence of the layer directions on the properties of 316L stainless steel parts fabricated through fused deposition of metals. Materials 13:2493. https://doi.org/10.3390/ma13112493
24. Gloeckle C, Konkol T, Jacobs O, Limberg W, Ebel T, Handge UA (2020) Processing of highly filled polymer–metal feedstocks for fused filament fabrication and the production of metallic implants. Materials 13:4413. https://doi.org/10.3390/ma13194413
25. Nestle, Nikolaus, Hermant, Marie-Claire, Schmidt, Kris (2016) Mixture for use in a fused filament fabrication process. 40
26. German RM, Bose A (1997) Injection molding of metals and ceramics. Metal Powder Industry, Princeton
27. Vieira MT, Martins AG, Barreiros FM, Matos M, Castanho JM (2008) Surface modification of stainless steel powders for microfabrication. J Mater Process Technol 201:651–656. https://doi.org/10.1016/j.jmatprotec.2007.11.162

28. Ferreira TJ, Vieira MT (2017) Optimization of MWCNT – metal matrix composites feedstocks. Ciência Tecnol Mater 29:87–91. https://doi.org/10.1016/j.ctmat.2016.07.010
29. Carreira P, Cerejo F, Alves N, Vieira MT (2020) In search of the optimal conditions to process shape memory alloys (NiTi) using fused filament fabrication (FFF). Materials 13:4718. https://doi.org/10.3390/ma13214718
30. Ferreira TJJ (2018) Microinjection moulding of austenitic stainless steel reinforced with carbon nanotubes, PhD Thesis. University of Coimbra
31. Tafti AA, Demers V, Majdi SM, Vachon G, Brailovski V (2021) Effect of thermal debinding conditions on the sintered density of low-pressure powder injection molded iron parts. Metals 11:264. https://doi.org/10.3390/met11020264
32. Cerejo F, Raimundo AM, Vieira MT, Barreiros FM (2019) Fused deposition of WC+Co powder. EPMA, Maastricht Exhibition & Congress Centre, Maastricht
33. Ferreira TJ, Vieira MT (2014) Behaviour of feedstocks reinforced with nanotubes for micromanufacturing. In: Euro PM 2014 Congr. Exhib. Proc. EPMA. The Messezentrum Salzburg, Austria
34. Dimitri C, Mohamed S, Thierry B, Jean-Claude G (2017) Influence of particle-size distribution and temperature on the rheological properties of highly concentrated Inconel feedstock alloy 718. Powder Technol 322:273–289. https://doi.org/10.1016/j.powtec.2017.08.049
35. Ibrahim MHI, Muhamad N, Sulong AB (2011) Rheological characterization of water atomised stainless steel SS316L for Micro MIM. Adv Mater Res 264–265:129–134
36. Kaleta J, Wiewiórski P, Wiśniewski W (2017) Investigation of martensitic transformation induced by cyclic plastic deformation in austenitic steels. In: Borek W, Tanski T, Brytan Z (eds) Austenitic Stainless Steels - New Aspects. InTech. https://doi.org/10.3390/ijerph14101126
37. Li JB, Xie ZG, Zhang XH, Zeng QG, Liu HJ (2010) Study of metal powder extrusion and accumulating rapid prototyping. Key Eng Mater 443:81–86. https://doi.org/10.4028/www.scientific.net/KEM.443.81
38. Matweb (2019) SS 316L. http://www.matweb.com/search/DataSheet.aspx?MatGUID=530144e2752b47709a58ca8fe0849969. Accessed 15/02/2021

Appendix C

Influence of Metallic Powder Characteristics on Extruded Feedstock Performance for Indirect Additive Manufacturing

materials

MDPI

Article

Influence of Metallic Powder Characteristics on Extruded Feedstock Performance for Indirect Additive Manufacturing

Cyril Santos [1,*], Daniel Gatões [2], Fábio Cerejo [3] and Maria Teresa Vieira [2]

[1] CDRSP—Centre for Rapid and Sustainable Product Development, Polytechnic Institute of Leiria, Rua General Norton de Matos, Apartado 4133, 2411-901 Leiria, Portugal
[2] CEMMPRE—Centre for Mechanical Engineering, Materials and Processes, University of Coimbra, Pinhal de Marrocos, 3030-788 Coimbra, Portugal; daniel.gatoes@uc.pt (D.G.); TERESA.VIEIRA@dem.uc.pt (M.T.V.)
[3] IPN—Pedro Nunes Institute, Rua Pedro Nunes, 3030-199 Coimbra, Portugal; phcerejo@gmail.com
* Correspondence: cyril.santos@ipleiria.pt

Abstract: Material extrusion (MEX) of metallic powder-based filaments has shown great potential as an additive manufacturing (AM) technology. MEX provides an easy solution as an alternative to direct additive manufacturing technologies (e.g., Selective Laser Melting, Electron Beam Melting, Direct Energy Deposition) for problematic metallic powders such as copper, essential due to its reflectivity and thermal conductivity. MEX, an indirect AM technology, consists of five steps—optimisation of mixing of metal powder, binder, and additives (feedstock); filament production; shaping from strands; debinding; sintering. The great challenge in MEX is, undoubtedly, filament manufacturing for optimal green density, and consequently the best sintered properties. The filament, to be extrudable, must accomplish at optimal powder volume concentration (CPVC) with good rheological performance, flexibility, and stiffness. In this study, a feedstock composition (similar binder, additives, and CPVC; 61 vol. %) of copper powder with three different particle powder characteristics was selected in order to highlight their role in the final product. The quality of the filaments, strands, and 3D objects was analysed by micro-CT, highlighting the influence of the different powder characteristics on the homogeneity and defects of the greens; sintered quality was also analysed regarding microstructure and hardness. The filament based on particles powder with D_{50} close to 11 µm, and straight distribution of particles size showed the best homogeneity and the lowest defects.

Keywords: additive manufacturing; copper; feedstock; MEX; filament; micro-CT

Citation: Santos, C.; Gatões, D.; Cerejo, F.; Vieira, M.T. Influence of Metallic Powder Characteristics on Extruded Feedstock Performance for Indirect Additive Manufacturing. *Materials* **2021**, *14*, 7136. https://doi.org/10.3390/ma14237136

Academic Editors: Ludwig Cardon and Clemens Holzer

Received: 22 October 2021
Accepted: 22 November 2021
Published: 24 November 2021

1. Introduction

Additive manufacturing (AM) has gained a great amount of interest in the past two decennia for various fields of applications [1]. After the boom of direct processes (i.e., selective laser melting (SLM), electron beam manufacturing (EBM), direct energy deposition (DED)), two indirect technologies assume more and more the future (binder Jetting (BJ) and material extrusion (MEX)), due to their simplicity, reliability, low cost (i.e., equipment) and a wide range of different printing materials available. The latter is well known, particularly for polymeric materials, under the name of fused deposition modeling (FDM). When applied to the mixing of metallic/ceramic powder particles and organic binder and/or additives based on polymers, it has adopted the standardised name of MEX [2–6]. This process for 3D object shaping is based on FDM, but filament manufacturing is similar to powder metal extrusion process (PEP) and powder injection moulding (PIM). Both these processes use, as feedstock, polymers and organic materials with the highest feasible metal powder content, designated by critical powder volume concentration (CPVC) [7]. A feedstock must consist of a powder with optimal characteristics and an appropriate binder, which are determinant factors to achieve quality in the final 3D object [8,9]. Similarly to

quality in the final 3D object [8,9]. Similarly to PEP/PIM, the parts produced by MEX use filaments with a high volume percentage of metals particles, typically between 50 and 65 vol.% [10–12], and need two subsequent steps: debinding, to promote binder removal, and sintering, to attain a dense 3D object (Figure 1). Nevertheless, PIM feedstocks result in a brittle filament form; thus, it is necessary to optimise the mixture to achieve filament requirements for MEX, such as a good balance between suitable rheology properties, stiffness, and flexibility.

PEP/PIM, the parts produced by MEX use filaments with a high volume percentage of metals particles, typically between 50 and 65 vol.% [10–12], and need two subsequent steps: debinding, to promote binder removal, and sintering, to attain a dense 3D object (Figure 1). Nevertheless, PIM feedstocks result in a brittle filament form; thus, it is necessary to optimise the mixture to achieve filament requirements for MEX, such as a good balance between suitable rheology properties, stiffness, and flexibility.

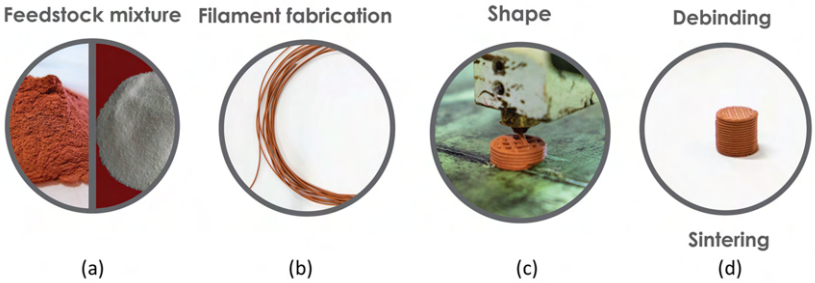

Figure 1. Stages of MEX for building 3D objects: (**a**) feedstock; (**b**) filament; (**c**) shaping; (**d**) debinding and sintering.

Figure 1. Stages of MEX for building 3D objects: (**a**) feedstock; (**b**) filament; (**c**) shaping; (**d**) debinding and sintering.

Nowadays, commercial filaments with metal particles are emerging, although most of them have a low metal powder content or use PLA or ABS as the binder, which means that the main goals are the aesthetic appearance of the products or to increase properties of the master polymer [13,14].

Nowadays, commercial filaments with metal particles are emerging, although most of them have a low metal powder content or use PLA or ABS as the binder, which means that the main goals are the aesthetic appearance of the products or to increase properties of the master polymer [13,14].

For stainless steel, different studies reveal that powder must have (3Ss): particle size D50 from 5 µm to 15 µm, a monomodal particle size distribution, and a shape factor close to 1 [12], similar to the ones used in PIM.

For stainless steel, different studies reveal that powder must have (3Ss): particle size D50 from 5 µm to 15 µm, a monomodal particle size distribution, and a shape factor close to 1 [12], similar to the ones used in PIM.

Copper, particularly pure copper, is a widely applied metal in engineering applications due to the combination of suitable mechanical strength and excellent thermal and electrical properties (391 W/(m·°C) and 103.6% IACS, respectively, at 20 °C) [15]. However, considerable research studies and advancements are still needed in processing copper by AM to match the industry requirements and process repeatability. A few studies investigated copper using SLM [2,16]. Although SLM has been demonstrated to successfully work with a comprehensive range of metals, it has disadvantages when it comes to the fabrication of copper due to the high reflectivity of this metal to the laser beam, particularly for near-infrared radiation [17], and high thermal conductivity that leads to rapid heat dissipation and an uncontrolled molten pool [18], thus resulting in parts with significant porosity (11.9–17.0%) [19–21]. In order to achieve dense copper parts, a higher laser energy density is required, which means a higher power laser source and, therefore, an increase in energy consumption. Some studies regarding SLM of pure copper using a greater output laser power reported theoretical density values between 96.6 and 99.4% in self-developed platforms [22–24]. These are the reasons for the selection of copper powder as a material to highlight the role of the MEX as an effective processing technology.

Copper, particularly pure copper, is a widely applied metal in engineering applications due to the combination of suitable mechanical strength and excellent thermal and electrical properties (391 W/(m·°C) and 103.6% IACS, respectively, at 20 °C) [15]. However, considerable research studies and advancements are still needed in processing copper by AM to match the industry requirements and process repeatability. A few studies investigated copper using SLM [2,16]. Although SLM has been demonstrated to successfully work with a comprehensive range of metals, it has disadvantages when it comes to the fabrication of copper due to the high reflectivity of this metal to the laser beam, particularly for near-infrared radiation [17], and high thermal conductivity that leads to rapid heat dissipation and an uncontrolled molten pool [18], thus resulting in parts with significant porosity (11.9–17.0%) [19–21]. In order to achieve dense copper parts, a higher laser energy density is required, which means a higher power laser source and, therefore, an increase in energy consumption. Some studies regarding SLM of pure copper using a greater output laser power reported theoretical density values between 96.6 and 99.4% in self-developed platforms [22–24]. These are the reasons for the selection of copper powder as a material to highlight the role of the MEX as an effective processing technology.

In summary, the production of 3D objects made of copper powder by direct AM, particularly those associated with the liquid state (SLM), entails several problems surmounted with the indirect MEX process. In addition to significant research on the role of powder characteristics, studies focus essentially on steel powder. However, the properties of steel and copper powder oblige a detailed analysis of these powder particles. Furthermore, according to the available literature, no scientific studies have investigated the influence of the application of MEX technology for the production of densified copper parts, in spite of the company, Markforged, having commercialised copper filaments for MEX recently [25]. According to the state of the art, no studies by the respective company have investigated the influence of copper powder particles characteristics on the products made by MEX technology. It is, therefore, crucial to have a complete understanding of all five steps involved in the manufacturing process—namely, mixing the constituents of the filaments (copper powder, binder, and

In summary, the production of 3D objects made of copper powder by direct AM, particularly those associated with the liquid state (SLM), entails several problems surmounted with the indirect MEX process. In addition to significant research on the role of powder characteristics, studies focus essentially on steel powder. However, the properties of steel and copper powder oblige a detailed analysis of these powder particles. Furthermore, according to the available literature, no scientific studies have investigated the influence of the application of MEX technology for the production of densified copper parts, in spite of the company, Markforged, having commercialised copper filaments for MEX recently [25]. According to the state of the art, no studies by the respective company have investigated the influence of copper powder particles characteristics on the products made by MEX technology. It is, therefore, crucial to have a complete understanding of all five steps involved in the manufacturing process—namely, mixing the constituents of the filaments (copper powder, binder, and

additives), extrusion (filament manufacturing), strands for shaping (3D objects), debinding (binder removal), and sintering (powder particle consolidation).

2. Characterisation Techniques and Material

2.1. Experimental Conditions

The powder particle size and the particle size distribution were measured by laser diffraction spectrometry (LDS) on a Malvern Instruments Mastersizer 3000 (Malvern Instruments Ltd., Worcestershire, UK), following ISO 13320:2009. The analysis of particles powder, filament, and strands morphology was made by scanning electron microscopy (SEM) on a Tescan Vega 3 (Tescan, Brno, Czech Republic) and an FEI Quanta 400FEG (FEI Europe BV, Eindhoven, The Netherlands). The phasic structure of the powder and greens were evaluated by X-ray diffraction (XRD) on a Philips X'Pert diffractometer (Philips, Eindhoven, The Netherlands); according to EN 13925:2003, the current intensity was 35 mA and voltage of 40 kV. The wavelength radiation was cobalt (Kα1 = 0.17810 nm and Kα2 = 0.17928 nm). The acquisition conditions used a Bragg–Brentano (θ–2θ) geometry ($40^\circ \leq 2\theta \leq 80^\circ$) and a step of 0.04°/s per point. The thermogravimetric analyses (TGA) were performed on a PerkinElmer STA 6000 (Waltham, MA, USA).

The filaments were analysed by a non-destructive method using X-ray microcomputed tomography (micro-CT), Bruker SkyScan 1275 (Bruker, Kontich, Belgium). An acceleration voltage of 80 kV and a beam current of 125 µA was set using a 1 mm copper filter and step-and-shoot mode. Pixel size was set to the equipment minimum of 5.67 µm, and the random mode was used. In total, 1056 projection images were acquired at 0.2° angular step with 3 frames average per step, using an exposure time of 65 ms. Regarding the strands, they were scanned with an acceleration voltage of 50 kV and a beam current of 80 µA, using as a filter aluminium with 1 mm thickness and an exposure time of 230 ms. The 3D objects and sintered filaments were scanned using an acceleration voltage of 100 kV and a beam current of 100 µA, using a 1 mm copper filter. Then, 3D objects' projection images (529) were acquired at 0.4° angular step with 8 frames average per step, using an exposure time of 245 ms, and sintered filaments projection images (1056) were acquired at 0.2° angular step with 3 frames average per step and a 225 ms exposure time. All omitted conditions on the strands and parts were similar to the ones used on the filament. The micro-CT images were reconstructed with dedicated manufacturer software.

Hardness measurements were performed with a microhardness tester Shimadzu HMV (Shimadzu Corporation, Kyoto, Japan). For each measurement, a load of 98 mN was applied for 15 s by a Vickers indenter.

2.2. Copper Powder Characterisation

Three copper powders with essentially two different characteristics—particle size and particle size distribution—were tested. A similar organic mixing based on polymeric materials (master binder, backbone, and plasticiser) with identical thermal cycle heat treatments for debinding and sintering were mixed (Table 1) [26]. In addition to the selected binder (a mixture of polyolefin waxes and ethylenic polymers) [27], the additives chosen are necessary to attain a feasible stiffness (backbone) and flexibility (plasticiser) in a filament, which means a thermoplastic elastomer (TPE) and a plasticizer, respectively. The green filaments developed based on this procedure were constituted by copper powder (purity 99.99%), with different particle sizes and particle size distributions.

Table 1. Composition of binder and additives.

	Master Binder	**Additives**	
		Backbone	**Plasticiser**
Vol (%)	77.5	17.5	5.0
Density (kg/m^3)	970	1025	96.5

Vol (%)	77.5	17.5	5.0
Density (kg/m³)	970	1025	96.5

The three different copper powder particles highlighted the role of partic
particle size distribution of particles in the quality of filament, strands, and con
in the final product, and were furnished by Ecka (Ecka Granules Gmb
Germany—type A) and Alfa Aesar (Alfa Aesar, Haverhill, MA, USA—type B,C

Table 2. Diameter of powder particles (D_{10}, D_{50}, D_{90}) and their density.

Powder	D_{10} [µm]	D_{50} [µm]	D_{90} [µm]	ρ [K
A	8.57	28.00	46.60	8
B	7.75	11.30	16.20	8
C	1.95	3.97	6.67	8

The three different copper powder particles highlighted the role of particle size and particle size distribution of particles in the quality of filament, strands, and consequently, in the final product, and were furnished by Ecka (Ecka Granules GmbH, Fürth, Germany—type A) and Alfa Aesar (Alfa Aesar, Haverhill, MA, USA—type B,C) (Table 2).

Table 2. Diameter of powder particles (D_{10}, D_{50}, D_{90}) and their density.

Powder	D_{10} [µm]	D_{50} [µm]	D_{90} [µm]	ρ [Kg/m³]
A	8.57	28.00	46.60	8896
B	7.75	11.30	16.20	8642
C	1.95	3.97	6.67	8427

The powder particle sizes were chosen as D_{50} equal to (A) 28.00 µm, (B) 11.30 µm, and (C) 3.97 µm, and particle size distribution ranged from a bimodal with wide distribution (A) up to monomodal with a very narrow distribution (C) (Figure 2).

The powder particle sizes were chosen as D_{50} equal to (A) 28.00 µm, (B) 11.30 µm, and (C) 3.97 µm, and particle size distribution ranged from a bimodal w
distribution (A) up to monomodal with a very narrow distribution (C) (Figure

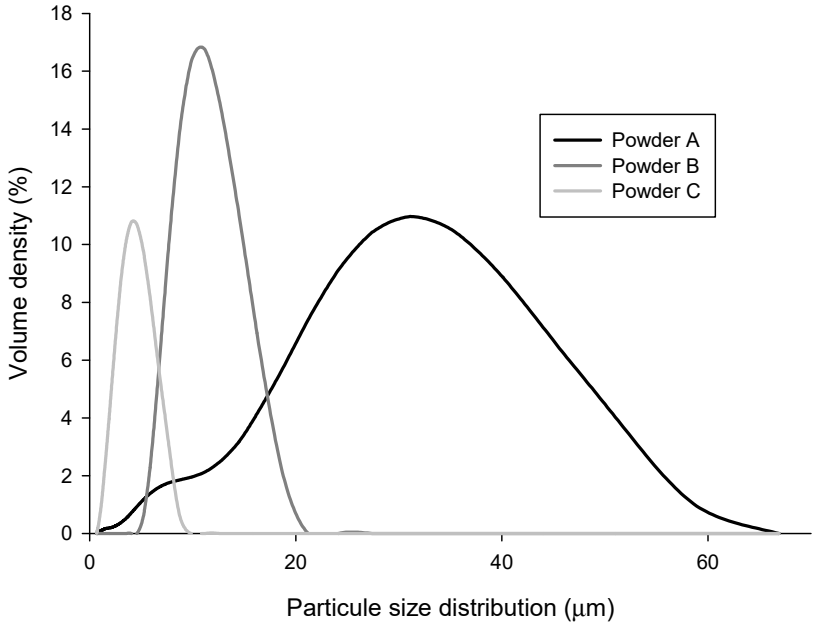

Figure 2. Particle size distribution of the different copper powder particles.

Figure 2. Particle size distribution of the different copper powder particles.

Table 2 shows the different particle size distribution of the three different copper powders selected in this study.

Table 2 shows the different particle size distribution of the three differe
powders selected in this study.

The density values revealed pre-oxidation of powder particles B and C (density of Cu = 8960 Kg/m³; density Cu_2O = 6310 Kg/m³) [28]. Moreover, the colour of the different copper powder particles indicated the presence of Cu_2O on the powder surface (B,C).

The density values revealed pre-oxidation of powder particles B and C (
Cu = 8960 Kg/m³; density Cu_2O = 6310 Kg/m³) [28]. Moreover, the colour of th
copper powder particles indicated the presence of Cu_2O on the powder surface

Regardless of the selected copper powder, the shape factor ($D_{minimum}$: $D_{maximum}$ close to 1 (Figure 3).

Regardless of the selected copper powder, the shape factor ($D_{minimum}$: $D_{maximum}$ close to 1 (Figure 3).

XRD of the highest D_{50} powder showed pure copper (ICDD 04-0836), and the presence of copper oxide phase (ICDD 075-1531) was not distinguishable (Figure 4). However, in powder particles B and C, the XRD diffractogram detected strong peaks of Cu and weak peaks of copper oxide. The weak peak of copper oxide confirmed the slight involvement of Cu with the atmospheric oxygen during conventional atomisation of powder, showing that a small oxide phase was present in the powder surface.

Table 3 summarises the 4Ss (particle Size, particle Size distribution, Shape, and Structure (topography and phases) of the copper powder particles used in this work.

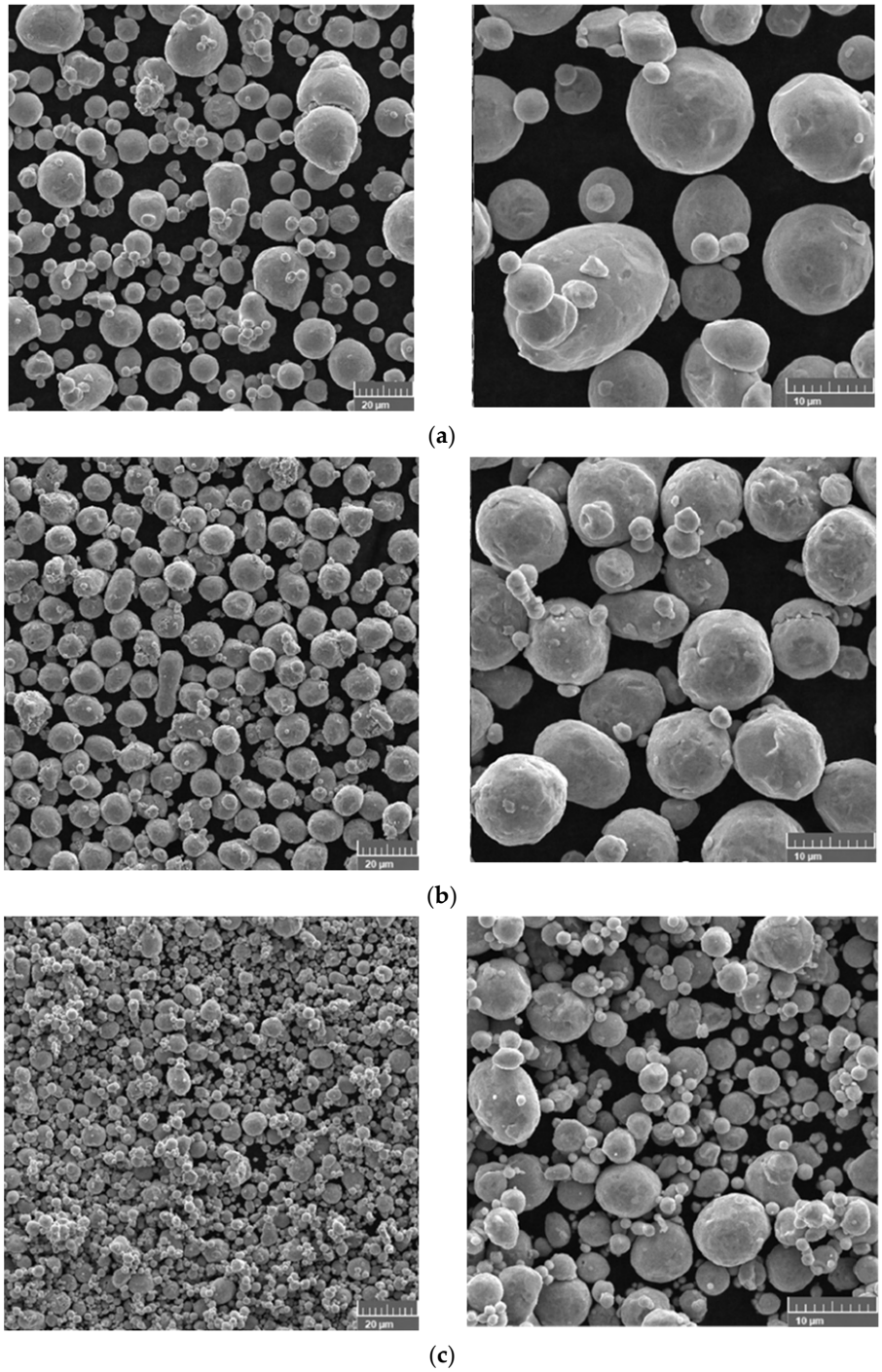

Figure 3. Morphology of powder particles (SEM): (**a**) powder A, (**b**) powder B, and (**c**) powder C.

XRD of the highest D_{50} powder showed pure copper (ICDD 04-0836), and the presence of copper oxide phase (ICDD 075-1531) was not distinguishable (Figure 4). However, in powder particles B and C, the XRD diffractogram detected strong peaks of Cu and weak peaks of copper oxide. The weak peak of copper oxide confirmed the slight involvement of Cu with the atmospheric oxygen during conventional atomisation of powder, showing that a small oxide phase was present in the powder surface.

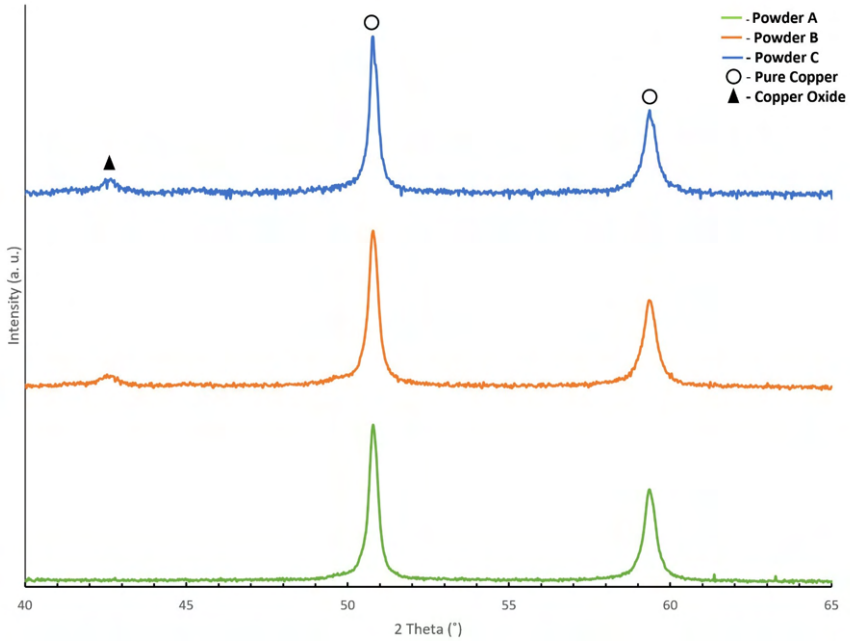

Figure 4. X-ray diffractograms of powder A (**bottom**), powder B (**middle**), and powder C (**top**).

Table 3. Particle size (D_{50}), particle size distribution, shape factor, and surface (topography and structure).

Powder	Particle Size D_{50} (μm)	Particle Size Distribution	Shape Factor *	Topography	Phase Composition
A	28.00	Bimodal	≈1	Uniform with some satellites	Cu + traces of copper oxide
B	11.30	Unimodal	≈1	Uniform with some satellites	Cu + traces of copper oxide
C	3.97	Unimodal	≈1	Uniform with some satellites	Cu + copper oxide

* Shape factor close to 1 means spherical particle.

3. Experimental Methodology

3.1. Processing of Filament Feedstocks

3.1.1. Evaluation of CPVC

The feedstocks were optimised in a torque rheometer (Plastograph® Brabender W 50, Brabender GmbH & Co. KG, Duisburg, Germany) at a temperature of 180 °C, 30 rpm, and a 38.5 cm^3 mixing chamber. The strategy was to establish the best compromise between the maximum volume concentration of copper powder in the feedstock and its extrudability, which leads to the best conditions to extrude the filament without disruptions. This compromise is named CPVC [27]. The optimum volume ratio has been widely studied in research studies related to PIM. In the processing of filaments (extrusion), the methodology was similar, but the role of backbone and plasticiser needed to manufacture a filament must be highlighted.

3.1.2. Filaments

After the evaluation of CPVC feedstocks, they were granulated into small pellets and extruded in filament form, using a single screw extruder (Brabender GMBH & Co. E 19/25 without calibration system) and a nozzle of 1.75 mm. The temperatures in different zones of the extrusion cylinder were 170, 175, and 180 °C (nozzle).

tests were carried out with a velocity of 0.5 mm/min and a gauge length of 1
three-point bending test, the loading span was 20 mm, and the cell load v
mm/min. For both tests (tensile and bending), six specimens (green filamen
for each reference powder particle (A, B, and C).

3.2. Three-Dimensional (3D) Printing

The filament was extruded in a Prusa i3 MK3S (Prusa Research, P
Republic) through a 0.4 mm nozzle diameter. The nozzle temperature was 2
platform temperature was 50 °C for the first layer and 80 °C for the remaini
print speed was 30 mm/s. The extrusion multiplier was set to 1.15 to offs
and create a more homogenous layer.

In order to support the quality of filament for the additive process (MEX), a function of powder characteristics, several tests of tensile and flexural strength were performed. The equipment was a Stable Micro Systems of Godalming, with a 5 kN load cell. Tensile tests were carried out with a velocity of 0.5 mm/min and a gauge length of 10 mm; for the three-point bending test, the loading span was 20 mm, and the cell load velocity of 1.3 mm/min. For both tests (tensile and bending), six specimens (green filament) were tested for each reference powder particle (A, B, and C).

3.2. Three-Dimensional (3D) Printing

The filament was extruded in a Prusa i3 MK3S (Prusa Research, Prague, Czech Republic) through a 0.4 mm nozzle diameter. The nozzle temperature was 200 °C, and the platform temperature was 50 °C for the first layer and 80 °C for the remaining layers. The print speed was 30 mm/s. The extrusion multiplier was set to 1.15 to offset the overlap and create a more homogenous layer.

3.3. Processing Conditions after Shaping

3.3.1. Debinding

The master binder and additives must be completely removed during
step. The elimination of the polymeric component is critical in the shapin
and sintering (SDS) process. The type of debinding selected was base
gravimetric analysis (TGA) of the filaments. The TGA curve highlights the
during the heating process where the loss of weight is disruptive, whi
temperatures at which the organic constituents of feedstock are ustulated. T
represents the weight loss evolution of the feedstock studied with temperatu
atmosphere of Ar + H_2 (5 vol.% H_2) and a heating rate of 1 °C/min. From
became clear that the temperature of 500 °C was enough to eliminate all t
additives of the feedstock (7.5 wt.% = 39 vol.%) (Figure 5).

3.3. Processing Conditions after Shaping

3.3.1. Debinding

The master binder and additives must be completely removed during the debinding step. The elimination of the polymeric component is critical in the shaping, debinding, and sintering (SDS) process. The type of debinding selected was based on thermal gravimetric analysis (TGA) of the filaments. The TGA curve highlights the temperatures during the heating process where the loss of weight is disruptive, which means the temperatures at which the organic constituents of feedstock are ustulated. The TGA curve represents the weight loss evolution of the feedstock studied with temperature, in an inert atmosphere of Ar + H_2 (5 vol.% H_2) and a heating rate of 1 °C/min. From this curve, it became clear that the temperature of 500 °C was enough to eliminate all the binder and additives of the feedstock (7.5 wt.% = 39 vol.%) (Figure 5).

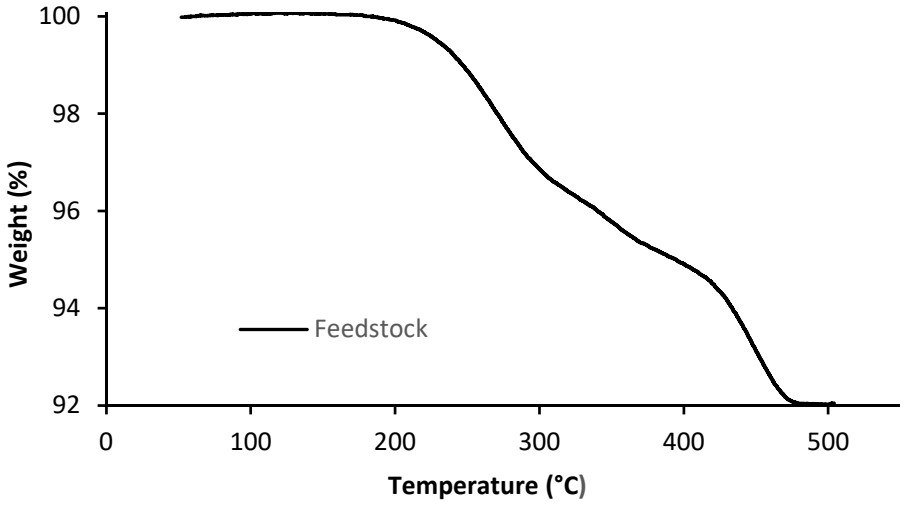

Figure 5. TGA of feedstocks (powder A).

Figure 5. TGA of feedstocks (powder A).

Figure 6 shows the thermal cycle selected for an efficient debinding of the parts (brown). The conditions were similar to the TGA, with the atmosphere being Ar + H_2 (5 vol.% H_2) and a heating rate of 1 °C/min.

Figure 6 shows the thermal cycle selected for an efficient debinding
(brown). The conditions were similar to the TGA, with the atmosphere be
vol.% H_2) and a heating rate of 1 °C/min.

Materials **2021**, *14*, x FOR PEER REVIEW 8 of 19

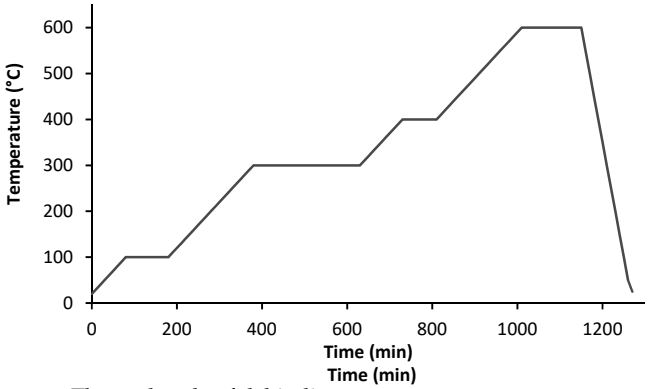

Figure 6. Thermal cycle of debinding.

Figure 6. Thermal cycle of debinding.

3.3.2. Sintering

3.3.2. Sintering

3.3.2. Sintering

The brown parts were sintered in the same atmosphere of debinding, but the heating rate was 5 °C/min and the maximum temperature was 1045 °C, for 3 h (Figure 7).

The brown parts were sintered in the same atmosphere of debinding, but the heating rate was 5 °C/min and the maximum temperature was 1045 °C, for 3 h (Figure 7).

The brown parts were sintered in the same atmosphere of debinding, but the heating rate was 5 °C/min and the maximum temperature was 1045 °C, for 3 h (Figure 7).

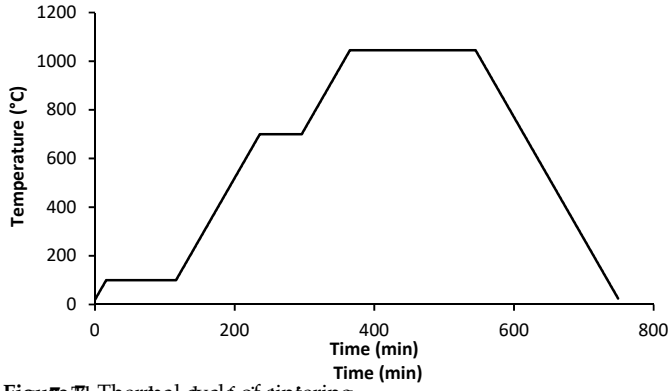

Figure 7. Thermal cycle of sintering.

Figure 7. Thermal cycle of sintering.

Figure 7. Thermal cycle of sintering.

3.3.3. Micrographic Analysis of Green and Sintered Filament

3.3.3. Micrographic Analysis of Green and Sintered Filament

3.3.3. Micrographic Analysis of Green and Sintered Filament

The filament green was analysed without polishing and etching. However, after sintering, the specimens of filament were polished and chemically etched for optical microscopy analysis (Nikon OPTIPHOT metallographic polarising microscope, Tokyo, Japan). For the evaluation of the grain size (ASTM 407) and microstructure, the selected etchant was iron chloride, hydrochloric acid, water, and glycerol (1:1: 3:5), and the duration of etching was 1 min.

The filament green was analysed without polishing and etching. However, after sintering, the specimens of filament were polished and chemically etched for optical microscopy analysis (Nikon OPTIPHOT metallographic polarising microscope, Tokyo, Japan). For the evaluation of the grain size (ASTM 407) and microstructure, the selected etchant was iron chloride, hydrochloric acid, water, and glycerol (1:1: 3:5), and the duration of etching was 1 min.

The filament green was analysed without polishing and etching. However, after sintering, the specimens of filament were polished and chemically etched for optical microscopy analysis (Nikon OPTIPHOT metallographic polarising microscope, Tokyo, Japan). For the evaluation of the grain size (ASTM 407) and microstructure, the selected etchant was iron chloride, hydrochloric acid, water, and glycerol (1:1: 3:5), and the duration of etching was 1 min.

4. Results and Discussion

4. Results and Discussion

4. Results and Discussion

4.1. Optimisation of Feedstocks for Copper Filaments

4.1. Optimisation of Feedstocks for Copper Filaments

4.1. Optimisation of Feedstocks for Copper Filaments

For the development of a new copper filament for material extrusion (MEX), several feedstocks were developed using torque rheometry equipment. CPVC established was 61 vol.% [29]. Table 4 shows the final composition and density of each feedstock, with its associated torque.

For the development of a new copper filament for material extrusion (MEX), several feedstocks were developed using torque rheometry equipment. CPVC established was 61 vol.% [29]. Table 4 shows the final composition and density of each feedstock, with its associated torque.

For the development of a new copper filament for material extrusion (MEX), several feedstocks were developed using torque rheometry equipment. CPVC established was 61 vol.% [29]. Table 4 shows the final composition and density of each feedstock, with its associated torque.

Table 4. CPVC of feedstocks, density, and maximum torque.

Feedstock	Cu (vol.%)	Binder + Additive (vol.%)	ρ (Kg/m^3)	Torque (N·m)
A	61	39	5345	3.8
B	61	39	5330	5.1
C	61	39	5205	4.4

B	61	39	5330	5.1
C	61	39	5205	4.4

4.2. Green

4.2.1. Filaments

The extruded filaments, all produced under the same conditions, had variations in diameter depending on the dimension and distribution of copper particles. Thus, filaments had the following diameters: for powder A = 1.76 mm, B = 1.70 mm, and C = 1.68 mm. The variation in the filaments was not significant, i.e., negligible.

The filaments were analysed in terms of homogeneity (distribution of Cu powder particles into the polymeric material). Figures 8–10 show micro-CT and SEM images of each type of filament with different particles size and particle size distributions. Filament A showed small pores distributed randomly throughout its volume. This could be the result of the large size distribution and particle size, which severely affects the powder behaviour during extrusion. Particle mobility is highly dependent on particle size. Filament B was almost an ideal case, since there was a uniform distribution and low interparticular distance, with no discernible defects (within the micro-CT resolution). Filament C showed random pores, even though less prevalent and smaller than in filament A. SEM micrographs indicated apparent high mobility of the binder and additives. This low wettability can severely affect the sintering and debinding dynamics. Moreover, micro-CT volume rendering of the filaments revealed low-to-no ovality on the different filaments and a constant diameter.

4.2. Green
4.2.1. Filaments
The extruded filaments, all produced under the same conditions, had variations in diameter depending on the dimension and distribution of copper particles. Thus, filaments had the following diameters: for powder A = 1.76 mm, B = 1.70 mm, and C = 1.68 mm. The variation in the filaments was not significant, i.e., negligible.
The filaments were analysed in terms of homogeneity (distribution of Cu powder particles into the polymeric material). Figures 8–10 show micro-CT and SEM images of each type of filament with different particles size and particle size distributions. Filament A showed small pores distributed randomly throughout its volume. This could be the result of the large size distribution and particle size, which severely affects the powder behaviour during extrusion. Particle mobility is highly dependent on particle size. Filament B was almost an ideal case, since there was a uniform distribution and low interparticular distance, with no discernible defects (within the micro-CT resolution). Filament C showed random pores, even though less prevalent and smaller than in filament A. SEM micrographs indicated apparent high mobility of the binder and additives. This low wettability can severely affect the sintering and debinding dynamics. Moreover, micro-CT volume rendering of the filaments revealed low-to-no ovality on the different filaments and a constant diameter.

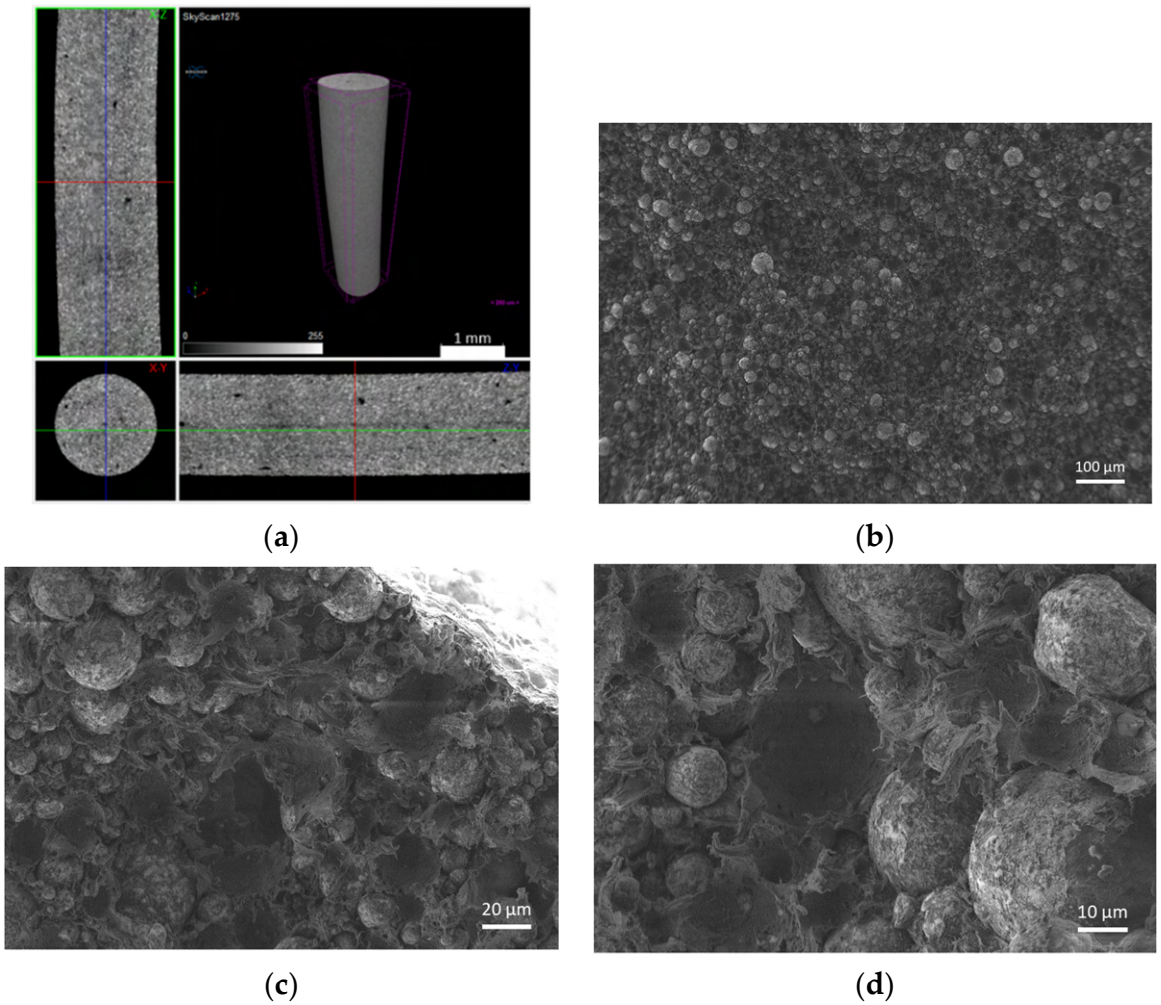

(**a**) (**b**)

(**c**) (**d**)

Figure 8. Filament A (green): (**a**) micro-CT; (**b**) feedstock (SEM) (100×); (**c**) feedstock (SEM) (500×); (**d**) feedstock (SEM) (1000×).

Figure 8. Filament A (green): (**a**) micro-CT; (**b**) feedstock (SEM) (100×); (**c**) feedstock (SEM) (500×); (**d**) feedstock (SEM) (1000×).

Figure 8. Filament A (green): (**a**) micro-CT; (**b**) feedstock (SEM) (100×); (**c**) feedstock (SEM) (500×); (**d**) feedstock (SEM) (1000×).

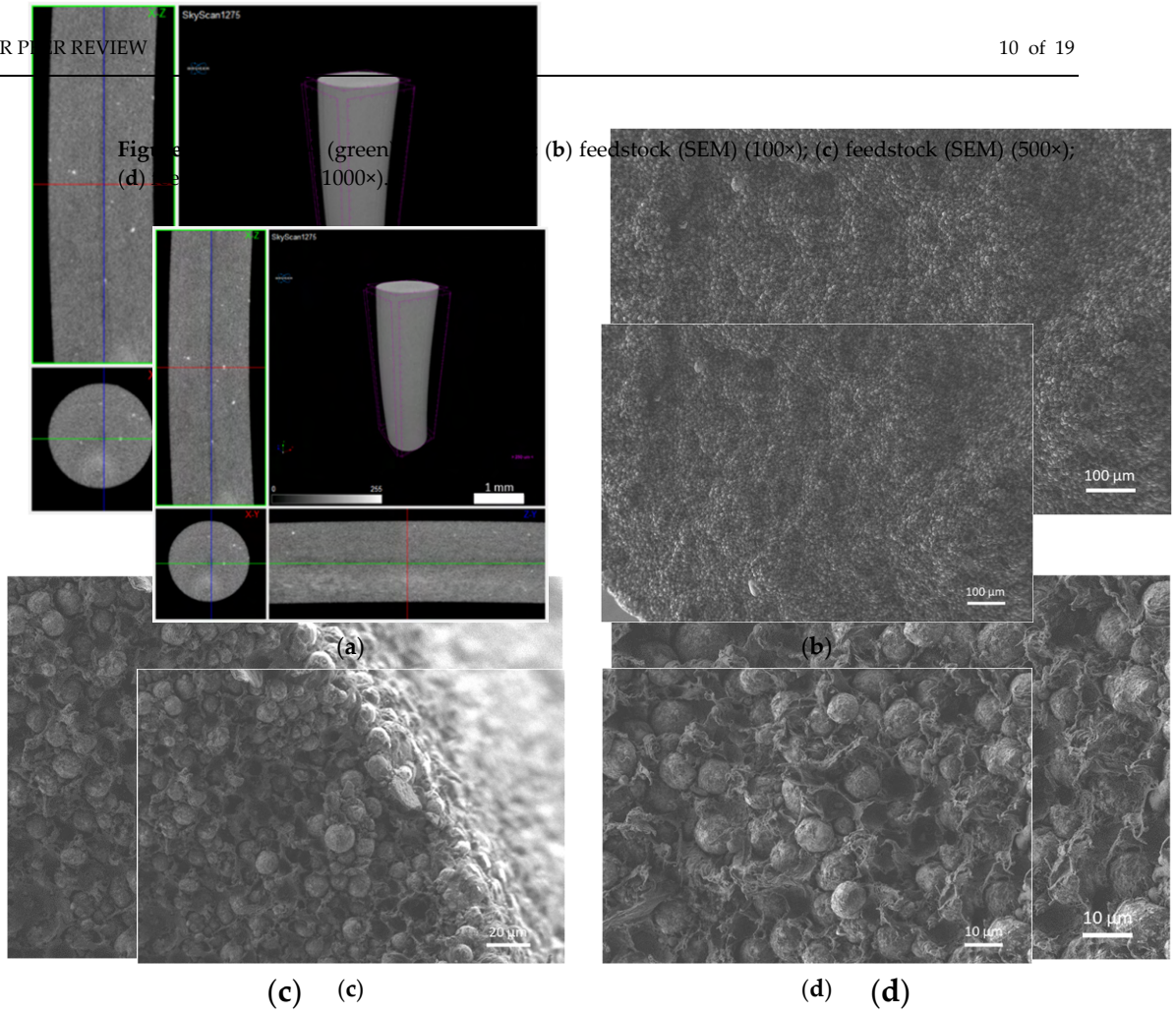

Figure 9. Filament B (green): (**a**) micro-CT; (**b**) feedstock (SEM) (100×); (**c**) feedstock (SEM) (500×); (**d**) feedstock (SEM) (1000×).

Figure 9. Filament B (green): (**a**) micro-CT; (**b**) feedstock (SEM) (100×); (**c**) feedstock (SEM) (500×); (**d**) feedstock (SEM) (1000×).

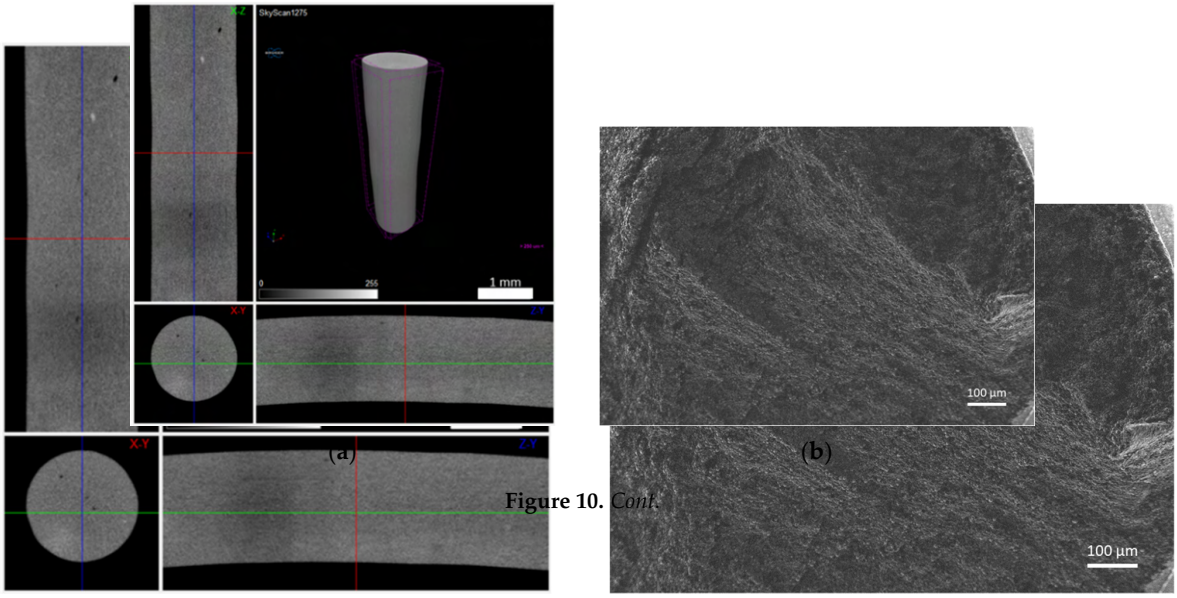

Figure 10. *Cont.*

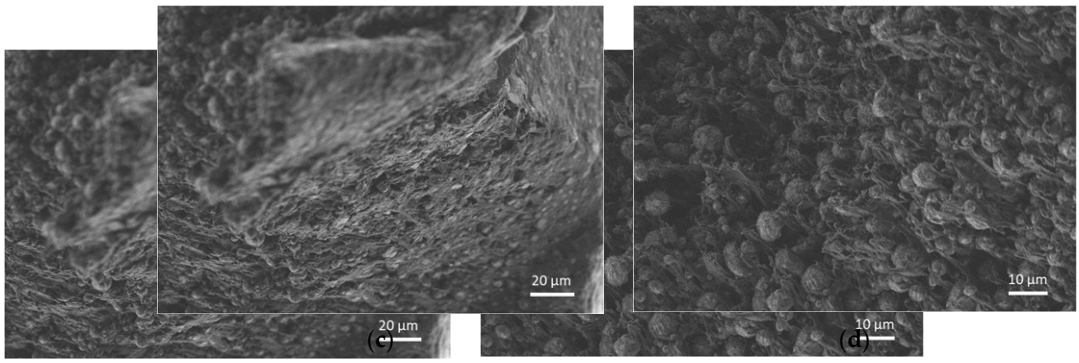

Figure 10. Filament C (green): (**a**) micro-CT; (**b**) feedstock (SEM) (100×); (**c**) feedstock (SEM) (500×); (**d**) feedstock (SEM) (1000×).

Figure 10. Filament C (green): (**a**) micro-CT; (**b**) feedstock (SEM) (100×); (**c**) feedstock (SEM) (500×); (**d**) feedstock (SEM) (1000×).

After detailed analyses of the filament morphology, tensile tests (Figure 11) and flexural tests (Figure 12) were performed. The mechanical characterisation revealed that filament A had more fragile behaviour than the others in the tensile tests, consistent with the porosity throughout the filament volume. Nevertheless, the tensile strength was the highest for filament B (12.1 MPa), followed by filament C (10.9 MPa), and the lowest value was measured for filament A (7.6 MPa). This decrease seems to be influenced by particle size and particle size distribution. Young's modulus showed the highest value for filament B (2.2 GPa). The mechanical results support the detailed analysis made by micro-CT. Flexural tests revealed that the highest deflection was detected in the filament with the highest homogeneity and fewer defects, which is filament B. Even so, the behaviour of the flexural modulus was very similar for the three different filaments. The high deflection at break and low flexural modulus was already established to be printable by [29].

After detailed analyses of the filament morphology, tensile tests (Figure 11) and flexural tests (Figure 12) were performed. The mechanical characterisation revealed that filament A had more fragile behaviour than the others in the tensile tests, consistent with the porosity throughout the filament volume. Nevertheless, the tensile strength was the highest for filament B (12.1 MPa), followed by filament C (10.9 MPa), and the lowest value was measured for filament A (7.6 MPa). This decrease seems to be influenced by particle size and particle size distribution. Young's modulus showed the highest value for filament B (2.2 GPa). The mechanical results support the detailed analysis made by micro-CT. Flexural tests revealed that the highest deflection was detected in the filament with the highest homogeneity and fewer defects, which is filament B. Even so, the behaviour of the flexural modulus was very similar for the three different filaments. The high deflection at break and low flexural modulus was already established to be printable by [29].

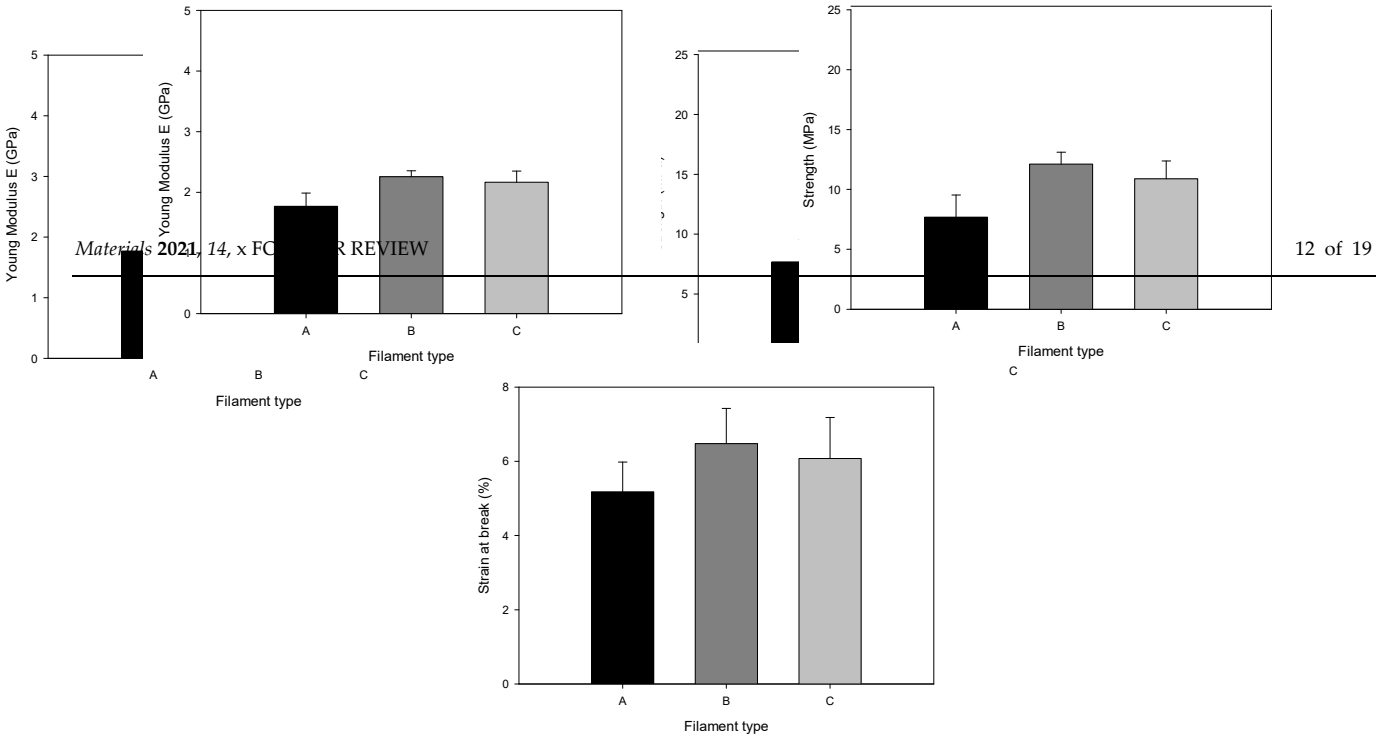

Figure 11. Young's modulus, maximum tensile strength, and strain of different filaments (tensile tests).

Figure 11. Young's modulus, maximum tensile strength, and strain of different filaments (tensile tests).

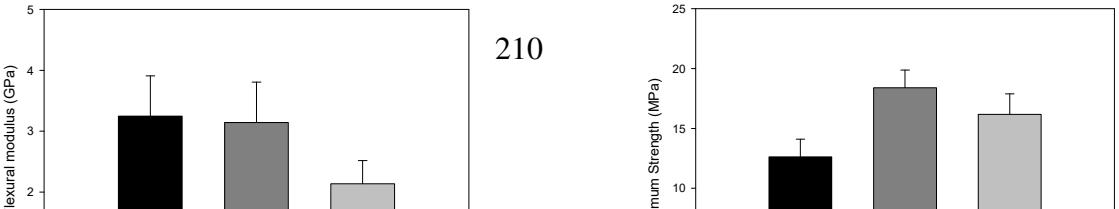

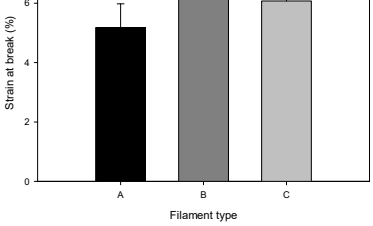

Figure 11. Young's modulus, maximum tensile strength, and strain of different filaments (tensile tests).

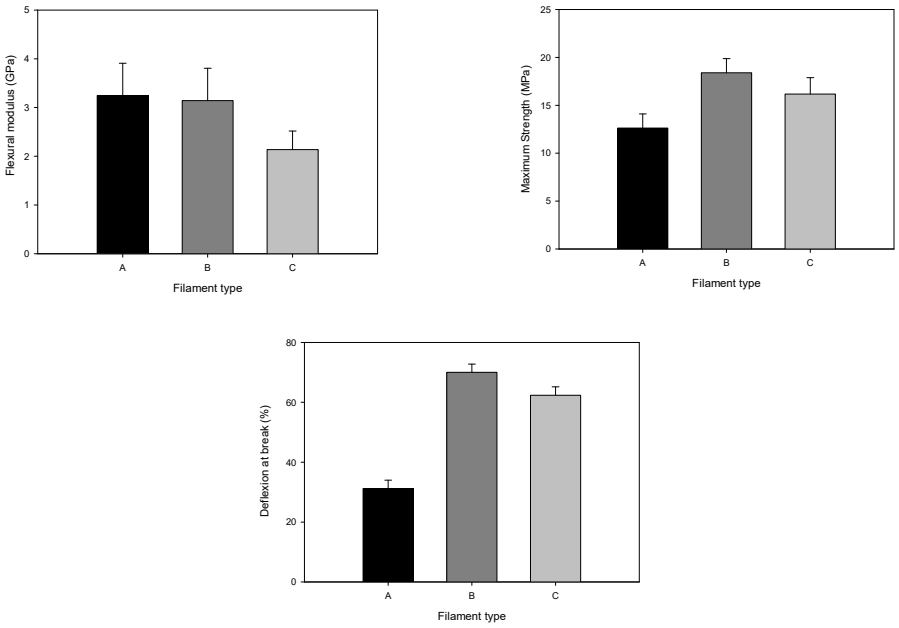

Figure 12. Flexural modulus, strength, and deflection at break of different filaments (three-point bending test).

4.2.2. Strands

The strands, subsequent to printer extrusion to build the 3D object, were analysed. The aim was to highlight the influence of the small nozzle (diameter = 400 µm) on powder distribution, which would be organised similarly in the final 3D object. The micro-CT analysis for the whole volume of the filament was confirmed using SEM. In the first case, powder A resulted in a non-uniform strand (denominated strand A), with larger particles randomly distributed throughout the volume (Figure 13). Henceforth, the strands were denominated by the powder name of their constituents. Micro-CT (high-density particles with a diameter larger than the lowest resolution, 5.67 µm, are in white) and the SEM images show particle distribution in the strand. In strand B, even though a low wettability of the binder + additives could be observed, and a very good distribution of the powder and interparticular distance, as seen in the original filament for (Figure 14). The results of strand C indicated that small defects, enlarged in the extrusion direction, may appear during printing and may be caused by the small hole diameter and particle compaction behaviour (Figure 15).

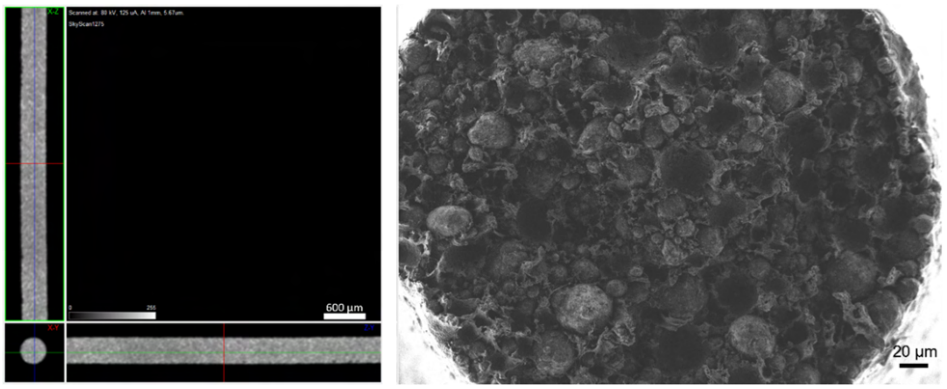

Figure 13. Strand A: (**a**) micro-CT and (**b**) cross section (SEM).

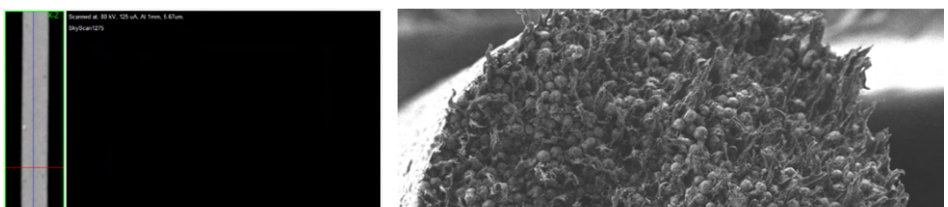

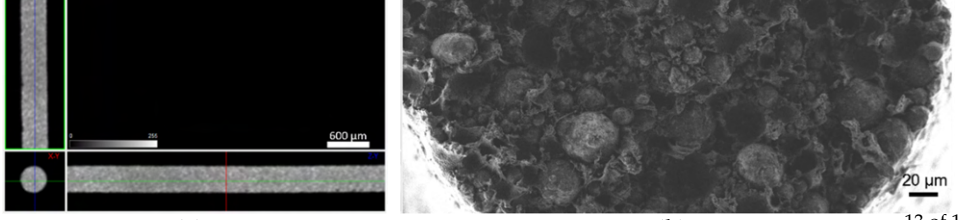

(a) (b)

Figure 13. Strand A: (a) micro-CT and (b) cross section (SEM).

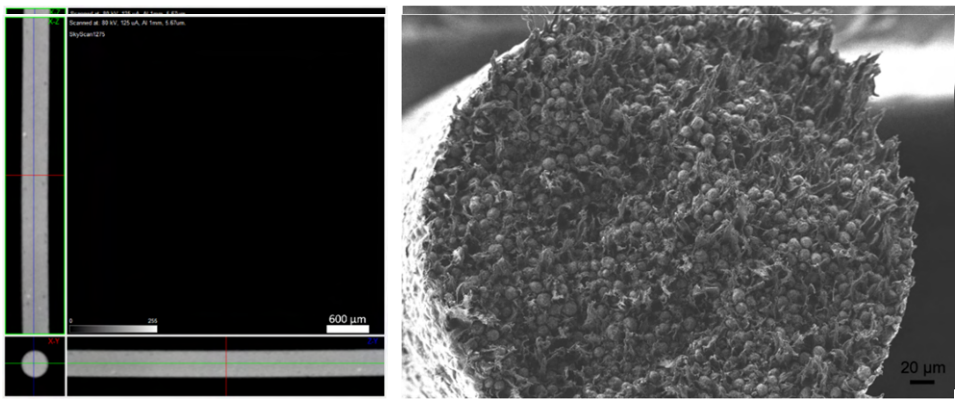

(a) (b)

Figure 14. Strand B (a) micro-CT and (b) cross section (SEM).

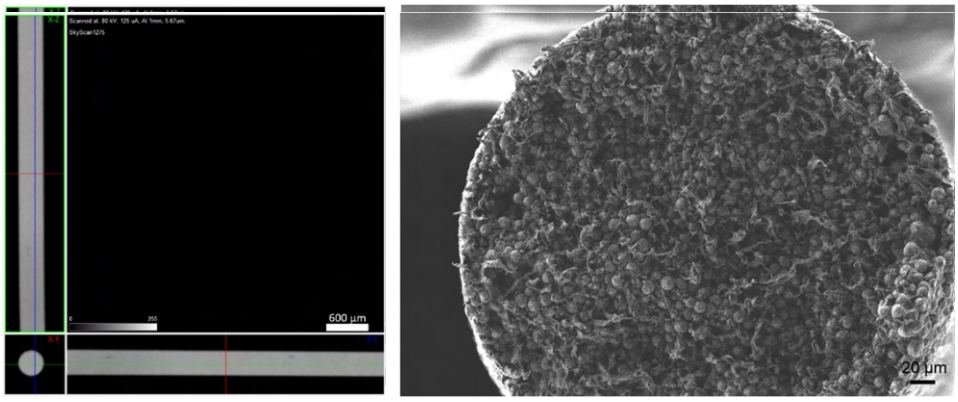

(a) (b)

Figure 15. Strand C (a) micro-CT and (b) cross section (SEM).

4.2.3. The 3D Objects after Shaping

Hereafter, the different 3Dobjects resulting from strands A, B, and C were designated by A, B, and C, respectively.

Micro-CT of the green 3D objects (Figures 16–18) was produced to observe the influence of powder size and powder distribution on the quality of a final 3D object produced with the same parameters. Since copper is a dense material, which affects the X-ray behaviour on micro-CT, as previously mentioned, only high-dimension pores were detected. Furthermore, 3D object A had a large number of defects that started halfway through building the object and a large open pore resulting from the use of the spiral printing strategy. This may be the result of the nozzle lacking heated bed pressure, which makes the strands flattened against the surface since the distance between the nozzle and substrate is not the same as each strand height. Similar to the filament, 3D object B seems to have no apparent defects and presents a better geometrical accuracy than A. object C also shows high density, but the micro-CT suggests that small defects may be present in its centre. This can be due to the extrusion multiplier parameter, as it may be creating enough strand flattening to mitigate the lack of the density apparent in each filament strand.

detected. Furthermore, 3D object A had a large number of defects that started halfway through building the object and a large open pore resulting from the use of the spiral printing strategy. This may be the result of the nozzle lacking heated bed pressure, which makes the strands flattened against the surface since the distance between the nozzle and substrate is not the same as each strand height. Similar to the filament, 3D object B seems to have no apparent defects and presents a better geometrical accuracy than A. object C also shows high density, but the micro-CT suggests that small defects may be present in its centre. This can be due to the extrusion multiplier parameter, as it may be creating enough strand flattening to mitigate the lack of the density apparent in each filament strand.

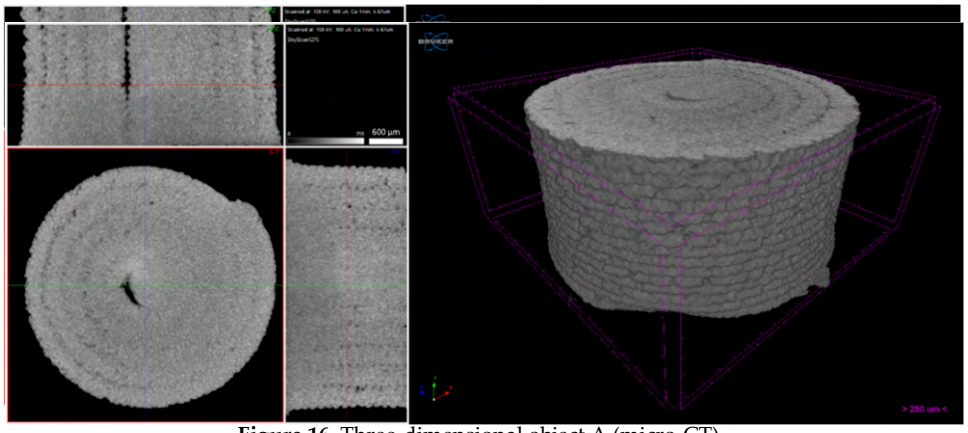

Figure 16. Three-dimensional object A (micro-CT).

Figure 16. Three-dimensional object A (micro-CT).

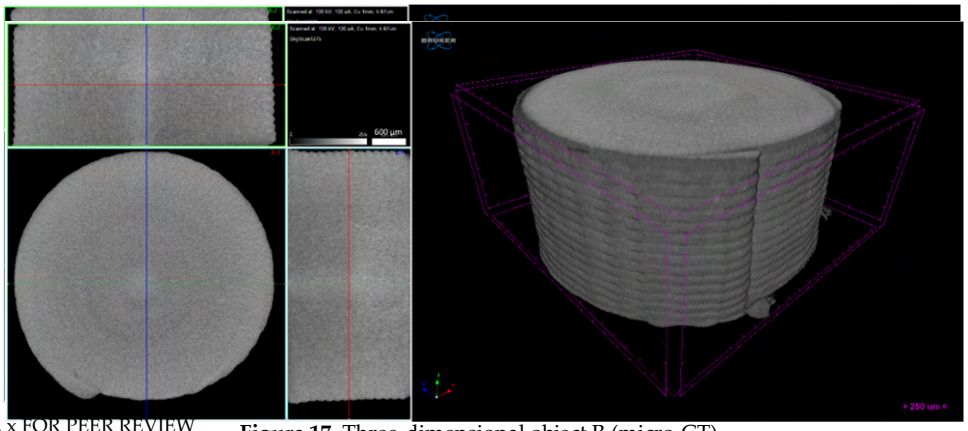

Figure 17. Three-dimensional object B (micro-CT).

Figure 17. Three-dimensional object B (micro-CT).

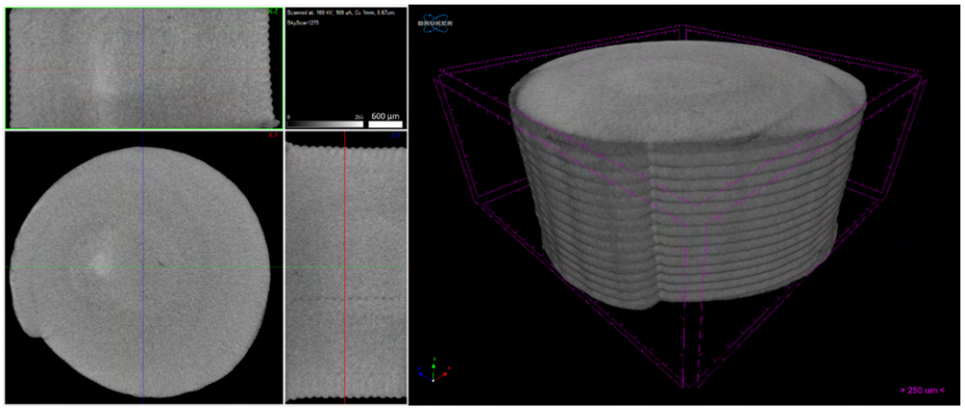

Figure 18. Three-dimensional object C (micro-CT).

Figure 18. Three-dimensional object C (micro-CT).

4.3. Debinding and Sintering

These stages, transversal to the greens (filament and 3D object), were applied only to the filaments. To prove the copper feedstocks' sinterability and avoid the influence of printing parameters on the final density, the three different filaments underwent the debinding (brown) process and were sintered. Figures 19–21 show a micro-CT and a macrography of the sintered filaments. If A and B show the same defects, filament C had different behaviour. The external part of the filament was sintered, and the central part had a low density, which means it was not sintered. This can be attributed to copper oxide present in filament C, resulting in a barrier to the sintering of the central part. In fact, the high surface area of powder C was responsible for the highest oxidation.

4.3. Debinding and Sintering

These stages, transversal to the greens (filament and 3D object), were applied only to the filaments. To prove the copper feedstocks' sinterability and avoid the influence of printing parameters on the final density, the three different filaments underwent the debinding (brown) process and were sintered. Figures 19–21 show a micro-CT and a macrography of the sintered filaments. If A and B show the same defects, filament C had different behaviour. The external part of the filament was sintered, and the central part had a low density, which means it was not sintered. This can be attributed to copper oxide present in filament C, resulting in a barrier to the sintering of the central part. In fact, the high surface area of powder C was responsible for the highest oxidation.

Figure 18. Three-dimensional object C (micro-CT).

4.3. Debinding and Sintering

These stages, transversal to the greens (filament and 3D object), were applied only to the filaments. To prove the copper feedstocks' sinterability and avoid the influence of printing parameters on the final density, the three different filaments underwent the debinding (brown) process and were sintered. Figures 19–21 show a micro-CT and a macrography of the sintered filaments. If A and B show the same defects, filament C had different behaviour. The external part of the filament was sintered, and the central part had a low density, which means it was not sintered. This can be attributed to copper oxide present in filament C, resulting in a barrier to the sintering of the central part. In fact, the high surface area of powder C was responsible for the highest oxidation.

present in filament C, resulting in a barrier to the sintering of the central part. In fact, the high surface area of powder C was responsible for the highest oxidation.

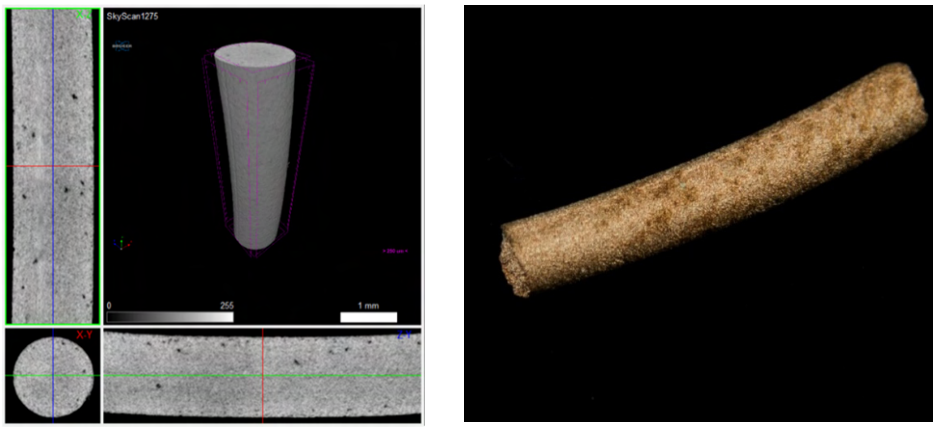

(**a**) (**b**)

Materials **2021**, *14*, x FOR PEER REVIEW 16 of 19

Materials **2021**, *14*, x FOR PEER REVIEW 16 of 19

Figure 19. Filament A sintered: (**a**) micro-CT and (**b**) macrography.

Figure 19. Filament A sintered: (**a**) micro-CT and (**b**) macrography.

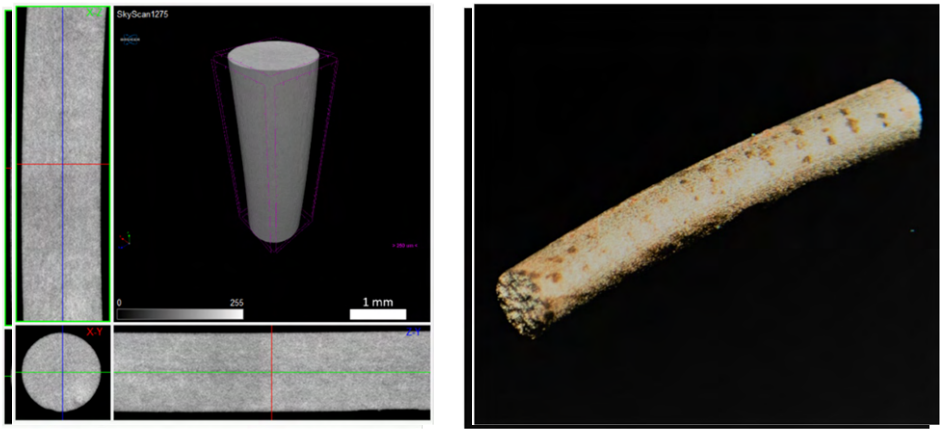

(**a**) (**b**)

Figure 20. Filament B sintered: (**a**) micro-CT and (**b**) macrography.

Figure 20. Filament B sintered: (**a**) micro-CT and (**b**) macrography.

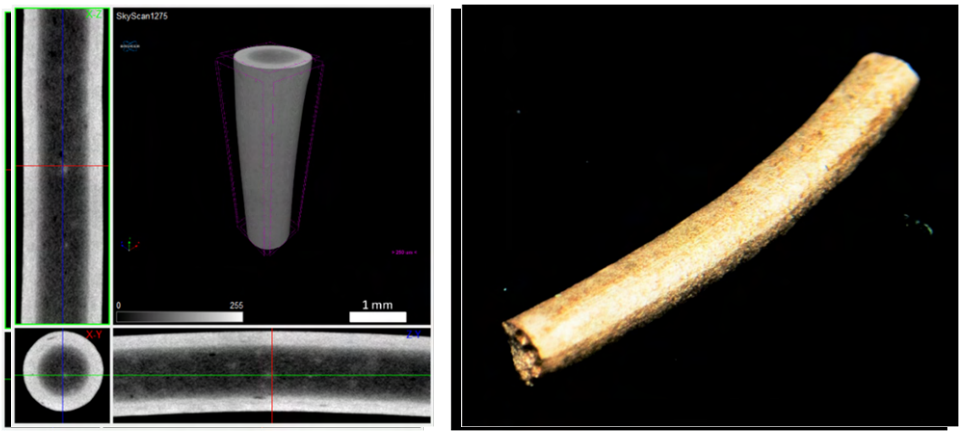

(**a**) (**b**)

Figure 21. Filament C sintered: (**a**) micro-CT and (**b**) macrography.

Figure 21. Filament C sintered: (**a**) micro-CT and (**b**) macrography.

4.4. Microstructures and Hardness

Figure 22 shows different representative metallographic images of sintered copper MEX filaments. All the sintered filaments presented a typical microstructure of copper. However, it is clear that A and C presented a significant porosity, A with higher porosity than C.

Figure 22 shows different representative metallographic images of sintered copper MEX filaments. All the sintered filaments presented a typical microstructure of copper. However, it is clear that A and C presented a significant porosity, A with higher porosity than C.

4.4. Microstructures and Hardness

Figure 22 shows different representative metallographic images of sintered copper MEX filaments. All the sintered filaments presented a typical microstructure of copper. However, it is clear that A and C presented a significant porosity, A with higher porosity than C.

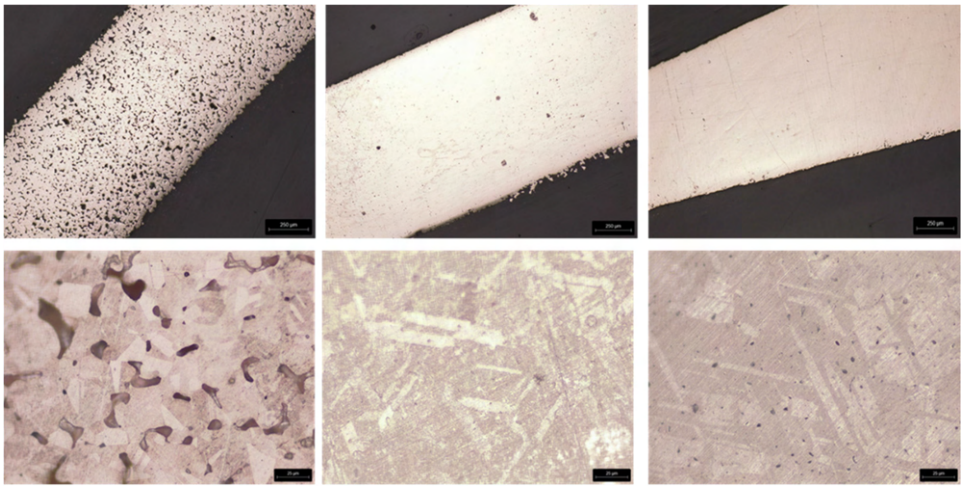

(**a**) (**b**) (**c**)

Figure 22. Macrography (top, 20×) and microstructure (OM) (bottom, 200×) of sintered filaments after etching: from powder A (**a**), B (**b**), and C (**c**).

In spite of C having the smallest particle size and particle size distribution, and consequently, the highest surface area, they had a difficult sintering process, evident in micro-CT. This behaviour is due to powder oxidation.

Table 5 summarises the different microhardness values measured in MEX 3D sintered objects from powder A, B, and C for the same thermal treatment (debinding and sintering) conditions. The microhardness values, particularly for powder C, support the presence of copper oxide 'reinforcement' on the powder surface [30,31].

Table 5. Microhardness of the sintered filament.

Specimens	A	B	C
Microhardness (HV0.1) (10 measurements)	68 ± 8.9	65 ± 2.7	80 ± 2.3

5. Conclusions

Highly filled composite materials were prepared with 61 vol.% of copper with three different particle size distributions. It was found that the filaments were successfully extruded with a good pressure distribution during extrusion. Moreover, it became evident that the green filament based on powder B had the maximum strength and deflexion at break. After debinding and sintering, the best filament (B) had a D_{50} close to 11 µm with a unimodal particle size distribution, shape factor 1, and a surface similar to other powder. The only negative aspect of copper that must be solved in MEX was the powder oxidation resulting from powder preparation, which depends on particle size, and it became evident by the density values of copper powder. This negative aspect, which had consequences in sintering, must be overcome by the selection of another environmental atmosphere than Ar + H_2, for example, H_2 [32].

Author Contributions: Conceptualization, C.S. and F.C.; methodology, C.S. and M.T.V.; validation, M.T.V.; investigation, C.S., D.G. and F.C.; micro-CT investigation and methodology, D.G.; writing—original draft preparation, C.S.; writing—review and editing, D.G. and M.T.V.; visualization, C.S. and D.G.; supervision, M.T.V.; project administration, M.T.V.; funding acquisition, M.T.V. All authors have read and agreed to the published version of the manuscript.

Author Contributions: Conceptualization, C.S. and F.C.; methodology, C.S. and M.T.V.; validation, M.T.V.; investigation, C.S., D.G. and F.C.; micro-CT investigation and methodology, D.G.; writing—original draft preparation, C.S.; writing—review and editing, D.G. and M.T.V.; visualization, C.S. and D.G.; supervision, M.T.V.; project administration, M.T.V.; funding acquisition, M.T.V. All authors have read and agreed to the published version of the manuscript.

Funding: This work was supported by the European Regional Development Fund (ERDF) under the Portuguese program—Programa Operacional Factores de Competitividade (COMPETE) (grant agreement No. POCI-01-0247-FEDER-024533)]; this research is also sponsored by FEDER funds through the program COMPETE—Programa Operacional Factores de Competitividade—and by national funds through FCT—Fundação para a Ciência e a Tecnologia, under the project UIDB/00285/2020 and UIDB/04044/2020.

Institutional Review Board Statement: Not applicable.

Informed Consent Statement: Not applicable.

Data Availability Statement: Data sharing is not applicable to this article.

Conflicts of Interest: The authors declare no conflict of interest.

References

1. Singh, S.; Ramakrishna, S.; Singh, R. Material Issues in Additive Manufacturing: A Review. *J. Manuf. Process.* **2017**, *25*, 185–200. [CrossRef]
2. Ngo, T.D.; Kashani, A.; Imbalzano, G.; Nguyen, K.T.Q.; Hui, D. Additive Manufacturing (3D Printing): A Review of Materials, Methods, Applications and Challenges. *Compos. Part B Eng.* **2018**, *143*, 172. [CrossRef]
3. Gonzalez-Gutierrez, J.; Godec, D.; Guráň, R.; Spoerk, M.; Kukla, C. Holzer 3D Printing Conditions Determination for Feedstock Used in Fused Filament Fabrication (FFF) of 17-4PH Stainless Steel Parts. *Metalurgija* **2018**, *57*, 117–120.
4. Orlovská, M.; Chlup, Z.; Bača, Ľ.; Janek, M.; Kitzmantel, M. Fracture and Mechanical Properties of Lightweight Alumina Ceramics Prepared by Fused Filament Fabrication. *J. Eur. Ceram. Soc.* **2020**, *40*, 4837–4843. [CrossRef]
5. Thompson, Y.; Gonzalez-Gutierrez, J.; Kukla, C.; Felfer, P. Fused Filament Fabrication, Debinding and Sintering as a Low Cost Additive Manufacturing Method of 316L Stainless Steel. *Addit. Manuf.* **2019**, *30*, 100861. [CrossRef]
6. ISO/ASTM Additive Manufacturing-General Principles-Terminology (ISO/ASTM DIS 52900:2018). Available online: https://www.techstreet.com/standards/din-en-iso-astm-52900-draft?product_id=2015850 (accessed on 24 May 2020).
7. German, R.M.; Bose, A. *Injection Molding of Metals and Ceramics*; Metal Powder Industry: Princeton, NJ, USA, 1997; ISBN 978-1-878954-61-9.
8. Goudah, G.; Ahmad, F.; Mamat, O.; Omar, M.A. Preparation and Characterization of Copper Feedstock for Metal Injection Molding. *J. Appl. Sci.* **2010**, *10*, 3295–3300. [CrossRef]
9. Hausnerova, B.; Kitano, T.; Kuritka, I.; Prindis, J.; Marcanikova, L. The Role of Powder Particle Size Distribution in the Processability of Powder Injection Molding Compounds. *Int. J. Polym. Anal. Charact.* **2011**, *16*, 141–151. [CrossRef]
10. Riecker, S.; Clouse, J.; Studnitzky, T.; Andersen, O.; Kieback, B. Fused Deposition Modeling-Opportunities for Cheap Metal AM. In Proceedings of the European Congress and Exhibition on Powder Metallurgy, European PM Conference Proceedings, Hamburg, Germany, 9 October 2016.
11. Cruz, N.; Santos, L.; Vasco, J.; Barreiros, F.M. Binder System for Fused Deposition of Metals. In Proceedings of the Euro PM2013, Congress & Exhibition, Gothenburg, Sweden, 15 September 2013; pp. 79–84.
12. Kukla, C.; Gonzalez-Gutierrez, J.; Duretek, I.; Schuschnigg, S.; Holzer, C. Effect of Particle Size on the Properties of Highly-Filled Polymers for Fused Filament Fabrication. In *AIP Conference Proceedings*; AIP Publishing LLC: Lyon, France, 2017; p. 190006.
13. Khatri, B.; Lappe, K.; Noetzel, D.; Pursche, K.; Hanemann, T. A 3D-Printable Polymer-Metal Soft-Magnetic Functional Composite—Development and Characterization. *Materials* **2018**, *11*, 189. [CrossRef]
14. Dehdari Ebrahimi, N.; Ju, Y.S. Thermal Conductivity of Sintered Copper Samples Prepared Using 3D Printing-Compatible Polymer Composite Filaments. *Addit. Manuf.* **2018**, *24*, 479–485. [CrossRef]
15. Copper as Electrical Conductive Material with Above-Standard Performance Properties. Available online: http://www.conductivity-app.org/single-article/cu-overview#L15 (accessed on 18 August 2021).
16. Huang, J.; Yan, X.; Chang, C.; Xie, Y.; Ma, W.; Huang, R.; Zhao, R.; Li, S.; Liu, M.; Liao, H. Pure Copper Components Fabricated by Cold Spray (CS) and Selective Laser Melting (SLM) Technology. *Surf. Coat. Technol.* **2020**, *395*, 125936. [CrossRef]
17. Sárosi, Z.; Knapp, W.; Kunz, A.; Wegener, K. Evaluation of Reflectivity of Metal Parts by a Thermo-Camera. *InfraMation 2010 Proc.* **2010**, 11. [CrossRef]
18. El-Wardany, T.I.; She, Y.; Jagdale, V.N.; Garofano, J.K.; Liou, J.J.; Schmidt, W.R. Challenges in Three-Dimensional Printing of High-Conductivity Copper. *J. Electron. Packag.* **2018**, *140*, 020907. [CrossRef]
19. Lykov, P.A.; Safonov, E.V.; Akhmedianov, A.M. Selective Laser Melting of Copper. *Mater. Sci. Forum* **2016**, *843*, 284–288. [CrossRef]

20. Trevisan, F.; Calignano, F.; Lorusso, M.; Lombardi, M.; Manfredi, D.; Fino, P. Selective Laser Melting of Chemical Pure Copper. In Proceedings of the Euro PM2017 Congress & Exhibition, Milan, Italy, 3 October 2017.
21. Silbernagel, C.; Gargalis, L.; Ashcroft, I.; Hague, R.; Galea, M.; Dickens, P. Electrical Resistivity of Pure Copper Processed by Medium-Powered Laser Powder Bed Fusion Additive Manufacturing for Use in Electromagnetic Applications. *Addit. Manuf.* **2019**, *29*, 100831. [CrossRef]
22. Ikeshoji, T.-T.; Nakamura, K.; Yonehara, M.; Imai, K.; Kyogoku, H. Selective Laser Melting of Pure Copper. *JOM* **2018**, *70*, 396–400. [CrossRef]
23. Colopi, M.; Caprio, L.; Demir, A.G.; Previtali, B. Selective Laser Melting of Pure Cu with a 1 KW Single Mode Fiber Laser. *Procedia CIRP* **2018**, *74*, 59–63. [CrossRef]
24. Jadhav, S.D.; Dadbakhsh, S.; Goossens, L.; Kruth, J.-P.; Van Humbeeck, J.; Vanmeensel, K. Influence of Selective Laser Melting Process Parameters on Texture Evolution in Pure Copper. *J. Mater. Process. Technol.* **2019**, *270*, 47–58. [CrossRef]
25. BASF Launches Ultrafuse 316LX for Fused Filament Fabrication of Metal Parts. Available online: https://www.metal-am.com/basf-launches-ultrafuse-316lx-fused-filament-fabrication-metal-parts/ (accessed on 18 April 2021).
26. Ferreira, T.J.; Vieira, M.T. Optimization of MWCNT–Metal Matrix Composites Feedstocks. *Ciência Tecnol. Dos Mater.* **2017**, *29*, e87–e91. [CrossRef]
27. Ferreira, T.J.J. Microinjection Moulding of Austenitic Stainless Steel Reinforced with Carbon Nanotubes. Ph.D. Thesis, University of Coimbra, Coimbra, Portugal, 2018.
28. Sigma-Aldrich Copper (I) Oxide Material Safety Data Sheet 2014. Available online: https://www.nwmissouri.edu/naturalsciences/sds/c/Copper%20I%20oxide.pdf (accessed on 18 August 2021).
29. Cerejo, F.; Gatões, D.; Vieira, M.T. Optimization of Metallic Powder Filaments for Additive Manufacturing Extrusion (MEX). *Int. J. Adv. Manuf. Technol.* **2021**, *115*, 2449–2464. [CrossRef]
30. Strąk, C.; Olesińska, W.; Siedlec, R. Influence of Carbon and Oxygen on Properties of Cu-C-O Composites. *Electron. Mater.* **2016**, *44*, 13.
31. Kreuzeder, M.; Abad, M.-D.; Primorac, M.-M.; Hosemann, P.; Maier, V.; Kiener, D. Fabrication and Thermo-Mechanical Behavior of Ultra-Fine Porous Copper. *J. Mater. Sci.* **2015**, *50*, 634–643. [CrossRef] [PubMed]
32. Hao, H.; Wang, Y.; Jafari Nodooshan, H.R.; Zhang, Y.; Ye, S.; Lv, Y.; Yu, P. The Effects of Sintering Temperature and Addition of TiH2 on the Sintering Process of Cu. *Materials* **2019**, *12*, 2594. [CrossRef] [PubMed]

Appendix D

Searching New Solutions for NiTi Sensors through Indirect Additive Manufacturing

materials

MDPI

Article

Searching New Solutions for NiTi Sensors through Indirect Additive Manufacturing

Pedro Carreira [1], Daniel Gatões [2], Nuno Alves [1], Ana Sofia Ramos [2,*] and Maria Teresa Vieira [2]

[1] CDRSP—Centre for Rapid and Sustainable Product Development, Polytechnic Institute of Leiria, 2411-901 Leiria, Portugal; pedrosilvacarreira@gmail.com (P.C.); nuno.alves@ipleiria.pt (N.A.)
[2] University of Coimbra, CEMMPRE—Centre for Mechanical Engineering, Materials and Processes, Department of Mechanical Engineering, Polo II, R. Luís Reis Santos, 3030-788 Coimbra, Portugal; daniel.gatoes@uc.pt (D.G.); teresa.vieira@dem.uc.pt (M.T.V.)
* Correspondence: sofia.ramos@dem.uc.pt; Tel.: +351-239700711

Abstract: Shape Memory Alloys (SMAs) can play an essential role in developing novel active sensors for self-healing, including aeronautical systems. However, the NiTi SMAs available in the market are almost limited to wires, small sheets, and coatings. This restriction is mainly due to the difficulty in processing NiTi through conventional processes. Thus, the objective of this study is to evaluate the potential of one of the most promising routes for NiTi additive manufacturing—material extrusion (MEX). Optimizing the different steps during processing is mandatory to avoid brittle secondary phases formation, such as Ni_3Ti. The prime NiTi powder is prealloyed, but it also contains $NiTi_2$ and Ni as secondary phases. The present study highlights the role of Ni and $NiTi_2$, with the later having a melting temperature (Tm = 984 °C) lower than the NiTi sintering temperature, thus allowing a welcome liquid phase sintering (LPS). Nevertheless, the reaction of the liquid phase with the Ni phase could contribute to the formation of brittle intermetallic compounds, particularly around NiTi and $NiTi_2$ phases, affecting the final structural properties of the 3D object. The addition of TiH_2 to the virgin prealloyed NiTi powder was also studied and revealed the non-formation of Ni_3Ti for a specific composition. The balancing addition of extra Ni revealed priority in the Ni_3Ti appearance, emphasizing the role of Ni. Feedstocks extruded (filaments) and green strands (layers), before and after debinding & sintering, were used as homothetic of 3D objects for evaluation of defects (microtomography), microstructures, and mechanical properties. The composition of prealloyed powder with 5 wt.% TiH_2 addition after sintering showed a homogeneous matrix with the $NiTi_2$ second phase uniformly dispersed.

Keywords: Nickel-Titanium (NiTi); Shape Memory Alloys (SMAs); Metal Extrusion (MEX); additive manufacturing (AM); Titanium Hydride (TiH_2)

check for updates

Citation: Carreira, P.; Gatões, D.; Alves, N.; Ramos, A.S.; Vieira, M.T. Searching New Solutions for NiTi Sensors through Indirect Additive Manufacturing. *Materials* **2022**, *15*, 5007. https://doi.org/10.3390/ma15145007

Academic Editor: Thomas Niendorf

Received: 9 June 2022
Accepted: 15 July 2022
Published: 19 July 2022

Publisher's Note: MDPI stays neutral with regard to jurisdictional claims in published maps and institutional affiliations.

1. Introduction

NiTi is classified as a shape memory alloy (SMA), and is defined as an intermetallic material, with the ability to restore its previously defined shape when exposed to a specific thermal cycle, either through shape memory effect or superelasticity, induced by solid state diffusionless, reversible phase transformation between austenite, the high temperature phase, and martensite, the low temperature one [1,2]. Two main properties of NiTi, such as superior corrosion resistance and super long fatigue life, make this material suitable for smart engineering structures and medical applications. Nevertheless, NiTi is extremely difficult to process by conventional processes [3]. Casting problems, such as segregation of alloying elements and the rapid work hardening and superelasticity of NiTi, make conventional machining a challenge and leads to poor quality workpieces. Although new processing approaches, particularly for NiTi machining, have been proposed [4], powder metallurgy (PM) has been demonstrating its efficiency, particularly in what concerns

additive manufacturing (AM). Direct processes, such as selective laser melting (SLM), creates a material with homogeneous microstructure and stable properties [5]. Current research on the AM of NiTi parts from prealloyed powders has been associated with difficulties concerning chemical homogeneity and chemical composition control caused by Ni evaporation during the melting process [6]. Moreover, the limits of SLM are mainly related to the ability to achieve complex microshapes and internal microfeatures, as well as high dimensional accuracy. These limitations open new paths to the indirect additive process (shaping = extrusion of a filament, debinding, and sintering) and denominated material extrusion (MEX) [7]. Research studies on NiTi and other metallic powder show the viability and importance of this AM technology to process 3D objects [8,9]. Nevertheless, MEX has some geometrical limitations of PIM (Powder Injection Moulding).

The main target of this study is to attain a suitable NiTi-based material with high densification and appropriate microstructure after MEX, compatible with a crack's sensor and predictive of component/system failure. Prealloyed NiTi powder is pointed out as the best solution for additive processes. A uniform austenitic structure, a suitable composition, and transformation temperatures for stress-induced martensitic transformation must be its characteristics. Nevertheless, secondary phases originated during prealloyed powder production (atomization) oblige us to search for mechanisms that could contribute to decreasing the Ni in excess by producing NiTi from $NiTi_2$, mainly by avoiding the formation of Ni_3Ti during processing [8]. Adding TiH_2 in different percentages can contribute to this target, particularly by favoring the disappearance of Ni_3Ti. In addition, using TiH_2 instead of Ti can protect powder from oxidation during post- shaping heat treatments (debinding and sintering) and create "brown" inside, a reducing atmosphere (TiH_2 decomposition temperature is lower than the temperature of post-heat treatments defined for NiTi [10]). The main strategy to reduce oxidation of Ti is to use TiH_2. Moreover, TiH_2 dehydrogenation releases Ti that could react with Ni and promote the formation of NiTi [11]. Dehydrogenation occurs up to 600 °C [12] to 650 °C [11,13], or 700 °C [10,14]. Although there is no defined temperature for dehydrogenation, all the temperatures mentioned are lower than the sintering temperature (1165 °C). Thus, total dehydrogenation is expected before sintering. Another advantage of using TiH_2 is that dehydrogenation will expose activated Ti enhancing the sintering process, meaning higher density; the oxygen and nitrogen pickup is expected to be lower [15,16]. However, some authors state that when using TiH_2, pore size reduces, but with more occurrence and is consistently distributed. Different authors studied the effect of TiH_2 addition with Ni elemental powders to obtain NiTi (Table 1). Li et al., in 1998 and 2000, observed in conventional powder processing that when using TiH_2, the general porosity and open-pore ratio tend to decrease, pore size also decreases, and the number of pores increases and becomes more uniform, meaning a reduction in shrinkage [17,18]. When increasing TiH_2 vol.%, together with temperature, sintering is enhanced, contributing to the formation of Kirkendall pores and the shrinkage of the large ones, which is also associated with the enhancement of the shape memory effect (SME). The phases present were NiTi, $NiTi_2$, and Ni_3Ti [17,18]. Bertheville et al. showed the presence of NiTi (B2), Ni_4Ti_3, Ni_3Ti, $Ni_2Ti_4O_x$, and $TiC_{0.7}N_{0.3}$ in the unpolished surface characterization [19]. The two last ones result from contamination of the virgin powder particles during processing [19]. After post-processing, the most prominent phases were NiTi (B2), Ni_4Ti_3, and $Ni_2Ti_4O_x$ [19]. Chen et al. used elemental compositions of 51 at.% of Ni with TiH_2 and observed a reduction in pore size and an increase in their number associated with a uniform distribution [11]. One significant difference was that Ni-Ti 3D objects swelled and Ni-TiH_2 shrinkage was observed. The most prominent phase was NiTi (B2), and the occurrence of $NiTi_2$ and Ni_3Ti was reduced compared with Ni-Ti virgin powder [20]. Bohua et al. observed that after sintering with Ni-Ti powder, among the NiTi main phase, $NiTi_2$, Ni_4Ti_3, TiO_2, and TiC phases were detected [12]. However, when using Ni-TiH_2, the TiO_2 and TiC phases were absent due to the reducing environment formed by the released hydrogen after dehydrogenation. When using Ni-TiH_2 powder, the 3D object presented a much smaller mean pore size and a homogeneous pore distribution [12].

Table 1. Sintering and post-processing conditions of elemental Ni-TiH_2 powder and final phases.

Temperature [°C]	Holding Time [h]	Vacuum Pressure [Pa]	Processing Technology	Porosity after Sintering (%)	Post-Processing	Phases	Ref.
950	1	1.33×10^{-2}	Pressing	33.9–37.6	-	NiTi $NiTi_2$ / $Ni_2Ti_4O_x$ Ni_3Ti	[17,18]
920	14	-	Pressing	29–34	Aged (Ar) 500 °C (1 h) Not polished	NiTi $Ni_2Ti_4O_x$ Ni_4Ti_3 Ni3Ti TiC0.7 N0.3	[19]
					HIP (Ar) 180 MPa 1050 °C (3 h) Aged (Ar) 500 °C (1 h) Not polished	NiTi $Ni_2Ti_4O_x$ Ni_3Ti $TiC_{0.7}$ $N_{0.3}$	
					Aged (Ar) 500 °C (1 h) Polished HIP (Ar) 180 MPa 1050 °C (3 h) Aged (Ar) 500 °C (1 h) Polished HIP (Ar) 180 MPa 1050 °C (3 h) Annealed (Ar) 1100 °C (1 h) Aged (Ar) 500 °C (1 h) Polished	NiTi $Ni_2Ti_4O_x$ Ni_4Ti_3	
1000 1100 1200	2	3×10^{-3}	Pressing	10–33.8	-	NiTi $NiTi_2$ Ni_3Ti	[11]
900 950 1000 1100 1200	2	3×10^{-3}	Pressing	19 (>900 °C)	-	Ni Ti NiTi $NiTi_2$ Ni_3Ti	[20]
1100 1200					1000 °C 6 h vacuum	NiTi $NiTi_2$	
1000	2	1×10^{-3}	Gel Casting	40–46	-	NiTi $NiTi_2$ Ni_4Ti_3	[12]

1000						NiTi	
1100	2	3×10^{-3}	Pressing	10–33.8	-	$NiTi_{12}$	[11]
1200						Ni_3Ti	
900						Ni	
950						Ti	
1000					-	NiTi	
1100	2	3×10^{-3}	Pressing	19 (>900 °C)		$NiTi_{12}$	[20]
1200						Ni_3Ti	
1100				1000 °C 6 h		NiTi	
1200					vacuum	$NiTi_{12}$	
						NiTi	
1000	2	1×10^{-3}	Gel Casting	40–46	-	NiTi	[12]
						Ni_4Ti_3	

2. Materials and Methods

The flowchart of the MEX process starting with the mixture of the NiTi powder with binder and additives is shown in Figure 1.

2. Materials and Methods

The flowchart of the MEX process starting with the mixture of the NiTi powder with binder and additives is shown in Figure 1.

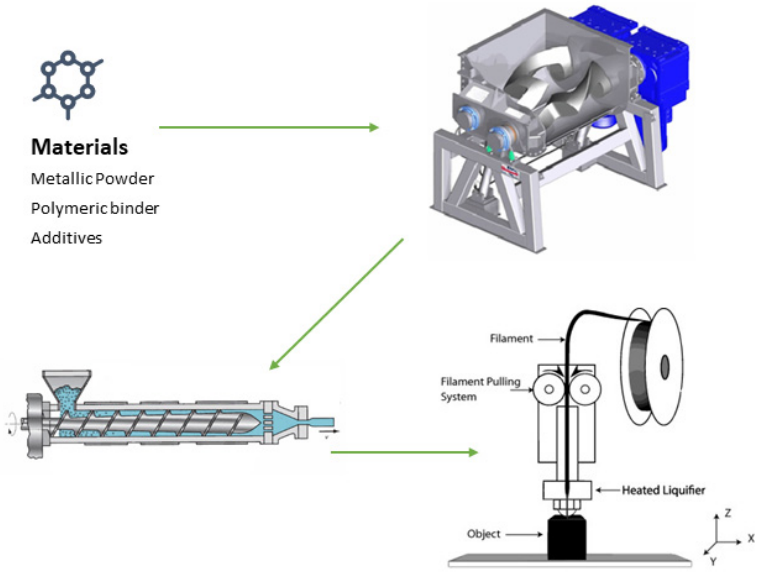

Figure 1. Flowchart of the MEX process (adapted from [21,22]).

Figure 1. Flowchart of the MEX process (adapted from [21,22]).

Prealloyed powder is the elective powder for SLM because the elemental Ni and Ti powder is predisposed to form $NiTi_{12}$ and Ni_3Ti intermetallics due to its high contamination by N_2 and O_2. Thus, the option for MEX was also prealloyed powder, with the expectation to yield the main targets of the SLM process, in particular to attain maximum densification and a more uniform microstructure. The virgin prealloyed NiTi powder particles were supplied by LPW Technology Ltd. (Runcorn, UK), nickel powder particles by Sandvik (Sandviken, Sweeden), and TiH_2 powder particles by Reade Advanced Materials (Riverside, RI, USA). Particle size distribution (PSD) was evaluated using laser diffraction spectrometry LDS, Malvern Panalytical (Egham, UK) with a Malvern Mastersizer 3000. A Philips X'Pert diffractometer (Egham, UK) at 40 kV with Bragg–Brentano geometry (0–2θ), with cobalt anticathode ($\lambda(k\alpha1)$ = 0.178897 nm and $\lambda(k\alpha2)$ = 0.179285 nm), and a current intensity of 35 mA was used to perform phase analysis. The x-ray diffraction scans were carried out from 20 to 100° in steps of 0.025°, with an acquisition time of 1 s per step.

Prealloyed powder is the elective powder for SLM because the elemental Ni and Ti powder is predisposed to form $NiTi_{12}$ and Ni_3Ti intermetallics due to its high contamination by N_2 and O_2. Thus, the option for MEX was also prealloyed powder, with the expectation to yield the main targets of the SLM process, in particular to attain maximum densification and a more uniform microstructure. The virgin prealloyed NiTi powder particles were supplied by LPW Technology Ltd. (Runcorn, UK), nickel powder particles by Sandvik (Sandviken, Sweeden), and TiH_2 powder particles by Reade Advanced Materials (Riverside, RI, USA). Particle size distribution (PSD) was evaluated using laser diffraction spectrometry LDS, Malvern Panalytical (Egham, UK) with a Malvern Mastersizer 3000. A Philips X'Pert diffractometer (Egham, UK) at 40 kV with Bragg–Brentano geometry (0–2θ), with cobalt anticathode ($\lambda(k\alpha1)$ = 0.178897 nm and $\lambda(k\alpha2)$ = 0.179285 nm), and a current intensity of 35 mA was used to perform phase analysis. The x-ray diffraction scans were carried out from 20 to 100° in steps of 0.025°, with an acquisition time of 1 s per step.

Characteristics of NiTi prealloyed powder, binder, and additives are described elsewhere [8]. Phase analysis by X-ray diffraction (XRD) of the prealloyed powder revealed

Characteristics of NiTi prealloyed powder, binder, and additives are described elsewhere [8]. Phase analysis by X-ray diffraction (XRD) of the prealloyed powder revealed a phase other than NiTi and Ni; it also included $NiTi_2$ [8]. TiH_2 and Ni powder particles have a unique phase present (Figure 2). Particle size analysis shows distinct sizes of the different powder particles. This multiplicity of particle sizes can be a promotor of density during the sintering process [23] (Table 2). Moreover, the D50 of powder particles is not the ideal where sintering is the consolidation step. In MEX, to guarantee an effective solid diffusion among powder particles, D50 should be lower than 10 µm.

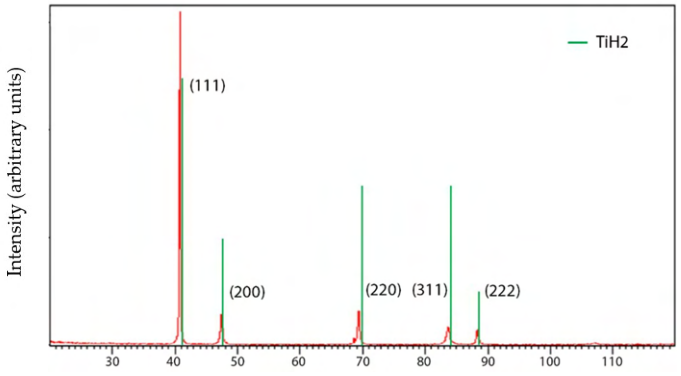

(**a**)

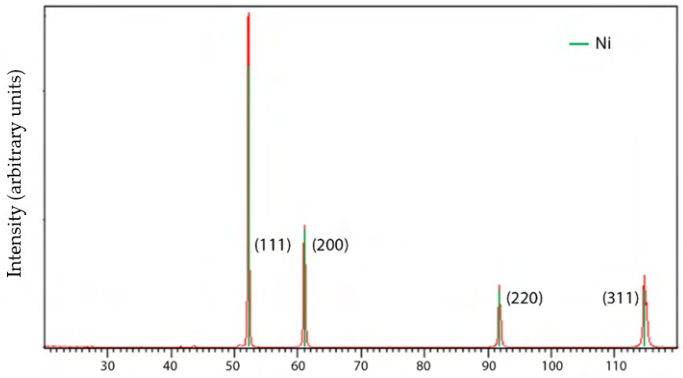

(**b**)

Figure 2. X-ray diffractograms of (**a**) TiH_2 and (**b**) Ni powder.

Table 2. NiTi, TiH_2, and Ni powder particles size, particle size distribution, and specific surface area (SSA).

	NiTi	NiTi	TiH_2	TiH_2	Ni	Ni
D_{10} [µm]	13.4	13.4	3.4	3.4	21.4	21.4
D_{50} [µm]	22.1	22.1	15.3	15.3	30.0	30.0
D_{90} [µm]	34.7	34.7	35.7	35.7	41.2	41.2
SSA [$m^2 \cdot kg^{-1}$]	293.4	293.4	750.2	750.2	207.7	207.7

The evaluation of the critical powder volume concentration (CPVC) [24–26] methodology used in powder injection molding (PIM) feedstocks allows for the optimization of the NiTi filament composition (NiTi powder, master binder, and additives). A torque rheometer, Plastograph Brabender GmbH and Co. (Duisburg, Germany) with a rotation blade speed of 30 rpm at a temperature of 180 °C, was used to optimize the feedstock. The feedstock was granulated and the filament shaped using a single screw extruder Brabender GMBH &

Co. E 19/25 (Duisburg, Germany) without a calibration system and with a nozzle diameter of 1.75 mm. The temperatures in different zones of the extrusion cylinder were 170, 175, and 180 °C (nozzle). In order to confirm the quality of the filament for the additive process (MEX) and function of the powder mixture, several mechanical tests were performed. The equipment was a Stable MicroSystems (Godalming, UK). Specimens with 25 mm in length, randomly removed from the filament spool, and were characterized by tensile and three-point bending tests with a 5 kN loading cell; tensile tests were carried out with a loading rate of 0.5 mm min^{-1} and a gauge length of 10 mm; for the three-point bending tests, the span size was 20 mm. For both tests (tensile and bending), twenty specimens of filament (green) were tested at room temperature for each reference powder particle:

A. NiTi prealloyed powder;
B. NiTi prealloyed powder + 1 wt.% TiH_2;
C. NiTi prealloyed powder + 5 wt.% TiH_2;
D. NiTi prealloyed powder + 5 wt.% TiH_2 and 6.2 wt.% Ni.

Solidworks software from Dassault Systèmes [27] was used to create the 3D models and to export the STL file. The G-Code was created with CURA software from Ultimaker B.V. [28]. A Hephestos2 from BQ (Madrid, Spain) with a nozzle diameter of 0.4 mm was used to create the 3D objects.

The thermal consolidation of the "green" filament/3D object was performed in two steps (debinding followed by sintering) in an H_2 atmosphere. The dwelling times and temperatures were previously optimized [8]. Debinding was performed at a heating rate of 10 °C min^{-1} up to 600 °C followed by sintering at a heating and cooling rate of 5 °C min^{-1} up to 1165 °C during 5 h in a MIM3002T furnace ELNIK Systems (Cedar Grove, NJ, USA). Optical microscopy (OM) and scanning electron microscopy (SEM) FEI Quanta 400 FEG ESEM/EDAX Genesis, Thermo Fisher Scientific (Waltham, MA, USA) were used to analyze the 3D objects. Thermal analyses of sintered parts were performed by differential scanning calorimetry (DSC), allowing for the transformation temperatures to be evaluated. The DSC analysis were carried out in a DSC 204 F1 Phoenix equipment (NETZSCH-Gerätebau GmbH, Selb, Germany), with thermal cycles from −150 °C to + 150 °C and a heating/cooling rate of 10 $K.min^{-1}$. Hardness was evaluated by microhardness testing with HMV equipment from Shimadzu (Kyoto, Japan). Four specimens of each composition were measured 40 times using a maximum load of 10 g. Surface and inside defects of filaments and strands were evaluated by X-ray microcomputed tomography using a Bruker SkyScan 1275 (Bruker, Kontich, Belgium). An acceleration voltage of 80 kV and a beam current of 125 μA was set while using a 1 mm aluminum filter with step-and-shoot mode. Pixel size was set to 6 μm and random mode was used. The images were acquired at 0.2° angular step with five frames average per step using an exposure time of 46 ms. The microCT images were reconstructed with the dedicated manufacturer software.

3. Results and Discussion

A steady state must occur to ensure homogeneity in the mixtures, which is crucial to prevent the formation of secondary phases where the ratio of Ni:Ti is unbalanced. The values of torque for A, B, C, and D are quite similar. However, there is a tendency for a slight increase of torque with the increase of TiH_2 and/or Ni (Table 3). Filaments for all compositions were produced with a CPCV of 60 vol.% of powder particles content, which was the best compromise with the torque value.

Table 3. Steady state torque.

	A	B	C	D
Steady state torque [Nm]	4.2	4.0	4.6	4.8

Table 3. Steady state torque.

	A	B	C	D
Steady state torque [Nm]	4.2	4.0	4.6	4.8

Figure 3 shows microstructures of the green filament cross sections where a multitude of sizes from their constituents is visible. All filaments show similitudes, with good distribution of the multiple particle sizes, which is good to attain an excellent interparticle closeness. This is very important, keeping in mind that the powder particles suitable to indirect additive process must have D50 lower than 10 µm. In filaments A, B, and C, the particles have a shape factor close to 1. However, in filament D (Ni addition), some sharpened particles are observed.

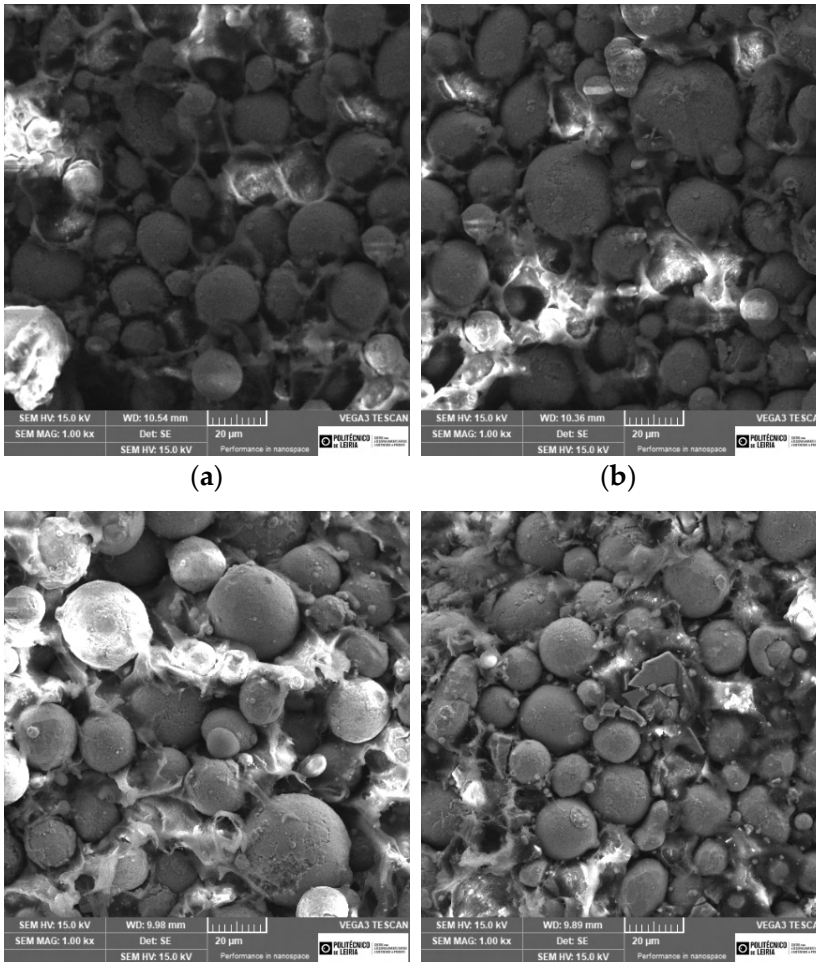

Figure 3. Micrographies of the green filaments (SEM): (**a**) A; (**b**) B, (**c**) C, and (**d**) D.

Regarding the mechanical properties, the Young modulus values are very similar for all compositions (Table 4). The filaments reveal a similar behavior on elastic domain, whatever the feedstock selected.

Table 4. Young modulus of the green filaments (powder + binder + additives).

	A	B	C	D
Young modulus [GPa]	2.6 ± 0.11	2.8 ± 0.15	2.7 ± 0.14	2.5 ± 0.28

Three-point bending tests were performed to highlight the filament homogeneity/reproducibility by the Weibull index (m). This index, when greater than is an indicator of reproducibility of the green filament. The Weibull modulus from the

Three-point bending tests were performed to highlight the filaments homogeneity/reproducibility by the Weibull index (m). This index, when greater than 10, is an indicator of reproducibility of the green filament. The Weibull modulus from the 3-point bending test show significative difference between filaments A, B, and C to the filament D, which has a value almost the double of the other ones (Table 5). This behavior can be attributed to the multiplicity of particle sizes of the different added powder and excellent homogeneity.

Table 5. Weibull modulus of green filaments from 3-point bending tests.

Tests	A	B	C	D
3-point bending	23	29	28	45

The shaping, debinding ,and sintering (SDS) were previously optimized, and the conditions of processing and composition are described elsewhere [8]. Sintering of the preallayed powder (1165 °C) must be enough to guarantee the consolidation of the powder particles, without formation of other intermetallic phases, different from the existent in virgin powder (NiTi + $NiTi_2$ + Ni) [8]. The sintering temperature (1165 °C) is enough to melt the $NiTi_2$ phase (Tm = 984 °C), which can contribute to a liquid phase sintering, accelerating the densification and homogenization processes.

After sintering, the SEM micrographies (backscattered electrons, BSE) suggest the appearance of a new phase (S2) rich in Ni (Ni_3Ti) (Figure 4, Table 6). X-ray diffraction of sintered A (standard) shows: NiTi as the master phase, $NiTi_2$ already present in virgin powder, Ni_3Ti resulting from the diffusion of loose nickel into NiTi and $NiTi_2$ and residual Ni (Figure 5). The semi-quantitative analysis of A shows a significant difference between NiTi and $NiTi_2$ volume percentages (85:15). The white phase distributed around the different grains of NiTi can be attributed to Ni_3Ti (Figure 4).

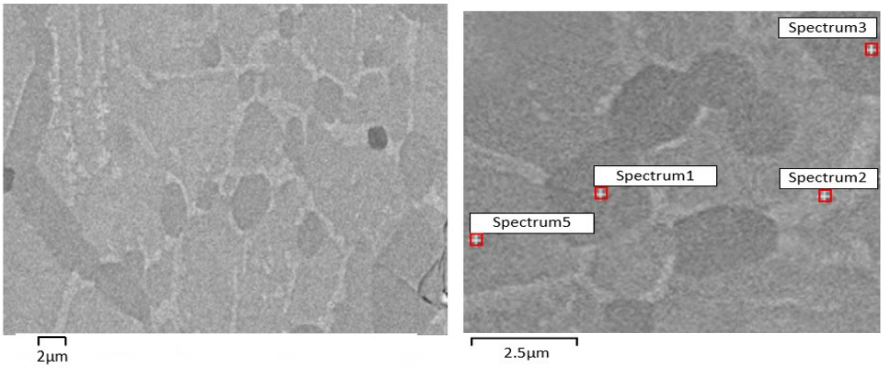

(**a**) (**b**)

Figure 4. Micrographies of 3D object from filament A (**a**) after sintering (SEM), (**b**) selected zones for evaluation of Ni:Ti ratio (S1, S2, S3 and S5) by SEM/EDS.

Table 6. 3D object phases from filament A after sintering (Spectra(5) 1, 2, 3, and 5 in Figure 4b).

Phase Composition (EDS)			
S1	**S2**	**S3**	**S5**
S1 NiTi + $NiTi_2$	S2 Ni_3Ti	S3 NiTi + $NiTi_2$	S5 NiTi

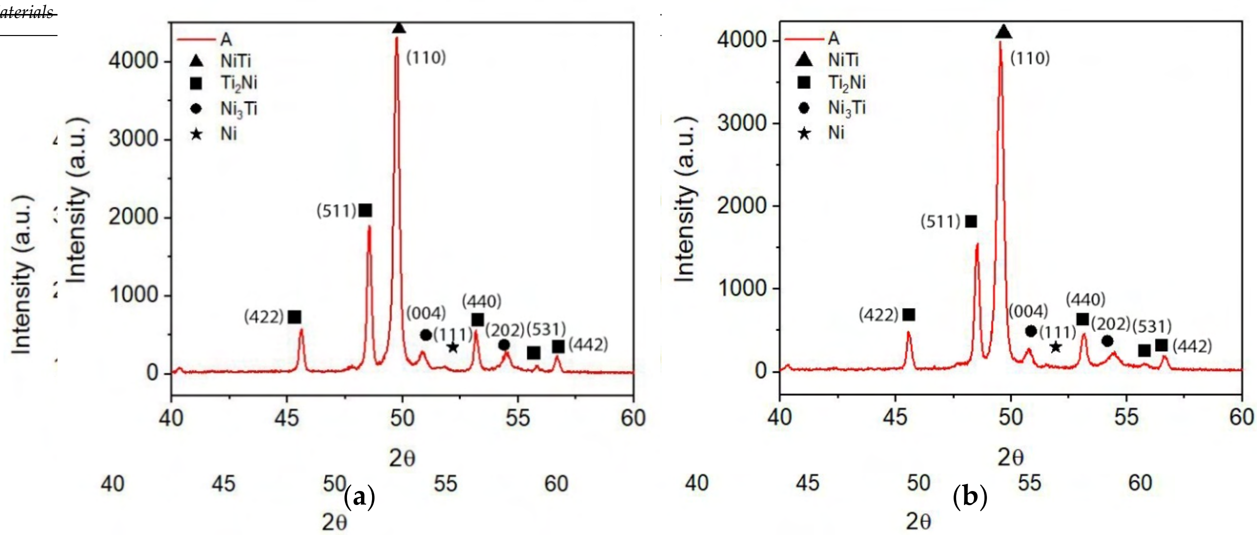

Figure 5. X-ray diffractograms of 3D object from filament A. (**a**) top, (**b**) bottom.

Figure 5. X-ray diffractograms of 3D object from filament A. (**a**) top, (**b**) bottom.

With the addition of 1 wt.% of TiH_2 to NiTi prealloyed powder, no notorious difference is observed. Based on the colors of the SEM micrographies (BSE) and EDS results, three distinct phases (NiTi, $NiTi_2$ and Ni_3Ti) are identified (Figure 6, Table 7). The x-ray diffractogram analysis clearly shows the presence of NiTi, $NiTi_2$ and Ni_3Ti and also Ni from virgin powder (Figure 7). In what concerns the percentages of NiTi and $NiTi_2$, there is a tendency for a small increase of $NiTi_2$ percentage in filament B.

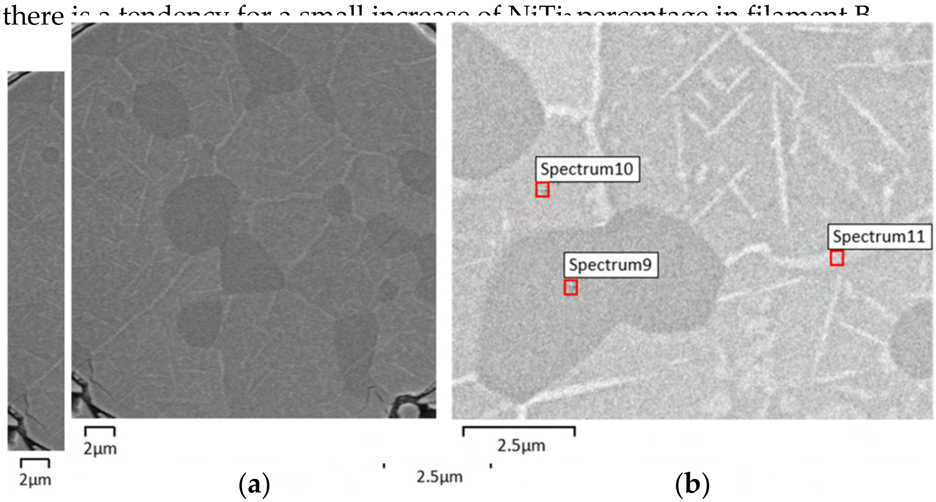

(**a**) (**b**)

Figure 6. Micrographies of 3D object from filament B (addition of 1 wt.% TiH_2). (**a**) after sintering (SEM), (**b**) selected zones for evaluation of Ni:Ti ratio (S9, S10, and S11) by SEM/EDS.

Table 7. Phases from filament B after sintering (Spectra 9, 10, and 11 in Figure 6b).

Phase Composition (EDS)		
S9	S10	S11
$NiTi_2$	NiTi	Ni_3Ti

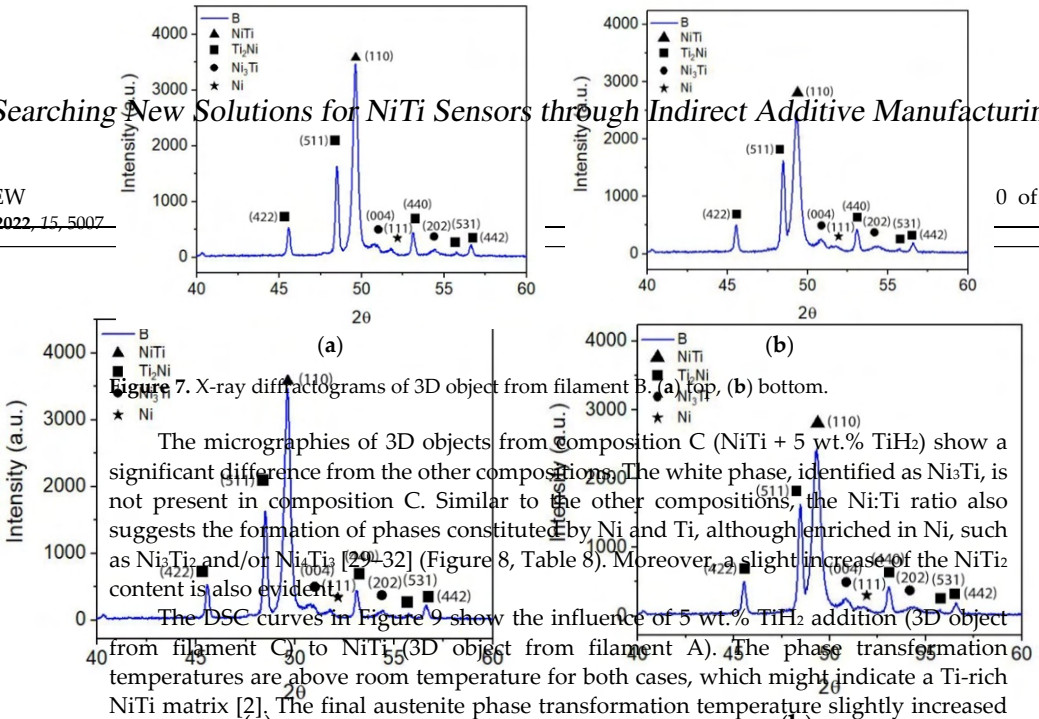

Figure 7. X-ray diffractograms of 3D object from filament B. (**a**) top, (**b**) bottom.

The micrographies of 3D objects from composition C (NiTi + 5 wt.% TiH_2) show a significant difference from the other compositions. The white phase, identified as Ni_3Ti, is not present in composition C. Similar to the other compositions, the Ni:Ti ratio also suggests the formation of phases constituted by Ni and Ti, although enriched in Ni, such as Ni_3Ti_2 and/or Ni_4Ti_3 [29–32] (Figure 8, Table 8). Moreover, a slight increase of the $NiTi_2$ content is also evident.

The DSC curves in Figure 9 show the influence of 5 wt.% TiH_2 addition (3D object from filament C) to NiTi (3D object from filament A). The phase transformation temperatures are above room temperature for both cases, which might indicate a Ti-rich NiTi matrix [2]. The final austenite phase transformation temperature slightly increased with the TiH_2 addition (A_f (A) = 68°C and A_f (C) = 69°C). Moreover, a 3D object from filament C displays the presence of R-phase on cooling, probably due to the increase of the Ti content.

X-ray diffractograms corroborate the SEM results in the apparent disappearance of the Ni_3Ti phase. The possible reaction of free Ti, resulting from dehydrogenation, may have contributed to the formation of $NiTi_2$. The XRD results also support the possible reaction of free Ti resulting from dehydrogenation with free Ni present in the virgin powder, since Ni is not identified in the X-ray diffractograms (Figure 10).

The micrographies of 3D objects from composition C (NiTi + 5 wt.% TiH_2) show a significant difference from the other compositions. The white phase, identified as Ni_3Ti, is not present in composition C. Similar to the other compositions, the Ni:Ti ratio also suggests the formation of phases constituted by Ni and Ti, although enriched in Ni, such as Ni_3Ti_2 and/or Ni_4Ti_3 [29–32] (Figure 8, Table 8). Moreover, a slight increase of the $NiTi_2$ content is also evident.

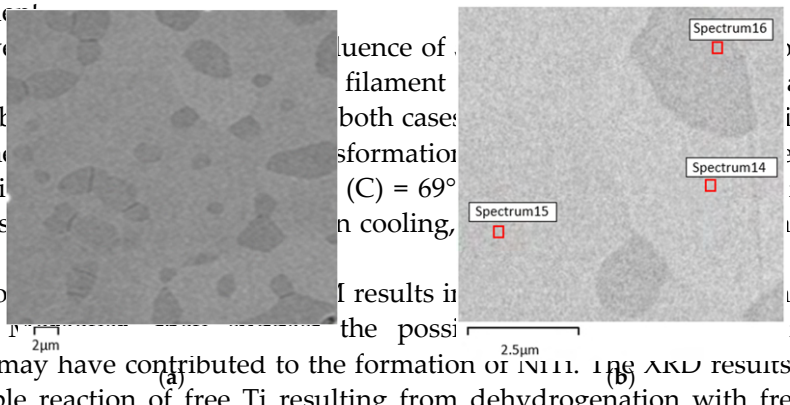

Figure 8. Micrographies of 3D object from filament C (addition of 5 wt.% TiH_2). (**a**) after sintering (SEM), (**b**) selected zones for evaluation of Ni:Ti ratio (S14, S15 and S16) by SEM/EDS.

Table 8. Three-dimensional object phases from filament C after sintering (Spectra 14, 15, and 16 in Figure 8b).

Phase Composition (EDS)		
S14	S15	S16
NiTi	NiTi	$NiTi_2$

The DSC curves in Figure 9 show the influence of 5 wt.% TiH_2 addition (3D object from filament C) to NiTi (3D object from filament A). The phase transformation temperatures are above room temperature for both cases, which might indicate a Ti-rich NiTi matrix [2]. The final austenite phase transformation temperature slightly increased with the TiH_2 addition (A_f (A) = 68°C and A_f (C) = 69°C). Moreover, a 3D object from filament C displays the presence of R-phase on cooling, probably due to the increase of the Ti content.

Figure 8. Micrographies of 3D object from filament C (addition of 5 wt.% TiH_2). (**a**) after sintering (SEM), (**b**) selected zones for evaluation of Ni:Ti ratio (S14, S15 and S16) by SEM/EDS.

Table 8. Three-dimensional object phases from filament C after sintering (Spectra 14, 15, and 16 in Figure 8b).

Phase Composition (EDS)		
S14	S15	S16
NiTi	NiTi	$NiTi_2$

Table 8. Three-dimensional object phases from filament C after sintering (Spectra 14, 15, and 16 in Figure 8b).

Phase Composition (EDS)		
S14	S15	S16

Mate 11 of 18

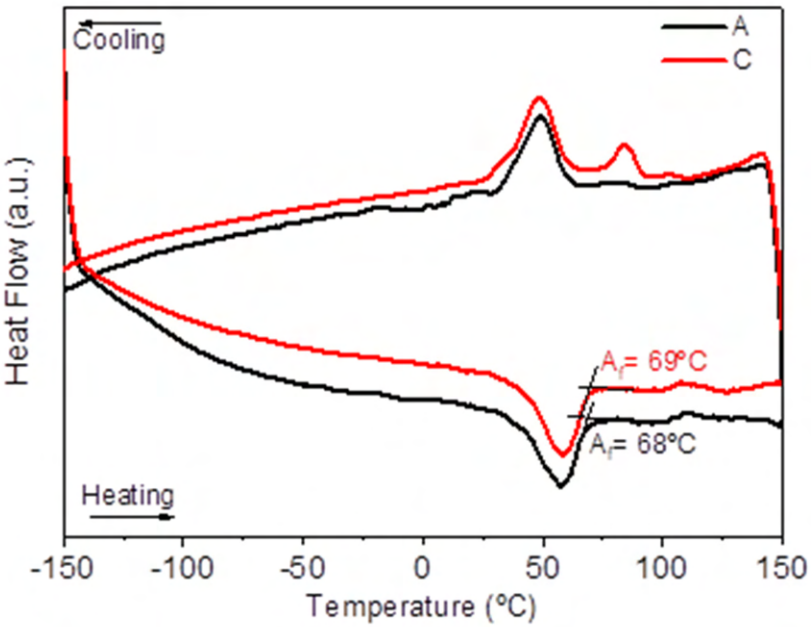

Figure 9. DSC curves of 3D objects from filaments A and C (addition of 5 wt.% TiH_2).

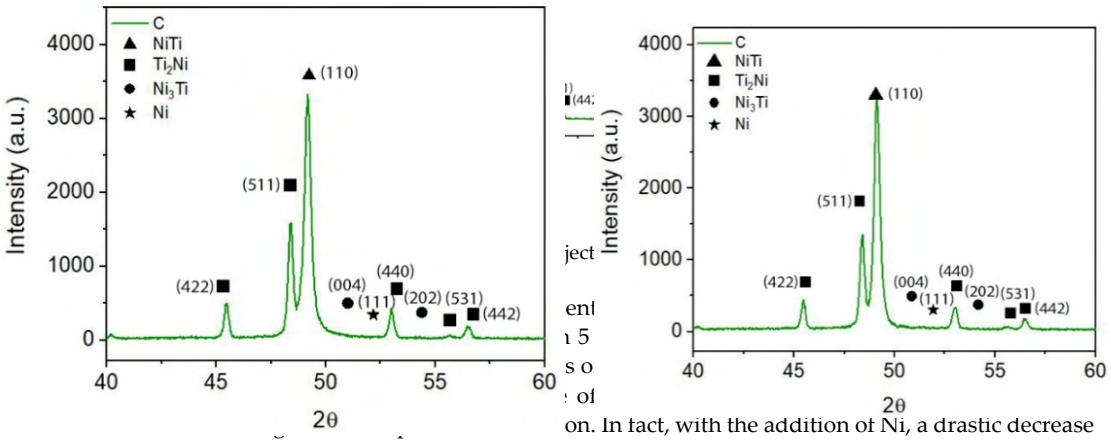

Figure 10. X-ray diffractograms of 3D objects from filament C: (**a**) NiTi; (**b**) NiTi + Ni_3Ti.

Composition D has a supplementary content of Ni (6.2 wt.%) mixed with virgin powder (NiTi + $NiTi_2$ + Ni) and with 5 wt.% TiH_2. This composition has two objectives: first, to highlight the role of the excess of Ni in the Ni_3Ti phase formed during processing, and the second, to analyze the role of the excess of Ni in the disappearance of $NiTi_2$ resulting from NiTi powder fabrication. In fact, with the addition of Ni, a drastic decrease of the $NiTi_2$ is observed, as evidenced in the SEM images of 3D object D (Figure 11) when compared to B (Figure 6) and C (Figure 8) 3D objects. Thus, powder Ni content could be tuned as a possible solution for the disappearance of $NiTi_2$ in order obtain only NiTi in prealloyed powders.

may have contributed to the formation of NiTi. The XRD results also support the possible reaction of free Ti resulting from hydrogenation with free Ni present in the virgin powder, since Ni is not identified in the x-ray diffractograms (Figure 10).

Composition D has a supplementary content of Ni (6.2 wt.%) mixed with virgin powder (NiTi + $NiTi_2$ + Ni) and with 5 wt.% TiH_2. This composition has two objectives: first, to highlight the role of the excess of Ni in the Ni_3Ti phase formed during processing, and the second, to analyze the role of the excess of Ni in the disappearance of $NiTi_2$ resulting from NiTi powder fabrication. In fact, with the addition of Ni, a drastic decrease of the $NiTi_2$ is observed, as evidenced in the SEM images of 3D object D (Figure 11) when compared to B (Figure 6) and C (Figure 8) 3D objects. Thus, powder Ni content could be tuned as a possible solution for the disappearance of $NiTi_2$ in order obtain only NiTi in prealloyed powders.

022, *15*, x FOR PEER REVIEW 12 of 18

Similar to sintered 3D objects from filaments with TiH_2 lower than 5 wt.%, micrographies and x-ray diffractograms from 3D objects with composition D (Ni in excess, other than the pristine one) show again the formation of a white phase identified as Ni_3Ti. Despite the addition of Ni, Figure 11 and Table 9 show the occurrence of a "new phase" almost depleted of Ni, suggesting the presence of Ti without any reaction with other metal present. However, there are no discernible Ti peaks in the x-ray diffractogram (Figure 12).

Similar to sintered 3D objects from filaments with TiH_2 lower than 5 wt.%, micrographies and x-ray diffractograms from 3D objects with composition D (Ni in excess, other than the pristine one) show again the formation of a white phase identified as Ni_3Ti. Despite the addition of Ni, Figure 11 and Table 9 show the occurrence of a "new phase" almost depleted of Ni, suggesting the presence of Ti without any reaction with other metal present. However, there are no discernible Ti peaks in the x-ray diffractogram (Figure 12).

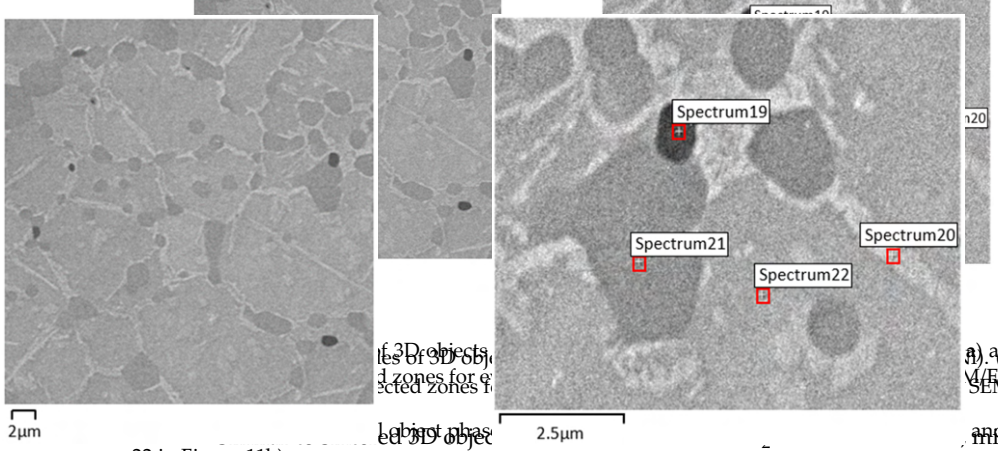

Figure 11. Micrographies of 3D objects from filament D (addition of 5 wt.% TiH_2 and Ni). (**a**) after sintering (SEM), (**b**) selected zones for evaluation of Ni:Ti ratio (S19, S20, S21 and S22) by SEM/EDS.

Table 9. Three-dimensional object phases from filament D after sintering (Spectra 19, 20, 21, and 22 in Figure 11b).

Phase Composition (EDS)			
S19	S20	S21	S22
Ti	Ni_3Ti	$NiTi_2$	NiTi

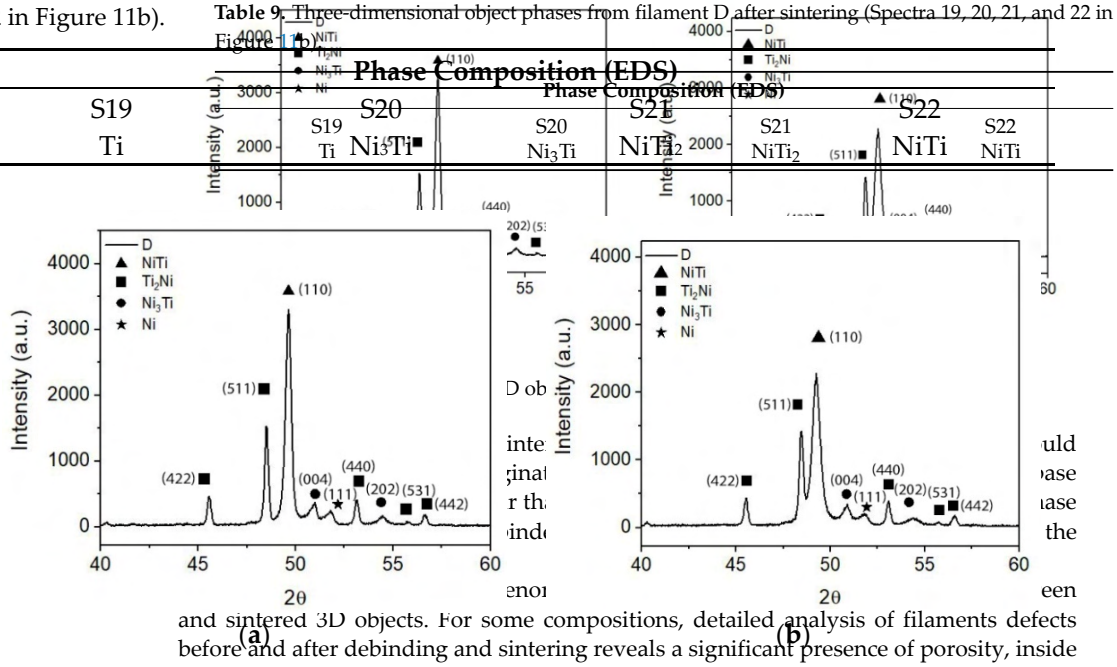

Figure 12. X-ray diffractograms of 3D object from filament D: (**a**) top; (**b**) bottom.

Considering that during sintering the 3D objects are on a platform that could compromise the process and originate the formation of new phases, both the top and base were analyzed by XRD. It is clear that the top and base of 3D objects show similar phase composition, meaning that all binder and additives were effectively removed, and the sintered phases are similar.

Tomography analysis is of enormous importance to detect failures inside the green and sintered 3D objects. For some compositions, detailed analysis of filaments defects before and after debinding and sintering reveals a significant presence of porosity, inside and at the surface. The defects are mainly present in filament D. Filaments A, B, and C,

Tomography analysis is of enormous importance to detect failures inside the green and sintered 3D objects. For some compositions, detailed analysis of filaments defects before and after debinding and sintering reveals a significant presence of porosity, inside and at the surface. The defects are mainly present in filament D. Filaments A, B, and C, sintered at 1165 °C for 5 h, show a low quantity of defects against D that shows a significant content of porosity (Figure 13). Defects in the strands can be inherited from filaments and consequently transmitted to the 3D object. A relation can be observed between filaments and strands of composition D that also shows a large amount of porosity and surface defects (Figure 13).

As a complement, the study of isostatic pressing (IP) was performed in the green filaments. IP is one of the most significant treatments to decrease porosity in filaments/3D objects in the green state (Figure 14). As expected, the most relevant observation is the reduction of porosity in Filament D.

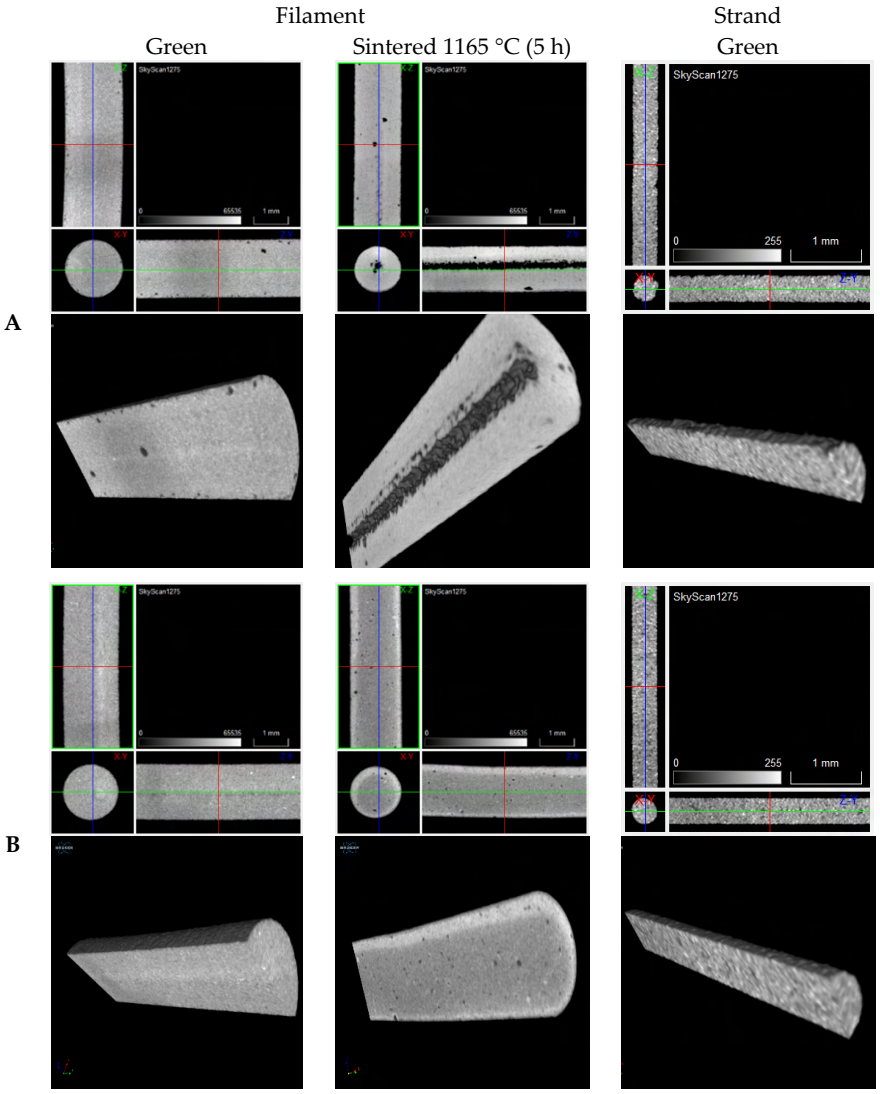

Figure 13. *Cont.*

Materials **2022**, *15*, 5007 *Materials* **2022**, *15*, x FOR PEER REVIEW

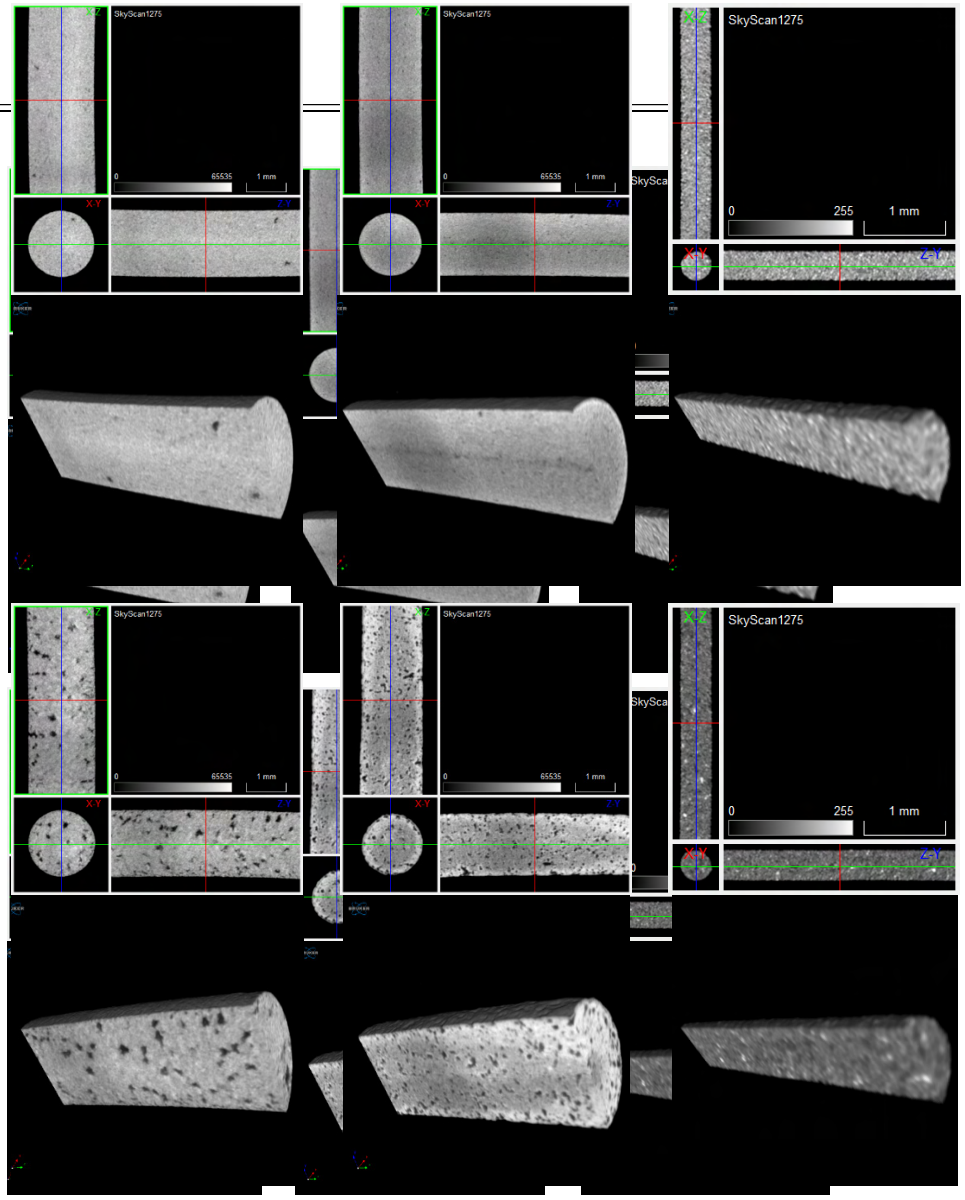

Figure 13. Tomographies of (**A**–**D**) filaments (green and sintered at 1165 °C during 5 h) and strands (**A**–**D**) (green).

Figure 13. Tomographies of (**A**–**D**) filaments (green and sintered at 1165 °C during 5 h) and strands (**A**–**D**) (green).

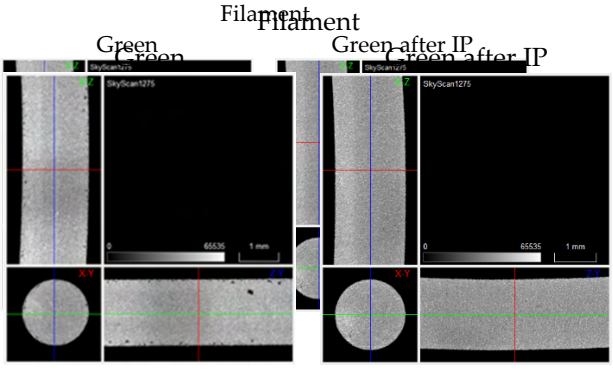

Figure 14. *Cont.*

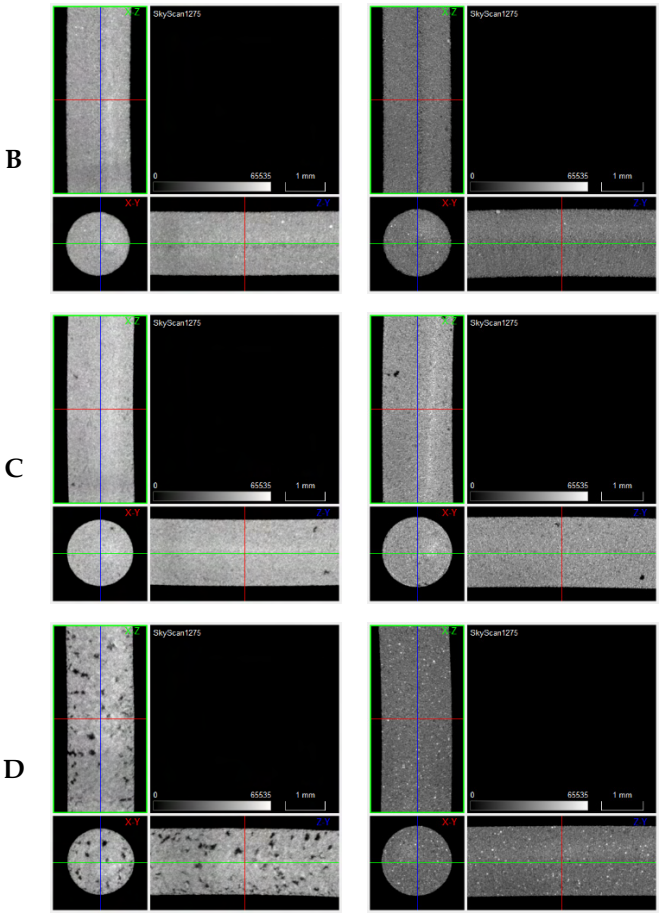

Figure 14. Tomographies of green vs. IP green filaments (**A**–**D**).

Indirect additive manufacturing, such as MEX, could be the sustainable technology ideal for applications where the geometry envisaged could be complex, but the thickness is less than 3 to 5 mm. Moreover, the densification could be improved by the formation of a liquid phase during sintering, allowing the sintering temperature/time to be decreased. For densification, the mechanism of LPS is valid in a system with a very small volume fraction of liquid (e.g., NiTi$_2$), so that the liquid is present only in the neck region between particles. The pore filling mechanism is justified for LPS, where the grain maintains an equilibrium shape. The microstructural evolution observed in the system studied supports the pore filling [33].

Hardness values are higher than the hardness of bulk NiTi (NiTi (B2) 275 HV, NiTi (B19) 112 HV, NiTi$_2$ 163 HV and Ni$_3$Ti 1071 HV [34–37]), confirming the presence of hard phases (i.e., Ni$_3$Ti) (Table 10). The hardness values are similar to those of NiTi 3D objects obtained from other non-conventional technologies (800 HV [38], 700 HV [39,40], and 742 HV [41]).

Table 10. Hardness of the sintered filaments/3D objects (1165 °C, 5 h).

	A	B	C	D
Hardness [HV$_{0.01}$]	887 ± 58	773 ± 68	715 ± 39	677 ± 59

Table 10. Hardness of the sintered filaments/3D objects (1165 °C, 5 h).

	A	B	C	D
Hardness [HV$_{0.01}$]	887 ± 58	773 ± 68	715 ± 39	677 ± 59

In composition C where Ni$_3$Ti was not detected, a lower hardness was expected. Instead, composition D, where Ni$_3$Ti was detected, presents the lowest value. A possible explanation for the decrease in hardness observed for composition D is the presence of the Ti-phase previously identified.

In composition C where Ni_3Ti was not detected, a lower hardness was expected. Instead, composition D, where Ni_3Ti was detected, presents the lowest value. A possible explanation for the decrease in hardness observed for composition D is the presence of the Ti-phase previously identified.

4. Conclusions

NiTi SMA 3D objects manufactured from prealloyed powder by MEX with the lowest possible porosity with a uniform and suitable microstructure were the main objective of the present study.

The presence of $NiTi_2$ with low melting temperature (984 °C) and Ni in the prealloyed powder are expected outcomes of the atomization process. The $NiTi_2$ phase can convert the conventional consolidation process of NiTi based on solid diffusion in a liquid phase sintering process. In addition to decreasing the porosity, the $NiTi_2$ intermetallic phase can also have a significant role when sintering is the consolidation process because it can contribute to the uniformization of the final microstructure. The porosity can be significantly reduced by the isostatic pressing of greens (P = 100 GPa, time = 2 h).

Both $NiTi_2$ and free Ni would be suitable to promote NiTi formation during the liquid phase sintering. The addition of 5 wt.% of TiH_2 to virgin prealloyed powder highlights that Ti (released after dehydrogenation), together with free Ni from pristine powder, contributes to the formation of NiTi instead of Ni_3Ti and total depletion of the loose Ni. The composition of prealloyed powder with 5 wt.% TiH_2 showed after sintering a homogeneous matrix, but yet with a $NiTi_2$ second phase uniformly dispersed. The sintering process was excellent and for all the mixtures studied the phases formed, both at the top and bottom, were similar.

Therefore, the use of MEX for processing NiTi prealloyed powder particles showed promising results, opening a field to new applications of NiTi, namely as a sensor. In the future, the role of $NiTi_2$ in the detection of failure cracks by mechanical sensors must be demonstrated.

Author Contributions: Conceptualization, M.T.V.; methodology, P.C, N.A. and D.G.; validation, A.S.R. and M.T.V.; investigation, P.C. and M.T.V.; writing—original draft preparation, P.C.; writing—review and editing, D.G., A.S.R. and M.T.V.; supervision, M.T.V.; funding acquisition, N.A. and A.S.R. All authors have read and agreed to the published version of the manuscript.

Funding: This work was financially supported by: Project PTDC/CTM-CTM/29101/2017—POCI-01-0145-FEDER-029101, funded by FEDER funds through COMPETE2020—Programa Operacional Competitividade e Internacionalização (POCI), and by national funds (PIDDAC) through FCT/MCTES. This research was also supported by FEDER funds through the program COMPETE—Programa Operacional Factores de Competitividade and by national funds through FCT—Fundação para a Ciência e a Tecnologia under projects UIDB/EMS/00285/2020 and UIDB/04044/2020.

Institutional Review Board Statement: Not applicable.

Informed Consent Statement: Not applicable.

Data Availability Statement: Data sharing not applicable to this article.

Conflicts of Interest: The authors declare no conflict of interest.

References

1. Buehler, W.J.; Gilfrich, J.V.; Wiley, R.C. Effect of Low-Temperature Phase Changes on the Mechanical Properties of Alloys near Composition TiNi. *J. Appl. Phys.* **1963**, *34*, 1475. [CrossRef]
2. Otsuka, K.; Ren, X. Physical metallurgy of Ti–Ni-based Shape Memory Alloys. *Prog. Mater. Sci.* **2005**, *50*, 511–678. [CrossRef]
3. Walker, J.; Elahinia, M.; Haberland, C. An investigation of process parameters on selective laser melting of nitinol. In Proceedings of the ASME 2013 Conference on Smart Materials, Adaptive Structures and Intelligent Systems, Snowbird, UT, USA, 16–18 September 2013. [CrossRef]
4. Vora, J.; Khanna, S.; Chaudhari, R.; Patel, V.K.; Paneliya, S.; Pimenov, D.Y.; Giasin, K.; Prakash, C. Machining parameter optimization and experimental investigations of nano-graphene mixed electrical discharge machining of nitinol shape memory alloy. *J. Mater. Res. Technol.* **2022**, *19*, 653–668. [CrossRef]

5. Yu, Z.; Xu, Z.; Guo, Y.; Xin, R.; Liu, R.; Jiang, C.; Li, L.; Zhang, Z.; Ren, L. Study on properties of SLM-NiTi shape memory alloy under the same energy density. *J. Mater. Res. Technol.* **2021**, *13*, 241–250. [CrossRef]
6. Chmielewska, A.; Wysocki, B.; Kwaśniak, P.; Kruszewski, M.J.; Michalski, B.; Zielińska, A.; Adamczyk-Cieślak, B.; Krawczyńska, A.; Buhagiar, J.; Święszkowski, W. Heat Treatment of NiTi Alloys Fabricated Using Laser Powder Bed Fusion (LPBF) from Elementally Blended Powders. *Materials* **2022**, *15*, 3304. [CrossRef]
7. *ISO/ASTM 52900*; Additive Manufacturing—General Principles—Fundamentals and Vocabulary. ISO: Geneva, Switzerland, 2021.
8. Carreira, P.; Cerejo, F.; Alves, N.; Vieira, M. In Search of the Optimal Conditions to Process Shape Memory Alloys (NiTi) Using Fused Filament Fabrication (FFF). *Materials* **2020**, *13*, 4718. [CrossRef]
9. Suwanpreecha, C.; Manonukul, A. A Review on Material Extrusion Additive Manufacturing of Metal and How It Compares with Metal Injection Moulding. *Metals* **2022**, *12*, 429. [CrossRef]
10. Chen, G.; Liss, K.D.; Auchterlonie, G.; Tang, H.; Cao, P. Dehydrogenation and Sintering of TiH_2: An In Situ Study. *Metall. Mater. Trans. A* **2017**, *48*, 2949–2959. [CrossRef]
11. Chen, G.; Cao, P.; Edmonds, N. Porous NiTi alloys produced by press-and-sinter from Ni/Ti and Ni/TiH_2 mixtures. *Mater. Sci. Eng. A* **2013**, *582*, 117–125. [CrossRef]
12. Bohua, D.; Yasong, Z.; Dezhi, W.; Yingrui, Z.; Chunge, X. Fabrication and Properties of Porous NiTi Alloy by Gel-Casting with TiH2 Powders. *J. Mater. Eng. Perform.* **2017**, *26*, 5118–5125. [CrossRef]
13. Bhosle, V.; Baburaj, E.; Miranova, M.; Salama, K. Dehydrogenation of TiH_2. *Mater. Sci. Eng. A* **2003**, *356*, 190–199. [CrossRef]
14. Chen, G.; Liss, K.-D.; Cao, P. An in situ Study of NiTi Powder Sintering Using Neutron Diffraction. *Metals* **2015**, *5*, 530–546. [CrossRef]
15. Peng, Q.; Yang, B.; Friedrich, B. Porous Titanium Parts Fabricated by Sintering of TiH_2 and Ti Powder Mixtures. *J. Mater. Eng. Perform.* **2017**, *27*, 228–242. [CrossRef]
16. Sun, P.; Wang, H.; Lefler, M.; Fang, Z.; Lei, T.; Fang, S.; Tian, W.; Li, H. Sintering of TiH_2—A new approach for powder metallurgy titanium. In Proceedings of the World Powder Metallurgy Congress and Exhibition, Florence, Italy, 10–14 October 2010.
17. Li, B.-Y.; Rong, L.-J.; Li, Y.-Y. Anisotropy of dimensional change and its corresponding improvement by addition of TiH_2 during elemental powder sintering of porous NiTi alloy. *Mater. Sci. Eng. A* **1998**, *255*, 70–74. [CrossRef]
18. Li, B.-Y.; Rong, L.-J.; Li, Y.-Y. The influence of addition of TiH_2 in elemental powder sintering porous Ni–Ti alloys. *Mater. Sci. Eng. A* **2000**, *281*, 169–175. [CrossRef]
19. Bertheville, B.; Neudenberger, M.; Bidaux, J.-E. Powder sintering and shape-memory behaviour of NiTi compacts synthesized from Ni and TiH2. *Mater. Sci. Eng. A* **2004**, *384*, 143–150. [CrossRef]
20. Chen, G.; Liss, K.-D.; Cao, P. In situ observation and neutron diffraction of NiTi powder sintering. *Acta Mater.* **2014**, *67*, 32–44. [CrossRef]
21. González-Gutiérrez, J.; Stringari, G.B.; Emri, I. Powder Injection Molding of Metal and Ceramic Parts. In *Some Critical Issues for Injection Molding*; Wang, J., Ed.; InTech: Rijeka, Croatia, 2012; pp. 65–88.
22. Carneiro, O.S.; Silva, A.F.; Gomes, R. Fused deposition modeling with polypropylene. *Mater. Des.* **2015**, *83*, 768–776. [CrossRef]
23. Heaney, D.F. *Handbook of Metal Injection Molding*; Woodhead Publishing in Materials; Woodhead Publishing: Thorston, UK, 2012.
24. Barreiros, F.; Vieira, M.; Castanho, J. Fine tuning injection feedstock by nano coating SS powder. *Met. Powder Rep.* **2009**, *64*, 18–21. [CrossRef]
25. Vieira, M.; Martins, A.; Barreiros, F.; Matos, M.; Castanho, J. Surface modification of stainless steel powders for microfabrication. *J. Mater. Process. Technol.* **2008**, *201*, 651–656. [CrossRef]
26. Cerejo, F.; Gatões, D.; Vieira, M.T. Optimization of metallic powder filaments for additive manufacturing extrusion (MEX). *Int. J. Adv. Manuf. Technol.* **2021**, *115*, 2449–2464. [CrossRef]
27. Dassault, S. Solidworks Student Version. 2019. Available online: https://www.3ds.com/products-services/solidworks/ (accessed on 10 May 2019).
28. Ultimaker, B.V. Ultimaker Cura 4.1. 2019. Available online: https://ultimaker.com/en/products/ultimaker-cura-software (accessed on 5 March 2019).
29. Bram, M.; Bitzer, M.; Buchkremer, H.P.; Stover, D. Reproducibility Study of NiTi Parts Made by Metal Injection Molding. *J. Mater. Eng. Perform.* **2012**, *21*, 2701–2712. [CrossRef]
30. Bram, M.; Köhl, M.; Buchkremer, H.P.; Stöver, D. Mechanical Properties of Highly Porous NiTi Alloys. *J. Mater. Eng. Perform.* **2011**, *20*, 522–528. [CrossRef]
31. Schöller, E.; Krone, L.; Bram, M.; Buchkremer, H.P.; Ståaver, D. Metal injection molding of Shape Memory Alloys using prealloyed NiTi powders. *J. Mater. Sci.* **2005**, *40*, 4231–4238. [CrossRef]
32. Bidaux, J.E.; Hidalgo, A.A.; Girard, H.; Rodriguez-Arbaizar, M.; Reynard, L.; Chevallier, J.; Aeby, F.; Giachetto, J.C.; Carreño-Morelli, E. Metal Injection Moulding of Superelastic TiNi Parts. *Key Eng. Mater.* **2016**, *704*, 173–182. [CrossRef]
33. Fang, Z.Z. (Ed.) *Sintering of Advanced Materials—Fundamentals and Processes*, 1st ed.; Woodhead Publishing: Cambridge, UK, 2010.
34. Alnomani, S.A.; Fadhel, E.Z.; Mehatlaf, A.A. Prepare Nitinol Alloys and Improve their Hardness Using Copper as an Alloying Element. *Int. J. Appl. Eng. Res.* **2017**, *12*, 4299–4308.
35. Xu, W.; Rivera-Díaz-Del-Castillo, P.; Wang, W.; Yang, K.; Bliznuk, V.; Kestens, L.; Van Der Zwaag, S. Genetic design and characterization of novel ultra-high-strength stainless steels strengthened by Ni_3Ti intermetallic nanoprecipitates. *Acta Mater.* **2010**, *58*, 3582–3593. [CrossRef]

36. Verdian, M.; Raeissi, K.; Salehi, M.; Sabooni, S. Characterization and corrosion behavior of NiTi–Ti_2Ni–Ni_3Ti multiphase intermetallics produced by vacuum sintering. *Vacuum* **2011**, *86*, 91–95. [CrossRef]
37. Akbarpour, M.; Alipour, S.; Najafi, M.; Ebadzadeh, T.; Kim, H. Microstructural characterization and enhanced hardness of nanostructured Ni_3Ti–NiTi (B2) intermetallic alloy produced by mechanical alloying and fast microwave-assisted sintering process. *Intermetallics* **2021**, *131*, 107119. [CrossRef]
38. Feng, Y.; Du, Z.; Hu, Z. Study on the Effect of Ni Addition on the Microstructure and Properties of NiTi Alloy Coating on AISI 316 L Prepared by Laser Cladding. *Materials* **2021**, *14*, 4373. [CrossRef]
39. Yoshida, M.; Shiraishi, H.; Ikk, N. Microstructure and Mechanical Properties of $NiTi_2$-TiB Composite Fabricated by Spark Plasma Sintering. *World J. Eng. Technol.* **2015**, *3*, 84–88. [CrossRef]
40. Wang, H.; Liu, Y. Microstructure and wear resistance of laser clad $Ti_5Si_3/NiTi_2$ intermetallic composite coating on titanium alloy. *Mater. Sci. Eng. A* **2002**, *338*, 126–132. [CrossRef]
41. Mokgalaka, M.; Popoola, P.; Pityana, S. In situ laser deposition of NiTi intermetallics for corrosion improvement of Ti–6Al–4V alloy. *Trans. Nonferrous Met. Soc. China* **2015**, *25*, 3315–3322. [CrossRef]